Biomolecular approaches to nanophase chemistry

Shenton, Wayne

Award date:
1998

Awarding institution:
University of Bath

Biomolecular Approaches to Nanophase Chemistry

Submitted by Wayne Shenton
for the degree of PhD
of the University of Bath
1998

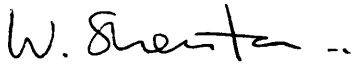

ProQuest LLC
789 East Eisenhower Parkway
P.O. Box 1346
Ann Arbor, MI 48106-1346

ABSTRACT

This thesis describes a new and exciting approach to the fabrication of materials, capitalising on the exquisite intricacies and unsurpassed physicochemical diversity of bio-materials. The macromolecules of life offer a rich cornucopia of chemical systems, specifically designed through evolution to participate in a network of complex chemical reactions. The work reported here aims to demonstrate this vast potential, through the systematic application of bio-systems from each branch of life to current technological goals in areas such as colloidal chemistry, materials synthesis and biomimetics.

Firstly, quantum dots have received much interest due to their non-linear optical and electronic properties, finding applications in a new generation of quantum computers and more efficient quantum lasers. The prokaryotic biomolecule addressing this area of research is lumazine synthase, which is a hollow icosahedral enzyme complex found universally in bacteria. This work shows how the enzyme, which possesses channels of both positive and negative potential, can control the mineralization of inorganic species. The protein is able to self assemble into a variety of architectures, which have been exploited to some degree in the preparation of iron oxide nanoparticles.

Secondly, the construction of superlattices consisting of semiconducting quantum dots could conceivably be used in the construction of ultra dense memory stores. Here, a prokaryotic system has been used for the production of such arrays. For this, S-layers- which are two dimensional protein crystals found universally on the surface of bacteria- have been shown to act as highly specific nucleation sites in the fabrication of both two and three dimensional arrays of cadmium sulfide nanocrystals.

A third aspect of this thesis concerns a eukaryotic system in which the specific molecular recognition properties of antibodies are employed to address current goals of 'matter organisation' on the nanoscale. By design of 'janus' antigens, possessing abilities to cross link nanocrystal surface-antibodies, huge self assembled macroscopic aggregates of colloidal particles are produced with a degree of order. A current goal in colloidal science is focused on the synthesis of bimetallic aggregates and antibody-antigen

interactions are shown to fabricate these materials, due to the inherent flexibility of the system.

A further aspect of antibody-antigen interactions applied to the fabrication of materials is then presented which investigates the fabrication of inorganic-organic aggregates from gold nanoparticles and the iron storage protein ferritin. Chemical modification of the surface of ferritin with biotin is shown to allow the formation of aggregates upon addition of Anti-biotin antibody/gold nanoparticle conjugates.

Finally, nanotubes generate a wealth of interest due to their possible applications in the new science of nanotechnology. The tubular architecture of tobacco mosaic virus is shown to act as a nanoscale template and is representative of the final class of biomolecules employed, namely viruses. It is demonstrated that the high stability of the virion, together with its symmetric arrangement of sub-units, allows the fabrication of a wide range of inorganic/organic nanotube composites. Sol-gel techniques are shown to produce micron sized linear TMV/silica composites and co-precipitation reactions result in CdS, PbS and Fe composites of TMV. The ability of TMV to self assemble into higher order structures further demonstrates the versatility of these structures.

For Mum, Dad, Katten and Family

Contents

Acknowledgements

I would first like to thank my supervisor, Professor Stephen Mann, for guidance and inspiration during this PhD.

I would also like to thank the following people for supplying the raw materials and also for very helpful discussions, without which none of the work would have been possible : Professor Gerald Stubbs, Vanderbilt University, Tennessee, USA ; Dr. J. Allan Dodds, Dept. Plant Pathology, University of California, USA; Dr. Dietmar Pum, Zentrum für Ultrastrukturforschung, Universität für Bodenkultur und Ludwig Boltzmann-Institut für Ultrastrukturforschung, Austria; Dr. Trevor Douglas, Temple University, Philadelphia, USA; Professor Wolfgang Baumeister, Max-Planck Institute for Biochemistry, Munich; Professor Adelbert Bacher, the Institiut für Organische Chemie und Biochemie, Technische Universität München; Dr. Markus Fischer, the Institiut für Organische Chemie und Biochemie, Technische Universität München, München; Dr. Helmut Cölfen, Max-Planck Institut für Kolloid und Grenzflächenforschung, Teltow, Berlin; Dr. Robin Hicks and Dr. Gary Taylor, Department of Biochemistry, The University of Bath, England.

Thanks to Dr. Sean Davis, Dr. Sandy Burkett and Dr. Kim Wong for help in experimental work.

A big shout to Giuseppe Ruggiero for work on computer generated images and for the many top japes and comedy gags over the past few years!
Thanks also to all the staff in the Department of Electron Optics, The University of Bath and thanks to the following, for making the three years bearable : Steve 'Simso' Sims, Chris Fowler, Eric Mayes, Mei Li, Simon Hall, Mikey 'I was there' Maxwell, Heidi Aubrey, Iggy, Clare Houghton, Michael Breulmann, Harish Patel and anyone else I forgot to mention.

Objectives

The nature of the work in this thesis is highly interdisciplinary, with aspects ranging from inorganic and organic chemistry, biology, biochemistry and materials synthesis. The theme of the work is the application of biomolecular systems to problems in materials chemistry and to show how the intrinsic properties of a variety of biomaterials can be tailored to meet current technological goals.

An aspect of the theme of this work is thus to establish a firm foundation for future work, through a systematic survey of bio-molecular systems from the two major divisions of life found on the planet, namely prokaryotic and eukaryotic. A third class of system studied is that of viruses, which cannot be considered 'living', although representing a marvel in biological engineering and important class of biomaterial. Through the systematic approach outlined in this thesis, it is hoped that this field of research will establish an identity, thereby becoming an interdisciplinary subset of materials synthesis. It should be said that there has been tremendous work done recently with bio-materials, ranging from DNA[1] and protein cages[2,3] to bacteria[4] and viruses[5], but the work presented in this thesis presents new systems from the full spectrum of bio-materials. In this respect, an attempt is made to demonstrate the potential of this field and to collate these disparate works into a single subject area, that of 'nanophase biomolecular chemistry'.

The introduction thus presents a general account of the biological concepts and terms used throughout the work, necessary to understand the full versatility of each system and to appreciate the underlying theme of this body of work. An understanding of the biological terminology evoked throughout the thesis, and the network of ideas pervading each chapter was deemed essential. Consequently the general introduction seemed a necessary prerequisite, introducing the terms eukaryotic, prokaryotic and virus, as well as an introduction to the architecture of the complex biomolecules used. The fledgling science of 'nanotechnology' is then introduced, allowing a glimpse into the potential applications for the biomolecular systems developed here.

Each chapter represents a distinct area of research and consequently is quite self contained, although submitting to the theme introduced in the abstract. For this reason the chapters are split into two parts, the former giving a description of the area of current technological interest the system aims to address and the latter giving a detailed description of the biological system employed, its physiochemical properties and the results obtained.

Overall, the aim of this work is to show the vast potential of bio-molecular systems in the field of materials synthesis and the myriad of unique properties inherent to each system. The two prokaryotic systems employed represent proteins of very different morphology, in that lumazine synthase is a hollow icosahedral enzyme and S-layers are two dimensional protein crystals. Antibodies -the Y-shaped proteins of the immune system- are representative of the eukaryotic system employed, the specific recognition properties of these extraordinary proteins being utilised in various guises. Finally, the viral system utilised is a plant pathogen called tobacco mosaic virus. This is a tubular array of proteins arranged helically around a single strand of RNA. Through the employing of such contrasting biomolecular systems, it is hoped that a modicum of the potential for this field of materials synthesis is conveyed to the reader.

One of the most intriguing aspects of this work was that every system, without exception, displayed unexpected higher properties on application to the area under investigation. Many systems displayed advantageous properties that eclipsed many current synthetic systems and some systems displayed characteristics that were completely unpredictable, resulting in a flood of different avenues of research. For this reason alone, this new era of nanophase biomolecular chemistry offers exciting promise for the future, with the possible fabrication of a wide range of novel materials.

W.S (1998)

References

1 E. Braun, Y. Eichen, U. Sivan, G. BenYoseph, (1998) DNA-Templated Assembly and Electrode Attachment of a Conducting Silver Wire, *Nature*, **391**, p775-778

2 F. C. Meldrum, B. R. Heywood, S. Mann, (1992) Magnetoferritin: In Vitro Synthesis of a Novel Magnetic Protein, *Science,* **257**, p522-523.

3 T.Douglas, D.P.E.Dickson, S.Betteridge, J.Charnock, C.D.Garner, S.Mann (1995) Synthesis and Structure of an Iron(III) Sulfide-Ferritin Bioinorganic Nanocomposite, *Science*, **269**, p54-57

4 S. A. Davis, S. L. Burkett, N. H. Mendelson, S. Mann (1997) Bacterial Templating of Ordered Macrostructures in Silica and Silica-Surfactant Mesophases, *Nature,* **385**, p420-423

5 T. Douglas, M. Young, (1998) Host-Guest Encapsulation of Materials by Assembled Virus Protein Cages, *Nature*, **393**, p152-155

Chapter 1

Introduction

As scientists attempt to understand a living system, they move down from dimension to dimension, from one level of complexity to the next. I followed this course in my own studies. I moved from anatomy to the study of tissues, then to electron microscopy and chemistry and finally to quantum mechanics. This downward journey through the scale of dimensions has its irony, for in my search for the secret of life I ended up with atoms and electrons, which have no life at all. Somewhere along the line, life has run out through my fingers.

Albert Szent-György

1.1 The Machinery of Life

The biosphere contains a bewildering number of evolutionary designed biomolecules that participate in a network of chemical reactions of inordinate complexity. This introduction presents an account of the emergence of the major class of biomolecules, that of proteins. The constituents, structure and specific adaptive architecture of proteins are then discussed, together with an introduction to the phyla of organisms found on Earth, in which proteins are of paramount importance .

Recent initiatives in materials science have employed the use of proteins, as well as other biomolecules in the fabrication novel materials. The introduction therefore concludes with an introduction to the science of molecular machines called nanotechnology. The biological aspects of this science are then presented in the subsection 'nanobiology', exploring some of the work currently utilising biological systems in the fabrication of new materials.

1.1.1 Molecular Evolution

All life on Earth is thought to have arisen around 3.5 million years ago. It is thought that prior to this time period simple organic molecules may have existed, generated in the primitive atmosphere of water vapour, methane, hydrogen and ammonia, the reactions being driven by lightning or UV light. This hypothesis is given credence by an experiment performed by two American chemists, Harold Urey and Stanley Miller[1]. The experiments set out to mimic the primordial conditions of earth in the laboratory by circulating a mixture of methane, water, ammonia and hydrogen through a reaction vessel. The vessel was heated and exposed to an electrical discharge to simulate lightening and the result was a chemical 'soup', which revealed substantial amounts of amino acids, the elements of all proteins.

Amino acids and nucleotides can associate to form the polymers proteins and nucleic acids, an ability recognised as essential for living systems. A recent hypothesis[2] suggests that the earliest forms of 'living' matter were entirely protein based, a so called 'protein world'. Auto-catalysis would then allow the evolution of the characteristics associated with life, such as reproduction and metabolism. Such a system could

conceivably be described as a very basic form of life, satisfying certain prerequisites such as competition and chemical equilibrium or 'death', resulting from environmental stresses, such as temperature change.

It is thought that over a period of time the protein based world evolved and was then replaced by an 'RNA world'[3]. The nucleic acid polymer is based on the more complex subunits of nucleotides. Polynucleotides allow the production of copies of themselves through the complementary base pairing of subunits, serving as an information storage system. The templating mechanism of RNA inevitably produced errors and through constant replication of these molecules new variants could be continually produced, leading to a form of natural selection. These properties, together with the establishment of catalytic 'ribozymes'[4], effected the dawn of the RNA world.

There is strong evidence[5] that self replicating RNA molecules associated with simple organic molecules such as polypeptides to begin the process of evolution around 4 billion years ago. It seems likely that the RNA guided a clumsy version of protein synthesis thus establishing the 'genetic code', where the specific sequence of constituent amino acids needed to form the protein molecule is 'spelled out' by a sequence of three letter words in the form of nucleotide sequences. The RNA used for storage of the genetic information was then superseded by the more stable DNA, although RNA retained a crucial role in the translation and transcription of proteins. The process of evolution thus established the current DNA based molecular form of all life on Earth.

1.1.2 Evolution of the Cell

These complex systems of replication and information storage, based on nucleic acid, necessitated the need for compartmentalisation. This need for containment was met by another class of molecule having the physiochemical property of being amphipathic. Amphipathic molecules of specific shape can spontaneously form bilayers[6] in aqueous environments. The formation of closed vesicles of amphipathic molecules surrounding the self-replicating mixture of nucleic acids and other molecules then led to the formation of primitive 'cells'[7].

It is believed that all organisms on earth derive from a single primordial cell termed the 'ancestral prokaryote'[8]. From the ancestral prokaryote there evolved three

basic forms of cell; prokaryotic, comprising bacteria; archaebacteria, comprising the extremophiles[9] and eukaryotic, comprising yeast, plants and animals. Prokaryotic cells are characterised by tough protective cell walls, beneath which a plasma membrane encloses a single cytoplasmic compartment containing DNA, RNA, proteins and small molecules. Most bacteria are prokaryotic and one of the oldest species is *cyanobacteris*[10] which produces energy from photosynthesis. The by-product of photosynthesis is molecular oxygen, an accumulation of which in the atmosphere, over millions of years, caused the development of the next evolutionary step in cellular evolution, the eukaryotic cell[11]. In contrast to prokaryotic cells, eukaryotic cells show a variety of internal structures such as nuclei and mitochondria, the latter believed to be symbiotically associated primitive prokaryotes[12]. Eukayotic cells then developed an aerobic energy producing pathway called oxidative phosphorylation.

In the classification of life forms found on the Earth, viruses occupy a unique position. They exist at the periphery of the definition of 'life' exhibiting several features common to all organisms and yet still remain as 'parasitic organic machines', intent only on replication. Viral life cycles occasionally constitute a parasitic relationship, subverting the genetic mechanisms of a cell for their own benefit. Invariably, this 'Trojan Horse' subterfuge results in complete devastation of the host cell. Essentially all viruses are composed of a single strand of nucleic acid, either RNA or DNA, and a protein coat called a capsid, the latter occurring in various forms, from the regular polyhedra found in satellite viruses to the protein tube of tobacco mosaic virus.

1.1.3 Proteins

Proteins have been described as the 'building blocks of life', this in no way being an underestimate. Indeed the word *protein* was coined by J.J.Berzelius[13] in 1838 from the Greek word *proteios* which means 'of the first rank', emphasising the importance of this class of biomolecule. Proteins are ubiquitous and intrinsic to life on earth, their functional diversity underlying all known biological processes. Some of the many functions include, acting as structural components, storage and transport of electrons in photosynthesis and energy production. They transmit information between cells and destroy potential pathogens and are crucial components of muscle, involved in the conversion of chemical

energy to mechanical energy. In spite of this diversity, proteins belong to the same class of homogeneous molecules, all being linear polymers comprised of various combinations of just 20 amino acids. The overwhelming functional adaptation of proteins can be partly accounted for by the chemical diversity of the amino acids, but primarily the diversity of function arises from the profusion of three dimensional structures proteins can adopt.

1.1.3.1 Amino Acids

The 20 amino acids found in biological systems possess a wide variety of chemical properties (Fig. 1). This variety is enhanced when the amino acid residues are combined in a polymer chain, giving a protein chemical properties far outweighing the sum of the properties of its constituent amino acid residues.

Thus, to understand the nature of a protein by analysis of the individual properties inherent to a single amino acid is meaningless, although such an analysis offers valuable insights into actual protein behaviour. Analysis of amino acid residues necessarily involves collation into groups of comparable chemical properties and similar chemical reactivity of the side chains offers a means of compartmentalisation. Thus, the amino acid residues are classified as aliphatic (Ala, Val, Leu, Ile), hydroxyl (Ser, Thr), acidic (Asp, Glu), amide (Asn, Gln), basic (Lys, Arg) and aromatic (Phe, Tyr, Trp). Several other residues are found in proteins, not conforming to these divisions, namely Gly, Pro, His and the two sulfur containing residues, Met and Cys.

1.1.3.2 Protein Architecture

The constituent amino acids of proteins are linked via the carboxyl and amino groups to form a peptide bond, this bond conveying important properties to the protein due to its rigidity and planarity, properties resulting from the partial double bond character between the constituent carbon and nitrogen atoms. The amino acids are therefore able to form polypeptide chains of varying length,

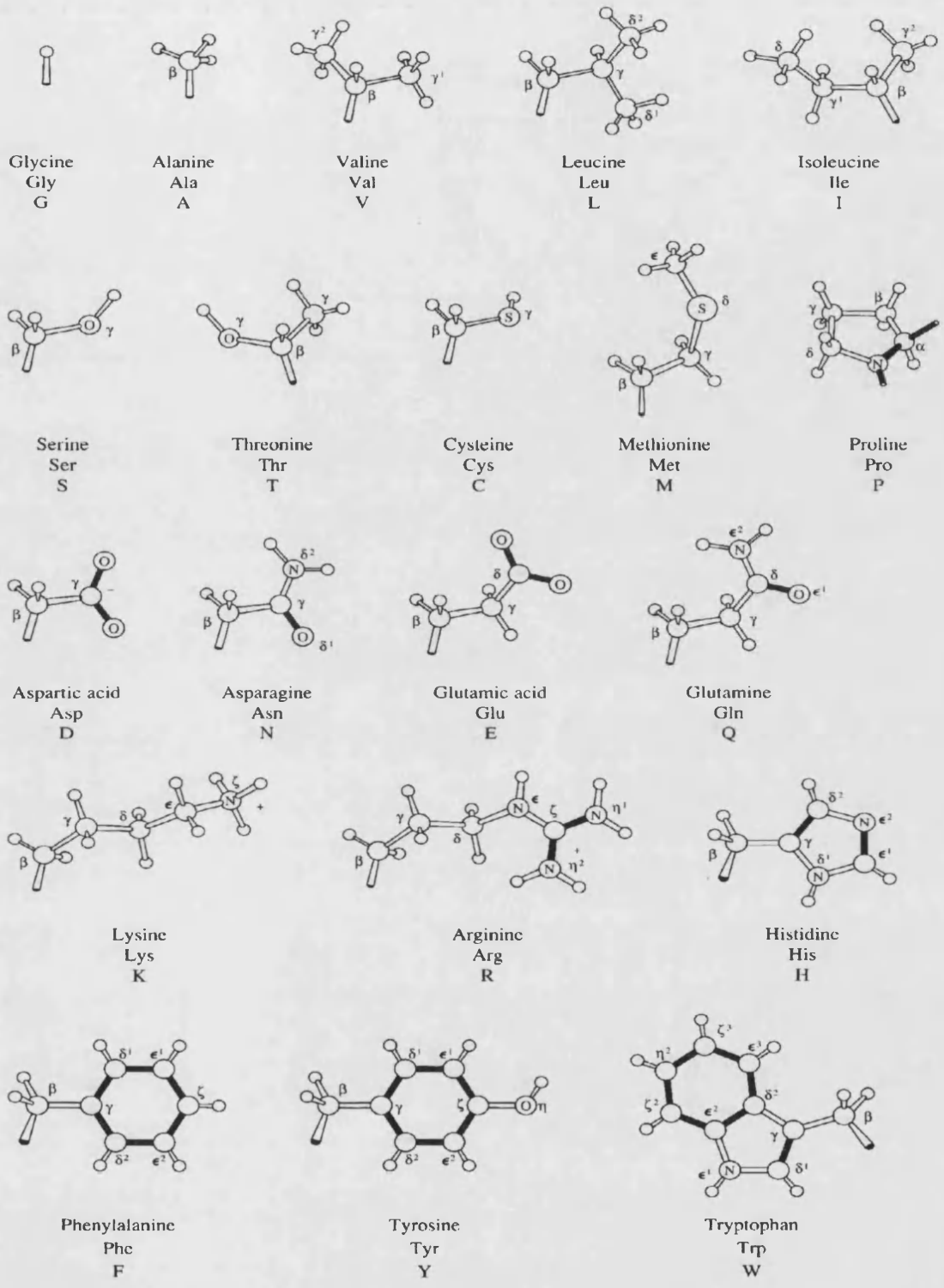

Figure 1 Diagram of the 20 amino acid side chain residues found in biological proteins[14].

having precisely defined amino acid sequences. A process know as 'protein biosynthesis' is responsible for converting the genetic code in DNA into its RNA equivalent, the RNA then being translated into the protein.

Many polypeptide chains are able to assume certain regular structures, known as the alpha helix and beta sheet. The α-helix is a tightly coiled cylindrical structure stabilised by hydrogen bonds between the NH and CO groups of the backbone. The β-sheet exists naturally in two conformations, the parallel and anti-parallel β-sheet. The parallel β-sheet has adjacent chains running in the same direction, whereas the anti-parallel has them in opposite directions. Structures such as silk consists of stacks of parallel β-sheets.

The architecture of proteins essentially consists of four levels of structure. The primary structure is the sequence of amino acids. The secondary structure is the spatial arrangement of amino acid residues, elements of which are the α-helix and β-sheet. A closely related structural classification is the tertiary structure. This refers to the spatial arrangement of secondary elements and their association from very different parts of the polypeptide chain, giving a closer indication of the three dimensional structure. Quaternary structure refers to the spatial arrangement of protein subunits that comprise many complex macromolecular protein assemblies.

1.1.3.3 Macromolecular Assemblies

A variety of proteins consist of many domains possessing specific functions. Proteins have evolved by the splicing together of genes coding for these domains resulting in huge multi-domain proteins with elaborate functions[15]. A still higher order assemblage results from those proteins comprised of multiple individual subunits forming huge protein 'machines'. Cells have evolved these protein machines for the same reason that humans have invented electronic and mechanical machines, for manipulations that are spatially and temporally co-ordinated through linked processes. Actions such as these are more easily achieved though protein assemblies, rather than the sequential use of individual tools. Some examples of protein machines are the photosynthetic macromolecule known as bacteriorhodopsin, the RNA translating ribosome, and the highly elaborate nuclear pore complex found in eukaryotes, which facilitates transport

across the nuclear membrane. Many such protein machines and assemblies have recently attracted much interest, due to their possible application in the fledgling science of nanotechnology, discussed in the next section.

1.2 Nanotechnology

In his lectures, the late Richard Feynman[16] asked his audience to imagine a future where drugs no longer exist. Instead of ingesting pills and potions, 'tiny machines' within the body arrange atoms into the desired molecule and precisely position the molecule for maximum effect. In this future, cancer patients defeat their disease by playing a video game in which actual cancer cells within the body are viewed on screen and zapped at the press of a button by a microscopic armada on manoeuvre in the blood stream. This, among other things, is the future envisioned by some theorists of nanotechnology.

Nanotechnology is a fusion of chemistry and engineering, the term referring to the fabrication of structures possessing nanometer dimensions. Success in this field would allow the synthesis of a wide variety of 'quantum structures' exhibiting properties that differ greatly from their bulk counterparts. For many theorists the ultimate goal is the fabrication of 'nanoengines', the processes of which allowing molecular reorganisation and the capacity to program matter with atomic precision, thus totally changing the economic, ecological and cultural fabric of society.

One aspect of nanotechnology is the production of nanomaterials possessing properties distinctly different from their bulk counterparts. Since nanomaterials possess unique, beneficial chemical, physical, and mechanical properties, they can be used for a wide variety of applications. A few examples of such potential applications include:

Next-generation computer chips. The microelectronics industry has been emphasising miniaturisation, whereby the circuits, such as transistors, resistors, and capacitors, are reduced in size[17]. By achieving a significant reduction in their size, the microprocessors which contain these components can run much faster, thereby enabling computations at far greater speeds. However, there are several technological impediments to these advancements, including lack of the ultrafine precursors to manufacture these components and poor dissipation of the tremendous amount of heat generated by these

microprocessors. Nanomaterials may help the industry break down these barriers by providing the manufacturers with nanocrystalline starting materials, ultra-high purity materials, materials with better thermal conductivity and longer-lasting, durable interconnections.

Phosphors for high-definition TV

The resolution of a television depends greatly on the size of the pixel. These pixels are essentially made of materials called "phosphors," which glow when struck by a stream of electrons inside the cathode ray tube. The resolution improves with a reduction in the size of the pixel, or the phosphors. Nanocrystalline zinc selenide, zinc sulfide, cadmium sulfide and lead telluride synthesised by the sol-gel technique are candidates for improving the resolution of monitors.

Large electrochromic display devices

An electrochromic device consists of materials in which an optical absorption band can be introduced, or an existing band can be altered by the passage of current through the materials or by the application of an electric field. Nanocrystalline materials, such as tungstic oxide ($WO_3.xH_2O$) gel, are used in very large electrochromic display devices. The reaction governing electrochromism (a reversible colouration process under the influence of an electric field) is the double-injection of ions (or protons) and electrons, which combine with the nanocrystalline tungstic acid to form a tungsten bronze. Electrochromic devices display information by changing colour when a voltage is applied. When the polarity is reversed, the colour is bleached. The resolution, brightness, and contrast of these devices greatly depend on the tungstic acid gel's grain size.

Advances in nanofabrication have suggested electronic devices may transcend the limitations of lithography and produce devices in the molecule range, one possible contender being the 'quantum dot'[18]. The potential of nanotechnology to produce the next generation of materials is currently under investigation and an enormous amount of recent work continues to add weight to these predictions. One goal envisioned by nanotechnologists is in the production of a new generation of 'nanocomputers'. This is best summed up by a quote from the Nobel lecture of J.-M.Lehn[19] and is indicative of the commitment of some people involved in this field of research.

'Components and molecular devices such as molecular wires, channels, resistors, rectifiers, diodes and photosensitive elements might be assembled into nanocircuits and combined with organised polymolecular assemblies to yield systems capable ultimately of performing functions of detection, storage, processing, amplification, and the transfer of signals and information by means of various mediators (photons, electrons, protons, metal cations, anions and molecules) with coupling and regulation.'

A new avenue in the production of nanomaterials takes nature as its inspiration, that of 'nanobiology'. Nanobiology involves such disciplines as biochemistry, molecular biology and biomimetics[20], producing new biologically based and biologically inspired materials.

1.3 Bionanotechnology

Nanotechnology offers the prospect of designing and building novel materials and devices at the atomic level. A long-term goal of this field is to devise nanomachines that will be able to store, retrieve and replicate programs accurately, acquire raw materials, assemble them according to their programming, and obtain or generate the energy needed to carry out these elementary processes[21]. Such capabilities are necessary before a nanomachine can ultimately replicate itself. Much of the current work in the design of nanomachines has utilised mechanical analogies in an attempt to duplicate macroscopic mechanisms, such as gears and rods, on a microscopic scale.

An alternative paradigm to the 'mechanical engineering' approach to nanomachines is provided by biological systems. At the cellular level, information is stored by sequences of nucleic acids, which constitute the programs for the key functions of the organism. With the aid of appropriate enzymes, the specific sequence of nucleic acids is replicated and when necessary, repaired. Other enzymes enhance the rates of chemical reactions in cells by several orders of magnitude. These reactions allow for building long bio-polymers and operating the cellular machinery in an accurate and highly controlled manner. Such complexity and specificity is the inspiration for bionanotechnology.

By definition, a nanobiological process could be described as any process which utilises the contrived manipulation of individual biomolecules or biomolecular structures to fulfil a desired task. Biophysicists in the past, studied life successfully at the molecular level (about 1nm) as well as at the cellular level (about 10μm) but left a wide gap in between, in which bio-molecular systems self-organise into supramolecular structures to carry out the regulation and expression of genes, locomotion, transport and other key functions. Micro-manipulation methods, like atomic force microscopy, have advanced nanometer scale observation considerably. Bionanotechnology is a true challenge to chemists, physicists and materials scientists since it deals with co-operative systems of many sub-units which undergo structural changes and concerted dynamics. Nanobiology furnishes, thereby, the conceptual bridge between physics, chemistry and biology since at the nanometer scale bio-molecules assume their collaborative roles which differentiate living from non-living systems.

There is currently being realised a great potential for the application of a variety of biological systems to current technological problems. Chemists, materials scientists and physicists are currently capitalising on the extraordinary properties of bio-molecular systems to produce novel materials, from bio-ceramics to bio-computers. Several examples of this emerging field are given in the next sub-sections, together with current nanobiological applications.

1.3.1 Bio-Molecular Devices

I) DNA Computers

For biological systems, DNA is a master problem solver, storing and manipulating prodigious amounts of information. Recently, researchers have been investigating whether the problem-solving power of DNA can be used to solve non-biological problems, specifically problems from computer science that are out of the reach of traditional computers. Would a DNA computer actually work? In his groundbreaking 1994 paper[22], Leonard Adleman described a laboratory experiment involving DNA and a problem known as the Directed Hamiltonian Path Problem. In his experiment, Adleman took the first step toward the solving of this problem by use of a biological computation device. Adleman's device did not solve the problem in all its

generality. What it did do was provide the first physical implementation of the idea of using DNA for computation. DNA computers are massively parallel. They can execute 10^{14} MIPS (Millions of Instructions Per Second) whereas the fastest conventional computers can only execute 10^{9} MIPS. The reason is that chemical reactions occur very fast and in parallel, so that if the DNA molecules are synthesised with a chemical structure that represents numerical information, a vast amount of number crunching is done as the reaction proceeds. With only 0.5kg. of DNA you have more computing power than all the computers ever made. A DNA computer can solve Hamiltonian Path problems in a matter of weeks, an electronic computer would take more time than the universe has been in existence.

II) Protein Based Computer Memories

Molecular electronics offers a powerful and cost-effective path towards computer miniaturisation and the generation of neural and three-dimensional architectures. Bio-electronics explores the use of native and genetically modified biomolecules and offers advantages because nature has generated unique materials with optimised properties through evolution and natural selection. Bacteriorhodopsin[23,24], a transmembrane protein found in 'purple' bacteria, is one such example.

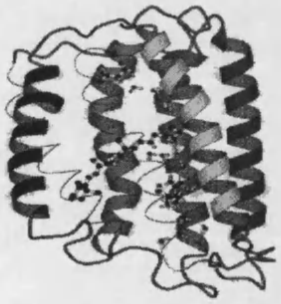

Figure 2 Computer generated image of the transmembrane protein bacteriorhodopsin[23]

The protein can exist in several stable states[25], P,K and Q and each of these states can be achieved through stimulation of the bacteriorhodopsin molecule with laser light. Green light converts the molecule from its ground state to the intermediate K. This then relaxes to an intermediate state, exposure of which to red light converts it to the P state which rapidly converts to the long term stability Q state. Stimulation with blue light converts the molecule to its original ground state. This aspect of bacteriorhodopsin is being investigated, with obvious applications in ultra high density memory storage elements.

1.3.2 Bio-Molecular Composite Materials

The production of biological/inorganic composites constitutes another initiative in the fabrication of nanostructured materials. There are numerous examples of such biocomposites, a few of which are mentioned below.

I) DNA Wires

Researchers in Israel have succeeded in building tiny silver wires using small strands of DNA as templates[26]. Short stretches of 12 base pair DNA were chemically anchored onto the surface of tiny gold electrodes. These anchored strands served as hooks for a longer strand of DNA to bridge the gap due to complementary base pairing. Positively charged silver ions were then added which stuck to the negatively charged DNA strand, due to the phosphodiester bonds of the backbone.

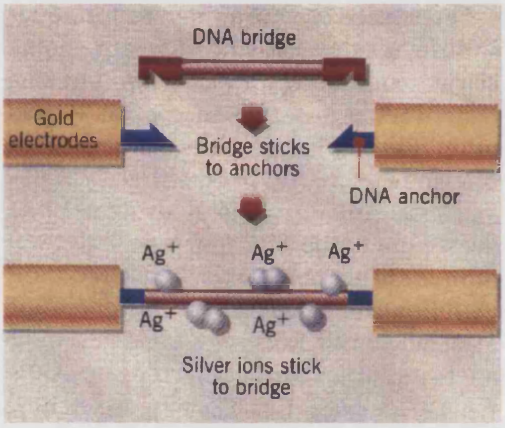

Figure 3 Schematic showing assembly of a DNA nanowire between electrodes[27].

Reduction of the silver ions to silver metal, with a solution of hydroquinone, then created a silver wire bridge 12 micrometres long between the two electrodes. One aspect of this approach to fabricating molecular wires is the versatility. By changing the anchor's base pairs, it is possible to select where the DNA bridge binds and so presents the possibility of constructing specific nanocircuitry. The only drawback at the moment is the unusual high resistivity of the wires, probably due to poor electrical contact between silver grains.

II) Ferritin Nano Composites

The iron storage protein ferritin has for a long time been used to produce a wide range of nanocrystalline composites (outlined in Fig. 4). The native function of ferritin -a protein cage 13nm in diameter- is to act as an iron storage molecule, to sequester iron in biological systems and to transport it around the body.

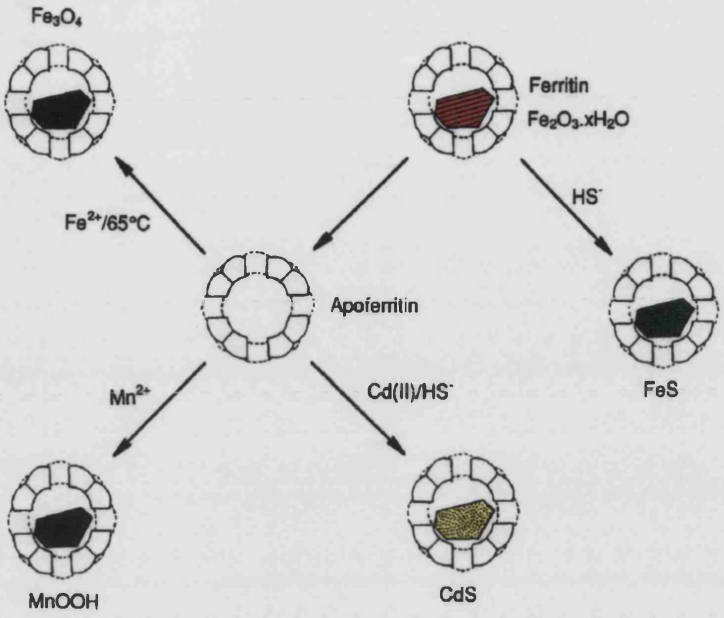

Figure 4 Schematic showing synthetic routes from Apo-ferritin to a variety of ferritin nanocomposites. (Diagram kindly provided by Dr.K.Wong).

This process has been circumvented to produce a wide range of nanocrystalline materials from magnetite to cadmium sulfide[27-30] ferritin composites.

III) Host-Guest Complexes Using Viruses

Viruses have recently entered the stage as possible candidates for the production of new materials. American chemists have recently utilised the properties of a specific icosahedral virus, called cowpea chlorotic mottle virus, to create nanoparticulate polyoxometalates[31]. This 180-subunit protein capsid controls the release of its nucleic acid in a pH dependent mechanism, above pH6.5 the capsids swell to form holes and below pH6.5 the holes close. The nucleic acid occupying the interior of the viral capsid is first removed to leave a hollow protein shell. Then, by coupling the pH dependent 'gating' mechanism of the capsid to a pH dependent inorganic polymerisation reaction, a tungsten species is entrapped and crystallised within the viral cavity. Current research in this area foresees such hybrid systems to have possible applications in areas such as biomedical imaging and cancer therapy.

IV) DNA Ordered Gold Particles

The ordering of matter on the nanoscopic scale represents a major goal in current nanotechnology, with applications ranging from new nanocircuitry to novel optical and magnetic devices. A recent nanobiological approach has used the unique specificity of the base pairing mechanism in DNA (Fig.5) to produce reversible aggregation of 12nm sized gold particles.[32,33] Although this system produces no ordered arrays, and the reversibility involves high temperatures, the ability of DNA to effect such a transformation has been exploited in new molecular biological assays[34].

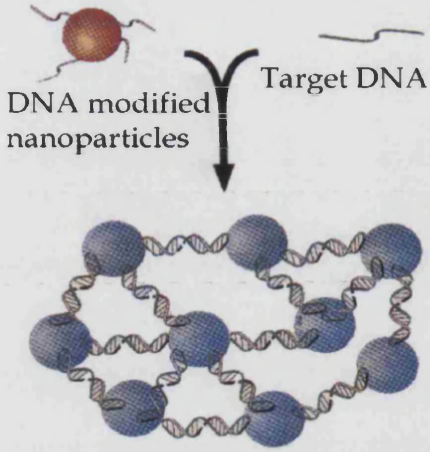

Figure 5 Schematic showing potential of DNA to aggregate gold particles through base pairing[32].

1.4 Thesis Overview

The systems introduced in the preceding subsection represent biological solutions to problems faced in inorganic materials chemistry. The production of nanocomposites, the organisation of inorganic nanocrystals into precise arrangements and the fabrication of wires only a few nanometers in length, represent some of the present days goals of nanotechnology applied to materials chemistry. A vast number of synthetic, non-lithographic protocols have been employed to realise these goals, including solvent evaporation of hydrophobic colloids [35-37], and molecular cross-linking in colloidal aggregates[38-40].

The work undertaken in this thesis adopts the 'bio-centric' view of materials synthesis, but employs biomolecules of a greater degree of complexity than those previously introduced, with a view to fabricating much more elaborate and complex structures. For example, the production of nanoparticles using the enzyme lumazine

1.5 References

1 S.L Miller (1987) Molecular Evolution, *Cold Spring Harbor Symp.Quant.Biol*, **52**, p17-27

2 M.Krakaver, P.M.D.Zanotto, M.Pagel (1998) Prions progress : Patterns and rates of molecular evolution, Journal of Molecular Evolution, 47, p133-145

3 G.F.Joyce (1989) RNA evolution and the origins of life, *Nature*, **358**, p217-224

4 A.I.Lamond, T.J.Gibson (1990) Catalytic RNA and the origin of genetic systems, *Trends Genetics*, **6**, p145-149

5 R.F.Doolittel (1979) *The Proteins*, 3rd ed., Vol 4, p1-118, Academic Press, New York

6 T.Cavalier-Smith (1987) The Origin of cells, *Cold Spring Harbor Symp. Quant. Biol.*, **52**, p743-749

7 K.Woese (1997) Microbiology's Scarred Revolutionary, *Science*, **276**, p699-702

8 D.Penny (1988) What was the first living cell? *Nature*, **331**, p111-112

9 E.Pennisi (1997) Extremophiles make their mark, *Science*, **276**, p705-706

10 R.A.Kerr (1997) Life goes to the extremes in the deep earth, *Science*, **276**, p703-704

11 G.Vidal (1984) The oldest eukaryotic cells, *Sci.Am*, **250**, p48-57

12 M.W.Gray (1989) The evolutionary origins of organelles, *Trends Genetics*, **5**, 294-299

13 L.Stryer (1988) *Biochemistry*, 3rd edition, W.H.Freeman and co., New York.

14 T.E.Creighton (1993) *Proteins: Structure and Molecular Properties*, 2nd ed., W.H.Freeman and co., New York.

15 M.Aebi, C.Weissman (1987) Precision and Orderliness in Splicing, *Trends Genet.*, **3**, p102-107

16 R.P.Feynman (1960) There's plenty of room at the bottom. *Eng. And Sci.*, **23**, p22-36

17 L.L.Sohn (1988) A quantum leap for electronics, *Nature*, **394**, p131-132

18 A.P.Alivisatos (1995) Semiconducting nanocrystals, MRS Bulletin.

19 J.-M.Lehn (1988) Supramolecular Chemistry- Scope and Perspectives: Molecules, Supermolecules and Molecular Devices, *Angew.Chem.Int.Ed.Engl.*, **27**, p89-112

20 S.Mann. (1996) *Biomimetic Materials Chemistry*, Vol. 1, VCH New York

21 K.E.Drexler (1992) Nanosystems, 1st ed., Wiley-Interscience, USA

22 L.M.Adelman (1994) Molecular Computation of Solutions to Combinatorial Problems, *Science*, **266**, p1021-1024

23 R.Henderson, P.N.T.Unwin (1975) Three-dimensional model of the purple membrane obtained by electron microscopy, *Nature*, **257**, p28-32.

24 W. Stoeckenhuis (1985) The purple membrane of salt-loving bacteria. *Sci. Amer.* **234**, p38-46

25 R.R.Birge (1995) Bacteriorhodopsin Computer memories, *Sci.Am.*, **272**, p90-95

26 E. Braun, Y. Eichen, U. Sivan, G. BenYoseph, (1998) DNA-Templated Assembly and Electrode Attachment of a Conducting Silver Wire, *Nature*, **391**, p775-778.

27 F. C. Meldrum, B. R. Heywood, S. Mann, (1992)) Magnetoferritin: In Vitro Synthesis of a Novel Magnetic Protein *Science,* **257**,p522-523.

28 K.K.W.Wong, S.Mann, (1996) *Adv. Mater.*, **8**, p928-931

29 T.Douglas, D.P.E.Dickson, S.Betteridge, J.Charnock, C.D.Garner, S.Mann (1995) Synthesis and Structure of an Iron(III) Sulfide-Ferritin Bioinorganic Nanocomposite, *Science*, **269**, p54-57

30 F.C.Meldrum, T.Douglas, S.Levi, P.Arosio, S.Mann (1995) Reconstitution of Manganese Oxide Cores in Horse Spleen and Recombinant Ferritins, *J.Inorg.Biochem.*, **59**, p59-69

31 T.Douglas, M.Young, (1998) Host-Guest encapsulation of Materials by assembled Virus protein cages, *Nature*, **393**, p152-155

32 C. A.Mirkin, R. L.Letsinger, R. C.Mucic, J. J.Storhoff, (1996) A DNA-based method for rationally assembling nanoparticles into macroscopic materials *Nature,* **382**,p607-609.

33 A.P.Alivisatos, (1996).Organization of "nanocrystal molecules" using DNA. *Nature,* **382**, p609-611

34 R.Elghanian, J.J.Storhoff, R.C. Mucic, R.L.Letsinger, C.A.Mirkin (1997) Selective colorimetric detection of polynucleotides based on the distance dependent optical properties of gold particles, *Science*, **277**, p1078-1081

35 C.Petit, A. Taleb, M.-P.Pileni (1998) Self-organization of magnetic nanosized cobalt particles. *Adv. Mater.*, **10**, p259-262

36 C. B.Murray, C. R.Kagan, M. G.Bawendi (1998) Self-organization of CdSe nanocrystals into three-dimensional quantum dot superlattices. *Science*, **270**, p1335-1338

37 T. Vossmeyer (1995) Self-assembly of a two-dimensional superlattice of molecularly linked metal clusters. *Science,* **267**, p1746-1479

38 B. A, Korgel, D. Fitzmaurice (1998) Self-assembly of silver nanocrystals into a two-dimensional nanowire array. *Adv. Mat.*, **10**, p661-665

39 R. P Andres (1996) Self-assembly of a two-dimensional superlattice of molecularly linked metal clusters, *Science*, **273**, p1690-1693

40 M.Brust, D.Bethell,. D.J.Schiffrin,. C.J.Kiely, (1995) Novel gold-dithiol nanonetworks with non-metallic electronic properties. *Adv. Mat.*, **7**, p795-797

Chapter 2

Experimental Methods

There is no higher or lower knowledge,
but one only, flowing out of experimentation

Leonardo da Vinci

Water Purification

Distilled de-ionised water was produced by feeding the local water supply into an Aquatron A4D commercial still, possessing dual boilers. The water from the still was then passed through a Purite Standard Stillplus™ system, containing a 0.2μm bacterial filter, activated carbon cartridge and mixed bed ion exchange column. The water produced had a typical conductivity of $<1\mu S\ cm^{-1}$.

Transmission Electron microscopy (TEM)

Data were collected using a JEOL 2000FX or JEOL 1200EX analytical TEM operated at 80, 100, 120 and 200KV. Analysis was capable of routine magnifications up to 400,000X, with an absolute limit in point to point resolution of better than 5.

All samples were prepared for TEM analysis by applying the material as loaded suspensions onto 3mm formvar coated nickel or copper TEM grids. All grids were carbon coated. Uranyl acetate was used as a negative stain to visualise protein components adsorbed onto the surface of each TEM grid.

Energy Dispersive X-ray Analysis (EDXA)

Qualitative elemental analysis was performed on the 2000FX TEM using the EDXA technique. The detector used was a Link AN10000 X-ray microanalysis system.

Poly-Acrylaminde Gel Electrophoresis (PAGE)

Gel electrophoresis was performed on an Anachem upright V2-DCM casting electrophoresis tank equipped with an Anachem Ongo power supply (model PSU 400/200). The glass plate size used was 205mm x 200mm.

Samples were loaded onto a 3% stacking gel (3% acrylamide, 0.125M Tris pH6.8, 0.1% TEMED, 0.05% ammonium persulfate) with a 7.5% separating gel (7.5% acrylamide/bisacrylamide, 0.375M Tris pH8.8, 0.1% SDS, 0.1% TEMED, 0.05% ammonium persulfate) and run at 120V for 4 hours with conventional anode polarity. The gel was stained with coomassie brilliant bluR250 (0.25% in water/methanol/glacial acetic acid = 5:5:1 v/v) for 30 minutes, then destained with a water/methanol/glacial acetic acid solution (6.5:2.5:1 v/v).

Gels were then dried on a Biometra Gel Dryer, possessing a 30cm x 40cm drying area, with a temperature selection of 30-110°C.

Ultra Analytical Centrifugation (UAC)

All ultra analytical centrifugation was undertaken by Dr. Helmut C¬lfen, Max-Planck Institute for Colloids and Interfaces, Teltow, Berlin. The UAC was performed with a Beckman Optima XL-I analytical ultracentrifuge (Beckman Instruments, Palo Alto, CA, USA) equipped with an integrated UV-vis absorption optics (190-800nm) and on-line Rayleigh interferometer. Titanium doublesector centrepieces with sapphire windows were used.

The sedimentation coefficient distributions were calculated using the radial derivative method, applying the program 'ULTRASCAN' by Boris Demeler, University of Texas.

H^1 NMR

NMR was performed on a JEOL 400MHz NMR spectrometer equipped with a superconducting, liquid nitrogen cooled, cryomagnet made by Oxford Instruments.

Mass Spectrometry

Fast atom bombardment (FAB) mass spectrometry was performed on a VG AutoSpec analytical mass spectrometer, made by Fisons Instruments. Very small amounts of sample were needed for analysis, typically <1mg.

Fourier Transform Infra Red Spectroscopy (FTIR)

Infra red spectra were obtained using a Nicolet510P Fourier transform infra red spectrophotometer, with attached computer interface. All spectra were scanned from 4000-400cm^{-1}.

Sample preparation involved the mixing of the sample with Nugol, which was then pressed between two NaCl discs.

UV-vis Spectrophotometry

UV analysis was performed using a Perkin Elmer Lambda II UV-vis spectrophotometer, equipped with Perkin Elmer UV Winlab (version 1.1) software. All samples were analysed using quartz cuvettes, possessing a 1cm path length.

PROKARYOTRIC SYSTEMS

Messieurs, c'est les microbes qui auront le dernier mot.

Louis Pasteur

Chapter 3

The Synthesis of Quantum Dots Using the β60 Capsid of Lumazine Synthase

Let no one ignorant of
geometry enter my door

Plato

3.1 Introduction

The synthesis of very small scale solids (<30nm), known as nanocrystals or quantum dots, has seen a surge of interest, due to their unusual non-linear, size dependent properties[1]. A large number of synthetic strategies have thus been employed, resulting in a wealth of contrasting systems attempting to attain the goal of quantum dot synthesis displaying a very small particle distribution size.

This chapter shows the potential of utilising the protein capsid of the bacterial enzyme lumazine synthase, a protein not involved in mineral formation, in the synthesis of quantum dots. The dynamic nature of the capsid also enables the templating of a variety of morphologies, an effect not seen in the static templates employed in this field.

3.1.1 Nanocrystals and Quantum Dots

Quantum dots (QD's), or nanocrystals, are essentially very small, solid state crystals, comprised of materials such as CdS and InAs, capable of holding integer numbers of electrons[1,2]. This attribute has lead quantum dots to be described as 'artificial atoms'[3]. These nanoscale 'electron boxes' are currently generating a wealth of interest due to their unusual properties and foreseeable applications. The two aspects of QD's under consideration here are the quantization of the QD's energy levels and the non-linear optical and electrical properties of semiconducting QD's.

The reduced dimensionality of semiconductors to that of QD's (<30nm) results in large quantum-sized effects, due to the size-dependent properties of bonding within the solid[4]. The bonding in bulk semiconductors can be explained by band theory, an extension of MO theory, where the closely spaced groups of MO's result in a continuum of energy levels. MO theory predicts that the bands are split into the 'conduction' band and the 'valence' band, the distance between these bands termed the 'band gap' and the size of the band gap determined by the strength of bond interaction. Band theory requires a conductor to possess a partially filled conductance band allowing the promotion of electrons to similar energy levels for conduction to occur. Bulk semiconductors have filled valence bands, but the band gap is so small that promotion of electrons to the conduction band can be achieved through room temperature thermal energies. Reduction in size of the bulk semiconductor, to produce crystallites having dimensions <30nm,

results in the emergence of discrete energy levels, due to the orbital overlap of proportionally fewer atoms. This leads to the emergence of quantum confinement effects in the quantum dot[5].

The non-linear optical properties of quantum dots are explained by these emergent quantized energy levels[5]. Bulk semiconductors have a single band gap and the promotion of an electron into the conduction band permits the electron to fall back to the valence band, the energy deficit balanced by the release of a packet of energy known as a photon, as the electron and hole combine. The frequency of this photon is related to the size of the band gap and consequently bulk semiconductors emit light of one colour. However, the production of quantum dots of different sizes results in each having different band gap values, thus the photons emitted have correspondingly different frequencies.

The fabrication of quantum dots has employed a diverse number of strategies in attempts to control the size distribution. Micelles[6,7], zeolites[8], polymers[9,10,11], dendrimers[12], thin films[13], molecular beam epitaxy (MBE)[14] and metal-organic vapour phase epitaxy (MOVPE)[15,16] are some of the techniques that have been used. Recently, bio-mimetic strategies have also allowed the biogenic production of quantum dots, using ferritin and viruses (see Chapter 1 : Introduction).

Quantum dots continue to attract attention due to the increasing number of applications envisaged. One application is in bio-imaging[17,18]. The current use of dyes in bio-imaging is severely limited to the optical system used, whereas nanocrystalline semiconductors can be fabricated to give a range of sizes. Illumination with the same frequency of light results in the emission of many colours which can be detected simultaneously. These QD's can then be used as nanocrystal probes in many areas of biology.

The quantization of energy levels in nanocrystals may also allow the fabrication of a new generation of super-fast computers[19]. The ability of nanocrystals to behave like 'artificial' atoms and hold integer numbers of electrons has been used to demonstrate the potential for the world's smallest transistor[20], the 'single electron transistor'. A FET (field effect transistor) is a simple 3-layer device (consisting of a metal 'gate', an insulator and a semiconductor) found in all modern microprocessors. Application of a voltage causes an accumulation of electrons in the semiconductor, turning the device 'on'. A single

electron transistor replaces the semiconductor with a semiconducting nanocrystal, in this case CdSe, placed between the two electrodes separated by space. The confinement of electrons to small regions allows the behaviour of the electron to be described by 'the particle in a box' analogy. A particle's behaviour, when confined to a one-dimensional box with walls of infinite potential, can be described by

$$-h^2/8\pi^2.d^2\psi/dx^2=E\psi \qquad (1)$$

Given a system where the barrier potentials are not infinite, as in a quantum dot, a phenomenon known as 'tunnelling' can occur. The probability of this occurring being proportional to the quantity

$$\exp\{-4\pi a/h.[2m(V-E)]^{1/2}\} \qquad (2)$$

where a is the thickness of the barrier. Thus, if a is not equal to infinity, there is always the probability that the electron can escape. The phenomenon of tunnelling is exploited in the single electron transistor, as the semiconductor is separated from the electrodes allowing electrons to enter and exit only by quantum mechanical tunnelling.

Another potential application of QD's is the 'quantum dot cascade laser'[2]. Existing quantum well lasers utilise the tunnelling of electrons through increasingly narrow strips of GaInAs, photons being emitted upon tunnelling. Lasers comprised of identical QD's would allow the fabrication of much more efficient lasers, but current obstacles are the arrangement of these QD's into 3D 'superlattices'.

3.1.2 Lumazine Synthase

The Bifunctional Enzyme Complex of Lumazine Synthase-Riboflavin Synthase

Riboflavin synthase and lumazine synthase are enzymes that form a bifunctional enzyme complex, called heavy riboflavin synthase (HRS), that catalyses the last steps of the biosynthesis of riboflavin[21]. This 1MDa complex consists of 60 β subunits (lumazine synthase), which forms a T=1 icosahedral capsid, enclosing three α subunits in the central core (riboflavin synthase) (Fig.1). The β subunits catalyse the condensation of 3,4-dihydroxy-2-butanone 4-phosphate (Fig. 2, (2)) with 5-amino-6-ribitylamino-2,4-(1H,3H)-pyrimidinedione (1) yielding 6,7-dimethyl-8-ribityllumazine (3). The subsequent dismutation is catalysed by the α subunits to give riboflavin (4) and the pyrimidinedione (1) which is re-utilised by the β60 capsid.[22]

Figure 1 Computer generated image of the bifunctional enzyme complex lumazine-synthase-riboflavin synthase[22].

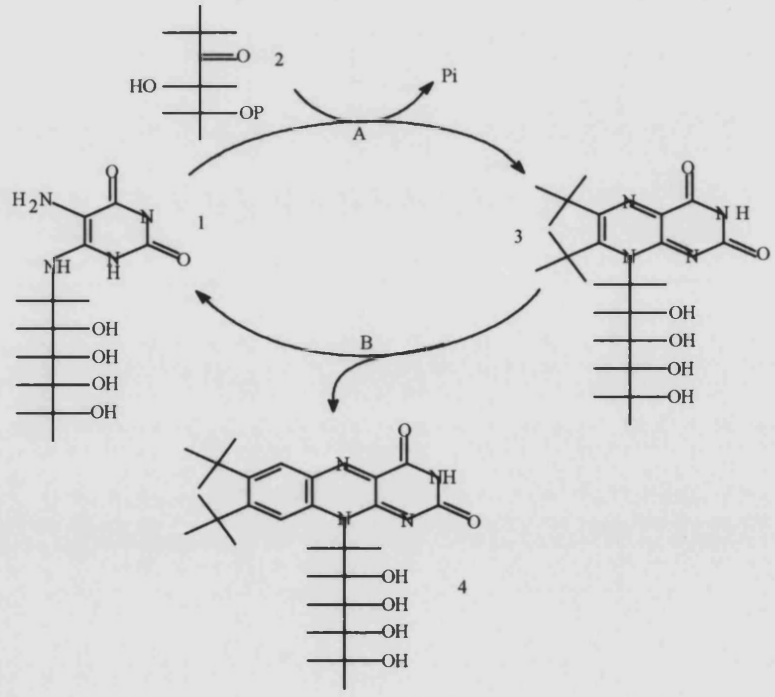

Figure 2 Reaction scheme showing the pathways catalysed by riboflavin synthase (A) and lumazine synthase (B) enzymes[2].

Structure of Lumazine Synthase

In oligomeric macromolecules, a common trait to achieve maximum stability is through arranging subunits in a symmetrical manner, such that all subunits form equivalent contacts. Consequently, icosahedral symmetry is a common structural motif in self-organised structures found in nature. Spherical viruses display a variety of icosahedral capsid motifs, where the structure permits the economic packing of nucleic acid through utilisation of a relatively small number of protein subunits. Icosahedral protein symmetry has been the exclusive domain of the spherical viruses until recently, when the icosahedral bifunctional enzyme HRS, Fig. 1, was isolated and found to exhibit the same icosahedral structural motif.

The HRS enzyme complex is composed of 60 identical β subunits (lumazine synthase), forming an icosahedral capsid which encloses a trimer of α-subunits (riboflavin synthase). The structure of lumazine synthase, from *Bacillus subtilis*, has recently been elucidated and X-ray structure analysis revealed a T=1 icosahedral capsid[23] (the exact structure of riboflavin synthase has yet to be elucidated). The capsid has an inner and outer diameter of 39Å and 78.5Å respectively[24]. The 154 residues that comprise a single β subunit of lumazine synthase are folded into an ellipsoidal shape and due to the symmetry relations in the icosahedral capsid, the intersubunit contacts are those of dimers, trimers and pentamers. Crystallographic data have revealed the nature of these intersubuint interactions[23]. Dimers appear to be both hydrophobic and hydrophilic, confined to a small region near the outer wall of the capsid. Trimer contacts are formed by several segments at the inner capsid wall (residues 21-29, 81-85, 120-143)[24], where an interesting contact region consisting of a cluster of three glutamic acid residues reside (Glu126, Glu126', Glu126''). These have no ligands to compensate their negative charge and so are reasoned to be involved in interactions between the positively charged residues of the α-subunits. Phase calculation procedures of lumazine synthase utilising the positively charged $[[W_3O_2(O_2CCH_3)_6](H_20)_3](CF_3SO_3)_2$ have revealed the molecule to bind to this group of three glutamic acids, on the interior of the capsid[25].

Channels are formed along the twelve 5-fold pentamer axes, consisting of symmetrically arranged α-helices, reminiscent of membrane channel proteins. Fig. 3 shows one such channel, with the lysine residues highlighted. It can be seen that the

channel therefore possesses a strong positive potential. This pore resembling channel is approximately 2.7nm long with a diameter of 0.9nm and spans the entire capsid wall. The inner surface of these pores is comprised primarily of polar residues, making the channel hydrophilic and so implicated in the substrate import and product export from the enzymatic catalytic centres[25]. The capsid structure is a very compact macromolecule, allowing limited diffusion through the capsid, implying a greater role for the channels in substrate exchange[26].

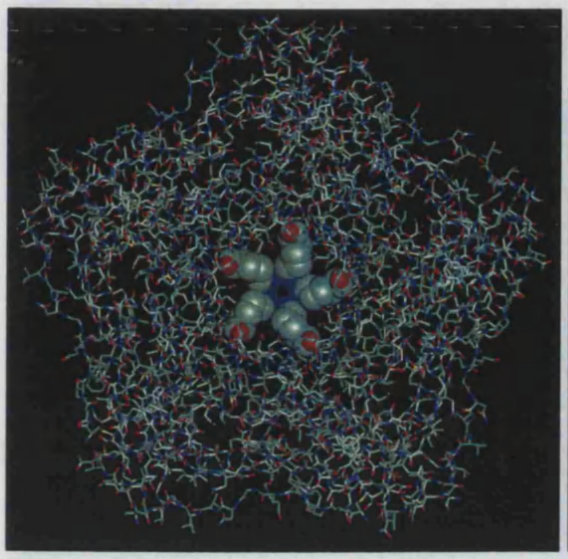

Figure 3 Computer reconstructed image of the 5-fold channel of lumazine synthase with the lysine residues highlighted.

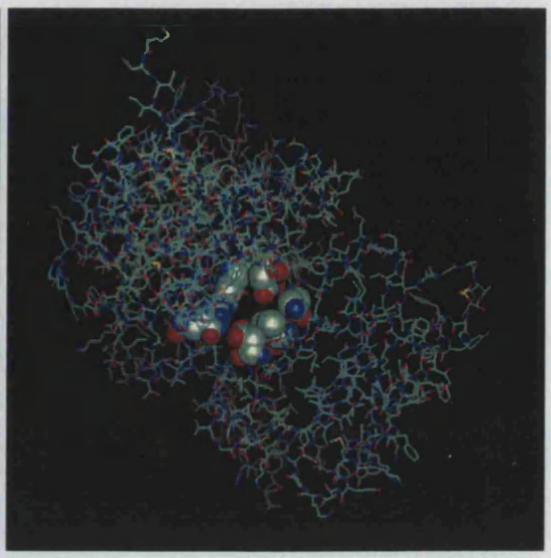

Figure 4 Computer image of the 3-fold channel of lumazine synthase with glutamic acid residues highlighted.

Funnel shaped channels also exist, along each of the 3-fold axes, which may also be involved in substrate exchange (Fig.4). This 3- fold channel is lined with glutamic acid residues, in contrast to the lysine residues of the 5-fold channel. The nature of the 5-fold channel has been revealed in an elegant experiment using large tungsten complexes, where a negatively charged tungstate, $[NaP_5W_30_{110}](NH_4)_{14}31H_20$, has been shown to 'plug' the 5-fold channel[25]. It has been reasoned that the 3-fold channel is also the port of entry for the $[[W_3O_2(O_2CCH_3)_6](H_20)_3](CF_3SO_3)_2$ molecule that binds to the glutamic acid residues on the interior wall of the capsid[25] mentioned previously.

The β-subunits have the capacity to form a wide variety of different molecular aggregates, in spite of the relatively small size of the capsid. Previous work[22] has shown that the lumazine synthase capsid possesses 60 substrate ligand binding sites at the

pentamer interfaces. The binding sites are located on the inner wall and consequently the stability of the capsid is dependent upon the presence of the substrate or substrate analogues of lumazine synthase. In the absence of these appropriate ligands, the capsid assembly is rather unstable and becomes sensitive to buffer composition and pH. This characteristic has been exploited in the isolation of the β60 capsid of lumazine synthase, where disruption of HRS results in the liberation of the α subunits and a re-assembly of the β60 capsid into a hollow sphere of radius 15nm (Fig. 5).

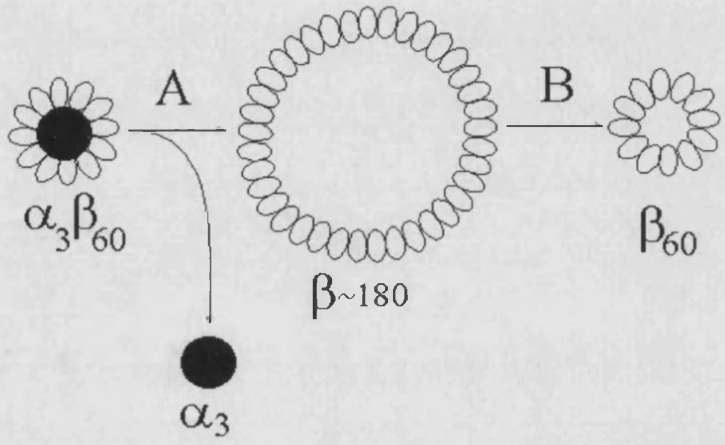

Figure 5 Schematic showing the steps involved in the isolation of lumazine synthase. A) 0.1 M Tris-HCl, pH 8.0 B) 10mM phosphate, pH 7.0, containing 1mM Na_2SO_3, 1mM substrate analogue 1, seen in Fig. 2.

The addition of phosphate and substrate analogues, then induces the reformation of the 8nm β60 lumazine synthase capsid. The molecular rearrangement of the β subunits has been shown to produce spheres of larger radius, if phosphate and ligands are absent. It has been speculated that these spheres are icosahedral capsids with triangulation numbers of T=3,4,5 etc. These hollow spheres can be re-aggregated into the smaller β60 capsids upon addition of appropriate ligands[26]. It should be noted that the ligand is only necessary for capsid stability and not for HRS stability, the α-subunits fulfilling the role of the ligand in the latter.

3.1.3 Structural Comparison of Lumazine Synthase to Ferritin and Spherical Viruses : A Study of the Potential of Lumazine Synthase as a Nanoscopic Template

Consideration of the morphological nature of the lumazine synthase molecule and the distribution of charges, initially lead to a structural comparison of the molecule to ferritin and viruses. Further investigation revealed resemblance of lumazine synthase to ferritin and so to speculation that the enzyme could partake in controlled mineralization within its internal cavity.

Icosahedral viruses, such as satellite tobacco mosaic virus, and HRS show a similar spherical structure when viewed by electron microscopy. In fact, the structure of the lumazine synthase β subunit capsid obeys the same icosahedral symmetry relation as the capsid of spherical viruses, but the β-subunit structures show no similarity in charge distribution. The internal cavity of icosahedral viruses is occupied with nucleic acids and consequently the inner surface of the virion is populated almost exclusively by positively charged residues. Conversely, HRS has a trimer of enzymatically active α-subunits occupying the interior, which present positively charged species to the interior of the HRS capsid. Consequently, the internal surface of the lumazine synthase capsid has a high concentration of negatively charged amino acid residues. These negatively charged residues are the glutamic acid residues described in the previous subsection. The residues have been shown to share no other ligands compensating their negative charge, suggesting their association with the riboflavin synthase subunits. By considering only one subunit of the lumazine synthase capsid, the outer wall carries five positively charged and six negatively charged residues. By contrast the inner wall contains four negative and one positive charge. This asymmetry may have importance in the enzymatic operation of the enzyme. This is a another very important difference between this enzyme complex and the capsids of viruses.

Morphologically, the iron storage protein ferritin resembles both viruses and lumazine synthase, in being spherical (see Chapter 1), although the charge distribution in ferritin is opposite to that of viruses, due to its role in the internalisation of iron and subsequent mineralisation. For this reason ferritin has a high density of negatively charged residues on the internal surface of the protein and therefore resembles lumazine

synthase more closely. Both capsids also possess 3-fold funnel shaped, negatively charged channels spanning the capsid wall, which permit access to the interior of the protein (Fig. 6 and 7).

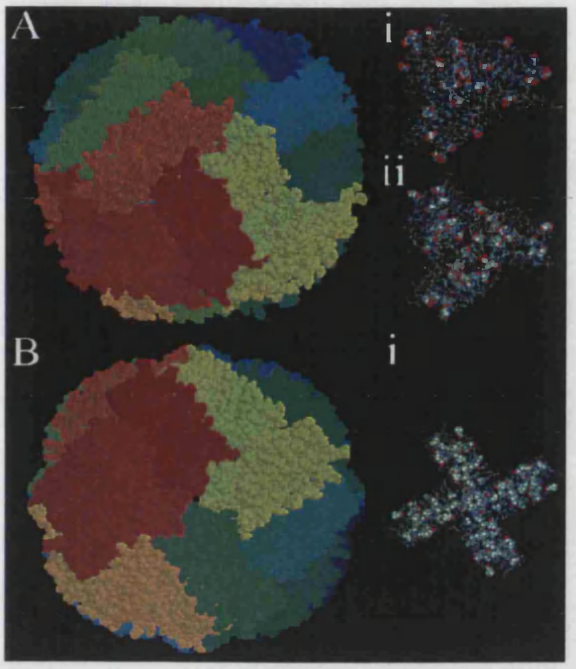

Figure 6 Computer generated images of ferritin showing, A) 3-fold channel with i) & ii) showing the 3-fold channel with highlighted glutamic and aspartic acid residues respectively. B) 4-fold channel with highlighted leucine residues.

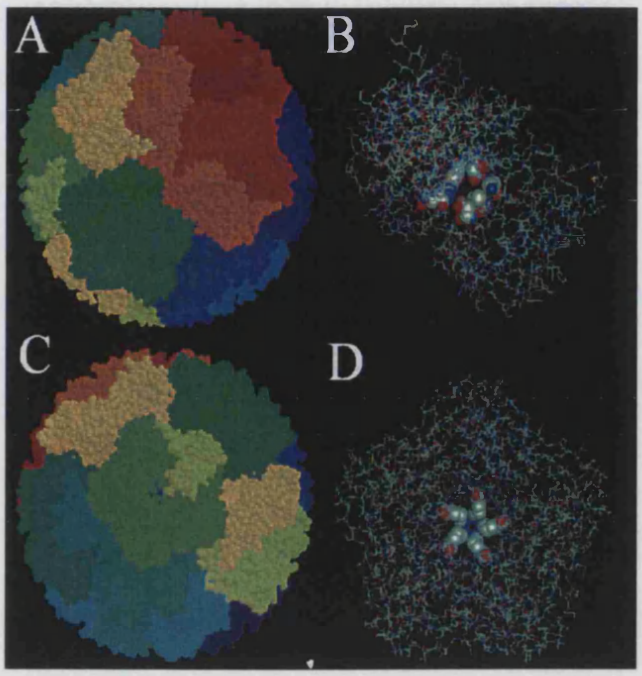

Figure 7 Computer generated image of lumazine synthase showing A) 3-fold channel B) 3-fold channel with highlighted glutamic acid residues C) 5-fold channel D) 5-fold channel with highlighted lysine residues.

The nature of this investigative comparison of molecular morphology between lumazine synthase, ferritin and viruses, together with computer modelling, provided a basis for the experimental use of lumazine synthase. It was predicted that lumazine synthase could act as a nanoscale mineralization template analogous to that of ferritin, subverting the function of the molecule and exploiting the molecular similarity to ferritin. Thus, mineralization experiments were initially undertaken utilising positively charged ionic species such as Fe^{2+} and UO_2^{2+}.

3.2 Materials and Methods

A lyophilised sample of lumazine synthase, from *Bacillus subtilis* and expressed in *Bacillus subtilis*, was kindly supplied by Professor Adelbert Bacher and Dr. Markus Fischer of the Institiut fJr Organische Chemie und Biochemie, Technische Universit←t MJnchen, MJnchen. The sample was re-hydrated with 500µl of distilled water to give a 10mg/ml concentration of lumazine synthase with a buffer composition of 50mM K_2CO_3, 0.5mM EDTA, 0.5mM Na_2SO_3 and 0.02% NaN_3.

Imaging

A total 5µl of the 10mg/ml lumazine synthase was added to a Cu transmission electron microscope (TEM) grid and 5µl of distilled water added to the droplet. The grid was blotted dry and stained with a 2% aqueous uranyl acetate solution for 1 minute. The grid was washed several times in distilled water before TEM analysis.

Buffer effect

The effect of the buffer composition was investigated through incubation of the lumazine synthase in MES (4-morpholineethanesulfonic acid, Aldrich). The buffer was made to pH6.5, through the dropwise addition of 0.5M NaOH. Samples of lumazine synthase were added to the buffer to give total concentrations of 0.1mg/ml. Samples were analysed after 24 hours to ascertain any buffer effects.

Uranium/Lumazine Synthase Composites

A 0.1mg/ml solution of lumazine synthase was prepared as follows. A 100mM MES buffer was prepared and pH adjusted to 6.5 by addition of 0.1M NaOH. 11.1µl of the 10mg/ml lumazine synthase solution, stored at 4°C, was added to give a concentration of 0.1mg/ml. A control sample was prepared which consisted of the same volume of buffer, without lumazine synthase.

A 100mM solution of uranyl acetate was prepared by dissolving the solid in doubly distilled water to give a clear yellow solution. The solution was filtered through a micro-pipette, equipped with a filter, to removed any solid residue. An estimated ratio of 2000 atoms of UO_2^{2+} per lumazine synthase capsid was required, thus aliquots of the

uranyl acetate solution were added slowly to both stirred samples every 30 minutes, giving the required ratio. Both samples were then allowed to stir for 24 hours in the dark.

An aliquot of the uranyl lumazine synthase was spun in a centrifugal filtration device (10kDa cut off, Millipore Ltd) to concentrate the lumazine synthase sample. Two TEM grids were prepared for analysis from the concentrated sample as follows. To the first grid, 5µl of the concentrated protein containing sample was added. The grid was then blotted and washed several times in distilled water. The second grid was prepared as for the first, but stained with 2% uranyl acetate for 2 minutes, blotted and washed several times in distilled water.

UV-vis spectroscopy of both samples was undertaken, with the blank comprised of the buffer (same molarity) used in the experiments. In both cases, 2ml aliquots of the respective samples were sequentially analysed in the spectrophotometer and their spectra recorded on the same graph for comparison.

Iron mineralization of lumazine synthase

Several iron mineralization experiments were performed, with different ratios of iron per lumazine synthase molecule, to examine the effect of iron concentration on the morphology of lumazine synthase. Each protocol followed the same methodology, with the difference being final ratio of iron per lumazine synthase capsid. Ratios of iron/lumazine synthase examined were 300, 1000, 1500 and 2000 atoms of Fe per protein molecule.

The iron mineralization protocol was as follows. A 1mM solution of $(NH_4)_2SO_4{\cdot}FeSO_4{\cdot}6H_2O$ was prepared and this was de-aerated under N_2 for 30 minutes prior to the start of the mineralization experiment. This aqueous Fe(II) solution was kept under N_2 for the duration of the experiment. A 0.1mg/ml solution of lumazine synthase was prepared in MES buffer, adjusted to pH 6.5 by addition of 0.1M NaOH. This solution was de-aerated for 15mins under N_2, after which the gas was removed to allow a slow aerial oxidation throughout the duration of the experiment.

The addition of the Fe(II) to the slowly stirred solution of lumazine synthase (and control sample) was dependent upon the ratio of iron per lumazine synthase molecule required. Thus, equal volumes of the de-aerated Fe(II) solution were added to both slowly

stirred samples every 30 minutes with a micro-syringe. The addition of each volume of Fe(II) was also added very slowly, over a period of 10 seconds, to ensure a very slow oxidation. For example, in the 1000Fe/lumazine synthase ratio, a total of 80.6µl Fe(II), added over a period of 3hrs, comprised 13.43µl of aqueous Fe(II) added every 30 minutes. Both samples were allowed to stir on the bench for a period of 24 hours.

UV-vis spectra were recorded at regular intervals, through removal of 3ml aliquots from the reaction vessel. Samples were returned to their respective reaction vessels upon completion of the analysis, before resumption of the experiment.

TEM analysis was performed upon each iron/lumazine synthase sample as follows. An aliquot of the sample, typically 0.4ml, was concentrated in a centrifugal filtration device (10kDa cut off, Millipore Ltd). The filtrate was removed and 10µl of the concentrated sample was added to a copper TEM grid. The grid was blotted and washed several times in distilled water prior to analysis. An identical procedure was followed to produce a TEM grid of the control sample.

Ultra analytical centrifugation was performed by Dr. Helmut C¬lfen, Max-Planck Institute for Colloids and Interfaces, Teltow, Berlin. The ratios of iron loaded lumazine samples examined was 300 and 2000 atoms of Fe per capsid, with the native β60 capsid in the same MES buffer. All samples were run at 25°C and the results plotted on the same graph, with the y-axis normalised, for comparison.

Tungsten Mineralization of Lumazine Synthase

Analogous experiments to those of iron mineralization were performed with tungsten. A solution of 100mM K_2PO_4, 10mM Na_2SO_3 was prepared and adjusted to pH8.2 by addition of 1M HCl. Lumazine synthase was added to this solution to give a final protein concentration of 0.1mg/ml. To this slowly stirred solution, a 10mM solution of Na_2WO_4 was added dropwise, over a period of 1hour, to give a final concentration of 1500 WO_4^{2-}/ lumazine synthase. The transparent solution was left to stir on the bench for 24 hours. The pH of the protein/tungsten solution was then reduced to 5.5, by addition of 0.5M HCl, to promote the formation of polytungstates. The solution was then left to stir for a further 6 hours. TEM analysis was performed on concentrated aliquots of this

solution. The resultant concentrated protein solution added to two TEM grids for analysis. To the first grid, 5µl of the concentrated tungsten/lumazine synthase sample was added, the grid then blotted and washed in distilled water several times. To the second grid, 5µl was added, the grid blotted, then 5µl of a 2% uranyl acetate solution added, the grid then blotted and washed several times in distilled water.

A further tungsten mineralization experiment was performed using a different buffer to assess the role of the phosphate and ionic strength on the potential mineralization of the interior of the capsid. A 50mM (2-([tris(hydroxymethyl)methyl)] amino)-1-ethane-sulfonic acid) TES buffer solution was prepared and adjusted to pH 8.2 by addition of 0.5M NaOH. Lumazine synthase was added to this solution to give a final concentration of 0.1mg/ml and 35mg of Na_2WO_4 was added to this solution giving a tungsten concentration of 7mg/ml. The solution was stirred until no solid remained and incubated at 4°C for 24 hours. The pH of the solution was then reduced to 5.5 and allowed to stir for a further 6 hours. TEM analysis was performed on aliquots of this solution concentrated in a centrifugal filtration device. The concentrated solution was re-suspended twice in 4ml of acidified (pH5.5) distilled water and re-spun to remove excess tungstate. The resultant solution, containing concentrated and washed protein, was analysed by adding 5µl aliquots to TEM grids, the grids then blotted and washed. One grid was also stained with 2% uranyl acetate.

3.3 Results and Discussion

Imaging the β60 lumazine synthase capsid

Analysis by TEM of a 10mg/ml sample of lumazine synthase, stained with a 2% uranyl acetate solution, revealed a hexagonally close packed arrangement of spherical particles, possessing an external diameter of 8nm (Fig. 8). The electron dense uranyl acetate also revealed a dark inner core to each particle, the diameter of which was approximately 4.5nm. These data suggest the hollow capsid of each lumazine synthase

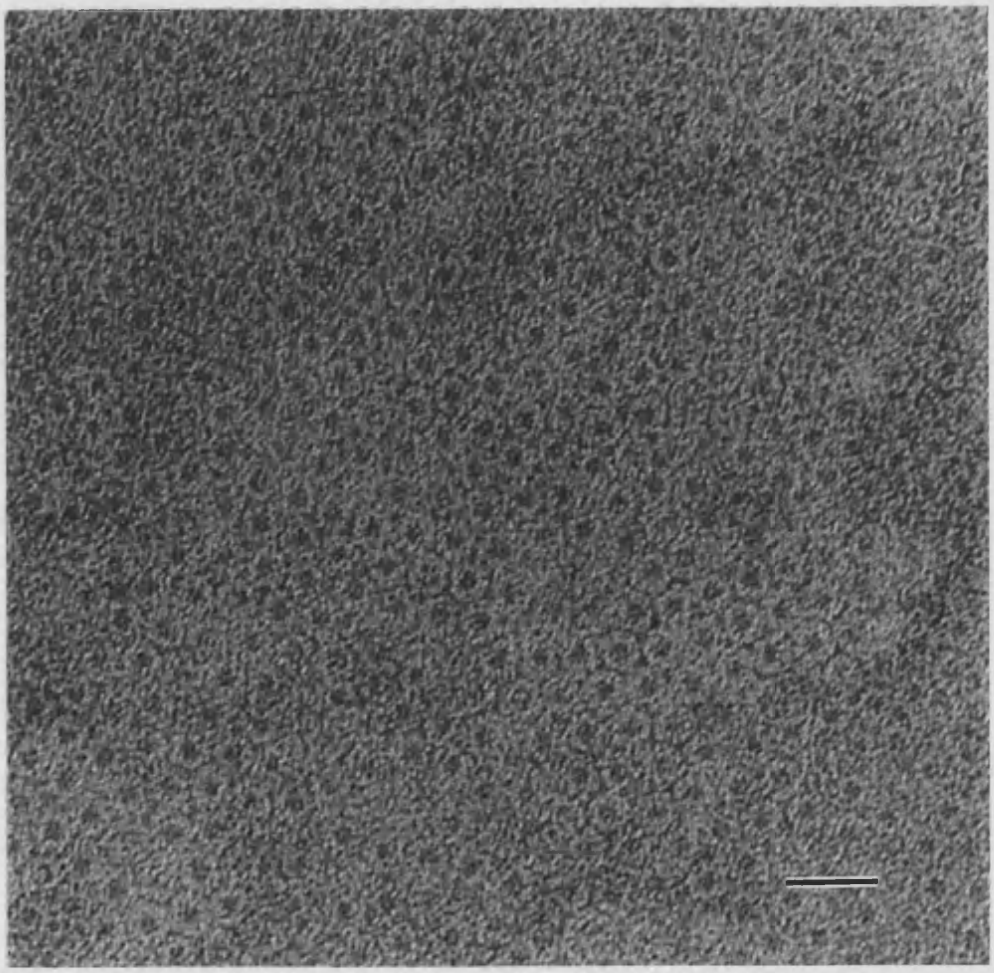

Figure. 8 TEM micrograph of a sample of lumazine synthase stained with a 2% uranyl acetate solution. Scale bar 20nm.

molecule allowed the diffusion of the uranyl ions through the protein shell to the interior, resulting in an electron dense inner core, the negative staining effect of the uranyl acetate simultaneously revealing the protein capsid. It should be noted that examination of

unstained TEM grids possessing adsorbed lumazine synthase molecules revealed no evidence of the protein.

Effects of buffer upon lumazine synthase morphology

The buffer composition and environment are important factors affecting the morphology of the capsid[25]. Subsequent experiments involving lumazine synthase necessitate the use of buffers, therefore experiments were performed to ascertain any effect the buffer chosen, in this case MES, has upon the capsid and also to establish a control. An ultraviolet absorbance spectrum of a 0.1mg/ml solution of lumazine synthase in MES buffer at pH6.5 gave the characteristic peak shown in Fig 9. This peak, at approximately 280nm, is characteristic for the presence of the aromatic side chains of proteins.

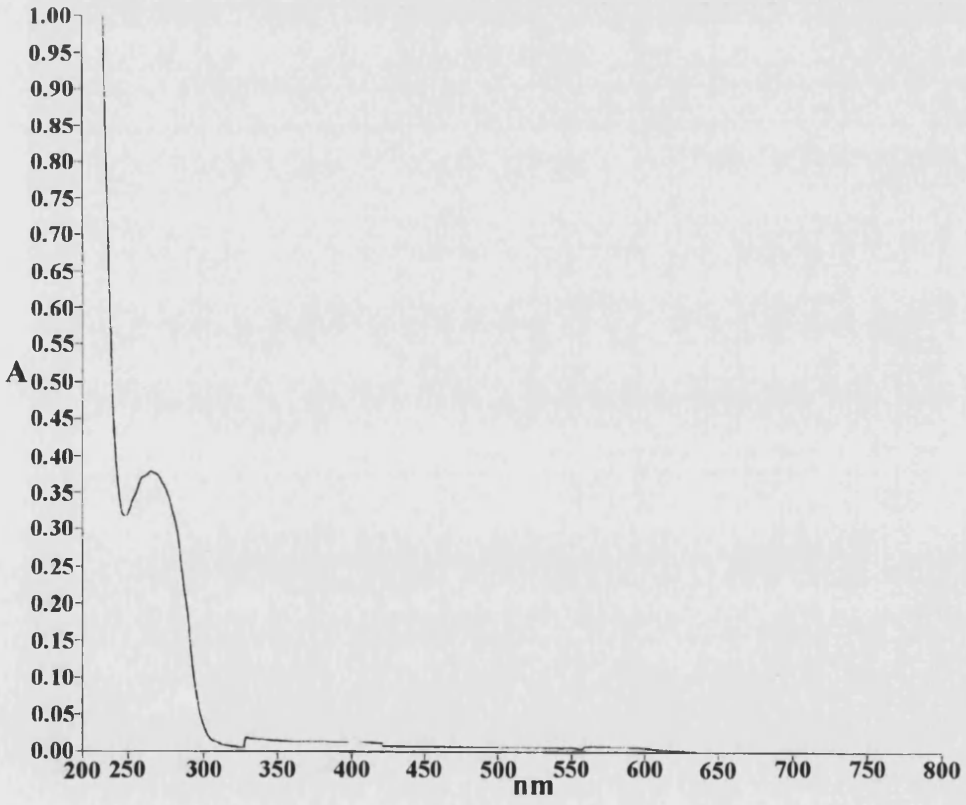

Figure 9 UV absorbance spectrum for a 0.1mg/ml aqueous sample of lumazine synthase.

The effect of buffer on the morphology of the lumazine synthase capsid was investigated by TEM. Lumazine synthase was added to an MES buffer, pH6.5, to give a final concentration of 0.1mg/ml. TEM analysis of this sample revealed the presence of a small number of much larger capsid structures, in the region of 15nm (Fig. 10).

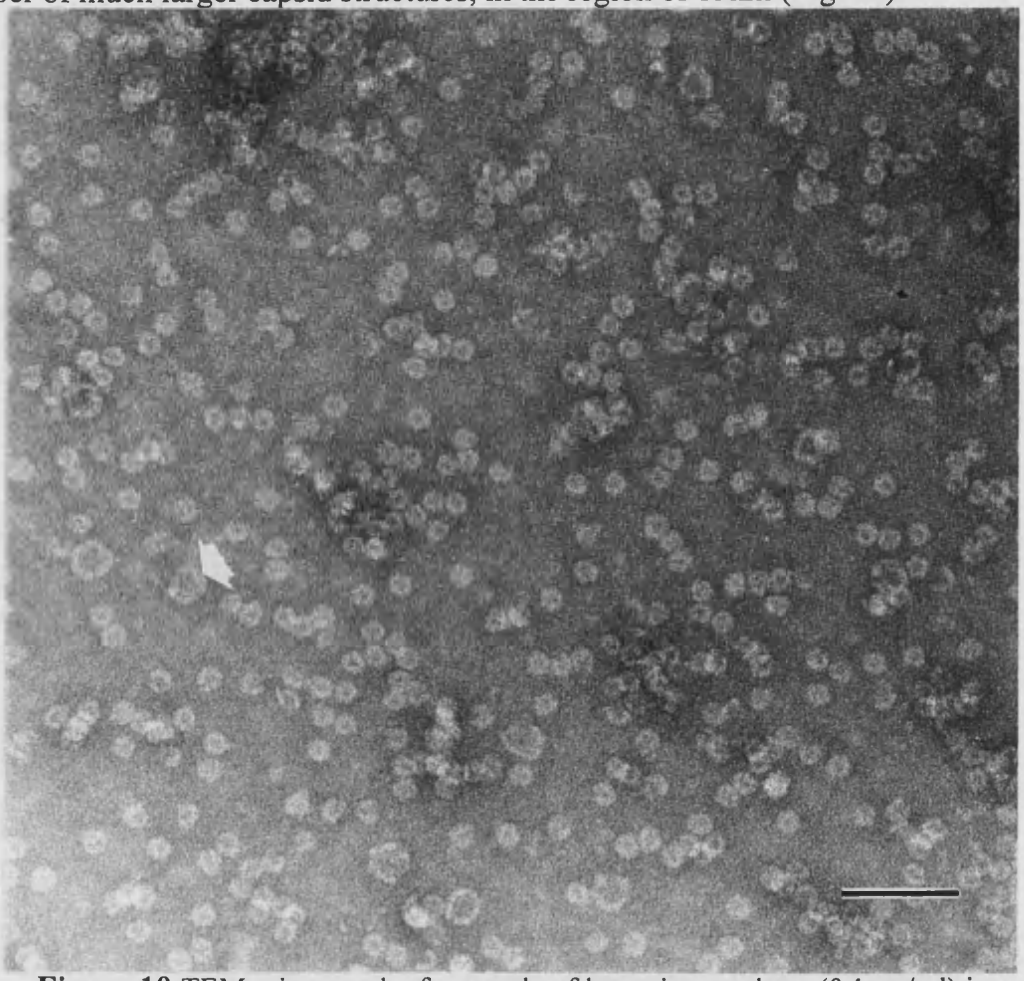

Figure 10 TEM micrograph of a sample of lumazine synthase (0.1mg/ml) in MES buffer. Larger 15nm capsids are indicated by arrows. Scale bar 50nm

This effect cannot be attributed directly to the influence of the buffer, as the addition of the lyophilised protein to the buffer would necessarily involve a dilution of the existing phosphate concentration, which is involved in the stability of the capsid. Examination of the sample after 24hrs revealed a similar distribution of 8 and 15nm capsids, indicating the stability of the capsid under these conditions to be altered, but not drastically. It is anticipated that addition of phosphate to the system would greatly increase the protein's structural integrity. The role of the cofactors, intimately involved in the stabilisation of the capsid structure, may also be an important stability factor upon dilution of the sample.

3.3.1 Uranium/Lumazine Synthase Composite

Images of lumazine synthase on a TEM grid stained with uranyl acetate suggested that the stain was able to penetrate the protein shell to give an electron dense interior. To verify that the hollow capsid allowed the uranyl ions to penetrate the shell, uranium ions were quantitatively added to a known concentration of lumazine synthase, giving an estimated final ratio of 2000 ions of UO_2^{2+} per molecule of lumazine synthase. It was anticipated that the UO_2^{2+} ions would be preferentially directed into the interior of the capsid.

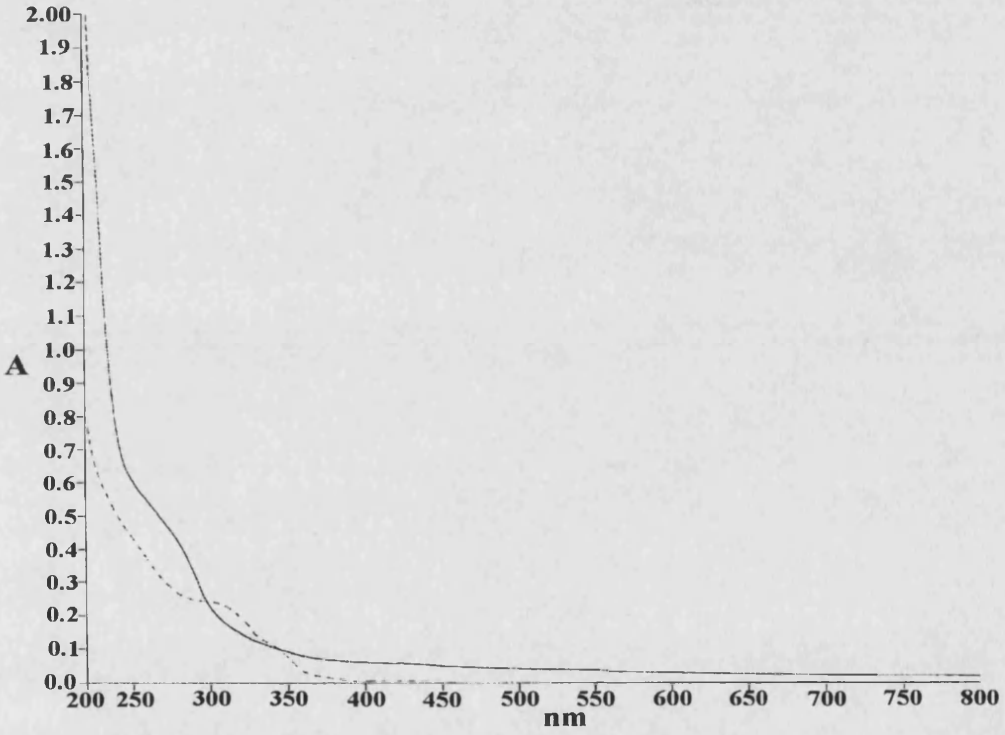

Figure 11 UV absorbance spectrum showing the effect of the presence of lumazine synthase on the absorbance profile of a buffered solution of uranyl acetate. The dotted line shows the spectrum obtained from the control sample, consisting of a buffered solution of uranyl acetate, and the thick line shows the spectrum from a sample of identical composition to which a known concentration of lumazine synthase was added. This should be compared to the protein absorbance profile seen in Fig. 9.

spectrum was obtained of both samples and these were plotted on the same graph for comparison (Fig. 11).

TEM analysis was employed to investigate the effect of UO_2^{2+} ions on the morphology of lumazine synthase. Examination of the control sample revealed no distinctive features, whereas examination of the sample containing lumazine synthase and no negative stain revealed small spherical particles. These particles displayed a varying particle distribution size, but had upper and lower bounds to their diameters of 2 and 4.5nm respectively (Fig. 12a). Energy dispersive X-ray analysis (EDXA) of the unstained sample (Fig. 13) revealed peaks for uranium, copper and potassium. Subsequent staining of this grid with uranyl acetate revealed the presence of a white halo around each particle, due to the negative staining effect. The micrographs obtained are reminiscent of those for negatively stained lumazine synthase (Fig. 8). The diameter of the particles, revealed by negative staining, was approximately 8nm, although some particles possessed diameters of 8.5-9nm. (Fig. 12b).

The observation that the control sample is yellow and the sample containing lumazine synthase remains transparent indicates that the lumazine synthase is exerting a effect upon the system. This effect is explicitly seen in the difference between UV absorbance profiles between the two samples. TEM micrographs support the hypothesis that the protein is able to concentrate the uranium ions into its interior. Unstained samples reveal electron dense spherical particles having a greatest diameter of 4.5nm, approximately that of the capsid interior. EDXA also reveals the particle to be comprised of uranium (the copper and potassium peaks due to the TEM grid and buffer salts respectively). Further investigation would establish if the particles are crystalline. Upon negative staining of the sample the protein shell is revealed to surround each core, possessing an upper diameter of 9nm. These dimensions are significantly larger, this may imply that the uranium is affecting a slight conformational change in the protein, which may be due to specific interactions or more global effects from the buffer and increase in ionic strength. The micrographs should be compared to those of Fig. 8, when considering the effect of buffer upon protein morphology.

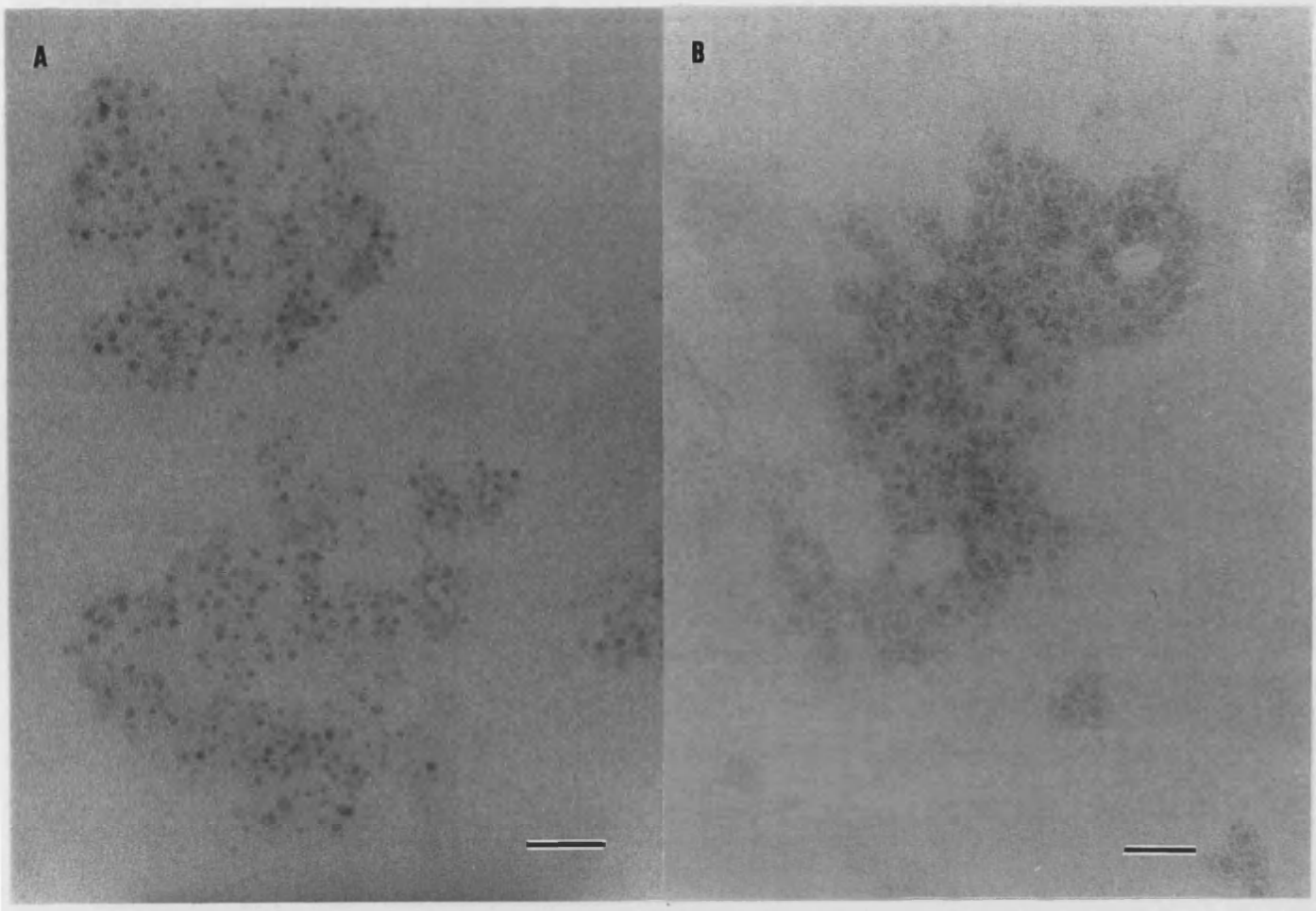

Figure 12 a) Shows an unstained sample of uranium/lumazine synthase sample. b) As for a, but stained with a solution of 2% uranyl acetate. Scale bars 20nm.

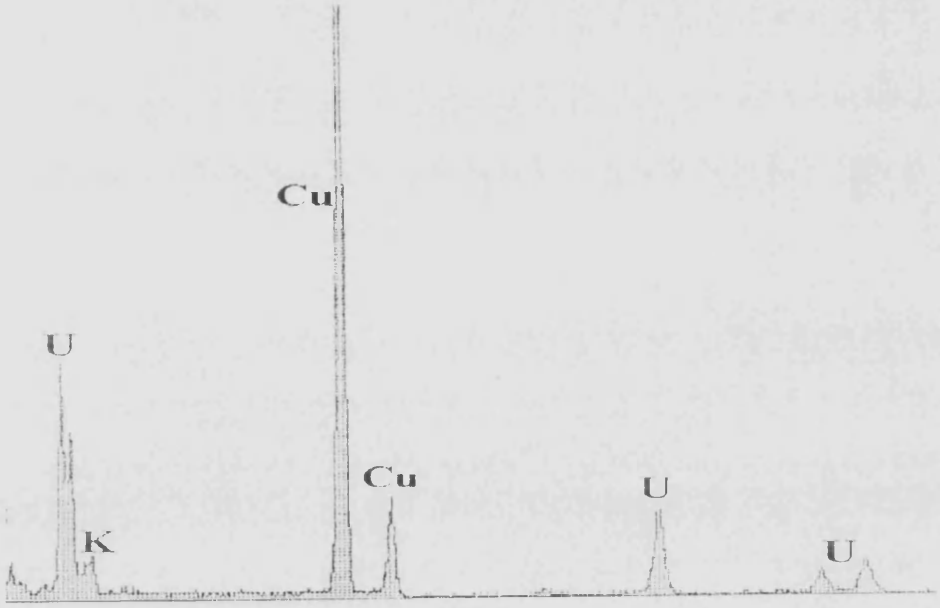

Figure 13 EDXA of unstained uranium/lumazine synthase composite, showing peaks for uranium, copper and potassium.

Comparison implies that, although a morphological change is evident, the capsid diameter does not deviate sufficiently from the buffered control sample.

These data suggest that the lumazine synthase capsid acts to sequester the uranium ions into its interior, resulting in the electron dense particles seen in the unstained sample. This contrasts greatly with the control, which revealed no similar structures, due to the very low concentration of uranyl acetate. It is reasoned that the sequestering of UO_2^{2+} into the capsid interior occurs through the shuttling of the uranium ions through the positively charged 3-fold channel. The interior of the capsid presents numerous glutamic acid residues to which the uranyl ions can bind and further investigation would need to be performed to discover the nature of the sequestered uranium. This process could conceivably act in an auto-catalytic way, the binding of uranyl ions to the interior allowing the further influx of ions to proceed along the potential gradient, resulting in particles of different diameter. It is suggested that the small difference in capsid morphology seen is due to the increase in ionic strength, although specific interaction of the UO_2^{2+} ions with the capsid cannot be ruled out.

3.3.2 Mineralization of Lumazine Synthase with Iron

The addition of Fe(II) ions to a known concentration of lumazine synthase was investigated. The positively charged iron atoms were expected to behave in an analogous fashion to the uranium ions and be preferentially directed to the interior of the capsid, whereupon a number of nucleation sites exist that might instigate the growth of a crystalline core within the protein capsid of lumazine synthase.

A range of iron loadings were explored to establish the effect of the increased iron concentration on the morphology of the lumazine synthase capsid. The ratios of iron atoms to protein molecules investigated were 300, 1000, 1500 and 2000 atoms per molecule.

The effect of 300 and 1000 atoms of Fe(II) added to lumazine synthase

The protocol described in the methods section was followed to achieve a ratio of 300 atoms of Fe(II) per molecule of lumazine synthase. Prior to this experiment a UV spectrum was obtained to verify the presence of the protein. The iron mineralization

protocol involved the slow addition of an Fe(II) solution to two samples, one containing 0.1mg/ml lumazine synthase and the other a control sample, consisting only of buffer. These conditions permitted the slow aerial oxidation of Fe(II) to Fe(III). After the addition of the final aliquot of Fe(II), it was noted that there was a drastic difference between the control sample and the sample containing the lumazine synthase. The former solution was brown, but the latter remained transparent, displaying a very faint straw colouration. Ultraviolet absorbance spectra were obtained, on completion of the experiment, of both the iron loaded lumazine synthase sample and the control sample. These spectra, together with the spectrum obtained for lumazine synthase in buffer, were plotted on the same set of axes for comparison (Fig. 14).

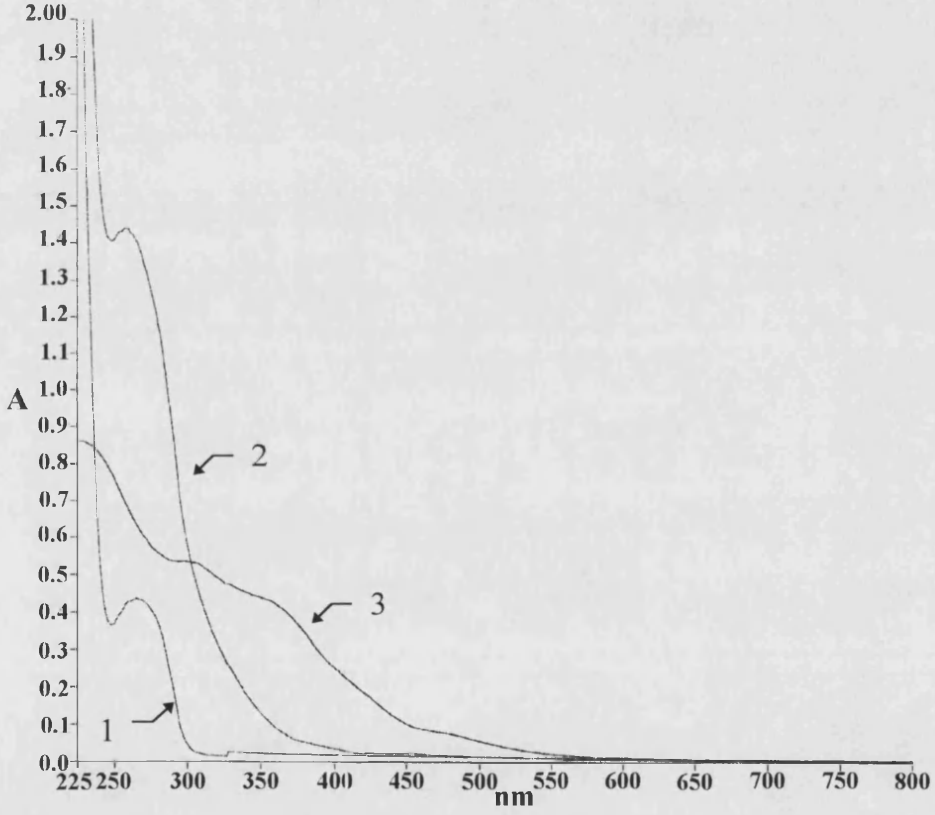

Figure 14 UV spectra obtained for the 300 atom Fe(II)/lumazine synthase experiment. 1) Shows the absorbance profile characteristic of protein in buffer, prior to addition of iron. 2) Shows the profile of sample containing lumazine synthase with a ratio of 300 Fe/protein molecule. 3) Control sample

Both samples were then left to slowly stir for 12 hours, whereupon re-examination revealed the control to have a brown pricipitate phase, but the sample containing lumazine synthase remaining transparent. The spectra obtained clearly demonstrate the effect of the addition of iron to lumazine synthase. The control sample displays the broad absorption peak (3) associated with bulk precipitation, an observable effect manifested as macroscopic material in the sample. The sample containing the lumazine synthase prior to the addition of iron (1) displays the characteristic 280nm absorption peak expected for proteins. On completion of the experiment, the spectrum recorded for the sample containing iron and protein shows a dramatic three fold increase in absorption (2), with the aromatic absorption peak shifted to the left.

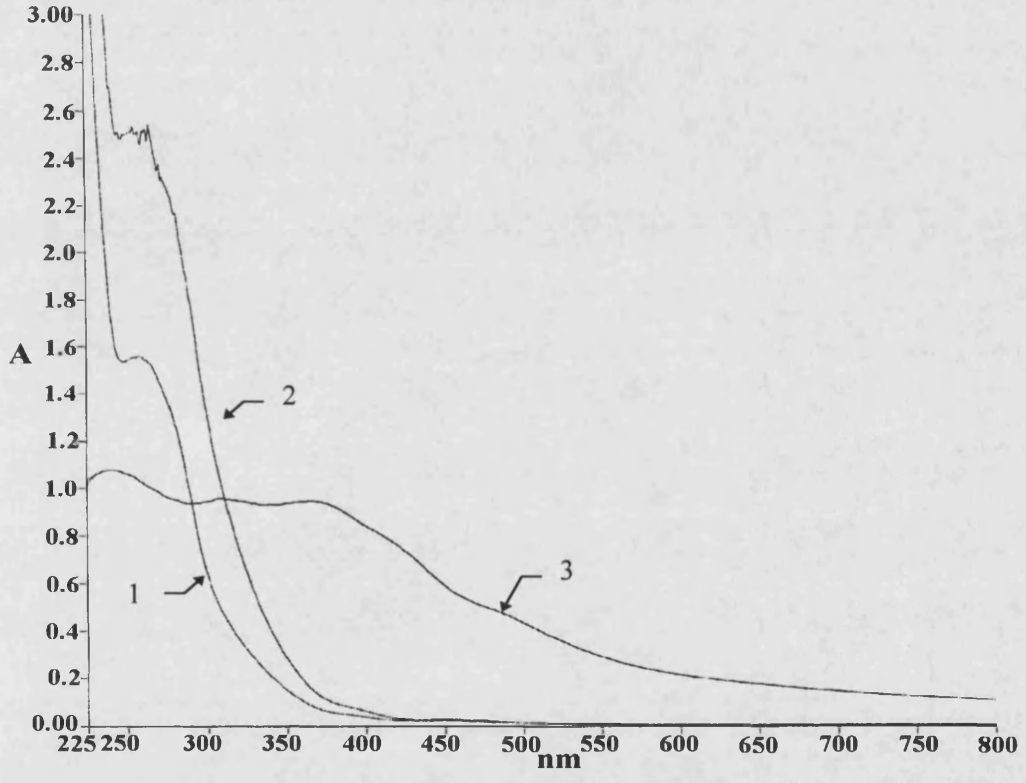

Figure 15 UV spectra obtained for the 1000 atom Fe(II)/lumazine synthase experiment. 1) Shows the absorbance profile obtained after the addition of 300 atoms of Fe(II)/protein. 2) Shows the profile obtained after the continued addition of iron to give a final ratio of 1000 Fe/capsid. 3) Control sample.

the remainder of the iron added. The spectrum obtained on completion of the experiment (2), giving the final ratio of 1000 atoms of Fe/ capsid, shows a much greater absorbance than that for the 300 Fe system. It should be noted that when the iron loading was increased to 1000 atoms per lumazine, the control sample revealed a greater degree of precipitation (resulting in the much broader peak 3), but in contrast, the sample containing lumazine synthase remained transparent.

In order to visualise the effect of the lumazine synthase molecules upon the oxidation of the Fe(II) ions, TEM analysis was employed. Aliquots of the control sample precipitate from the 300 Fe/capsid experiment, applied to TEM grids and examined under the electron microscope, revealed large crystalline masses, as would be expected for a slow oxidation of Fe(II) to Fe(III). Electron diffraction confirmed these crystalline masses to be the iron polymorph lepidocrocite. No analogous large precipitous masses were observed in the samples containing lumazine synthase. The 300 Fe atom/protein sample revealed small, spherical particles, displaying a range of diameters, from 4nm to approximately 12nm (Fig. 16a). Negative staining of this sample delineated the protein capsid, but revealed that a number of the capsids possessed diameters exceeding 20nm (Fig. 16b). The effect of the protein on the oxidation of Fe(II) is explicitly seen when comparing Fig. 16a to Fig 16c, the latter TEM micrograph giving an example of the precipitate seen in the control. To assess the effect of time upon the iron loaded lumazine synthase sample, TEM micrographs were taken of the same sample after a duration of 4 days. The sample was negatively stained with uranyl acetate to visualise the protein (Fig. 16d). The results indicate that the protein capsids were on average larger than those examined 4 days previous.

To ascertain the nature of the small spherical particles, selected area electron diffraction (SAED) was performed on several areas of the TEM grid displaying a high number of the stained particles (Fig. 17a). The diffraction pattern immediately confirms the presence of iron and it to be crystalline, due to the presence of the concentric ring pattern. The presence of rings indicates a number of non-crystallographically orientated nanocrystals. The d-spacings measured for the iron mineralized lumazine synthase also

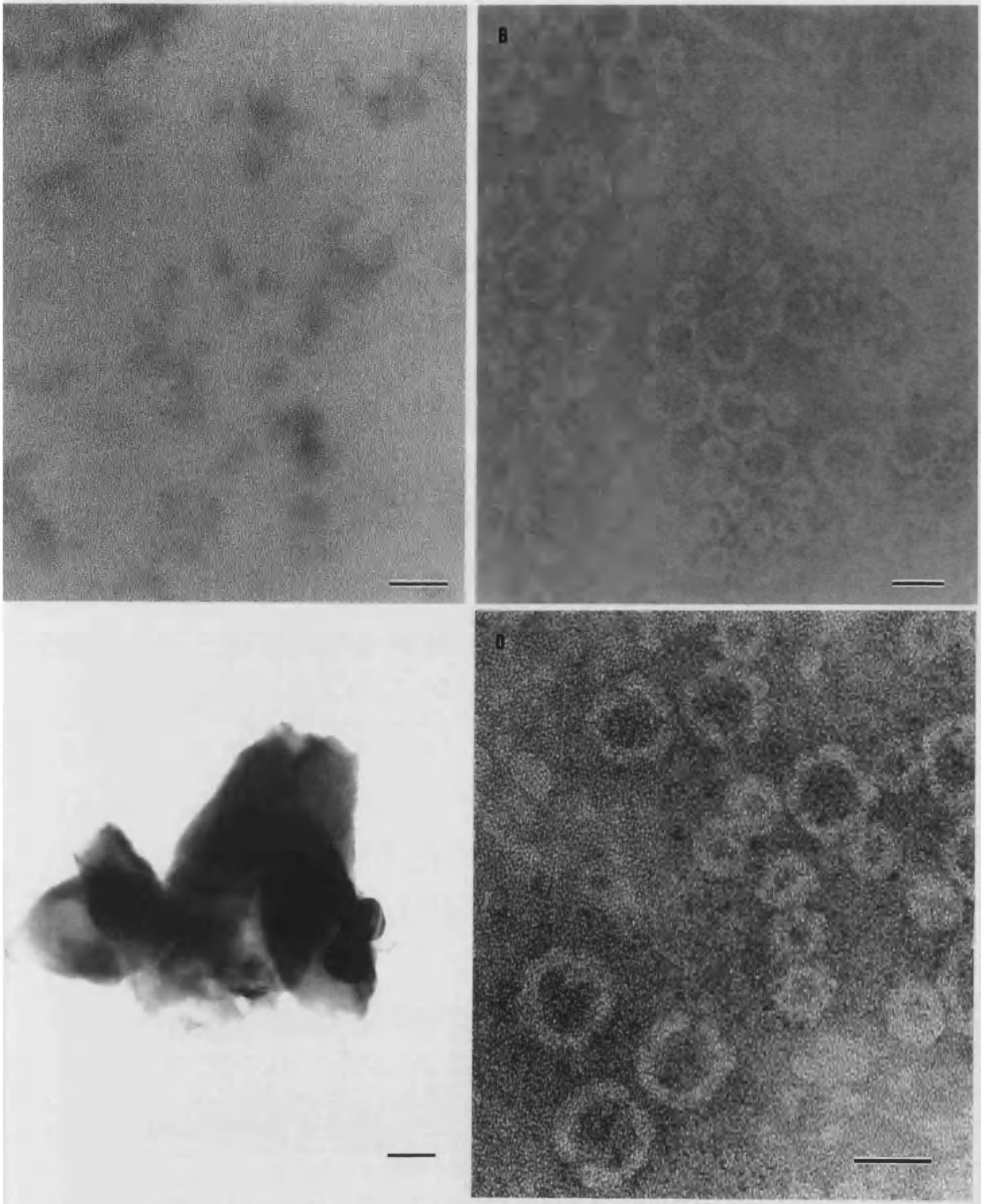

Figure 16 A) Unstained sample of the 300 Fe/capsid ratio, scale bar 20nm B) Stained sample stained 300 Fe/capsid ration, scale bar 20nm C) Precipitate from control sample, scale bar 100nm D) HRTEM image of stained 300 Fe/capsid after 4 days, scale bar 20nm.

A

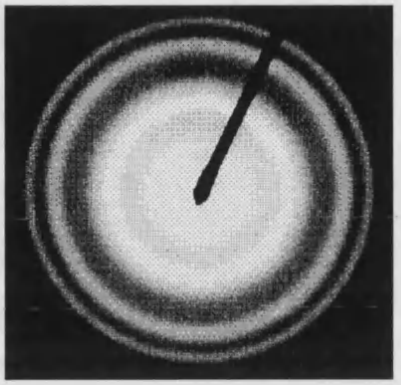

Lepidocrocite d-Spacings (nm)	Iron loaded lumazine synthase d-spacing (nm)
3.29	3.20
1.94	1.96
1.73	1.66

B

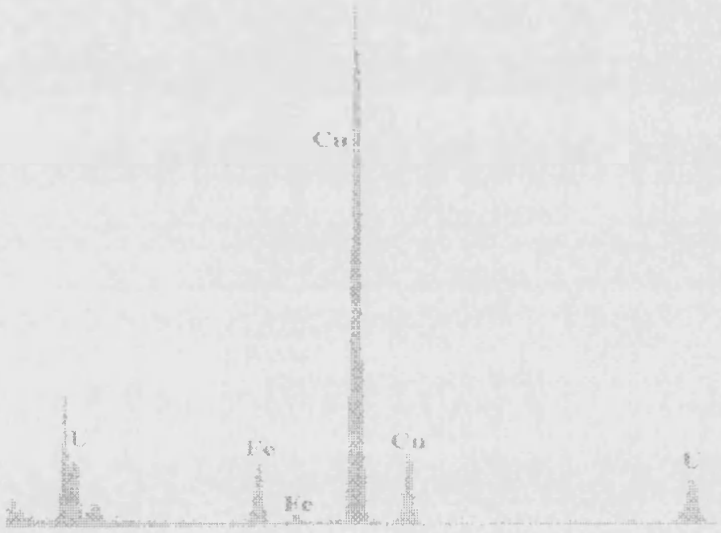

Figure 17 a) SAED pattern of unstained lumazine synthase and table showing the d-spacings obtained, compared to those for lepidocrocite b) EDXA of a stained sample confirming the presence of iron. Cu and U peaks are due to the TEM grid and negative stain respectively.

correspond to those for the iron polymorph lepidocrocite. EDXA of a stained sample of the iron mineralized lumazine synthase also confirmed the presence of iron. (Fig. 17b).

These data collectively suggest the lumazine synthase capsid is able to sequester the iron into its interior, whereupon the iron is oxidised to the iron polymorph lepidocrocite. The TEM micrographs of the iron mineralized lumazine synthase show the presence of small particles, possessing diameters between 4 and 12nm, contrasting sharply to the control sample which showed large, irregularly shaped crystals. TEM also reveals that a conformational change occurs in accordance with the conditions employed for

for mineralization. The presence of large capsids, some with diameters of > 15nm, cannot be due to the buffer, as comparison with Fig. 10 shows that in the system containing iron, there is a much greater instance of these larger capsids. Re-examination of the sample after a duration of 4 days reveals the presence of still larger capsids with diameters exceeding 20nm. This suggests that the conditions of the experiment are exerting a much greater influence on the capsid morphology than can be explained by buffer effects alone. This process appears continual, as the conformational changes seen continue with respect to time. One interesting aspect of the capsid structure seen is the corrugated appearance of the protein. It is suggested that the gaps seen in the protein are the channels, enlarged due to conformational change. The increase in the ionic strength of the solution may have an effect on the capsid structure, but is seems more feasible that the iron ions are directly affecting the conformation of the protein. This effect may be exerted in a variety of ways including direct binding of iron to the protein, resulting in conformational change or the mineralization process within the capsid somehow coercing a structural change. It has been shown that the stability of the capsid is strongly influenced by the environment, but under conditions of a high concentration of phosphate, the capsid is extremely stable. For this reason, introduction of iron to the capsid may affect stability through complexation of the phosphate, resulting in a less stable capsid. This effect, coupled with the increase in ionic strength and the mineralization of iron in the capsid interior, may result in an increase in the dynamic nature of the capsid, demonstrated by the formation of very large capsids. This process may also continue to produce even larger capsids.

UV absorbance spectra of the 1000 Fe atoms per lumazine synthase gave similar increases in absorbance as seen in the 300 system. The control samples differed in that a greater degree of precipitation was observed when compared to the 300 system, revealed as a broader peak for the 1000 Fe system, although the sample containing the protein continued to be transparent. To visualise the effect of this 3-fold increase in iron concentration per lumazine synthase molecule, TEM analysis was performed on concentrated samples, one left unstained and the other stained with 2% uranyl acetate (Fig. 18), for comparison with TEM micrographs for the 300 Fe/capsid results.

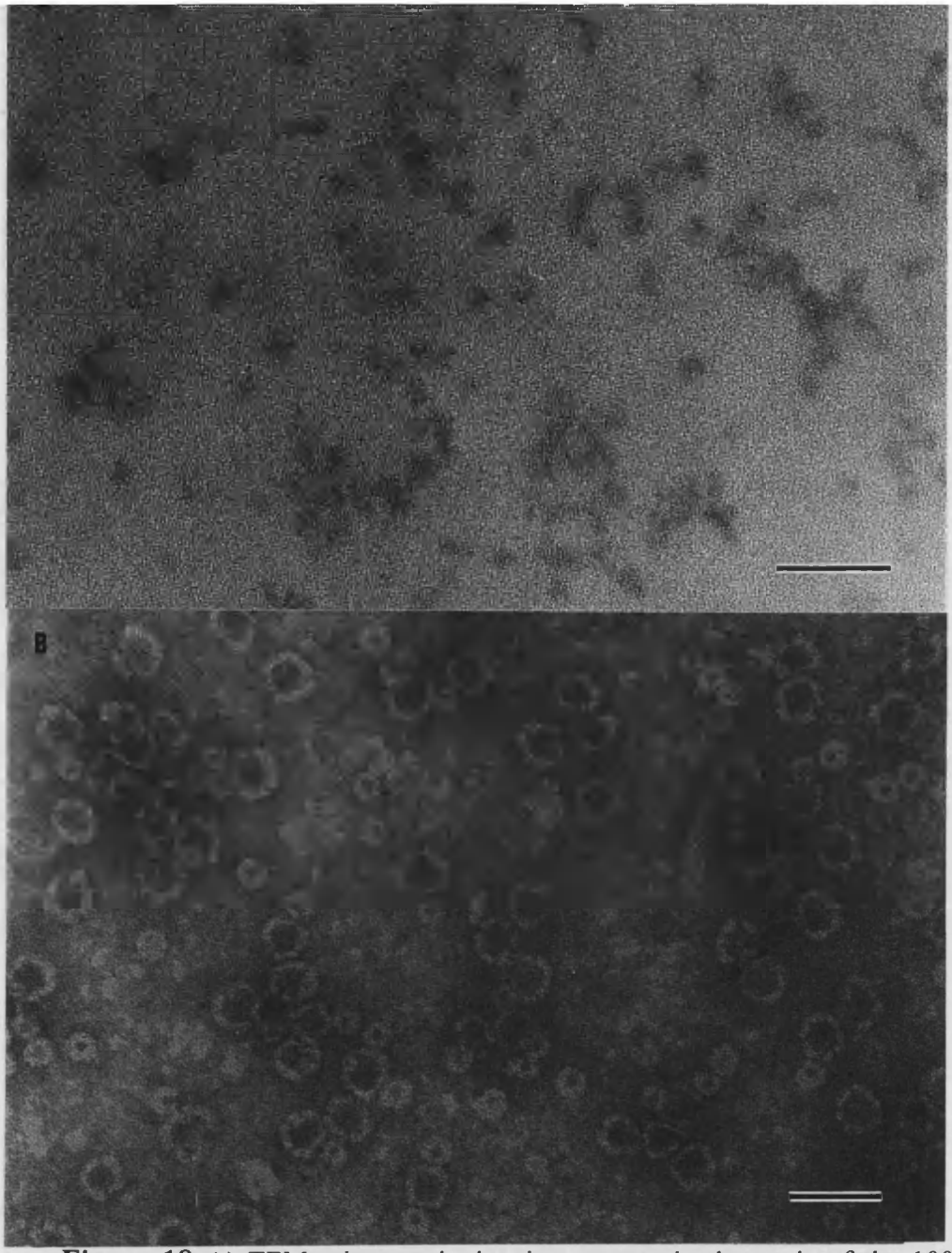

Figure 18 A) TEM micrograph showing an unstained sample of the 1000 Fe/capsid experiment, scale bar 50nm. B) Micrograph showing a uranyl acetate stained sample of the 1000 Fe/capsid experiment, scale bar 50nm.

Unstained samples revealed a greater concentration of small spherical particles, possessing diameter from 5 to 20nm. It can also be seen that, when compared to Fig. 16 which shows the effect of 300 atoms of Fe per lumazine synthase molecule after a few hours, there is a greater instance of the large capsids. There are also much larger capsids present (>30nm), that were not observed in the 300 atom sample. These data reinforce the hypothesis that the increase in concentration of iron in the sample results in a greater conformational change in the protein capsid.

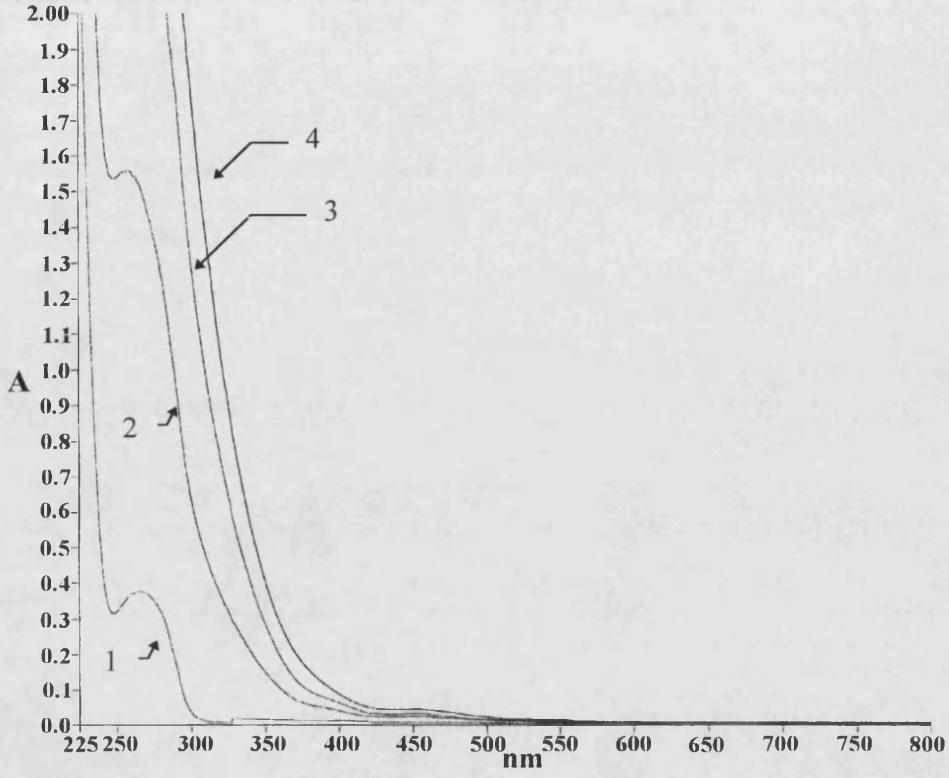

Figure 19 UV absorbance spectra of the 1500 Fe/Lumazine synthase sample. 1) Absorbance spectrum obtained prior to the addition of iron. 2) Absorbance profile after the addition of 300 atoms of Fe/protein. 3) Profile obtained after addition of 1000 Atoms of Fe/protein. 4) profile obtained after addition of 1500 atoms of Fe/protein.

To further investigate the effect of increased Fe concentration on protein morphology, an experiment employing 1500 Fe atoms/ lumazine synthase molecule was performed. UV absorbance spectra were obtained at regular intervals, as for the previous two experiments (Fig. 19). The spectra recorded clearly show that the addition of the aliquots of Fe(II), to the sample containing lumazine synthase, results in a concomitant increase in the absorbance of the sample. No precipitation was observed in the sample containing the protein, which exhibited a very light brown colouration. Conversely, the control sample contained huge brown macroscopic particles that quickly separated into two phases.

TEM analysis performed on concentrated samples of the iron/protein system again confirmed the presence of small spherical particles (Fig 20). Negative staining also

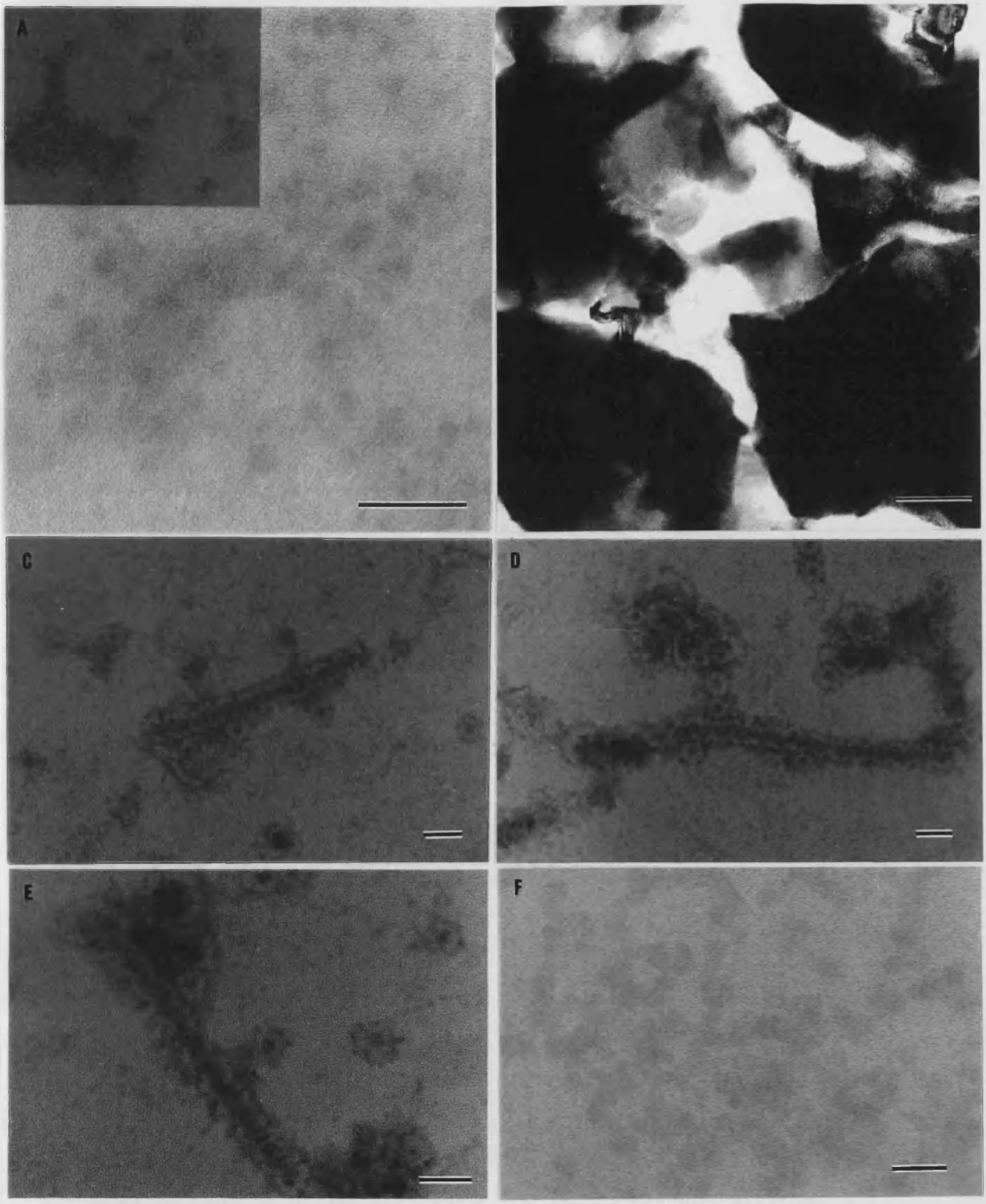

Figure 20 A) TEM micrograph showing unstained sample of 1500 Fe/capsid, scale bar 20nm, inset showing a stained sample. B) Precipitate seen in the control sample, scale bar 100nm. C) & D) Stained images of the lumazine synthase tubular morphology seen with high concentrations of iron, scale bar 20nm E) HRTEM of tube, scale bar 20nm. F) Unstained image of sample containing tubes, showing elongated particles, scale bar 20nm.

showed a greater presence of the huge capsids with diameters exceeding 30nm (Fig. 20, inset), suggesting that the addition of even larger concentrations of iron induces a greater capsid conformational change. The iron mineralized lumazine synthase sample was allowed to age for 4 days at 4°C and re-examination of the sample was performed to compare with those results obtained for the 300 atom Fe system. It was predicted that even larger capsids would be present, TEM analysis confirmed this hypothesis, but also revealed a different phase of capsid structure, where the capsids merge to form tubular conformations (Fig 20c,d,e). These micrographs show the range of capsid morphologies seen. Unstained samples of this aged 1500 Fe atom/protein sample examined by TEM (Fig.20f) indicated the presence of elongated iron particles, although tubular templating could not be unambiguously verified. SAED of this sample again confirmed the crystalline nature of the iron particles but showed a greater degree of crystallinity, indicated by to the presence of stronger lines. This phenomenon is explained by the 5-fold increase in the concentration of iron added to the protein, when compared to the 300 atom Fe system.

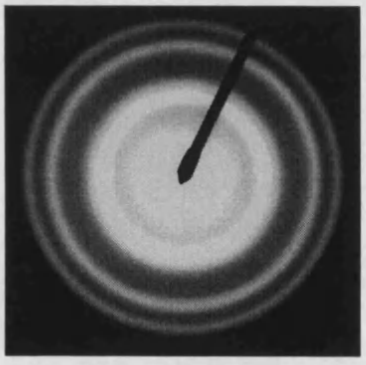

Lepidocrocite d-Spacings (nm)	Iron loaded lumazine synthase d-spacings (nm)
3.29	3.29
1.94	1.92
1.73	1.73
1.52	1.52

Figure 21 SAED pattern and corresponding comparison to lepidocrocite for 1500 Fe/capsid experiment.

These data again support the hypothesis that the lumazine synthase prevented the oxidation of the Fe(II) to bulk Fe(III), through directed channelling of the Fe(II) ions into the interior of the capsid, resulting in the formation of nanocrystalline iron particles. The dramatic contrast between the sample containing protein and the control, demonstrates the effectiveness of this process.

The ability of the lumazine synthase capsid to prevent the bulk formation of iron oxide was also shown to occur with samples that had been aged for several days. The 1500 Fe atom sample was allowed to age for 4 days at 4°C and the addition of 500 atoms more of Fe(II)/capsid was then added to the sample. The sample remained transparent and continued to be stable for several months. This indicates that iron could be added to an existing iron mineralized sample of lumazine synthase and still no precipitate would be seen, suggesting the sequestering of iron to still occur.

To verify the increase in density of these mineralized samples and also the variation in size catalysed by the presence of iron, ultra analytical centrifugation (UAC), was performed (Fig. 22).

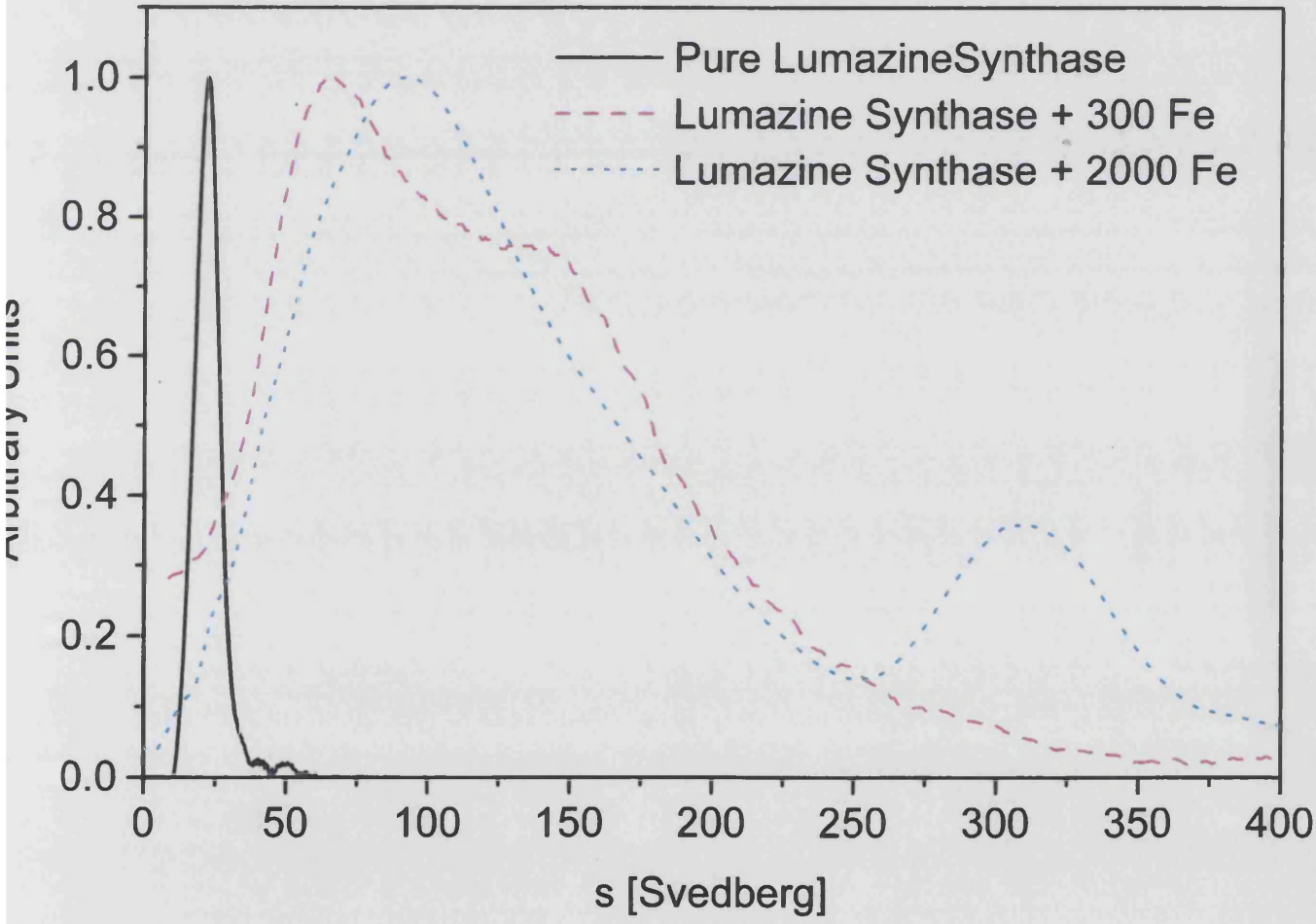

Figure 22 Graph showing the sedimentation coefficients obtained from the 300 and 2000 Fe/capsid ratios compared to a buffered solution of native lumazine synthase.

The graph shows the difference in sedimentation coefficient between three lumazine synthase samples; lumazine synthase in MES, iron mineralized lumazine synthase at a ratio of 300 Fe/capsid and iron mineralised lumazine synthase at a ratio of 2000 Fe/capsid. The sample of lumazine synthase in buffer shows a single peak at approximately 25S with two very small peaks at higher values. This suggests the larger peak to correspond to the 8nm β60 capsid of lumazine synthase, with the small, noisy peaks representative of the trace of 15nm capsids and maybe even larger capsids, albeit in very small numbers. The 300 and 2000 Fe samples show a greater sedimentation coefficient and also bimodality. The 300 Fe sample shows peaks at 75S and 140S and the 2000 Fe sample displays two distinct peaks at 95S and 320S. These data give a good correlation to the TEM data obtained, with respect to the change in particle size and the suggested iron mineralization. Although UAC data detect changes in both particle size and/or density, the major contribution in the data comes from the increase in density. Therefore, these data support the hypothesis for the mineralization of the internal cavity of lumazine synthase with iron, resulting in a particle of greater density than native lumazine synthase. The spectra clearly show that the increase in the concentration of iron results in a greater sedimentation coefficient and therefore a more dense particle. The bimodality of each spectrum also supports the observation of capsids of different diameters, the diameter being a function of iron concentration. The broadness of each peak also suggests there to be a particle size range around a mean value for particle size/density, which again was seen in TEM. Overall, it can be inferred from the UAC data that the addition of iron to a sample of lumazine synthase results in the formation of a particle possessing a greater density to that of empty capsids, with a concomitant increase in particle diameter. Combining these data with those from TEM, gives compelling evidence for the ability of lumazine synthase β60 capsids to act as a nanoscale template, internalising Fe(II) through the 3-fold channel and allowing the bounded oxidation to Fe(III) to occur. The amino acid residue distribution on the internal surface of the capsid allows the sequestered Fe ions to nucleate at the numerous glutamic acid residues, resulting in the formation of nanocrystalline lepidocrocite.

3.3.3 Mineralization of Lumazine Synthase with Tungsten

The potential of lumazine synthase in the production of tungsten mineral composites was next explored using two protocols. The first protocol employed the incremental addition of aliquots of aqueous Na_2WO_4 to a slowly stirred solution of lumazine synthase, giving a final ratio of 1500 atoms of tungsten per capsid. This solution was allowed to stir for 24 hours at 4°C, after which the pH was reduced to 5.5. Examination of the stained sample revealed the presence of the protein capsid in its entirety, with the majority of the capsids in the 8nm form (Fig. 23a). Examination of the control sample revealed small spherical particles (Fig. 23a, inset), which EDXA revealed to contain tungsten (Fig. 23b).

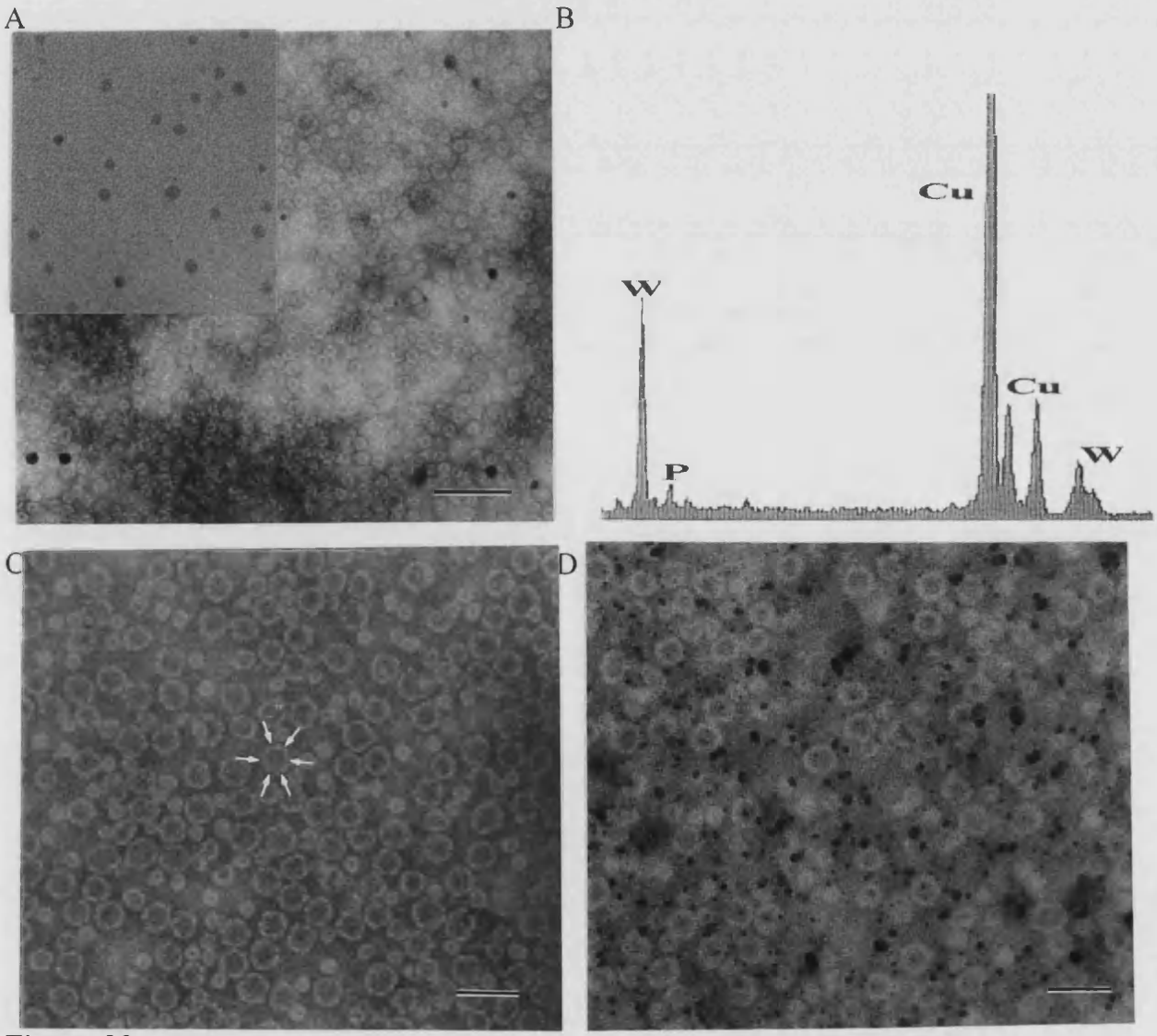

Figure 23 A) TEM micrograph showing stained sample of tungsten mineralized lumazine synthase, scale bar 100nm. Inset shows unstained sample. B) EDXA of the tungsten/lumazine synthase sample. C) Micrograph showing sample of lumazine synthase incubated with tungsten prior to the reduction of pH, scale bar 50nm. Arrows indicate channels revealed by tungsten staining. D) As for C) after the reduction of pH to 5.5, scale bar 50nm.

The next protocol assessed the effect of the buffer on the mineralisation of the lumazine synthase capsids. The experiment involved the incubation of 35mg of $NaWO_4$ with 0.1mg lumazine synthase in a TES buffer, adjusted to pH8.2 by addition of 1M NaOH. The solution was incubated for 24 hours at 4°C, the pH then reduced to 5.5 by the addition of 1M HCl. The results obtained again were similar to those obtained in the first protocol. Despite several attempts to remove excess tungsten, imaging of an unstained sample at pH8.2 revealed the presence of the capsids, the excess tungsten acting as a negative stain (Fig. 23c). It should be noted that the tungsten acts as a very efficient negative stain, revealing the channels in the capsid. Reduction in pH revealed electron dense particles as in Fig. 23a and the excess tungsten again revealed the protein. The polymerised tungsten appears not to be associated with the capsids.

These data suggest that the lumazine synthase capsid did not induce the mineralization of a polytungstate in the interior of the capsid. Electron micrographs revealed that although the capsid remained intact in all experiments, the interior of the capsid did not reveal an electron dense core, characteristic of the mineralisation. It can be inferred from the micrographs that the tungsten is able to penetrate the capsid to give a negative staining effect, similar to that seen for uranyl acetate. It has been suggested that the only possible port of entry for the positively charged uranyl and iron ions is through the negatively charge 3-fold channel, permitting access to the interior of the protein. Thus, it seems probable that the negatively charged WO_4^{2-} ions can gain access to the interior of the protein only through the positively charged five fold channel, allowing a solvent exchange between the interior and exterior of the protein. Indeed, the negative staining effect of the excess tungsten reveals the presence of the channels through the capsid wall (Fig. 23c). An important structural difference, with respect to mineral nucleation, is the distribution of potential binding sites for metal ions. The three fold channel may permit the passage of Fe(II) ions to the interior of the capsid and once inside the iron atoms are able to bind to the numerous negatively charged Glu residues, which can serve as nucleation sites. In contrast, the negatively charged WO_4^{2-} ions may penetrate the protein capsid via the positively charged 5-fold channel, but are not presented with sufficiently large numbers of nucleation sites. The presence of such an abundance of negative charge on the internal surface of the capsid may even create a

gradient of repulsion, preventing ion binding. This effect would explain the absence of any tungsten mineralized lumazine synthase capsids. Fig. 23c also shows the dramatic effect of a high ionic strength upon the morphology of the lumazine synthase capsid. As can be seen, the vast majority of the capsids are approximately 15nm in diameter. It should be borne in mind that the creation of tungsten mineralized lumazine synthase capsids could conceivably be created through a 'ship-in-a-bottle' mechanism. The lowering of pH would initiate the formation of polytungstate species, which, if they already are within the protein shell, would be prevented from diffusing out of the capsid due to size exclusion.

3.4 Conclusions and Future Work

This work has shown for the first time that a non-native mineral producing enzyme, found in bacteria and fungi, can serve as a mineralization template in the fabrication of quantum dots of iron. Moreover it has been shown that the template is a dynamic system that allows the formation of a variety of inorganic morphologies, a trait not seen in similar static bio-templating systems.

The β60 capsid protein represents a unique structural system, possessing two types of channel lined with positive and negative amino acid residues respectively. The staining of a concentrated sample of lumazine synthase revealed the spherical capsid shape and also the hollow inner core, due to penetration of the shell by the positively charged UO_2^{2+} ions. This inference was substantiated by performing experiments that consisted of adding small amounts of uranyl acetate to a solution of lumazine synthase. TEM analysis of this solution revealed small spherical particles, commensurate with the internal diameter of the lumazine synthase capsid. The absence of any negative staining suggests the uranyl ions to have penetrated the protein shell, presumably through the negatively charged 3-fold channel.

The role of the 3-fold channel in the exchange of ions from the bulk solvent to the interior of the protein shell was further explored through the specific iron mineralization of the interior of the lumazine synthase capsid. The slow addition of Fe(II) to a de-aerated buffered solution of lumazine synthase produced a marked difference in comparison to the control sample. The former remained transparent whereas, in stark contrast, the latter possessed a brown colouration which eventually resulted in a brown precipitate. Even at relatively high ratios of iron atoms to lumazine molecules, only a very faint straw coloured solution was observed, with no precipitate.

The interior of the protein capsid then presents an inner wall studded with potential nucleation sites in the form of glutamic acid residues. Computer generated images of the β60 capsid show the distribution of these amino acid residues on the internal surface of lumazine synthase (Fig. 24). The image compares the distribution of glutamic acid residues to another negatively charged residue, aspartic acid (A and B).

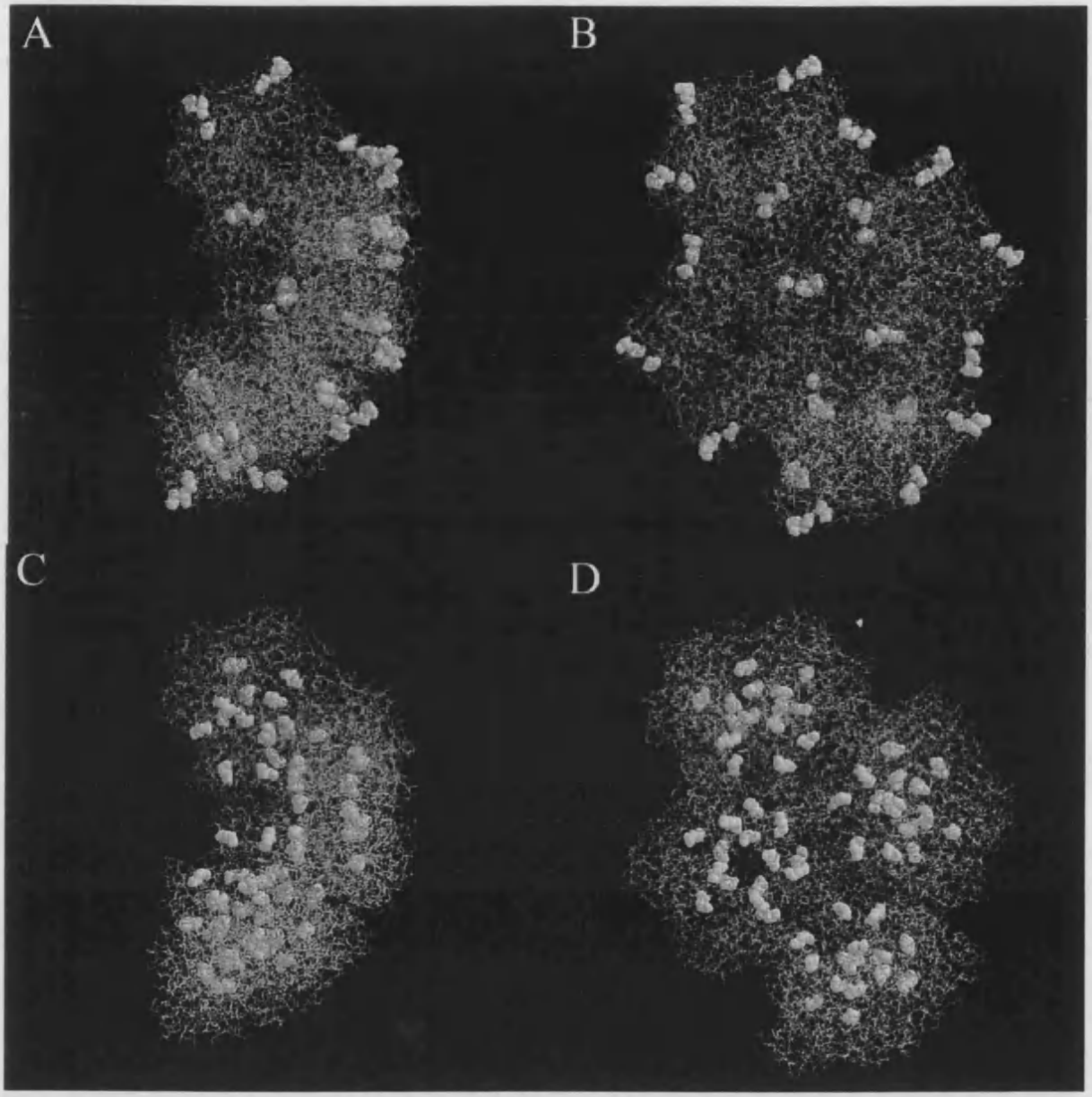

Figure 24 Computer generated images of 5 pentagonal subunits of lumazine synthase showing the distribution of Glu and Asp residues on the interior surface of lumazine synthase. A and B show Asp distribution and C and D show Glu distribution.

The Asp residues are located at the corners of the pentamer subunits and are implicated in the association of capsid subunits. In comparison, the three Glu residues per trimer (C and D) are distributed on the inner surface of each subunit and provide a number of potential nucleation sites for the growing iron crystal. The nucleated nanomineral has been shown by electron diffraction to be lepidocrocite. This presents an interesting difference when compared to the mineralization aspects of ferritin, which nucleates ferrihydrite. The effect is within the bounds of the proposed mechanism of iron mineralization, as the mineral

expected upon a slow aerial oxidation of Fe(II) is lepidocrocite. The use of an aqueous solution of lumazine synthase as nanocavities in the mineralization of Fe(II) results in a myriad of encapsulated domains that allow this oxidation to proceed. The protein shell then ensures the oxidation is confined to a bounded space. In contrast, the role of ferritin is that of an iron storage protein that demands a quick mineralization/demineralization of the stored iron for use in cells. The role of ferrihydrite has been suggested to facilitate this process[27].

The large five fold channel would be expected to allow the passage of large negatively charged ions. This was the premise for the employing of negatively charged WO_4^{2-} ions. It was shown that the tungstate was able to penetrate the protein shell of lumazine synthase and even to allow the visualisation of the channels, although high resolution TEM revealed no crystallinity within the cavity, showing only extraneous polytungstate particles. This may be explained due to the lack of positively charged nucleation sites within the cavity of the protein. An additional effect may also come from repulsion by the negatively charged residues that line the internal wall.

This work represents only a small survey of the potential of this remarkable molecule and sets the ground work for a full characterisation of the use of this molecule in the future. Research into the morphology of this molecule is in its infancy and consequently much is not known. One aspect of the work is the dynamic nature of the capsid protein and the higher order structures the protein is able to assume, an avenue of research not explored previously. The iron mineralization of lumazine synthase necessitates investigation into the conformational changes that lumazine synthase displays and has prompted researchers at the Institiut fJr Organische Chemie und Biochemie, Technische Universitat MJnchen, MJnchen to instigate further collaboration. It has been shown that the addition of iron to a buffered solution of lumazine synthase results in substantial conformational changes. The concentration of iron was shown to be related to the degree of morphological change, where high concentrations, such as 1500 atoms of Fe per capsid, resulted in capsids possessing diameters greater than 30nm. These effects cannot be explained by buffer effects alone, suggesting a more direct interaction of the iron with the capsid, possibly through complexation with bound phosphate. The effect of increasing iron concentration was explicitly seen in the production of protein

tubes. This tubular morphology represents an unusual mode of self assembly and has previously been observed only in extreme conditions, thus further work would investigate this effect to establish the nature of the conformational change with respect to iron. Future work would thus concentrate on ways to control this protein rearrangement, employing sophisticated techniques, such as neutron diffraction, to understand the nature of this phenomenon. Other collaborative ventures will use a variety of techniques to investigate the effect of mineralization on the capsid, including density gradient centrifugation to establish a particle distribution, field-flow fractionation to give a particle size distribution independent of density and dynamic light scattering to estimate the density independent polydispersity of particles.

It has been shown that phosphate has a great effect on the stability of the protein, but this work did not investigate the effect of adding the substrate analogues to the system. This would represent a direction of further research, investigating ways of controlling the morphology of the capsid through addition, or synthesis, of substrates able to stabilise or destabilise the protein. This work could lead to the production of a variety of controllable nanoscopic mineralization templates from spheres of differing radii to tubes.

The production of uranyl/lumazine composites presents a potentially useful therapeutic system. Uranium is an element, together with boron, which has potential in the treatment of certain cancers by a process known as 'neutron capture therapy'[28]. These elements are useful due to their ability to absorb neutrons from a source and emit alpha particles, the alpha particles having a path length roughly the same as the diameter of a human cell and hence the capability of destroying cancer cells. The ability to target tumours with nanoscopic materials, such as the uranium/lumazine synthase composite through antibodies, could offer highly specific techniques to combat cancer.

An aspect of future work currently being investigated in collaboration is the production of lumazine mutants from site directed mutagenesis. These mutants could be tailored to meet the specific mineralization requirements of the system. For example, it was shown that tungsten was able to penetrate the protein capsid but not to crystallise, the port of entry suggested to be the large 5-fold channel. The production of mutants, in which the carboxyl groups lining the interior of the capsid, implicated in iron

mineralization, are replaced by lysines, may offer the required nucleation sites. One project currently being initiated is the use of a temperature stable mutant able to retain structural integrity at temperatures greater than 80°C. Such mutants have potential for the synthesis of magnetic cores inside the capsid.

Lumazine synthase represents an entirely new class of nanoscopic mineralization template. Its unique design comprising both positive and negative channels, may also offer the production of a wide range of polymetallic nanocomposites, where each ionic species is presented with an unhindered path to the nucleation site in the interior of the capsid. This phenomenon may lead to the production of a new class of nanomaterials with novel electronic, optical and magnetic phenomena, these materials possessing 'tuneable' qualities, due to the architecture of the lumazine synthase capsid.

The specificity of lumazine synthase to pathogenic bacteria and fungi may allow the enzyme to serve as a target for tailored treatments against infection. For example the synthesis of a variety of lumazine synthase nanocomposites may find applications ranging from alternative agents in cancer therapy, antibiotic alternatives, bio-medical imaging and drug delivery systems.

3.5 References

1 A.P.Alivisatos (1995) Semiconductor Nanocrystals, *MRS Bulletin*, p23-32

2 E.Corcoran, G.Zorpette (1997) Diminishing Dimensions, *Sci. Am.*, **8**, p24-34

3 M.Brooks (1998) Take a Quantum Dot..., *New Scientist*, **159**, p22-25

4 R.F.Service (1996) Small Clusters Hit the Bigtime, *Science*, **271**, p920-922

5 A.P.Alivisatos (1996) Semiconductor Clusters, Nanocrystals and Quantum Dots, *Science*, **271**, p933-937

6 M.P.Pileni, L.Motte, C.Petit, (1992) Synthesis of CdS in situ in reverse micelles-influence of the preparation modes on size, polydispersity and photochemical reaction, *Chem. Mater.*, **4**, p338-345

7 B.A.Korgel, H.G.Monbouquette (1996) Synthesis of size-monodisperse CdS Nanocrystals Using Phosphadtidylcholine Vesicles as Reaction Compartments, *J.Phys.Chem*, **100**, p346-351

8 G.A.Ozin, A.Kuperman, A.Stein (1989) Advanced Zeolite Materials Science, *Angewandte Chemie Int. Ed.*, **28**, p359-76

9 L.Spanhel, H.Hasse, H.Weller, A.Henglein (1987) *J.Am.Chem.Soc.*, **109**, p5649-5651

10 E.S.Smotkin, R.M.Brown, L.K.Rahenburg, K.Salomon, A.J.Bard, A.Campion, M.A.Fox, T.E.Mallouk, E.S.Webber, J.M.White (1990) *J.Phys Chem.*, **94**, p7453-7455

11 M.Gao, Y.Yang, B.Yang, F.Bian, J.Shen (1994) Synthesis of PbS Nanoparticles in Polymer Matrices, *J.Chem.Soc., Chem.Comm.*, **12**, p2779-2780

12 K.Sooklal, L.H.Hanus, H.J.Ploehn, C.J.Murphy (1998) A blue-emitting CdS/dendrimer nanocomposite, *Adv.Mater.*, **10**, p1083-1087

13 S.Guo, R.Popovitz-Biro, I.Weissbuch, H.Cohen, G.Hodes, M.Lahav (1998) Quantum dots of CdS and PbS, *Adv.Mater.*, **10**, p121-125

14 D.Leonard, M.Krishnamurty, C.M.Reaves, S.P.Denbaars, P.M.Petroff. (1993) Direct formation of quantum sized dots from uniform coherent islands of InGaAs on GaAs surfacesm, *Appl.Phys.Lett.*, **63**, p3203-3206

15 J.Oshinowo, M.Nishioka, S.Ishida, Y.Arakawa (1994) Highly uniform InGaAs/GaAs quantum dots (similar to 15nm) by metal organic chemical vapour deposition, *Appl.Phys.Lett*, **65**, p1421

16 H.Asahi (1997) The fabrication of quantum wires and quantum dots, *Adv.Mater.*, **9**, p1019-1026

17 M.Bruchez, M. Moronne, P.Gin, S.Weiss, A.P.Alivisatos (1998) Semiconductor Nanocrystals as Fluorescent Biological Labels, *Science*, **281**, p2013-2015

18 W.C.W.Chan, S.Nie (1998) Quantum Dot Bioconjugates for Ultrasensitive Nonisotopic Detection, *Science*, **281**, p2016-2018

19 L.L.Sohn (1988) A quantum leap for electronics, *Nature*, **394**, p131-132

20 D.L Klein, R.Roth, A.K.L.Lim, A.P.Alivisatos, P.L.McEuen (1997) A single-electron transistor from a cadmium selenide nanocrystal, *Nature*, **389**, p699-701

21 Ritsert, K., Huber, R., Turk, D., Ladenstein, R., Schmidt-Bäse, K., Bacher, A. (1995). Studies on the lumazine synthase/riboflavin synthase complex of Bacillus subtilis: crystal structure analysis of reconstituted, icosahedral -subunit capsids with bound substrate analogue inhibitor at 2.4 Å resolution. *Journal of Molecular Biology*, **253**, p151-167

22 S.Mortl, M.Fischer, G.Richter, J.Tack, S.Weinkauf, A.Bacher (1996) Biosynthesis of riboflavin, *J.Biol.Chem.*, **271**, p33201-33207

23 Bacher, A., Weinkauf, S., Bachmann, L., Ritsert, K., Baumeister, W., Huber, R., Ladenstein, R., Schneider, M., Huber, R., Bartunik, H. D., Wilson, K., Schott, K., & Bacher, A. (1988). Heavy riboflavin synthase from Bacillus subtilis. Crystal structure analysis of the icosahedral capsid at 3.3 Å resolution. *Journal of Molecular Biology*, **203**, p1045-1070

24 Ladenstein, R., Ritsert, K., Huber, R., Richter, G., & Bacher, A. (1994). The lumazine synthase/riboflavin synthase complex of Bacillus subtilis. X-ray structure analysis of hollow reconstituted -subunit capsids. *European Journal of Biochemistry*, **223**, p1007-1017.

25 K.Kis, A.Bacher (1995) Substrate channelling in the lumazine synthase/riboflavin synthase complex of *Bacillus subtilis* , *J.Biol.Chem.*, **270**, p16788-16795

26 R.Ladenstein, A.Bacher, R.Huber (1987) Heavy atom complexes binding to proteins, *J.Mol.Biol.*, **195**, p751-753

27 H.Heqing, R.K.Watt, R.B.Fraenkel, G.D.Watt (1993) Role of Fe^{2+} binding to horse spleen ferritin, *Biochemistry*, **32**, p1681-1687

28 M.F.Hawthorne (1998) New horizons for therapy based on the boron neutron capture reaction, *Molecular Medicine Today*, **4**, p174-181

Chapter 4

The Synthesis of Cadmium Sulfide Superlattices from Self-Assembled Bacterial S-Layers

I must say that, in 1980, whenever I told my friends that I was just starting with J.H Hubbard a study of polynomials of degree 2 in one complex variable they would all stare at me and ask: Do you expect to find anything new?

A.Douady

4.1 Introduction

The synthesis of periodic arrangements of quantum dots presents a considerable technological obstacle, but one that would reap great rewards. The ability to create two and three dimensional 'superlattice' arrays may result in materials possessing novel properties with possible applications. Areas of applied quantum dot superlattice research include the fabrication of ultra dense computer memory devices and the production of highly efficient quantum lasers.

This chapter offers an alternative to current techniques in the fabrication of quantum dot superlattices through the application of bacterial S-layer proteins. These two dimensional 'biocrystals' are shown to act as highly specific mineralization templates in the production of periodic arrangements of CdS quantum dots. The inherent self assembly properties of this biosystem allows the fabrication of both two and three dimensional arrays of semi-conducting CdS quantum dots.

4.1.1 Quantum Dot Superlattices

One of the most significant problems concerning the application of quantum dots is the collation of physicochemical properties possessed by individual dots to give a coherent output. This requires the dots to be of identical size and to be positioned symmetrically in space, in the form of two and three dimensional superlattices. A superlattice can be described as a multilayer structure in which atomic, molecular, polymer or extended planes are stacked coherently[1]. Nanochemistry is an active area trying to solve nanofabrication problems, emphasising the synthetic method of construction, as opposed to the engineering approach, the latter involving techniques such as nanolithography (used in the manufacture of silicon microprocessors)[2], MBE[3] and atomic force microscopy[1]. Synthetic chemical strategies in the production of superlattice structures offer alternative fabrication paradigms when compared to the traditional engineered approaches, a reason why there continues to be unabated interest in such methodologies.

The nanochemical approach to the production of quantum dot superlattice structures can be divided into two main areas, template based host-guest inclusion chemistry and self assembly methods. The former involves a degree of self organisation,

but is dependent upon the presence of a template or framework, whereas the latter involves directed self assembly, independent of three dimensional spatial templates, this distinction facilitating the use of these generic terms. There are a variety of hosts that have been used to create inorganic superlattice structures. Some examples of hosts include sodalite[4,5], organic polymers[6], vesicles[7] and Langmuir-Blodgett films[8,9]. In all examples, the host consists of a framework which can be one, two or three dimensional and guest molecules having an affinity for the host. Nucleation of the guest ions is initiated within the confines of the host framework, the framework also serving to arrest the growth of the inorganic guest, resulting in a composite material comprised of spatially distinct nanocrystals within a host matrix.

The self assembly approach to the construction of two and three dimensional superlattice structures offers a number of advantages over the template method. These methods involve the spontaneous emergence of pattern, independent of templates. The structures made possess a greater flexibility, allowing the tailored synthesis of a range of precise spatial arrangements of nanomaterials. Synthetic strategies for self assembled nanostructures often have a reversibility, allowing a number of higher order architectures to be realised. This area of nanoscale materials organisation is explored in Chapter 5- 'Directed Self-Assembly of Nanoparticles into Macroscopic Materials using Antibody-Antigen Recognition'.

The spectrum of applications for self-organised quantum dots will probably expand over the next few years. More ideas for using these structures will undoubtedly arise as investigators learn more about their fabrication. Arrays of well-organised nanoscale structures will have numerous applications, providing it is possible to address the structures individually. Since one cannot, at present, attach electrical leads to the quantum dots, they must be addressed optically. A regular 3D array of optically addressable quantum dots has the potential of packing considerable information in space, with obvious application to computer memory storage devices.

4.1.2 Bacterial S-Layer Protein Biocrystals

With the possible exception of those prokaryotic organisms which have developed strategies to live under very specialised and frequently extreme natural conditions, most

bacteria have to survive in highly competitive habitats. Thus, the diversity observed in the molecular architecture of prokaryotic cell envelopes, particularly the structure of the outermost boundary layers, must reflect evolutionary adaptations of the organisms to specific environmental and ecological conditions.

Among the most commonly observed bacterial cell surface structures are two-dimensional crystalline arrays of proteinaceous subunits termed 'S-layers'[10]. S-layers have now been identified in hundreds of different species of every taxonomic group of walled eubacteria and are an almost universal feature of archaebacterial cell envelopes[10,11,12]. Structural, chemical and morphogenetic studies have shown that S-layers are one of the most primitive membrane structures developed during evolution. They cover the cell surface completely, are usually composed of a single protein or glycoprotein species and are endowed with the ability to assemble into monomolecular arrays by an entropically driven process.

The observation that prokaryotes carrying S-layers are ubiquitous in every part of the biosphere supports the concept that these supramolecular structures can fulfil a broad spectrum of functions. Based on the data obtained by fundamental studies on S-layers, a considerable potential for the crystalline arrays in biotechnological, biomedical and non-biological applications, including areas such as molecular nanotechnology has become evident.

I) Location and Ultrastructure

The location and ultrastructure of S-layers have previously been investigated by different electron microscopic procedures, including freeze-etching, thin sectioning, freeze-drying in combination with heavy metal shadowing and negative staining[13,14](Fig. 1). Although there exists considerable variation in the molecular architecture and complexity of prokaryotic envelopes it is reasonable to classify cell-wall profiles containing S-layers into three main groups. Negative stained preparations of isolated S-layers have primarily been used for high resolution studies on the mass distribution of the crystalline arrays. Two- and three-dimensional analysis, in combination with computer image enhancement procedures, revealed structural information down to approximately 1.5nm[14,15,16]. Most S-layer lattices exhibit oblique (p2), square (p4), or hexagonal (p6) symmetry. Preliminary data indicate that p1 and p3 lattices may also exist (Fig.2).

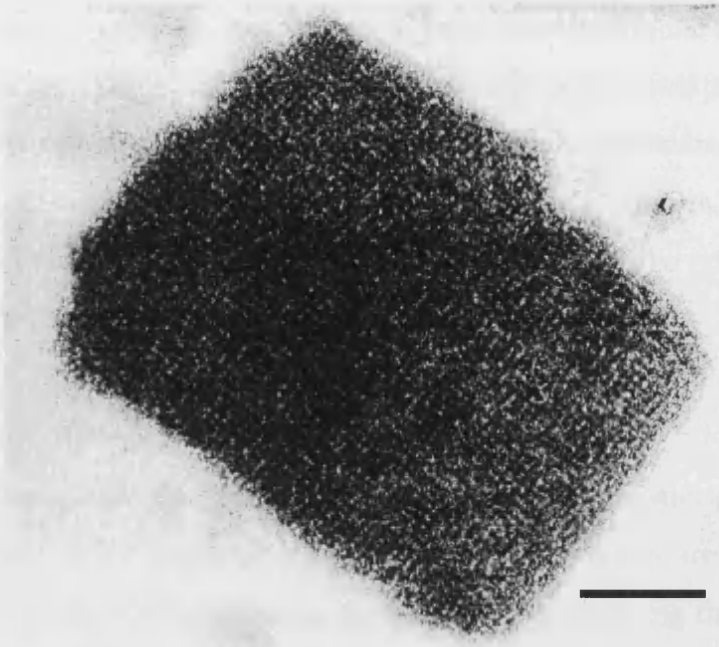

Figure 1 Self assembled square p4 S-layer lattice stained with 1% uranyl acetate (Scale bar 100nm). Sample prepared as described in 'Materials and Methods' section.

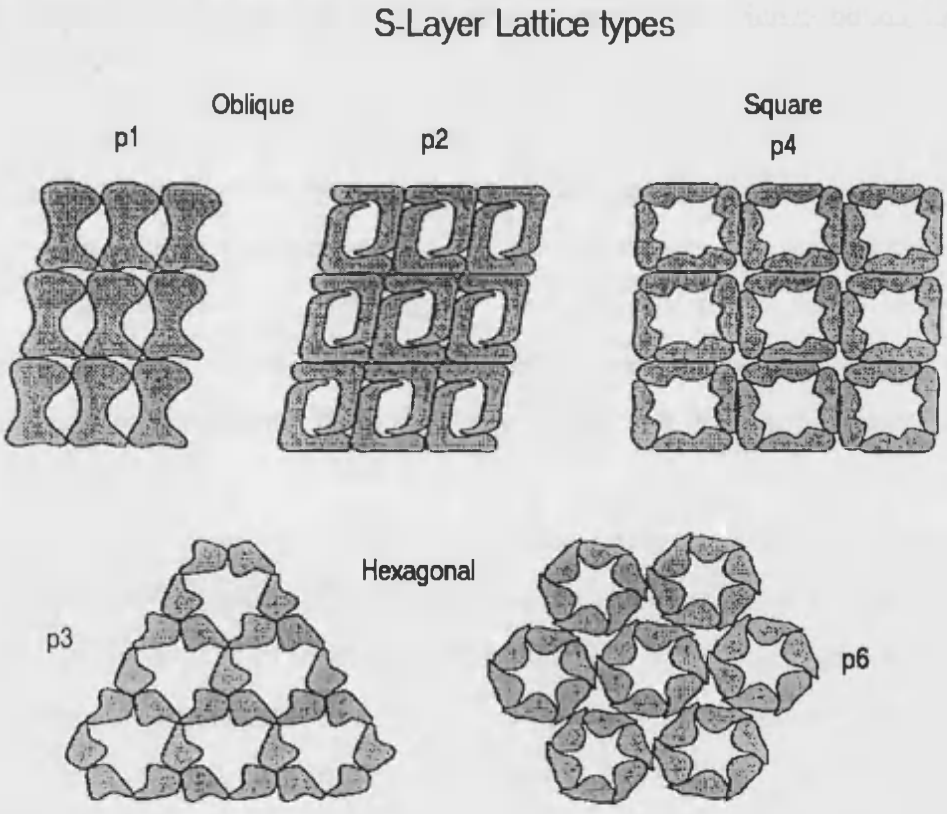

Fig. 2 Schematic diagram showing the range of different S-layer lattice geometries that occur[1].

Depending on the lattice type, the morphological units constituting the crystal lattice consist of one, two, three, four or six identical monomers respectively and the morphological units can have centre-to-centre spacings ranging from 3 to 32nm. High resolution studies have shown that pores of identical size and morphology exist between the regularly arranged S-layer subunits. Pore sizes between 2 and 8nm have been estimated and the porosity of the protein network can reach 70% and the thickness of S-layers may vary between 5 and 15nm.

II) Chemical Characterisation

S-layers reveal considerable differences with respect to their mechanical stability and ease of disintegration into their constituent subunits. Generally S-layers are isolated from cell-wall fragments, which are obtained by breaking up the cells and removing the cell content including the cytoplasmic membrane. In some organisms pure S-layer preparations can be obtained by extraction of intact cells. With a few exceptions among archaebacteria[17-20], the constituent subunits of most S-layers are linked with each other, and to the supporting envelope component, through non-covalent forces, including hydrophobic interactions, ionic bonds and hydrogen bonds. Consequently, common procedures for the detachment and solubilization of S-layers involve treatment with hydrogen bond-breaking and metal-chelating agents. Other methods are based on cation substitution or changes in pH and/or ionic strength[11,12,21,22,23]. Results from such experiments indicated that the integrity of the S-layer lattice is maintained by different combinations of weak bonds which are stronger than those binding the lattice to the underlying cell envelope component. This property is considered to be a basic requirement for a continuous recrystallization of the regular array during cell growth, leading to an arrangement with low free energy on the cell surface[18-20].

Comparison of amino acid analyses and genetic studies on S-layers from different phylogenetic origins have shown that the constituent subunits are usually composed of weakly acidic proteins[11,12]. The content of hydrophobic amino acids is generally high whereas, if present, the amount of cysteine or methionine is low. The apparent molecular weights of the protein subunits have been shown to range from approx. 40000 to 200000 by SDS-PAGE electrophoresis[12]. Involvement of more than one protein species in generating an S-layer was demonstrated with *Clostridium difficile* GAl 0714. This important pathogen, which causes

human pseudomembranous colitis, has an S-layer composed of two proteins with different molecular weights which exhibit no antigenic relationship[24].

III) Surface and Permeability Properties

Three-dimensional analysis of S-layers by high resolution electron microscopy, in combination with digital image processing methods, has shown considerable asymmetry in the topography of the outer and inner face[16] (Fig.3). Generally, the inner face of the crystalline protein network is more corrugated than the outer face. Labelling experiments, using charged topographical marker molecules and chemical modification of the amino and carboxyl groups, have revealed that the two surfaces can have a different net charge[28]. With S-layers of different *Bacillaceae*, it has been shown that the outer face is of neutral charge,

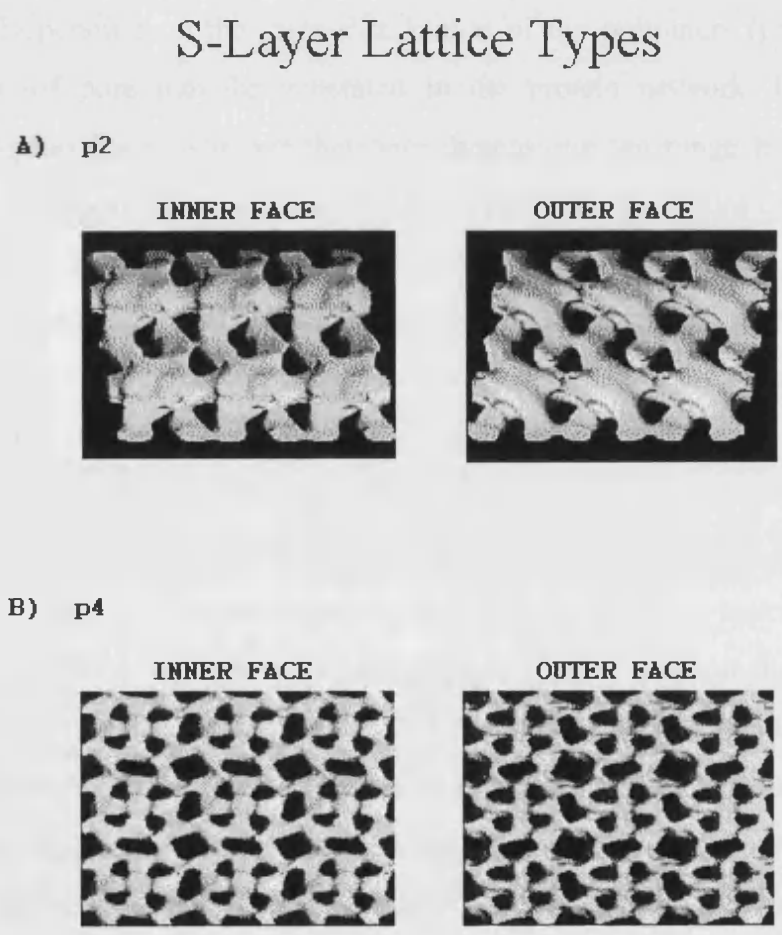

Figure 3 Computer generated images showing the inner and outer faces of the oblique (p2) and square (p4) S-layer lattices. (Courtesy of Dr.D.Pum, Ref: M.Sara *et al* (1993), *J.Bacteriol*, **176**, p848-860)

due to an equal number of amino and carboxyl groups, while the inner face is net negatively charged as a consequence of an excess of free carboxyl groups [29-31]. In this context it is interesting to note that even in the glycosylated S-layer of *Clostridium symbiosum* HB25, the positively and negatively charged constituents of the polysaccharide chain are arranged in such a way that the charged groups are capable of intermolecular neutralisation on the cell surface[32]. Comparison of the cell surface charge and hydrophobicity of an S-layer-carrying strain of *Bacillus stearothermophilus* and of an S-layer-deficient mutant strain by electrostatic and hydrophobic interaction chromatography has revealed significant differences[33]. Although both strains exhibited a hydrophilic surface, the hydrophilic properties were more pronounced with the S-layer lacking strain. In *Aeromonas salmonicida*[34] the relatively hydrophobic characteristics of the S-layer surface are even required for the pathogenic behaviour of these organisms.

Since S-layers are composed of identical subunits, they possess pores of identical size and morphology. Depending on the mass distribution of the protomers (protein monomers), more than one type of pore may be generated in the protein network. High-resolution electron microscopy studies have indicated that pore dimensions can range from 2 to 8nm[16,18]. More precise data on the pore size can be derived from permeability studies on S-layer vesicles and S-layers which had been deposited on porous supports[35,36]. Since the pores in the lattice are generated by identical protomeric units they also exhibit identical physicochemical properties. Both amino groups and carboxyl groups have been identified in the pore area, but they appear to be located closely enough to permit electrostatic interactions [37,38].

IV) Morphogenesis and Assembly In Vitro

Isolated S-layer subunits frequently maintain the ability to assemble into regular arrays upon dilution and complete removal of the disrupting agent used for their isolation[26] .This self-assembly process is entropy-driven and leads to crystalline arrays, identical to those observed on intact cells. From the limited data available, it appears that the formation of crystalline arrays is initiated by a rapid nucleation of the subunits into oligomeric precursors, followed by a subsequent slow assembly into larger products[39]. Re-crystallisation of isolated subunits can take place with or without surfaces for adhesion. Self-assembly products generated in suspension may have the form of flat sheets, open ended cylinders, or vesicles. Depending on the chosen environmental conditions (e.g. pH, temperature, ionic strength, presence or absence of divalent

ions) different assembly products may be obtained. Both, flat and cylindrical self-assembly products are frequently composed of double layers, whereby the two constituent monolayers are bound either by their inner or their outer faces[18,39]. S-layer fragments isolated from cell wall preparations or those obtained by self-assembly of subunits frequently have the ability to fuse and re-crystallise. Many Gram-positive and Gram-negative organisms have been reported which produce two superimposed S-layers[26]. They are generally composed of different subunit species.

Self-assembly of S-layer subunits can also be studied in the presence of supporting layers[26]. For example, S-layers from mesophilic and thermophilic *Bacillaceae* have shown the ability to reattach to the peptidoglycan containing layer from which they had been removed to those of other organisms or to charged and uncharged inanimate surfaces[24,40,41]. Reattachment of isolated S-layer subunits to the outer membrane of Gram-negative eubacteria frequently requires divalent cations[42,43,44]. Two-dimensional crystallisation of a bacterial S-layer protein, isolated from a Gram-negative organism, was also reported on lipid vesicles made of dimyristoylphosphatidylcholine[45].

From all these *in vitro* self-assembly systems studied it has become evident that the crystallisation properties, contained within the individual S-layer subunits, are sufficient for the formation of a regular array on a bacterial cell surface. An additional requirement for maintaining a closed S-layer on a growing cell is the continuous synthesis of subunits and their translocation to areas of lattice growth. In Gram-positive eubacteria, lattice growth occurs primarily by insertion of multiple bands of S-layers on the cylindrical part of the cell and at new cell poles. In Gram-negative eubacteria however, S-layers appear to grow by insertion of new subunits at diffuse sites over the main cell body[26].

Now it is evident that S-layers represent dynamic closed surface crystals with the intrinsic ability to assume a structure of low free energy during cell growth[13]. From high-resolution electron microscopical studies, it appears that particular dislocations serve as incorporation sites for new subunits in the closed lattice. Analysis of the distribution of lattice faults in *Methanocorpusculum sinense* indicated that they are not only a geometrical necessity on the surface of a closed protein crystal, but also play an important role in the formation of the lobed cell structure and in the cell fission process[39]. In most organisms the regulation of synthesis and translocation of S-layer subunits to the cell surface seems to be closely linked with a complete coverage of the cell surface with the crystalline array. Studies on *B. stearothermophilus* strains

have shown that a pool of S-layer subunits, at least sufficient for generating one complete S-layer on the cell surface, is present in the thin peptidoglycan network. It can be even assumed that the translational transport of the S-layer protein is regulated by the packing density of the S-layer subunits within the periplasmic space delineated by the outer S-layer and the cytoplasmic membrane[46]. The matrix of the rigid wall obviously inhibits the assembly of the S-layer protein into regular arrays before reaching the outer face[57].

V) Functional Aspects

Since prokaryotes carrying S-layers are ubiquitous in the biosphere and have been shown to inhabit the most diverse ecologies, it is not surprising that this porous protein or glycoprotein lattices can fulfil a broad spectrum of functions. Although only relatively few firm data are available, there is strong evidence that the crystalline arrays have the potential to function as :

(1) protective coats, molecular sieves, and molecule and ion traps;
(2) structures involved in cell adhesion and surface recognition; and
(3) as frameworks which determine and maintain cell shape in those archaebacteria which possess S-layers as an exclusive wall component[11,12,44'47].

Particular attention has been paid to S-layers present as structural components on cell envelopes of pathogenic organisms. Detailed studies on *Aeromonas salmonicida*[49,50] and *Campylobacter frius*[52] have shown that S-layers are required for infection. Since crystalline surface layers have been identified on many pathogens of humans and animals including *Chlamydi.*, *Treponema* spp., *Helicobacter (Campylobacter) pylori*[12]. It is likely that they will be proved to be of great relevance as virulence factors.

In particular, attachment of bacteria to surfaces is a significant event in colonisation and infection of hosts. This initial step is frequently based on a very accurate fit between microbial surface structures and complementary receptors on the host cells. It is likely that S-layers as physicochemically and morphologically well-defined surface structures fulfil such functional requirement.

4.2 Materials and Methods

Extraction of S-layer proteins

S-layer samples were provided by Prof. Uwe Sleytr, Zentrum für Ultrastrukturforschung, Universität für Bodenkultur, und Ludwig Boltzmann-Institut für Ultrastrukturforschung, Austria. The oblique lattice was derived from the bacterial strain *Bacillus stearothermophilus* NRS 2004/3a. The square lattice was obtained from *Bacillus sphearicus* CCM 2177.

The oblique lattice has a centre-to-centre spacing of a=8nm, b=10nm and a base angle of 80°, where a and b are the base vectors of the S-layer unit cell. The square S-layer has a centre-to-centre spacing of a=b=13nm with a base angle of 90°.

S-layer proteins were extracted from clean cell wall fragments with guanidinium hydrochloride (GHCl) (5 M in 50 mM Tris hydrochloride buffer, pH 7.2) for 2 h at 20 °C. The peptidoglycan cell walls were separated from the extracted S-layer protein by centrifugation at 40,000g for 60 min at 4°C, and the supernatant (5 mg/ml protein) dialysed against 10 mM $CaCl_2$ solution for 2 h at 4°C. The protein solution was centrifuged at 40,000g for 15 min at 4°C and the clear supernatant adjusted to 1mg protein monomers per ml buffer with a 10 mM $CaCl_2$ solution.

S-layer self-assembled double layer structures were isolated from S-layer/guanidinium hydrochloride cell wall extracts, that had been previously dialysed against 10 mM $CaCl_2$ solution, by sedimentation for 15 min at 40,000g at 4 °C. Guanidinium hydrochloride addition (GHCl; 5 cm^3, 5 M) was added to the wet pellet (100 mg) and stirred for 20 min at 20°C. GHCl extracts were then centrifuged at 40,000g for 30 min at 20 °C, and clear supernatants were dialysed against distilled water for 48h at 4 °C.

Formation of monolayers of S-layers

The formation of S-layer monolayers was carried out by Dr. D. Pum, Zentrum für Ultrastrukturforschung, Universität für Bodenkultur, und Ludwig Boltzmann-Institut für Ultrastrukturforschung, Austria. S-layer subunits were reassembled on carbon coated formvar-covered nickel TEM grids by placing grids onto the surface of a 1mg/ml buffered solution of

protein monomers for 2 hours, after which the grids were removed by horizontal lifting, washed in distilled water and the layers fixed with gluteraldehyde.

Cadmium sulfide mineralization of S-layers

S-layer self assembled double layer products (oblique and square lattices) were incubated for 24 hours in $CdCl_2$(10mM)/ 50mM (2-([tris(hydroxymethyl(methyl]amino)-1-ethane-sulfonic acid) (TES,), buffered to pH7.2 by addition of NaOH (1M). Drops of the solution were then placed on nickel TEM grids. Copper TEM grids were not used to avoid reaction with the H_2S. These grids were placed in a vacuum dessicator containing acidified Na_2S. H_2S was then allowed to diffuse into the droplets on the TEM grids. A time course experiment was allowed to run in which the grids were removed sequentially at regular intervals. On removal of each grid, surplus solution was wicked away and the grid left to air dry. The grids were examined by transmission electron microscopy (TEM). The same experimental protocol was also employed in the mineralization of a square S-layer lattice with cadmium sulfide.

Mineralization of monolayers was performed by Dr. D.Pum in an identical fashion, utilising the self assembled monolayers on the TEM grids.

The controls were S-layers examined by TEM that had been incubated with only $CdCl_2$ and $CdCl_2/H_2S$ without protein.

Electron microscopy

Negative staining of the S-layer self assembled double layers was achieved by addition 1% uranyl acetate for 5 minutes. Electron microscopy was done on both JEOL 1200EX and JEOL 2000EX transmission electron microscopes, both with low dose facilities operating at 80 and 120kV.

Image Processing

Electron micrographs were processed by Dr. Dietmar Pum. Micrographs were scanned with an optical diffractometer and selected for subsequent computer image processing when several high resolution spots were found beyond a 1/2.5 nm^{-1} threshold. Digitized data (512 by 512 pixels) were pre-processed and Fourier transformed amplitudes and phases of the diffraction maxima were interpolated with the use of a peak profile fitting procedure. Symmetry related pairs were complex averaged. Several tilt angle series with different orientations of the tilt axis against the lattice orientation were used for calculation of the 3D models (Personal communication with Dr.D.Pum).

4.3 Results and Discussion

The results and discussion are split into two sections as follows. The first section deals with the CdS mineralization of S-layer double layers, the double layers resulting from a self assembly process in solution. The section proceeds by comparing the mineralization of oblique and square double layers.

The second section outlines work carried out by Dr. Dietmar Pum on the mineralization of S-layer monolayers and includes computer reconstructions of the mineralized lattices, giving conclusive data on the specificity of the mineralization process.

4.3.1 CdS Mineralisation of S-Layer Double Layers

I) CdS Mineralization of the Oblique S-layer Double Layer

Incubation of oblique S-layer self assembly products with Cd(II) ions in a buffered solution at pH7.2, resulted in a transparent solution revealing no precipitate. The solution remained transparent for several months, whereupon a slight flocculent precipitate was observed. These observations indicate the S-layer structures are stable to the addition of cadmium ions for several months.

The sample supplied, upon which all subsequent experiments in this subsection were performed, consists of S-layer 'double layers'. This is a natural form the isolated S-layer subunits exist in when stored in buffer for extended periods. Both the hydrophobic effect and entropic considerations result in the formation of a two-tiered double-layer structure, the structure invariably consisting of a back-to-back arrangement, with internal faces matched and external faces exposed to solution[60].

A mineralization time course experiment was performed with the oblique S-layer self assembly products to investigate the potential of self assembled double layer S-layers as mineralization templates. Sequential removal and subsequent examination of mineralized S-layers by TEM was performed, as described in Materials and Methods, with a view to establishing a range of CdS mineralization states. Consequently a progressively heavier mineralization was observed and the results monitored by TEM.

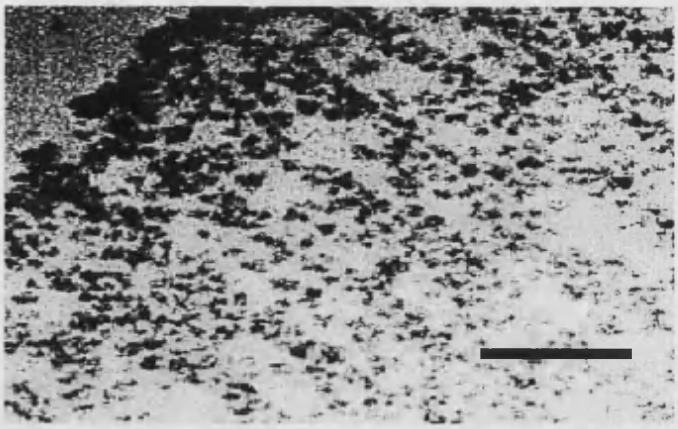

Figure 4 Periodicity seen in CdS of double layer S-layer self assembly products. Scale bar 100nm.

Electron microscopical examination of S-layers exposed to H_2S for less than 30 minutes revealed a slight negative staining effect, although no substantial CdS mineralization was seen. Fig. 4 shows the extent of mineralization after exposure of the Cd(II) incubated oblique lattice to H_2S for a period of 60 minutes. The resulting mineralization is confined to stripes, each mineralized stripe being composed of individual crystal 'doublets'. The spacing of the stripes is 50nm and the individual stripe width is in the region of 20nm.

To investigate the emergence of this CdS periodicity, the H_2S exposure time was increased. The electron micrograph in Fig.5 shows the extent of Cd(II) incubated lattice mineralization after an H_2S exposure time of 100 minutes. A highly ordered array of individual crystallites are apparent that appear to merge and form a continuous stripe. The stripe spacing was found to be 32nm with an individual stripe width of 16nm. One interesting phenomenon revealed by the micrograph is the appearance of what seem to be individual rectangular crystals arranged in a periodic linear fashion. In the lower part of the micrograph, an additional set of fringes can be seen interspaced between the stripes to give a 16nm spacing. Fine fringes transverse the 16nm stripes at an 80^{o} angle with a 7nm spacing. The crystals also appear to lie in the plane with a corresponding base angle of approximately 80^{o}, with respect to the base vectors.

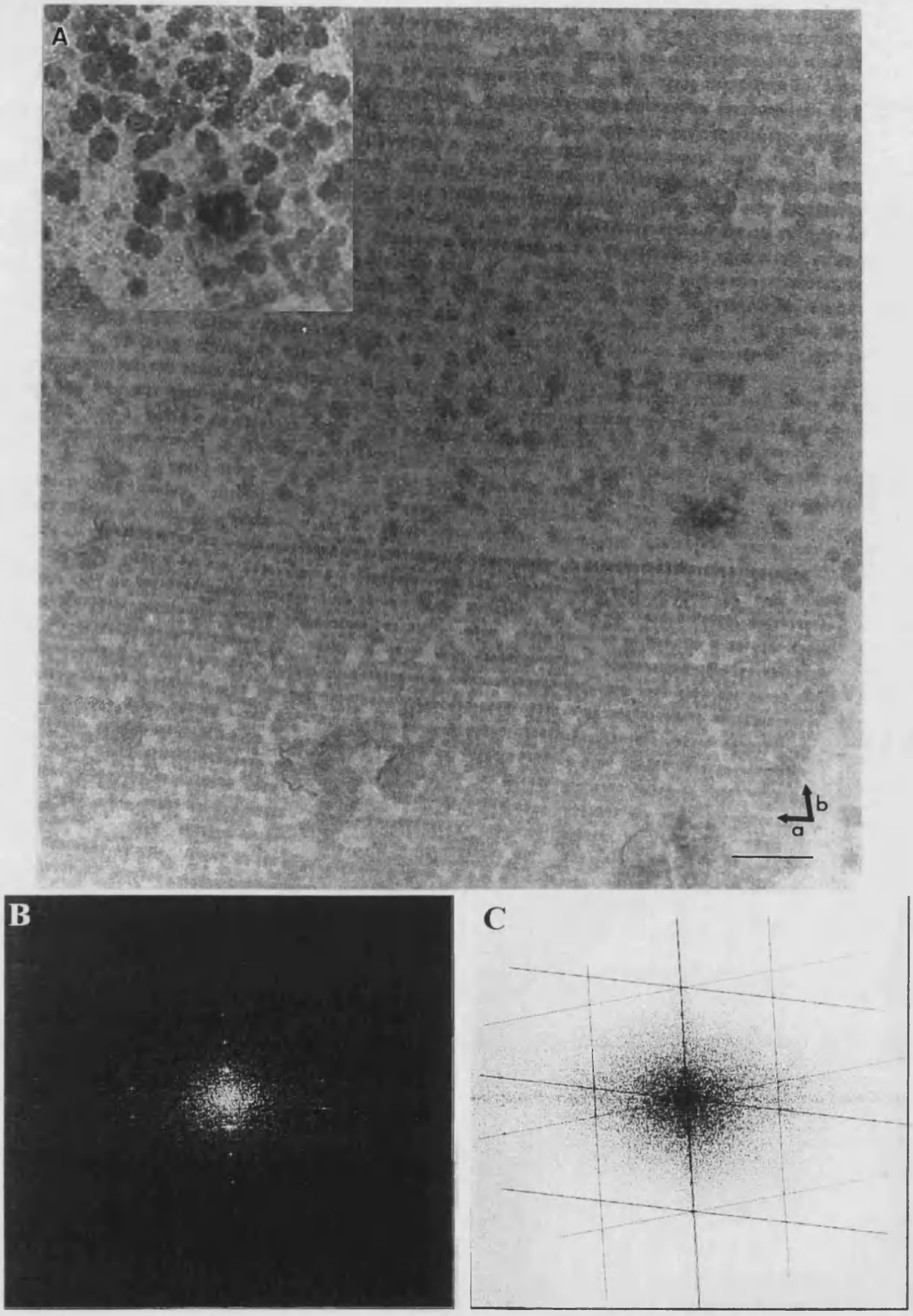

Figure 5 A) TEM micrograph showing the effect of the presence of S-layers on the mineralization of CdS after an H_2S exposure time of 100 minutes to the Cd(II) incubated S-layers. Inset shows control sample. Scale bar 100nm B) Optical diffraction pattern of the CdS mineralization pattern. C) Image reconstruction of the underlying lattice of the CdS mineralization pattern seen in A.

A control sample consisting of the same concentration of buffered $CdCl_2$, with subsequent exposure to H_2S for a period of 100 minutes, resulted in the formation of spherical CdS particles randomly oriented over the TEM grid (Fig. 5A, inset). These data suggest the presence of the protein lattice induces the formation of a regular array of crystals on the surface of the S-layer template. To verify the presence of the underlying S-layer protein lattice, diffraction patterns were obtained from the micrographs of the mineralized S-layers in order to reconstruct the orientation of the double layer lattice. Fig. 5B shows an optical diffraction pattern obtained through image processing of the TEM negative of Fig. 5A, the diffraction pattern is then used to reconstruct the underlying lattice orientation (Fig. 5C). Analysis of the reconstructed lattice from the diffraction pattern reveals the two constituent lattices of the double layer to be in back-to-back orientation, having the longer base vector in common. This results in a mirror symmetric reciprocal lattice. The stripe patterns are also visible in the diffraction pattern as low order reflections of only a quarter of the longer reciprocal base vector length. In turn this demonstrates that the periodicity of the stripes is 4 times the lattice constant. This is in perfect agreement with the stripe periodicity found of approximately 32nm. (i.e. the difference vector between the two shorter reciprocal base vectors is the reciprocal base vector of the stripe pattern). The stripe patterns observed in the mineralization of the oblique double layer S-layer can thus be explained by the Moiré effect. The resulting Moiré pattern being due to the superposition of the two constituent oblique mineralized lattices of the double layer.

The electron micrograph in Fig. 6A shows a mineralized S-layer having the same two dimensional parameters as in Fig 5 (i.e. centre to centre spacing of ~32nm and stripe width of 16nm). A similar underlying fringe lattice can also be seen, corresponding to the S-layer. The arrow in the lower right-hand corner shows a mineralized monolayer lattice clearly demonstrating the difference between mineralized double layer and monolayer. Fringe spacing was found to be around 8nm with an intersecting fringe angle of about 80°. The electron micrograph demonstrates the formation of the mineralized stripe of CdS from stripes consisting of clearly defined crystal doublets (bottom left of the micrograph), to the heavier mineralized stripe as seen in Fig 5 (top of micrograph). Fig. 6B shows an optical diffraction pattern obtained through image processing of Fig. 6A. The diffraction pattern is then used to reconstruct the lattice orientation. (Fig. 6C). It can be seen that the S-layer lattice is composed of a double layer of two lattices in a back to back orientation.

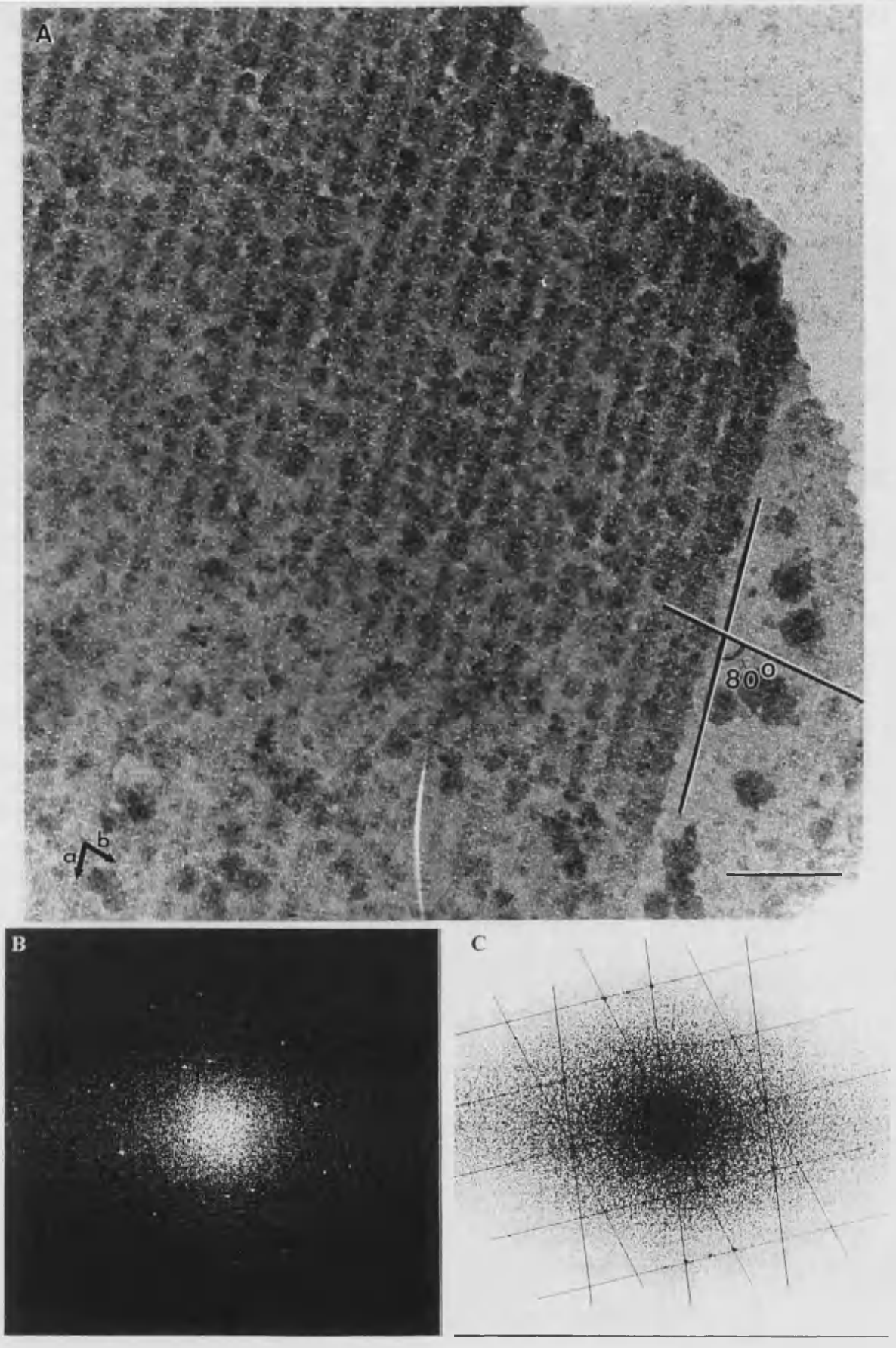

Figure 6 A) TEM micrograph showing the effect of 125 minutes exposure time of H_2S to the Cd(II) incubated S-layers. Scale bar 100nm. B) Optical diffraction pattern of the mineralized lattice seen in A. C) Reconstruction of the underlying lattice seen in A.

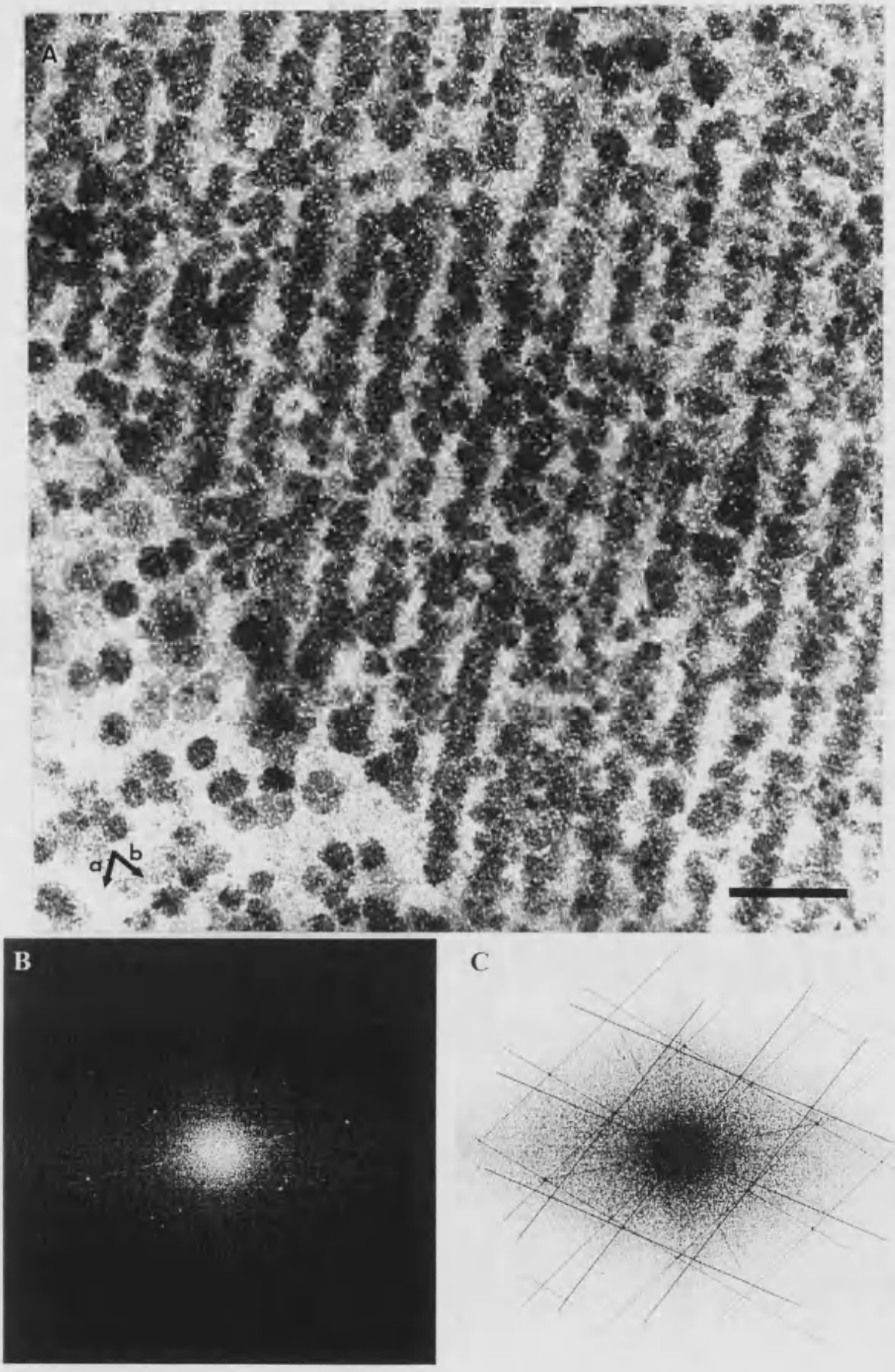

Figure 7 A) TEM micrograph showing the effect of H_2S exposure, for 150 minutes, on the Cd(II) incubated S-layers. Scale bar 100nm B) Optical diffraction pattern obtained for the mineralized lattice seen in A. C) Reconstruction of the mineralized lattice from optical diffraction pattern.

Again, a mirror symmetric lattice is obtained with the constituent S-layers in a back-to-back orientation.

The electron micrograph in Fig. 7A shows greater mineralization of the lattice, due to the longer H_2S exposure time of 150 minutes. The stripes themselves retain the spatial geometry of the mineralized lattice in Fig. 6, but now each stripe consists of an almost uniform band where stripe spacing was found to be 50nm and an individual stripe width of 30nm. Smaller fringes can also be seen running both parallel and transverse to the cadmium sulfide stripes. Each stripe spans approximately 5 parallel fringes, with a fringe spacing of about 6nm. The angle between fringes was found to be about 80^0. Fig. 7B shows the optical diffraction pattern from the lattice in Fig. 7A. The reconstruction of the lattice orientation in Fig.7C shows the double layer to be composed of two overlapping S-layer monolayer lattices. The difference in lattice constants found for this micrograph are shown to correspond to this different type of double layer. A similar effect is seen in the Fig. 4.

The electron micrograph in Fig. 8 is of an S-layer exposed to H_2S for 200 minutes. This triangular crystal morphology was observed over the entire viewing field of the TEM grid, totally obscuring the underlying protein lattice.

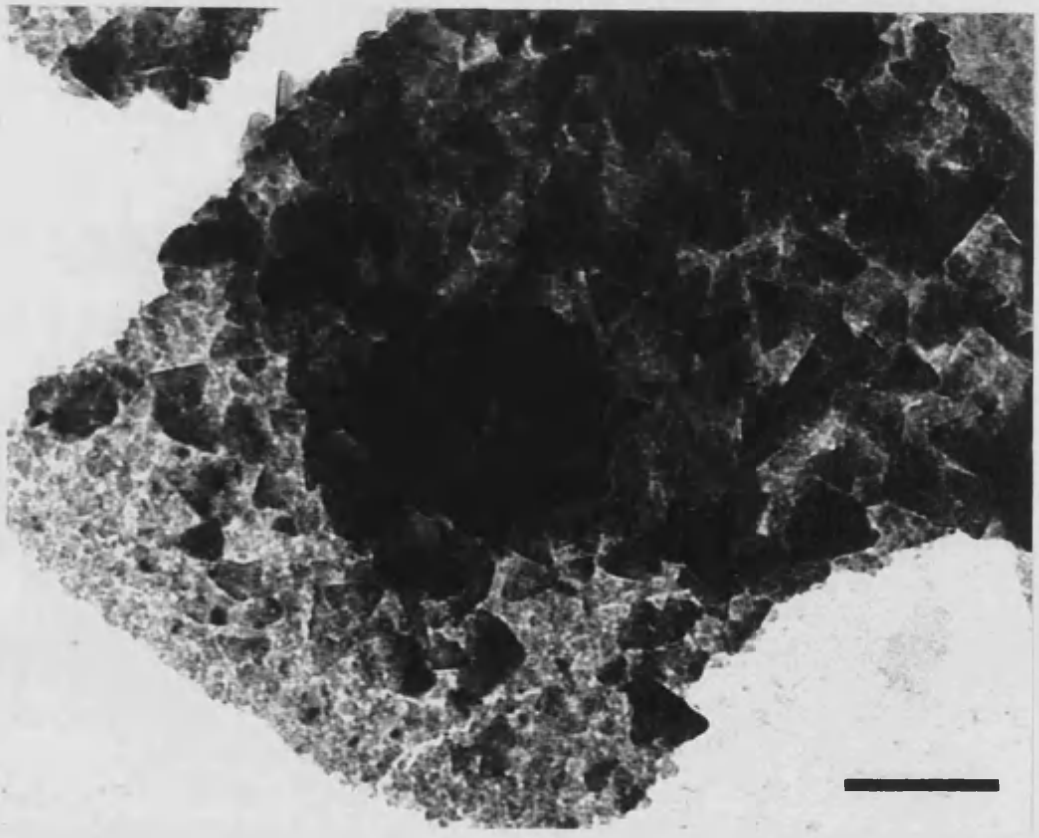

Figure 8 TEM micrograph showing the effect of H_2S exposure on cadmium incubated S-layers for 200 minutes. Scale bar 100nm

The previous micrographs, showing the effect of S-layers on the mineralization of CdS over incremental time periods, suggest the S-layers to act as specific templates for this mineralization. To ascertain the nature of this mineralization process and to verify and characterise the nature of the nucleated mineral, HRTEM, electron diffraction and EDXA were employed.

The electron micrograph in Fig. 9 is a high magnification micrograph, taken at 500K, of the oblique mineralized lattice in Fig. 5, which displayed a high degree of periodicity. Lattice images of individual nanocrystals nucleated on the surface of the S-layer were directly imaged.

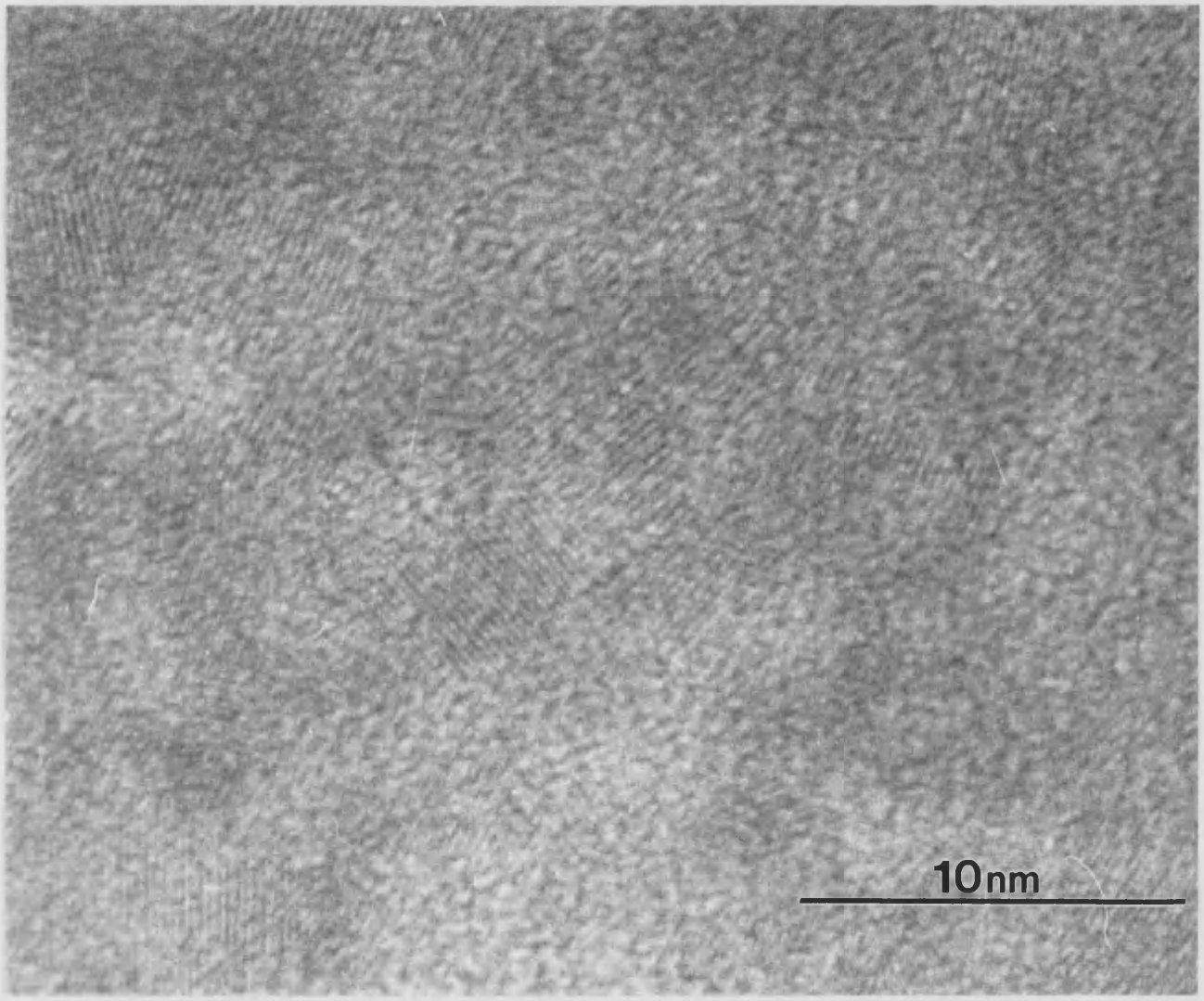

Figure 9 HRTEM image of the CdS mineralized S-layer lattice shown in Figure 5. Individual nanocrystals nucleated on the surface of the S-layer can be seen, a d-spacing of 3.4Å was found corresponding to the 110 face of CdS.

The d-spacing of the lattice fringes was found to be 3.4Å, which indicates the 110 face of zinc blende cadmium sulfide nanocrystals growing on the lattice. The lattice images also show the CdS crystals to be non-crystallographically orientated. Examination of the nanocrystals implies a random orientation, although the fact that the templating S-layer is a double layer necessarily means that the image is a three dimensional stack of CdS crystals and therefore not necessarily random. The individual nanocrystals are found to have sizes in the region of 5-10nm.

The EDXA spectrum in Fig. 10 of a CdS mineralized S-layer, shows strong peaks for both cadmium and sulfur, verifying the presence of cadmium sulfide. There is also a peak indicating nickel, due to the use of a nickel TEM grid. The inset shows an electron diffraction pattern obtained for the mineralized lattice seen in Fig. 5.

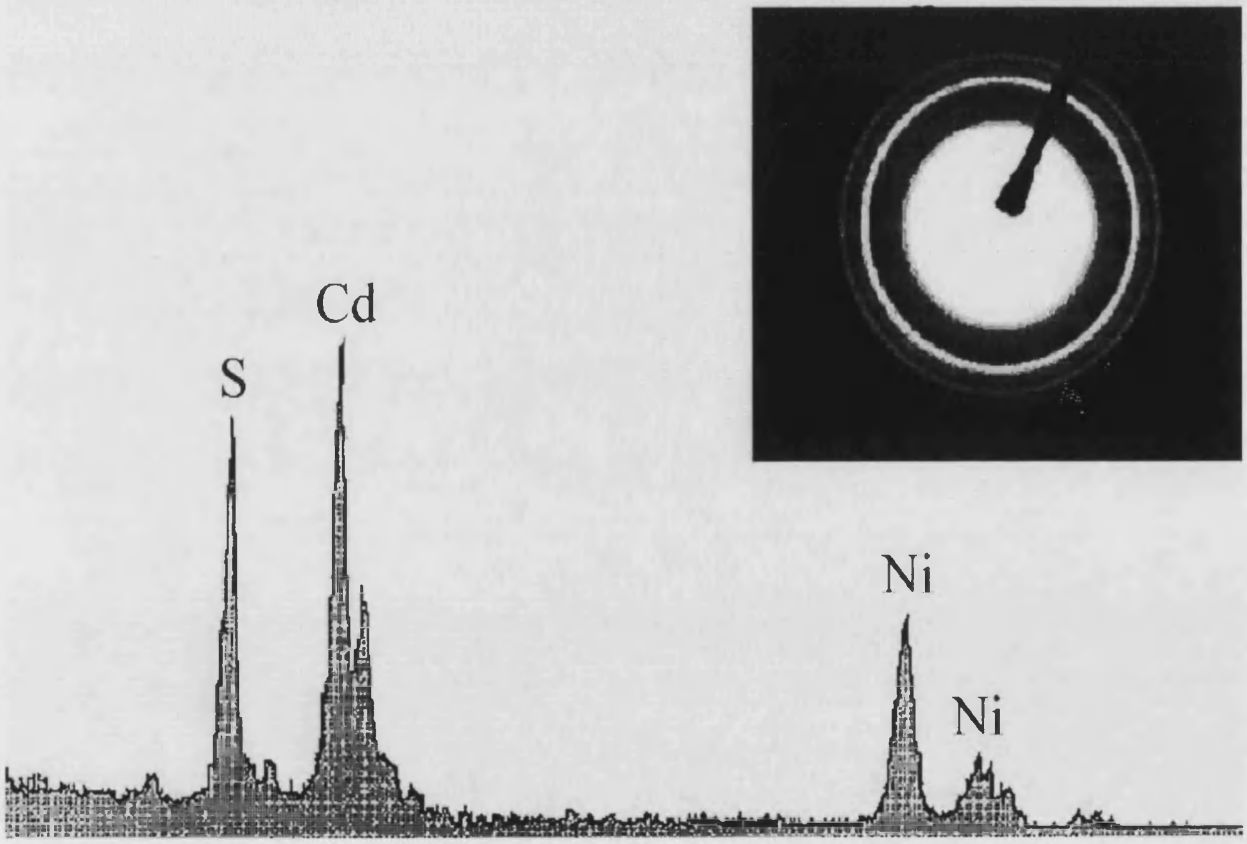

Figure 10 EDXA spectrum of a CdS mineralized S-layer lattice, confirming the exclusive presence of cadmium and sulfur. The presence of nickel is due to the nickel TEM grid used. Inset shows electron diffraction pattern obtained.

The SAED data, shown in Fig. 10, confirms the nanocrystals nucleated on the surface of each S-layer to be non-crystallographically orientated, due to the presence of the concentric ring pattern. Analysis of the electron diffraction pattern ring diameters gives d-spacings of; 0.336nm (111), 0.205nm (220), 0.173nm (311), 0.133nm (331), 0.118nm (422)Å confirming the CdS to be the zinc blende polymorph (Table 1).

Electron diffraction d-spacings for zinc blende (nm)	Electron diffraction d-spacings for CdS nanocrystals grown of S-layers (nm)
3.38	3.36
2.07	2.05
1.75	1.73
1.33	1.33
1.18	1.18

Table 1 Results from the electron diffraction analysis showing the CdS nanocrystals nucleated on the surface of the S-Layer to be the zinc blende polymorph of CdS.

II) CdS Mineralization of the Square S-layer Double Layer

The electron micrograph in Fig.11A shows a CdS mineralized square S-layer lattice with an H_2S exposure time of 100 minutes.

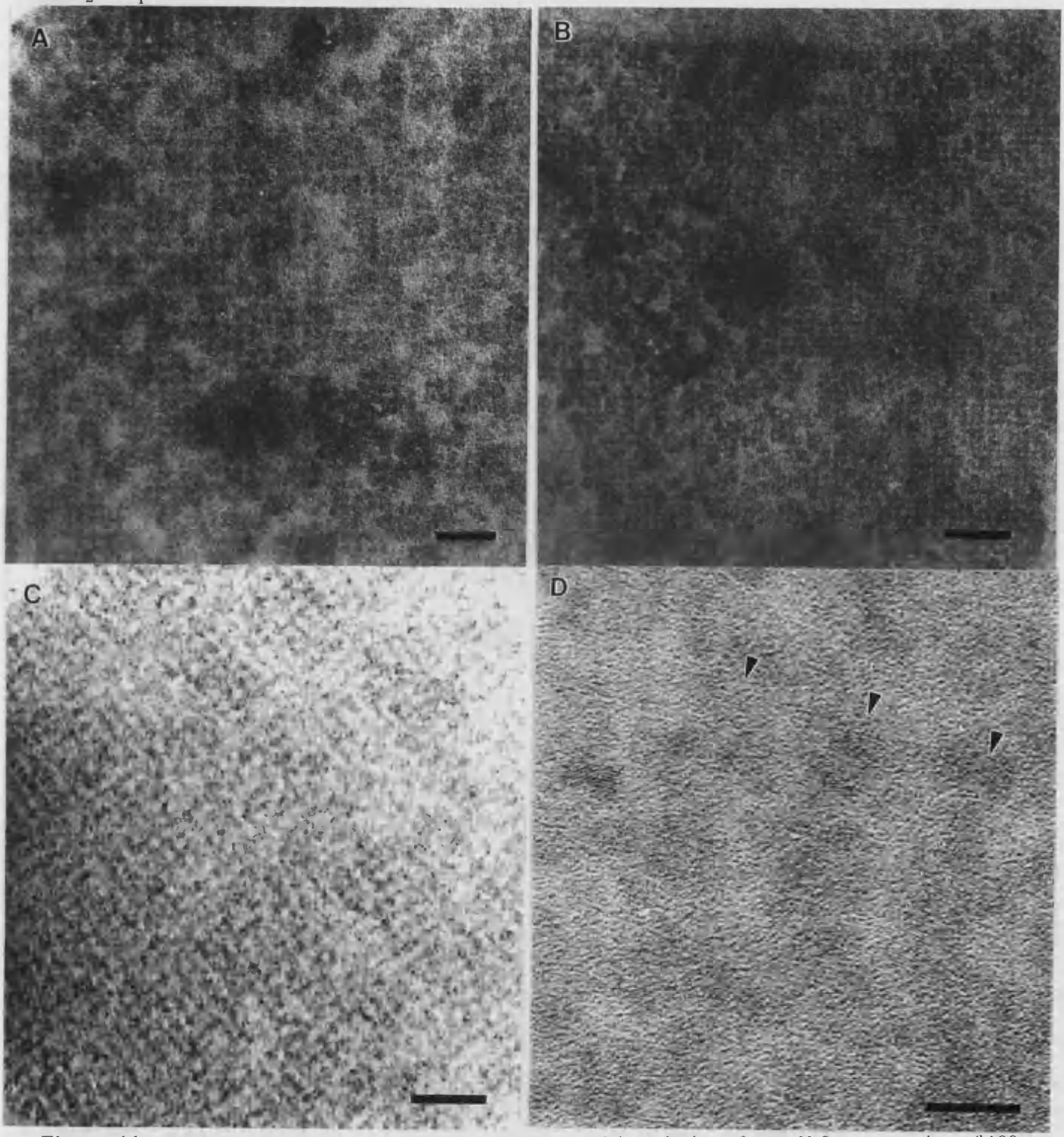

Figure 11 A) TEM micrograph of a cadmium incubated square S-layer lattice, after an H_2S exposure time of 100 minutes. Scale bar 100nm. B) TEM micrograph showing the extent of CdS mineralization after an H_2S exposure time of 150 minutes. Scale bar 50nm. C) Micrograph showing very early stage in CdS mineralization of the square S-layer, resulting from an H_2S exposure time of 80 minutes. Scale bar 100nm. D) HRTEM showing individual nanocrystals of CdS on the square S-layer confined to the dark linear regions (arrows) of the micrograph. Scale bar 10nm.

Lattice spacing was found to be about 12nm and the individual CdS crystals have square dimensions of about 9nm. These parameters are in close agreement with those of the protein lattice. The protein lattice is represented by the white regions on the micrograph with the contrast coming solely from the CdS precipitated on the lattice. The electron micrograph in Fig. 11B shows the extent of lattice mineralization after a H_2S exposure time of 150 minutes. Large dark patches of CdS begin to obscure the lattice. Further mineralization was found to produce large CdS crystals, similar to those in Fig. 8, that cover and completely obscure the lattice.

By careful control of the H_2S exposure time, it was possible to obtain a very light mineralization of the surface of the square lattice (Fig. 11C) in an attempt to obtain lattice images of the nucleated nanocrystals. Fig. 11D is an enlarged electron micrograph, at a magnification of 200K, of the lattice seen in Fig. 11C. Lattice images of individual nanocrystals can be seen that, upon analysis, possess a d-spacing of 3.4Å, corresponding to the 110 face of zinc blende CdS. EDXA and SAED also confirmed the mineral phase to be the zinc blende polymorph of CdS. As in Fig 9, the crystals are non-crystallographically orientated with respect to the underlying lattice. Crystal dimensions were found to be in the range of 5 to 10nm. It can also be seen that the majority of nanocrystals appear to lie in specific linear domains, delineated by the dark patches seen in the picture (indicated by arrows). The width of these domains is about 8nm. One very important difference on comparison of the oblique and the square CdS mineralized S-layers was in the morphology of the mineralization. In every oblique system there occurred regularly spaced mineralized stripe patterns, due to the Moiré effect. This was not observed in the mineralization of the square lattice, the CdS acting in an analogous way to a negative stain.

4.3.2 CdS Mineralisation of S-Layer Monolayers

The results for the CdS mineralization of S-layer double layers, detailed in the previous section, were repeated for self assembled monolayers by Dr. Dietmar Pum of The Ludwig Boltzmann Institute, Vienna. Figure 12 shows the results obtained for the CdS mineralization of square and oblique S-layer monolayers.

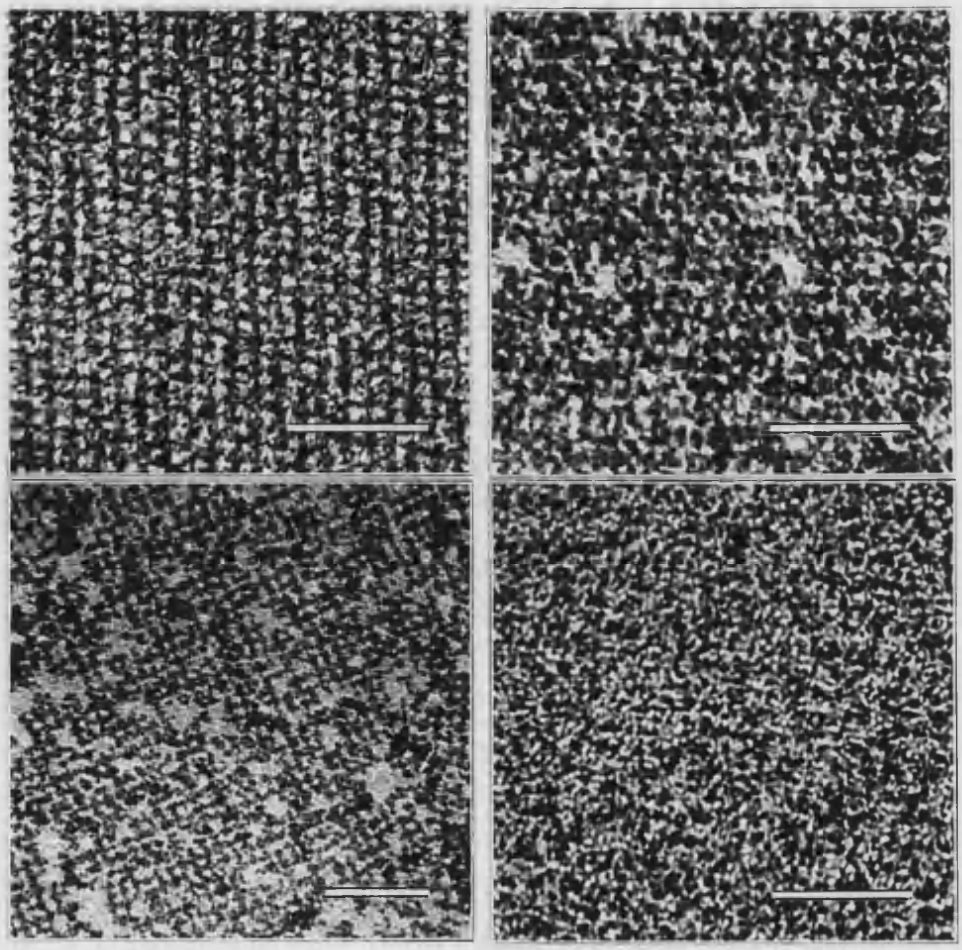

Figure 12 A) TEM micrograph of a uranyl acetate negatively stained self assembled oblique S-layer. Scale bar 60nm B) As for A, but without staining and after CdS mineralization of the exposed inner face. The image shows an oblique periodic array of uniform 5nm CdS nanocrystals. C) TEM micrograph showing a square CdS superlattice on the inner surface of a self-assembled S-layer. Scale bar 100nm. D) TEM micrograph of the mineralized outer face of an oblique S-layer, formed under a Langmuir monolayer of DPPE lipid, showing a weak periodicity of CdS nanoparticles on the surface of the protein. Scale bar 60nm.

The TEM micrographs in Fig. 12 show that the re-crystallised S-layers were decorated with an organised array of CdS nanoparticles in register with the underlying periodicity of the protein lattice. For comparison, a negatively stained (uranyl acetate) self assembled oblique lattice is shown (Fig. 12A) with visualisation of the protein lattice. An oblique

inorganic superlattice (a = 9.8 nm, b = 7.5 nm, θ = 80°) was formed using oblique self-assembled *B. stearothermophilus* NRS 2004/3a S-layers (Fig. 10B), whereas a square superlattice (a = 13nm) was templated on the inner face of recrystallized *B. sphaericus* CCM 2177 S-layers (Fig. 10C). In both systems, the CdS clusters were discrete, relatively uniform in size (mean values; 5nm (oblique lattice); 8nm (square lattice)) and rounded in shape. Mineralized arrays with domain sizes up to 1 μm were observed. The mineralized lattice shown in the Fig. 12D is the outer face of an S-layer from *B. stearothermophilus*. The array shows a weak periodicity.

To give a greater understanding of the nature of the mineralization, computer generated reconstructions were obtained from the TEM micrographs of CdS mineralized oblique S-layer monolayers. Cross correlation averaging was used to identify the position and orientation of S-layers/CdS unit cells (Fig. 13) and to improve the signal-to-noise ration of fine image details.

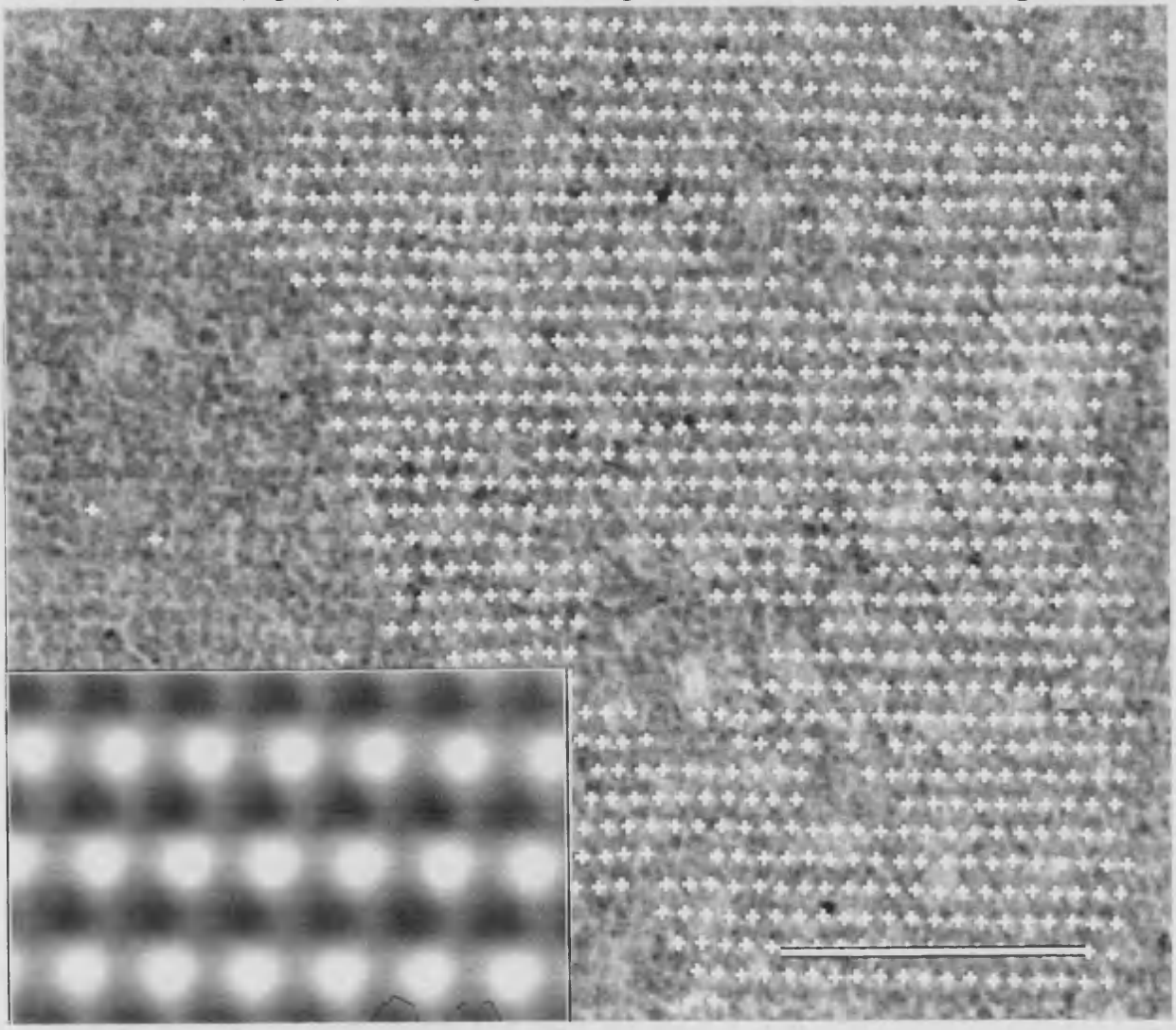

Figure 13 TEM with superimposed white crosses showing the position of individual CdS nanocrystals on the surface of the oblique S-layer lattice. Scale bar 100nm. Inset shows a computer generated image of the CdS mineralised S-layer verifying one CdS particle (dark circles) nucleated periodically on the S-layer (white circles correspond to pores and grey to protein).

An average resolution was assessed by the Radial Correlation Function (personal communication with Dr. D.Pum) and several micrographs were processed. The centre-to-centre spacings of the crystalline lattices were obtained from digital diffraction patterns. The peaklist superimposed on the original micrograph demonstrates a perfect crystallinity of the CdS mineralized S-layer. Computer image reconstruction (Fig. 12, inset) then demonstrated that one CdS particles is nucleated per S-layer subunit.

4.3.3 Discussion

These data suggest that both mono and double layer S-layers can be used to produce both two and three dimensional superlattice arrays of semiconducting CdS quantum dots respectively. Consideration of the mineralization of monolayers showed that S-layers were able to induce site specific nucleation of CdS resulting in an almost perfect crystalline array of CdS nanocrystals. Electron diffraction patterns indicated that the CdS nanoparticles were crystalline and showed no preferential orientation, indicating that the particles were not crystallographically aligned on the hydrophilic inner face of the assembled S-layer subunits. For example, when considering the mineralization of an oblique monolayer the inorganic array dominated the TEM images, a faint pattern of the protein structure with its typical handedness of connecting arms being visible in the background. This observation suggests that Cd(II) also stains the S-layer template, and that the CdS nanoparticles are deposited within the network of nanopores which are located between the protein subunits This was confirmed by the digital diffraction patterns which showed only low order reflections for the reciprocal oblique lattice of the S-layer monolayer.

CdS mineralization of the exposed outer face of *B. stearothermophilus* NRS2004/3 S-layer monolayers produced arrays of discrete 2 to 3nm sized CdS particles that were preferentially deposited on the S-layer template (Fig. 11D). Electron diffraction gave broadened ring patterns with *d* spacings consistent with the Zn blende structure. Close examination of the micrographs revealed some periodicity in the CdS array, but the extent of replication was significantly less than that observed for the nanoparticles formed on the inner surface of the protein template (Fig 11B). In both cases, the results suggest that the inorganic clusters are located within the nanopores of the protein matrix. The inter-subunit spaces are larger on the inner face because of the higher surface corrugation compared with the relatively flat outer surface[26]. This difference in topography could account for the larger size of the CdS nanoparticles, as well as the increased fidelity in the

periodicity of the inorganic arrays deposited on S-layers recrystallized with the inner face exposed. In addition, the inner face is net negatively charged and less hydrophobic than the charge-neutral outer surface, suggesting that electrostatic binding of Cd(II) ions might also be important in site-directed nucleation.

Dispersions of self-assembled S-layer double layers were shown to possess the same potential in the templating of CdS nanocrystal arrays although very different morphologies were obtained. A well-defined square superlattice (a = 13nm) of 5nm sized CdS crystallites was deposited on S-layers of *B. sphaericus* CCM2177 after 100 minutes of exposure to H_2S in the presence of Cd(II). This superlattice became obscured by larger CdS aggregates for longer exposure times (>150 hours) (Fig 11b). Thus, although these experiments gave results analogous to those using mounted S-layers (Fig. 12b), the procedure was more difficult to control.

Mineralization of the dispersed double layer microstructures formed in suspensions of *B. stearothermophilus* NRS2004/3a variant 1 S-layers, produced characteristic stripe patterns of organised CdS nanocrystals (Fig. 3d, 4a). Energy dispersive X-ray analysis showed the presence of cadmium and sulfur throughout the S-layer sheets, and electron diffraction and high resolution lattice imaging indicated that the individual CdS nanoparticles within the striped regions were non-oriented, approximately. 5nm-sized single crystals with the zinc blende structure.

Digital diffraction patterns of the negatively stained self assembly products (Figs 5,6 and 7), revealed the oblique lattices to be composed of double layers. The stripes were found to be caused by Moiré effects, through interaction of the S-layer double layers in a back to back orientation and the electron beam. Geometrical Moiré patterns[54,55] result from the superimposition of two identical gratings. If one of the gratings is then rotated through an angle θ, a series of dark fringes crossing the gratings occur. Thus, if D is the separation of the Moiré fringes and d is the grating interval of each grating, then $D=d/\theta$. Therefore, electron beam Moiré results from the back to back arrangement of two oblique S-layer lattices is opposing orientation, where the electron beam serves to illuminate the sample revealing the Moiré fringes of the mineralized double S-layer. Two examples of Moiré patterns are shown in Fig. 13, a computer generated image and a crystal of PbS.

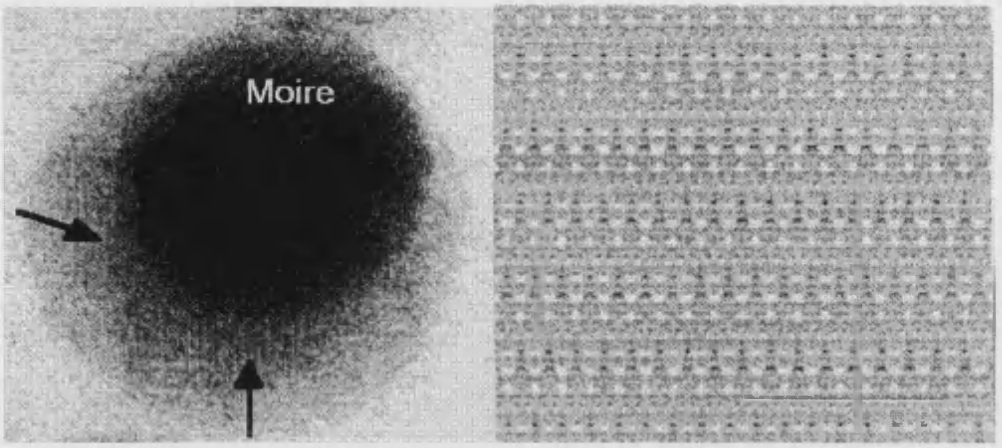

Figure 14 Two example of the Moiré effect. A) A PbS nanocrystal approximately 20nm in diameter. The Moiré pattern is the result of the superposition of two sets of lattice planes, indicated by arrows. B) A computer generated Moiré pattern made through the superposition of two mirror images lattices. (Moiré pattern kindly provided by Dr. D.Pum).

In the back to back orientation, the two associated S-layers are in accurate register at every fourth row of the composite layer. Areas where only fine fringes are visible are monolayers. This was unambiguously deduced from the digital diffraction patterns which showed two mirror symmetric reciprocal lattices. The stripe pattern was also represented in the diffraction pattern by a low order reflection of only one quarter of the longer base vector, which corresponds to the difference vector between the two shorter reciprocal base vectors. This characteristic orientation generates a periodicity of the stripes of approximately 30nm, which is four times the corresponding lattice constant. The width of the stripe pattern was approximately 16nm. These parameters agree with the empirical measurements made upon the electron micrographs. Computer reconstructions of the mineralized monolayer oblique lattice also showed the perfect crystallinity of the mineralized S-layer lattice, indicating one CdS particle nucleated per subunit.

The data indicate that the double-layered protein template can be used to produce a stacked inorganic-organic assembly, consisting of an ordered two-tier arrangement of CdS nanocrystalline arrays. Previous experiments with polycationic ferritin, which is a topographical marker for net negatively charged domains on S-layer lattices, showed that the inner faces of the two constituent layers of the double-layered sheets were juxtaposed[23]. Thus, inorganic precipitation directly onto the exposed surfaces of the dispersed sheets should replicate the nanoporous lattice of the flat outer faces. As this face was relatively ineffective as a template when mounted as a

lipid/protein monolayer on TEM grids (Fig 12*c*), mineralization of the double-layered structure possibly involves Cd(II) penetration of the architecture followed by *in situ* sulfidation within the confined spaces of the corrugated internalised inner faces. Further work is required to determine the precise location of the CdS nanocrystallites in these hierarchical materials.

4.4 Conclusion and Future Work

This work has shown for the first time the potential of S-layer biocrystals to act as templates in the chemical fabrication of two and three dimensional superlattice arrays of CdS nanocrystals (Fig. 15). Although the inorganic nanoparticles are not crystallographically oriented within the S-layer matrix, the preferential deposition of CdS in association with the dispersed S-layers, rather than in bulk solution, suggests that molecular interactions between the functional groups of the protein surface and Cd(II) ions in solution could be important for the construction of the superlattice arrays.

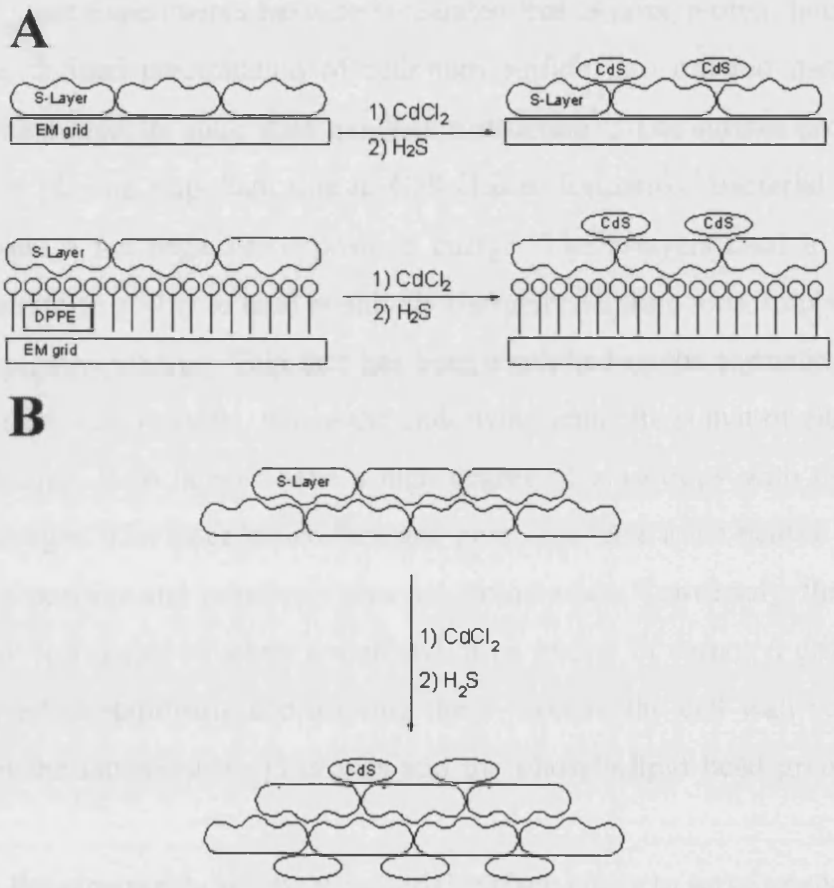

Figure 15 Schematic showing routes to the formation of superlattice arrays of CdS nanocrystals. A) Shows the formation of monolayer arrays of CdS nanocrystals from mineralisation of either the inner or outer face of a self assembled monolayer. B) Shows the formation of a two tier stack of CdS nanocrystals from the mineralization of self assembled double layers.

As previous studies have shown, S-layer proteins can be chemically modified with many different types of functional groups and molecules[21],tailoring the surface properties of these

biocrystal templates to wet chemical synthesis could have significant advantages over metallization procedures[53] in fabricating a wide range of organised inorganic nanomaterials with semiconducting, magnetic or electronic properties. In particular, there is currently great interest in the formation of metal cluster arrays for coulomb charging behaviour in nanoelectronic digital circuits[29]. The stringent requirement for particle size monodispersity in such applications might be circumvented by directly synthesising the nanoparticles in the presence of a suitable patterning agent. For this reason, the chemical synthesis of Au superlattices using S-layer templates is the principal objective of current and future work.

Specifically, these experiments have demonstrated that S-layer protein lattices can serve as templates for the defined precipitation of cadmium sulfide into ordered nanometric point patterns, forming a biomolecular solid state nanoheterostructure[56]. The surface properties of the S-layer protein lattice play an important role in CdS cluster formation. Bacterial surfaces have been shown to possess a net negative or positive charge. The S-layers used in this series of experiments demonstrate an ability to bind positively charged cadmium ions, implying the lattice to have regions of negative charge. This fact has been exploited in the formation of a regular array of cadmium sulfide nanocrystals, where the underlying template is that of either the square or oblique S-layer lattice. Both lattices have a high degree of anisotropy with regards to their respective surface charges. The outer lattice face and pore area have a net neutral charge due to the equal numbers of positive and negatively charged amino acids. Conversely, the inner face of the lattice is a highly corrugated structure comprised of an excess of carboxyl groups, these are thought to be involved in stabilising and affixing the S-layer to the cell wall via electrostatic interactions between the lattice carboxyl groups and the phospholipid head groups of the cell wall lipid bilayer[12].

In summary, the remarkable ability of bacterial surface layers to serve as spatially specific nucleation sites has been shown, producing ordered two dimensional arrays of semiconductor nanocrystals. Work undertaken in this field has concentrated purely on the production of ordered semiconductor arrays using techniques such as nanolithography and colloidal crystallisation. Here for the first time a biological protein matrix has been employed, utilising its geometry of charge distribution to induce the crystallisation of cadmium sulfide and the consequent formation of a quantum dot superlattice.

Ordered arrays of semiconductor nanocrystal find many applications in industry. For example, arrays of semiconducting nanocrystals have recently been used in laser technology[57]. Current attempts at producing quantum dot lasers have shown the need for size specific arrays and recently it has been found that stacked arrays offer greater potential in the production of equal wave length photons necessary for the production of laser light. Both criteria may be met by S-layer technology, as stacked S-layers can easily be produced using Langmuir-Blodgett techniques[57]. A lot of work has also been done on the use of S-layers in bioelectronics and biosensors, due to their ability to self assemble on metal surfaces such as gold and silicon. This may offer a unique interface between electronics and biology, such as in the production of "biochips". Thus, as nanotechnology proceeds, the role of self assembly continues to be paramount in the production of molecular machines. S-layers offer a system where all the information needed to produce the regular protein lattice resides in the amino acid sequence of each monomer. This fact alone confers a great potential in the use of S-layers in current nanotechnological developments.

4.5 References

1 G.A.Ozin (1992) Nanochemistry: Synthesis in diminishing dimensions, *Adv.Mater.*, **4**, p612-649

2 C.R.Barrent (1997) From Sand to Silicon : Manufacturing Microprocessors, *Sci.Am.*, **8**, p56-61

3 D.Leonard, M.Krishnamurty, C.M.Reaves, S.P.Denbaars, P.M.Petroff. (1993) Direct formation of quantum sized dots from uniform coherent islands of InGaAs on GaAs surfacesm, *Appl.Phys.Lett.*, **63**, p3203-3206

4 A.Stein, P.MacDonald, G.A.Ozin, G.D.Stucky, (1990) *J.Phys.Chem.*, 94, p6943-

5 A.Stein, M.Meszaros, P.Macdonald, G.A.Ozin, G.D.Stucky (1991) Adv.Mater., 3, p306-

6 M.Gao, Y.Yang, B.Yang, F.Bian, J.Shen (1994) Synthesis of PbS Nanoparticles in Polymer Matrices, *J.Chem.Soc., Chem.Comm.*, **12**, p2779-2780

7 B.A.Korgel, H.G.Monbouquette (1996) Synthesis of size-monodisperse CdS Nanocrystals using phospatidylcholine vesicles, *J.Phys.Chem.*, **100**, p346-351

8 V.L.Colvin, A.N.Goldstein, A.P.Alivisatos (1992) Semiconductor nanoparticles covalently bound to metal surfaces with self assembled monolayers, *J.Am.Chem.Soc.*, **114**, p5221-5230

9 B.O.Dabbousi, C.B.Murray, M.F.Rubner, M.G.Bawendi (1994) Langmuir-Blodgett Manipulation of Size-selected CdSe Nanocrystallites, *Chem.Mater*, **6**, p216-219

10 Sleytr, U.B., Messner, P., Pum, D. and Sara, M. (ed.) (1988) *Crystalline Bacterial Cell Surface Layers.*, Berlin, Springer Verlag.

11 Sleytr, U.B. and Messner, P. (1983) *Annual Review of Microbiology* ,**37**, p311-339.

12 Messner, P. and Sleytr, U.B. (1992) *Advances in Microbial Physiology*, Vol.33 ed., Springer-Verlag.

13 Sleytr, U.B. and Glauert, A.M. (1975) *Journal of Ultrastructure Research,* **50**, p103-116.

14 Sleytr, U.B., Messner, P., & Pum, D., (1988), *Methods in microbiology,* London Academic press.

15 Beveridge, TJ. (1981) *International Review of Cytology*, **72**, p229-317.

16 Baumeister W. and Engelhardt, H. (1987). *Electron Microscopy of Proteins* , Vol. 6, *Membraneous Structure* ed. Harris, J.R. and Home, R.W. pp. 109-154. London: Academic Press.

17 Beveridge, TJ., Stewart, M., Doyle, R.J. and Sprott, G.D., (1985) **162**, 728-737.

18 Messner, P., Pum, D & Sleytr, U.B., (1986) Journal of Ultrastructure and molecular structure research, **97**, p73-88.

19 Konig, H. and Stetter, K.O. (1986) *Systematic and Applied Microbiology 7*, p300-309.

20 Konig, H. (1988) *Canadian Journal of Microbiology,* **34**, p395-406.

21 Thompson, B.G., Murray, R.G.E. and Boyce, J.F. (1982) *Canadian Journal of Microbiology* **28**,1081-1088.

22 Koval, S.F. and Murray, R.G.E. (1984) *Canadian Journal of Biochemistry and Cell Biology* **62**, p1181-1189.

23 Smit, J. (1987) *Bacterial Outer Membranes as Model Systems*, ed. M.Inouye, p343-376, New York, John Wiley &Sons.

24 Sleytr, U.B. and Glauert, A.M. (1982) *Electron Microscopy of Proteins,* Vol. 3 ed. Harris, J.R. pp. 41-76. London: Academic Press.

25 Sleytr, U.B. (1978) *International Review of Cytology,* **53**, 1-64.

26 Sleytr, U.B. and Messner, P. (1989) *Electron Microscopy of Sub-cellular Dynamics* ed. Plattner, H. pp. 13-31. Boca Raton: CRC Press.

27 Takeoka, A., Takumi, K., Koga, T. and Kawata, T. (1991) *Journal of General Microbiology* **137**, 261-267.

28 Kornfeld, R. and Komfeld, S. (1980) *The Biochemistry of Glycoproteins and Proteoglycans* ed. Lennarz, W.J pp. 1-34. New York: Plenum Press.

29 Sara, M and Sleytr, U.B. (1987). *Journal of Bacteriolog,y* **169**, p2804-2809

30 Sara, M and Sleytr, U.B.(1989) *Applied Microbiology and Biotechnology,* **30** ,p184-189

31 Sara, M., Kalsner, I and Sleytr, U.B.(1988) *Archives of microbiology*, **149**, p527-533

32 Messner, P., Pum, D. Sara, M., Stetter, K.O., Sleytr, U.B. (1986) *Journal of Bacteriology* **166**, 1046-1054

33 Messner, P., Bock, K., Christian, R., Schultz, G., Sleytr, U.B.(1990) *Journal of Bacteriology* **172**, p 2576-2583

34 Gruber, K. and Sleytr, U.B. (1991). *Archives of Microbiology,* **156**, p181-185.

35 Sara, M., and Sleytr, U.B.(1987) *Journal of Bacteriology*, **169**, p4092-4098

36 Sara, M., Kupucu, S., and Sleytr, U.B.(1992) *Journal of Bacteriology*, **174**, p3487-3493

37 Sara, M., and Sleytr, U.B.(1987) *Journal of membrane science*, **33** ,p27-49

38 Sara, M., Kupucu, S., and Sleytr, U.B.(1989) *Archives of microbiology*, **151**, p416-420

39 Pum, D., Messner, P. and Sleytr, U.B.(1991) *Journal of bacteriology*, **173**,p 6865-6873

40 Masuda, K., and Kawata, T.(1985) *Microbiology and immunology,* **29**, 927-938

41 Pum, D., Messner, P., and Sleytr, U.B.(1989) *Journal of vacuum science and technology,* **B7** p1391-1397

42 Beveridge, T.J. and Murray, R.G.E. (1976). *Journal of Ultrastructure Research,* **55**, p105-118.

43 Buckmire, F.L.A. and Murray, R.G.E.(1976) *Journal of Bacteriology* **125**, p290-299.

44 Beveridge, TJ. and Graham, L.L.(1991) *Microbiology Reviews*, **55**, p684-705.

45 Paul, A., and Englehardt, H.(1992) *Biophysical journal,* **61**, 172-188

46 Graham, L.L., Beveridge, T.J. and Nanninga, N. (1991) *Trends in Biochemical Sciences,* **16**, p328-329.

47 Baumeister, W., Wildhaber, I. and Engelhardt, H.(1988) *Biophysical Chemistry* , **29**, p39-49.

48 Koval, S.F.(1988) *Canadian Journal of Microbiology*, **34**, p407-414.

49 Kay, W. W., Buckley, J.T., Ishiguro, E.E., Phipps, B.M., Monette, J.P.L., Trust, TJ.(1981). *Journal of Bacteriology,* **147**, p1077-1084.

50 Evenberg, D., Versluis, R. and Lugtenberg, B.(1985). *Biochimica et Biophysica Acta,* **815**, p233-244.

51 Blaser, MJ., Smith, P.E., Repine, J.E. and Joiner, K.A.(1988).*Journal of Clinical Investigation,* **81**, p1430-1444.

52 Dubreuil, J.D., Kostrzynska, M., Austin, J.W. and Trust, T.J(1990) *Journal of Bacteriology,* **172**, p5035-5043.

53 Messner, P. (1986) *Journal of ultrastructure and molecular research,* **97**, p73-88

54 Post, D.(1991) *Experimental mechanics,* **3**, p276-280

55 Parks, V.J., *Geometric Moire* (1987) p282-313, Prentice-Hall Englewood cliffs, N.J

56 Mann, S., (1996) *Biomimetic Materials Chemistry*, Vol 1 VCH New York

57 A.P.Alivisatos (1996) Semiconductor Clusters, Nanocrystals and Quantum Dots, *Science*, **271**, p933-937

58 U.B.Sleytr, M.Sara, P.Messner, D.Pum (1994) Two-dimensional protein crystals : Fundamentals and applications, *Journal of Cell Biochemstry*, **56**, p171-176

EUKARYOTIC SYSTEMS

Living cells are self-regulatory chemical engines, tuned to operate on the principle of maximum economy

A.L.Lehninger

Chapter 5

Directed Self-Assembly of Nanoparticles into Macroscopic Materials using Antibody-Antigen Recognition

Order is heaven's first law

Alexander Pope

5.1 Introduction

The organisation and patterning of inorganic nanoparticles, into two and three dimensional structures, is a potential route to chemical, optical, magnetic and electronic devices with useful properties[1-3]. The production of self-assembling materials at this scale represents a major goal of chemistry, materials science and nanotechnology.

This chapter demonstrates that the precise antigen recognition properties of antibodies (or immunoglobulins) can be utilised to realise these goals, resulting in self assembled materials from colloidal particles. IgE or IgG antibodies, with specificities to dinitrophenyl (DNP) and biotin respectively, were attached to individual Au and Ag nanoparticles. Antigens (or more correctly 'haptens') were added, with appropriate double-headed functionalities, to induce the formation of metallic or bimetallic macroscopic filaments and aggregates, comprising linked Au, or Au and Ag nanoparticles. Antigen connectors with homo- (DNP-DNP) or hetero- (DNP-biotin) "janus" structures, connected by at least an eight-atom spacer, are synthesised for this purpose, thereby introducing the technique of 'antigen engineering'.

5.1.1 Nanophase Self Assembly of Materials

The self assembly of materials at the nanometer scale represents a pivotal and fundamental aspect of nanotechnology. The full exploitation of the nanotechnological revolution relies upon the ability to self assemble constituents along precise pathways, into nanomaterials with distinct mesoscopic architectures and high symmetry, using both covalent and non-covalent interactions. These self assembled materials are expected to find potential applications from the next generation of nanoelectronic devices, to materials possessing inordinate complexity with novel properties.

One of the most alluring aspects of biological systems, when applied to nanotechnology, is their penchant for self-assembly. Mechanisms of self assembly in biological systems have been studied intensively, the archetypal system being the plant pathogen, tobacco mosaic virus (see Chapter 7 'Inorganic-Organic Nanotube Composites From Template Mineralization of Tobacco Mosaic Virus'). Self assembly in biological systems is mediated largely by non-covalent interactions, such as hydrogen bonds and van der Waals interactions, ensuring a dynamic equilibrium in the assembly process. This

allows an error-detection and correction mechanism, analogous to that found in the branch of mathematics known as Code Theory. For example, the weak reversible interactions directing self assembly lead to a thermodynamic minimum, thus incorrect structures are rejected in this dynamic equilibrium. Biological self assembly involves certain key processes, like the aforementioned use of non-covalent interaction. Others include the modularization of assembly, a small number of interacting subunits and the complementarity of surfaces, the latter interaction being strengthened by ionic and hydrogen bonds. The overall scheme is to use a small number of identical subunits, displaying a high degree of topological complementarity. The association of these structures, by a large number of non-covalent interactions distributed over the resultant structure, confers great stability.

The thermodynamics of biological self-assembly gives a greater insight into the nature of the self assembly process, albeit general due to the huge number of interactions involved. The dependence upon weak non-covalent interactions and the equilibrium nature of the system in the self assembly process implies a greater influence of entropy (ΔS) in the system. The individual loss of translational and conformational entropy for individual interactions is minimal, but the process of molecular recognition involves large numbers of these interactions, resulting in a substantial loss of entropy. The design of the subunits involved in a self assembly process counters this entropy loss, through utilisation of rigid subunits that achieve good molecular contact, thus minimising the loss of conformational entropy. The release of structured water around hydrophobic binding regions, due to the hydrophobic affect, also compensates greatly for the loss of entropy. These compensatory mechanisms are a simplification of the driving forces involved in self assembly, for example conformational changes and the huge number of non-specific interactions involved are considerable, but give a general account of the mechanism.

Nanochemistry offers a synthetic methodology for the production of self assembled nanostructured materials. The organisation and patterning of inorganic nanoparticles into two- and three-dimensional functional structures is a potential route to chemical, optical, magnetic and electronic devices with useful properties. A range of non-lithographic protocols, including solvent evaporation of hydrophobic colloids[1-3] and molecular cross-linking in colloidal aggregates[4-6] have been reported to give close packed

arrays of nanometer size metal clusters. In the technique employed by Andres *et al*[5], gold nanoparticles are encapsulated by thiols, which are subsequently displaced by aryl dithiols to form a close packed monolayer (Fig. 1B).

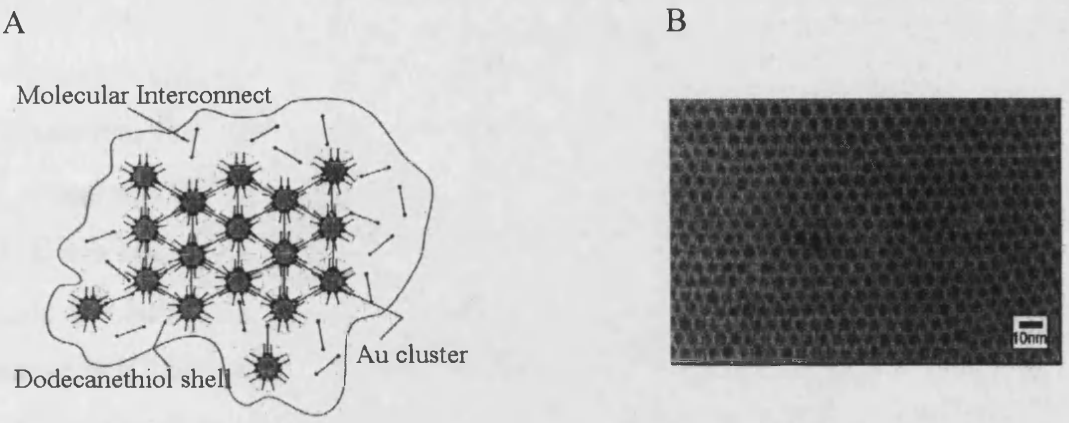

Figure 1 A). Schematic showing an example of a synthetic scheme to create two dimensional self assembled arrays using molecularly linked metal clusters. B) Electron micrograph showing the resultant 2D array of gold particles[5].

Several biological systems have also been employed to address the area of self assembled superstructures, for example template-directed synthesis using porous protein crystals[7,8] or bacterial superstructures[9] have been reported. Recently, two reports have highlighted the potential of using complementary DNA oligonucleotides attached to the surfaces of gold nanoparticles[10,11](see Chapter 1 Introduction).

5.1.2 Antibodies (or Immunoglobulins)

The immune system is a well designed co-operative system that defends its host against foreign invasion, the sentinels of this fortress being macrophages that continually roam the bloodstream of their host. When challenged by infection, or immunisation, macrophages respond by engulfing invaders marked with foreign molecules (antigens). This event, mediated by helper T cells, sets forth a chain of responses, resulting in the stimulation of B-cells. These B-cells in turn, produce proteins called 'antibodies' which bind to the foreign invader. Antibodies (or immunoglobulins, abbreviated to Ig) are the most abundant protein constituents of the blood. The binding event between antibody and antigen marks the foreign invader for destruction via phagocytosis or activation of the complement system[12].

Antibody structure

Five different classes of antibodies exist: IgA, IgD, IgE, IgG, IgM[13]. They differ not only in their physiological roles, but also in their structures, although IgG and IgE are almost identical morphologically. From a structural point of view, IgG antibodies are a particular class of immunoglobulins that have been extensively studied, perhaps because of the dominant role they play in the immune response. The structure of an IgG antibody is shown schematically in Fig. 2. IgG antibodies are Y-shaped proteins (Fig. 3) composed of two heavy chains and two light chains joined by disulfide linkages[14]. The IgG molecule can be broken down into two regions, the Fc and Fab. The Fc region, so called because it is the fragment of the IgG molecule that most readily crystallises, is involved in eliciting further immune responses. Two identical Fab fragment are present at the NH_3^+ends of the "Y" in every IgG structure. The Fab region is named as such because it is the IgG fragment that contains the antibody binding site. The Fab fragment contains a region of highly conserved amino acids, as well as a region of highly variable amino acids (Fv). These variable sequences are confined to 6 protein loops that cluster together at the end of the Fab fragments, forming a continuous hypervariable surface. It is this region that is responsible for the binding of foreign antigens[15].

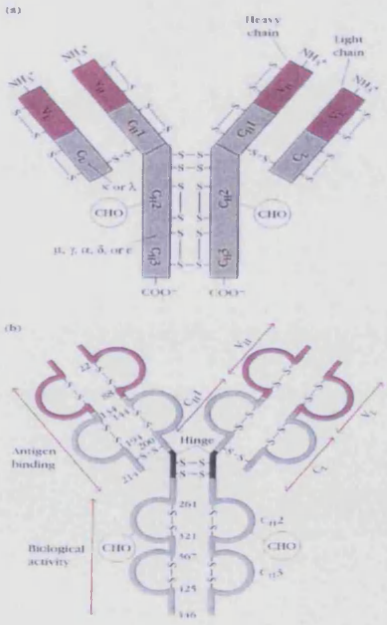

Figure 2 Schematic diagram showing the structure of an IgG antibody (http://www.antibodyresource.com.)

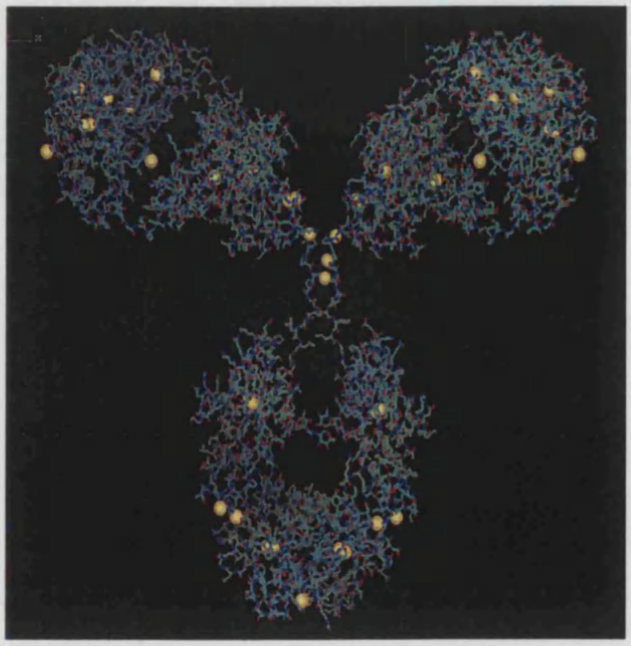

Figure 3 Computer generated image of the three dimensional structure of an IgG antibody with highlighted sulfur atoms.

Antibody-Antigen Interactions

In order to perform their crucial role in the line of defence, antibodies must be extremely versatile. Indeed, even on a daily basis, the immune system encounters a great variety of foreign substances (e.g. bacteria, viruses, toxins). As a result, antibodies must be extremely diverse to counter a large number of unexpected and unknown possibilities. Through the complex process of gene splicing[18], B-cells have been estimated to produce between 10^8 to 10^{10} IgG antibodies that differ in the composition of their binding sites. This capacity to generate an enormous number of unique binding motifs makes antibodies a formidable line of defence. Another attribute of antibodies is specificity. In order to distinguish between both self and a multitude of foreign species, antibodies need to have a highly discriminating method of recognition on the molecular level. This specificity arises from the complementary nature of antibody binding. This characteristic of antibody binding is the result of immunologically-tuned interactions (i.e. charge-charge, dipole-dipole, H-bonding, and van der Waals) between the antigen and amino acid residues present in the antibody binding pocket. By taking advantage of the varied chemical properties of the 20 amino acids, the immune system is able to generate an array of antibody binding pockets, that can accommodate the shape, charge, and hydrophobicity of seemingly any given antigen. To date, a variety of crystal structures of Fab fragments with small molecular ligands have been solved. In all cases, extensive use of intermolecular attractive forces are employed.

Van der Waals contacts are used extensively by antibodies to conform to the shape of an antigen[16]. In antibody-antigen complexes, water is often excluded from the contact interface between the antibody binding site and the protein antigen[17], (although in some acting as a form of 'glue') this exclusion of interfacial water, seen in many complexes between Fabs and antigens, is a feature of antibody binding. The strength of the interaction between the antibody and its respective antigen is termed 'antibody affinity', where a high affinity antibody forms a strong bond with its antigenic determinant[19-21]. This results in an antibody-antigen complex that has a low tendency to dissociate. Conversely low affinity antibodies form complexes that require less energy for dissociation. Affinity is thus a thermodynamic measurement of the strength of antigen-

antibody interaction, expressed as the equilibrium constant K. The quantitative relationship between antibody and antigen at equilibrium is represented by :

$$Ab + Ag \underset{k_d}{\overset{k_a}{\rightleftharpoons}} AbAg$$

where Ab represents free antibody, Ag the free antigen, AbAg the antibody-antigen complex and k_a and k_d, the association and dissociation constants respectively. The Law of Mass Action states that the rate of formation of complex is proportional to the concentration of reactants, thus the rate of association becomes $k_a[Ab][Ag]$ and rate of dissociation $k_d[AbAg]$. Thus, at equilibrium

$$k_a/k_d = K = [AbAg]/[Ab][Ag]$$

where K is the equilibrium constant.

After this primary antibody-antigen interaction has occurred, other 'secondary' interactions occur, such as precipitate formation due to the self assembly of large three dimensional 'lattices' of antibodies and antigens. Thus, as increasing amounts of antigen are added to a fixed amount of antibody, the quantity of antibody precipitated increases. This increase in precipitate continues until a point is reached where no free antibody or antigen is detected in the supernatant, this is the 'equivalence zone'. At this point, optimal proportions of antibody and antigen form a continuous, stable, antibody-antigen 'lattice' which precipitates out of solution[20]. In conditions of extreme antigen excess, the amount of precipitate is markedly reduced, due to the formation of soluble complexes.

Isolation of Antibodies

Two types of antibody sample can be used in the study of antibody-related phenomena. The first type, 'polyclonal' antibodies[22], can be obtained by immunising a mammal, such as a goat, sheep, mouse, or a rabbit. After immunisation, blood is removed and the antibodies purified directly from the serum. The name polyclonal is derived from the Greek word for many ('polloi') and sprout ('klon'). As implied by the name, polyclonal antibodies originate from a variety of B-cells that differ in the genetic material that encodes for antibody production. In a polyclonal sample, some of the antibodies will be specific for the antigen with which the animal was immunised, but the remaining antibodies have been elicited from encounters with other foreign antigens that the animal has been exposed to throughout its lifetime.

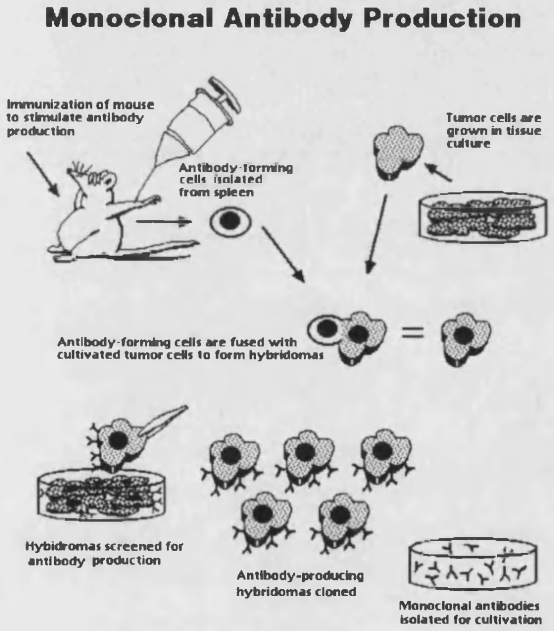

Figure 4 Diagram outlining the production of monoclonal antibodies. (http://www.antibodyresource.com.)

The second type of antibody sample, the 'monoclonal antibody'[23], is derived from a more complex process. The technology associated with the production of monoclonal antibodies is shown schematically in Fig. 4. Here, a mammal, almost always an inbred mouse, is immunised with an antigen. After repeated immunisations, the spleen of the animal is removed. Because the spleen is responsible for B-cell production, the spleen cells contain the genetic information that gives rise to antibody production. Spleen cells cannot be cultured, therefore they are fused with "immortal" myeloma cells, so-called because of their ability to proliferate *in vitro*. The resulting fused cells, called hybridoma cells, are screened with a colourimetric enzyme-linked immunoabsorbant assay (ELISA). Use of this assay allows for the selection of hybridoma cells that produce antigen-specific antibodies. Because a given hybridoma cell is derived from a single B-cell, it produces a

monoclonal antibody. Here, the prefix mono-, derived from the Greek word for single ('monos'), is used to indicate that a monoclonal antibody is derived from the genetic code of a unique B-cell. Once a single hybridoma line is selected, it is injected into a healthy mouse. Hybridoma cells, like myeloma cells, have the ability to produce tumours. Consequently, after injection with a hybridoma line, a tumour grows inside the host mouse. When this tumour grows, it produces ascites fluid, a fluid that is rich in the monoclonal antibodies.

5.2 Materials and Methods

Immunoglobulins

Monoclonal Anti-Dinitrophenyl[24](Anti-DNP) and Anti-Biotin[25] immunoglobulins were obtained form Sigma Immunochemicals. Monoclonal Anti-DNP is a mouse IgE isotype and derived from the hybridoma produced by the fusion of mouse myeloma cells and splenocytes from an immunised mouse. The product is affinity purified from ascites fluid and supplied in phosphate buffered saline, pH7.4, containing 15mM NaN_3, at a concentration of 1.1mg/ml. Monoclonal Anti-Biotin is a mouse IgG1 isotype isolated by the same procedure as for Anti-DNP and supplied in a buffer of the same composition, but at a concentration of 2.4mg/ml.

Colloid Synthesis

I) Gold Colloid. Gold colloids were prepared according to the procedure described by Turkevich et al[26]. A solution of tetrachloroauric acid was prepared by dissolving 10mg $HAuCl_4.3H_2O$ (Aldrich) in 95ml distilled, deionized water. This solution was heated to boiling and 5ml of a 1% aqueous sodium citrate (Aldrich) solution was then added to the vigorously stirred solution. A claret red sol formed after several minutes and remained stable for several months when stored in the dark.

II) Silver Colloid. A silver colloid was prepared according to the procedure described by Lee and Melsel[27], with the reaction vessel wrapped in aluminium foil. $AgNO_3$ (10mg, pH6.8, Aldrich) was dissolved in 500 ml of distilled de-ionised water and brought to boiling. A solution of 1% sodium citrate (10ml) was added and the solution kept boiling for 1hr. The resulting sol possessed a metallic green/yellow colour. The sols were stable, if kept in the dark, at pH 6.8.

Antigen Synthesis

I) Homo-Janus DNP-DNP antigen: 1.0g of 1,8-diaminooctane (7mmoles, Aldrich) was added to 15ml H_2O followed by 1.5g Na_2CO_3 (14mmoles) and dissolved by heating to 50°C on a water bath. 1.0g of 2,4-dinitrofluorobenzene (5mmoles, Aldrich) was added directly to the rapidly stirred solution, followed by 50ml of water, the temperature then

raised to 60°C for 20mins, then left to cool. The resulting yellow precipitate was filtered through a Buchner funnel and washed with aliquots of dilute Na_2CO_3, followed by dilute HCl. The yellow precipitate was placed in an oven at 80°C for 30 minutes and then in a vacuum dessicator for 24 hours. The product showed low solubility in aqueous solutions and all experiments were subsequently performed using a saturated aqueous solution of the antigen.

II) Hetero-Janus DNP-Biotin Antigen : 30 mg of DNP-Lysine (100 μmoles, Aldrich) was dissolved in 20 ml H_2O. The pH of the solution was raised to 10.5 by addition of 1M NaOH. 50 mg of sodium sulfosuccinimidyl-6-biotinamidohexanoate ('long-arm biotin', 90 μmoles, Vector Laboratories) was added slowly to the vigorously stirred solution. The pH of the solution was maintained at 10.5 over 48 hours and the reaction monitored by thin layer chromatography. Dilute HCl was then added to give a pH of 2.5, resulting in the formation of a yellow precipitate, which was filtered through a Buchner funnel and washed with 30ml of acidified distilled water, then air dried for 10 minutes. The yellow precipitate was placed in a vacuum dessicator for several days. The product was reasonably soluble in aqueous solutions, although saturated solutions were usually employed in subsequent experiments.

Antibody Conjugation

Monoclonal anti-DNP IgE and anti-biotin IgG were attached to the surfaces of the synthesised Au nanoparticles by identical procedures as follows. Preliminary titrations, utilising the red to blue colour change of the native Au colloid upon exposure to high salt concentrations, were used to determine the minimum antibody/colloid ratio required for inhibition of salt induced colloidal aggregation. This was established by the increased stability (no red to blue colour change) of the Au colloid due to the presence of a monolayer of surface-adsorbed antibodies. Thus, exposure of these antibody-conjugated Au particles to a 10% aqueous NaCl solution, revealed no particle growth, as shown by UV-vis spectroscopy, indicating that the colloidal ripening observed under these conditions for the unconjugated colloid was arrested, due to the adsorbed protein molecules. This was an important consideration because saline solutions were necessary

for all antibody-antigen recognition self-assembly experiments. Similar methods were used for the Ag colloid, except that the Anti-biotin IgG antibody was coupled to the nanoparticles at a lower pH of 6.8, due to the comparative instability of the silver colloid.

Conjugation experiments involved raising the pH of the Au sol to 9 (above iso-electric point of the protein), by the addition of 0.5 M NaOH, followed by addition of the predetermined amount of antibody (established by the preliminary titration) in borax buffer ($Na_2B_4O_7 \cdot 10H_2O$, 2mM, Aldrich) (typically, 10 μl of the 40 μg/ml antibody/borax, pH9, solution was added to 0.1 ml of the colloid). The sols were stable for several months, showing no sign of precipitation, upon addition of 0.01% NaN_3 to prevent contamination.

Antigen-Directed Self-Assembly of Aggregated Structures.

I) Homo-Janus Antigen Induced Aggregation

Synthesised homo-janus antigens were added to saline solutions (0.1 M NaCl, pH9) of the antibody-coated colloidal dispersions and left unstirred at 37°C for 30 minutes, then incubated at 4°C for 12 to 24 hours. The amount of antigen required to achieve the equivalence ratio, and hence extensive cross-linking, was determined by a series of concentration-dependent experiments. Typically, between 10 and 30 μl of the saturated antigen solution was added to 0.1 ml of the Au/Antibody colloid.

II) Hetero-Janus Antigen Induced Aggregation

Initial experiments utilising the hetero-janus antigen involved identical procedures to those for the homo-janus antigen. It was then found that the heating stage could be omitted and that an incubation at 4°C for the duration of the experiment produced the best results.

5.3 Results and Discussion

The results are partitioned into several sections. Colloidal synthesis and the conjugation of antibodies to colloidal particles are introduced first, followed by the synthesis of the antigens. These materials are then used to produce the mono- and bi-metallic aggregates of gold and silver particles, each using the synthetic antigens, described in the final section.

5.3.1 Colloid Synthesis

I) Gold colloid

The gold sol, produced by the method outlined in the Materials and Methods section, possessed a claret red colour and this colour remained for several months, with a minimal amount of precipitation. TEM analysis was performed to verify the nature of the colloidal particles, by applying droplets of the sol to TEM grids. The grids were immediately blotted and washed several times in doubly distilled water prior to analysis. Examination of the grid revealed a large number of spherical, electron dense particles with average diameters of 12nm (Fig.5a).

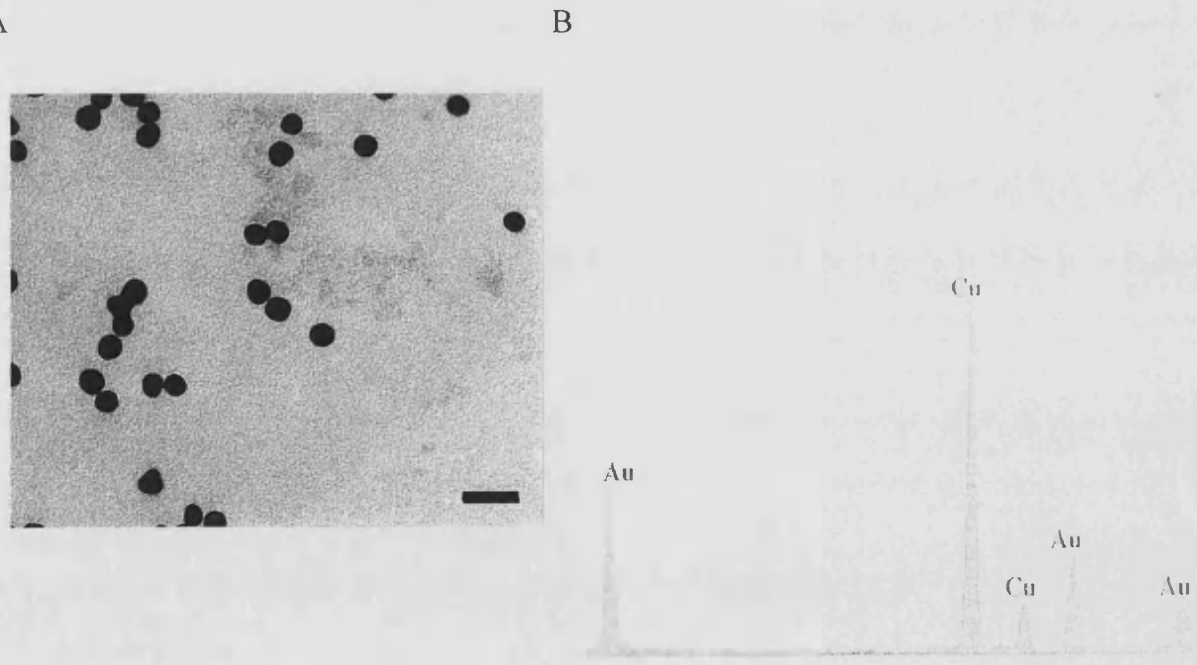

Figure 5 A) TEM micrograph of gold colloid. Scale bar 20nm. B) EDXA of the gold colloid.

A

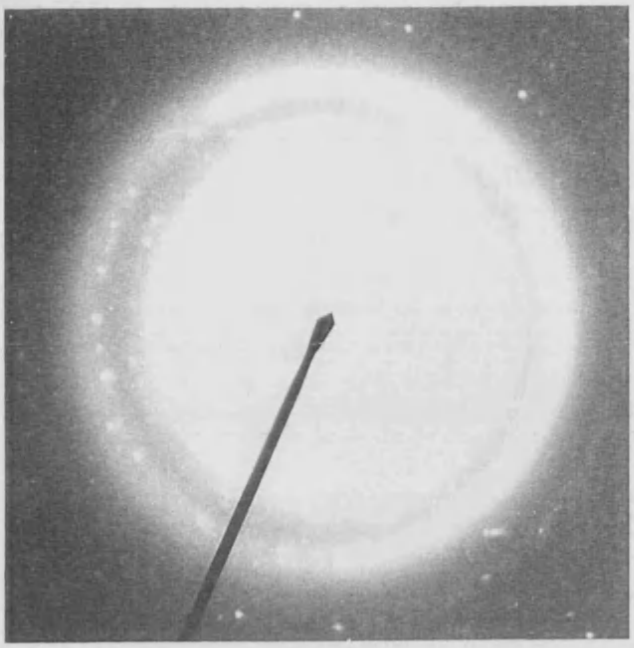

B

D-Spacings for gold (nm)	D-Spacings for gold colloid (nm)
0.235	0.230
0.203	0.205
0.144	0.146
0.123	0.124

Figure 6 A) SAED pattern of gold colloid B) Table comparing d-spacings for gold and gold colloid.

EDXA confirmed these particles to be comprised of gold, due to the exclusive presence of peaks for gold and copper, the latter due to the TEM grid (Fig.5b). The crystalline nature of the colloidal particles was verified by SAED, which showed a concentric ring pattern (Fig. 6a), indicative of a non-crystallographically orientated plane of nanocrystalline gold particles. Measurement of the d-spacings confirmed the presence of crystalline gold (Fig. 6b). These data suggest the synthesis was successful in the production of a homogeneous sol of gold particles, displaying a small particle distribution size. One important observation is that the drying down of the gold nanocrystals on the TEM grid produced a high degree of colloidal 'necking', where individual particle are so close, they appear to be joined.

II) Silver colloid

The synthesis of a silver sol employed a similar citrate reduction protocol to that for the synthesis of the gold sol. The resulting colloid possessed a characteristic green/yellow colouration, remaining stable for several months upon the exclusion of light. TEM analysis was performed on droplets of the sol applied to TEM grids, in an identical fashion to the examination of the gold colloid. Micrographs revealed the colloid to be composed of nanoparticulate clusters displaying a much greater particle size distribution,

on comparison with the gold colloid (Fig. 7a). A range of elliptical and elongated particles were seen, together with spherical particles. EDXA confirmed the presence of silver (Fig. 7b), although peaks for sulfur, chlorine and phosphorous are evident, most likely due to inefficient washing of the TEM grid in attempts to remove excess salts from the sol. SAED confirmed the presence of nanocrystalline silver (Fig 7c) with corresponding d-spacings (Fig. 7d).

A

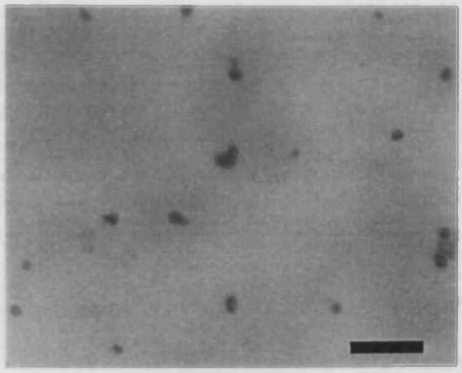

B

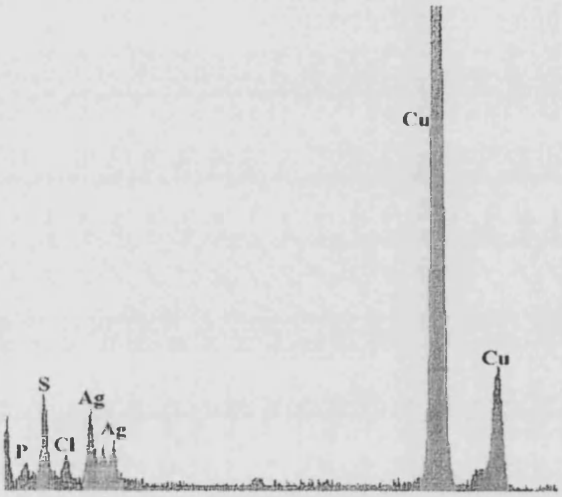

C

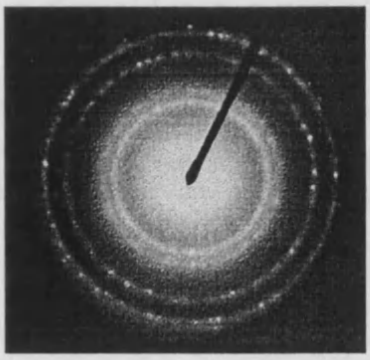

D

D-Spacings for silver (nm)	D-Spacings for silver colloid (nm)
2.35	2.35
2.04	2.00
1.44	1.45
1.23	1.20

Figure 7 a) TEM micrograph of silver colloid. Scale bar 20nm b) EDXA of silver colloid c) SAED pattern of silver colloid d) Table comparing d-spacings for silver and silver colloid.

5.3.2 Conjugation of Antibodies to Colloids

The conjugation procedures, described in section 5.2, were undertaken to produce antibody/gold particle complexes that would allow the antigen binding pocket to remain accessible to the antigen. Immunological conjugation procedures were followed, in an attempt to conjugate antibodies to gold and silver nanoparticles, allowing three protocols

(described in section 5.3.3) to be employed in the fabrication of both mono and bimetallic aggregates of gold and silver.

Anti-DNP IgE antibodies were attached to 12nm-sized gold nanoparticles, as described in section 4.2. The resulting antibody/gold colloid solution remained a claret red colour which, unlike the non-conjugated (citrate-coated) colloid, was stable for months and revealed no precipitate, even when exposed to light during that period. The addition of a 10% solution of NaCl to the non-conjugated gold colloid resulted in the red to blue colour change then, on standing for several hours, a black precipitate was observed. This sensitivity of the gold colloid to ionic strength and the accompanying colour change (a result of the increase in particle size), were utilised to ascertain the minimum amount of antibody needed to stabilise the colloid against NaCl induced aggregation. This was established by performing an antibody titration experiment, outlined in Table 1, where the antibody concentration is 40μg/ml.

Well number	Antibody (μl)	Au Colloid (μl)	Buffer (μl)	NaCl (μl)
A1	1	0.1	199	50
A2	2	0.1	198	50
A3	4	0.1	196	50
A4	6	0.1	194	50
A5	8	0.1	192	50
A6	10	0.1	190	50
A7	15	0.1	185	50
A8	20	0.1	180	50
A9	25	0.1	175	50
A10	50	0.1	150	50
A11	75	0.1	125	50
A12	100	0.1	100	50
A13	125	0.1	75	50
A14	150	0.1	50	50
A15	175	0.1	25	50
A16	200	0.1	0	50
D1	0	0.1	200	0
D2	0	0.1	150	50

Table 1 Shows the volumes of antibody used in the antibody conjugation titration experiment.

The titration was performed in a micro-titre dish and the results can be seen in Fig. 8. The first photograph shows the result of the titration immediately upon completion of the experiment, the second photograph shows the same micro-titre dish, 24 hours later. Wells D1 and D2 are the control samples, showing gold colloid and gold colloid with a 10% NaCl solution added respectively. The colour change upon addition of salt to the gold colloid, from red to blue, can clearly be seen when comparing these control samples.

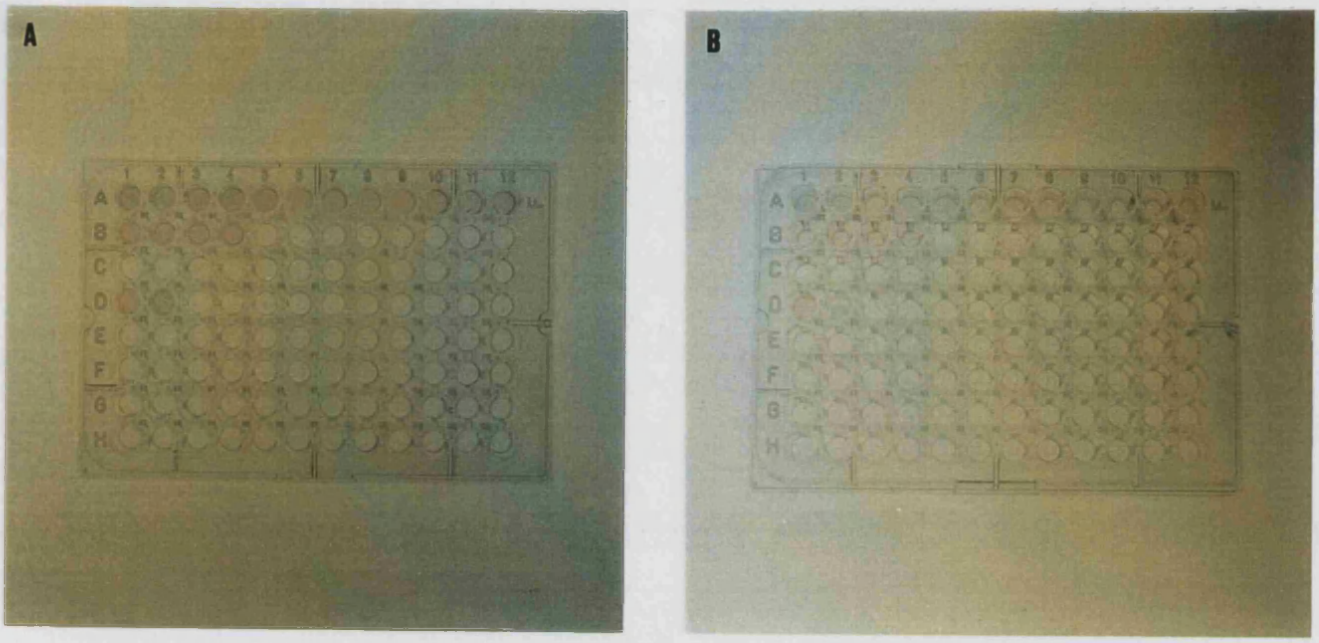

Figure 8 A) Shows the results of the antibody (Anti-DNP) titration experiment after several hours. Wells D1 and D2 are the controls B) Shows the same micro-titre dish after 24 hours.

The titration demonstrates that the antibody does prevent the aggregation of colloidal particles when a sufficient concentration of antibodies is added to the colloid, inferred from the absence of the red to blue colour change. The minimum amount of antibody necessary for colloidal stabilisation, against the addition of salt, is seen in well A6. This corresponds to 10μl of a 40μg/ml solution of antibodies in borax buffer, giving a concentration of 1.33μg/ml of Anti-DNP antibodies. It should be noted that wells A3,4 and 5 initially show a purple colouration, suggesting that the protein interacts with the colloidal particles in such a way to inhibit NaCl induced aggregation. After 24 hours a blue colouration develops in these wells, implying the concentration of protein to be insufficient to prevent the aggregation of the gold particles with respect to time. Identical

titration experiments, substituting the Anti-DNP IgE antibody with the same concentration of Anti-biotin IgG antibody, produced identical results.

The stabilisation of colloidal gold particles against NaCl by conjugation of Anti-DNP antibodies was also followed by UV-vis spectroscopy. An absorbance profile of the gold sol added to borax buffer is shown in Fig. 9a.

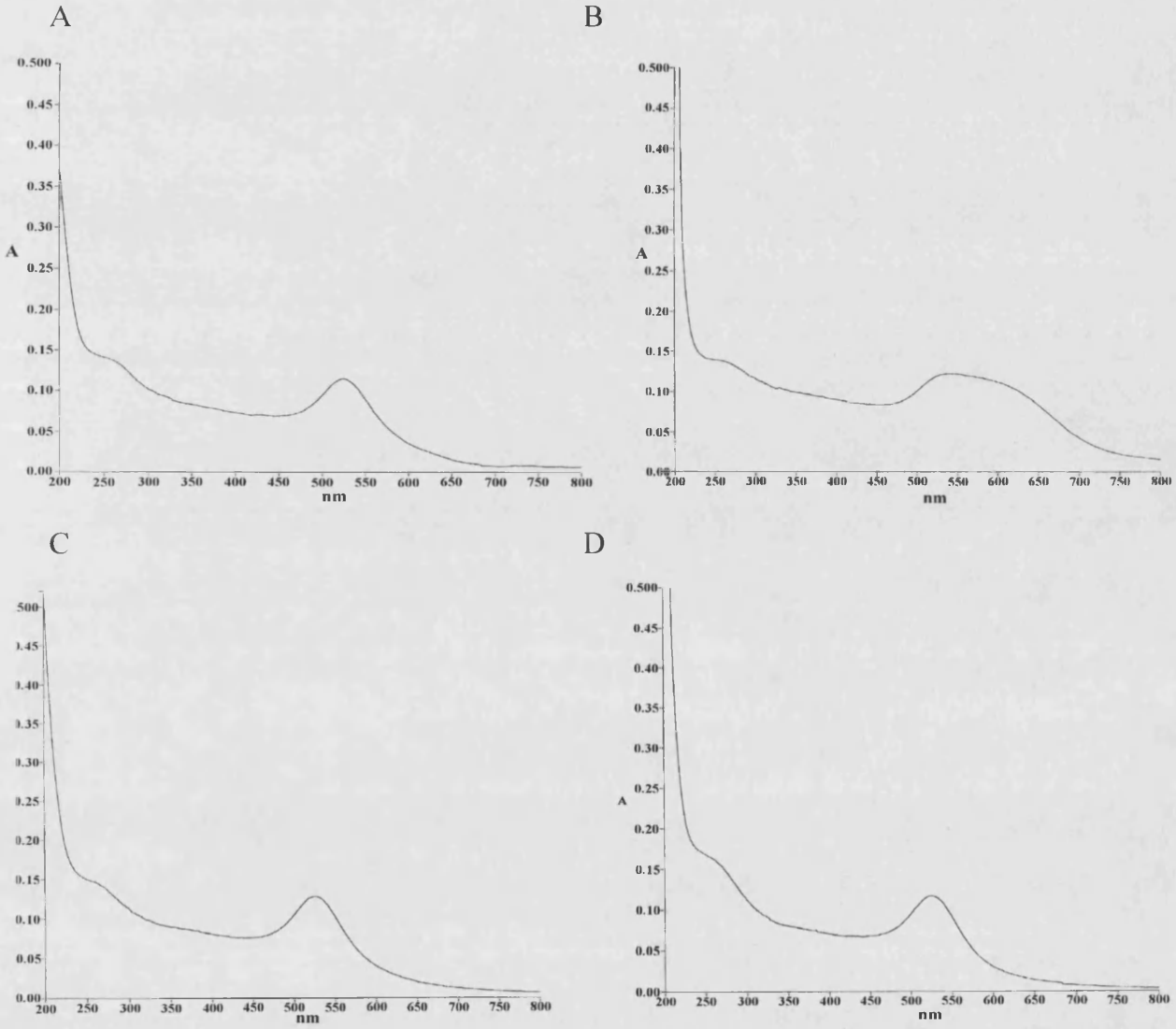

Figure 9 A) Au colloid in borax buffer B) Au colloid in borax buffer with 10% aqueous NaCl C) Antibody conjugated Au colloid D) Antibody conjugated Au colloid and 10% aqueous NaCl.

The spectrum clearly shows the characteristic absorbance peak at approximately 530nm for a gold colloid. The additional peak seen at around 260nm is a contribution from the buffer used. The addition of a 10% aqueous NaCl solution to this colloid immediately induces a red to blue colour change and the corresponding absorbance spectrum is shown

in Fig. 9b. This spectrum shows a much broader peak, indicative of the increase in absorbance associated with the increase in gold particle size.

The addition of the minimum concentration of Anti-DNP antibodies found in the titration experiment, necessary to prevent NaCl induced colloidal aggregation, gave the absorbance profile shown in Fig. 9c. The peak seen at 260nm now becomes slightly broader due to the presence of protein. Addition of the same volume of aqueous NaCl to this conjugated colloid did not induce a colour change in the colloid, which remained red. The corresponding absorbance spectrum is seen in Fig. 9d. This spectrum is almost identical to that for the conjugated gold colloid in Fig. 9c, showing no broadening of the peak at 530nm. It should be noted that when the Anti-biotin IgG antibody was substituted for the Anti-DNP IgE antibody, exactly the same absorbance profiles were obtained, with respect to the addition of NaCl.

The addition of salt to the antibody conjugated gold colloids resulted in a system that was stable to the addition of salt. TEM micrographs showed discrete Au nanoparticles of uniform size distribution, which were well-separated when air-dried onto the TEM support film (Fig. 10a). This differs from the unconjugated gold colloid which, when dried down onto a TEM grid, displays a greater degree of 'necking' of colloidal particles, where adjacent particle appear joined (Fig. 10b).

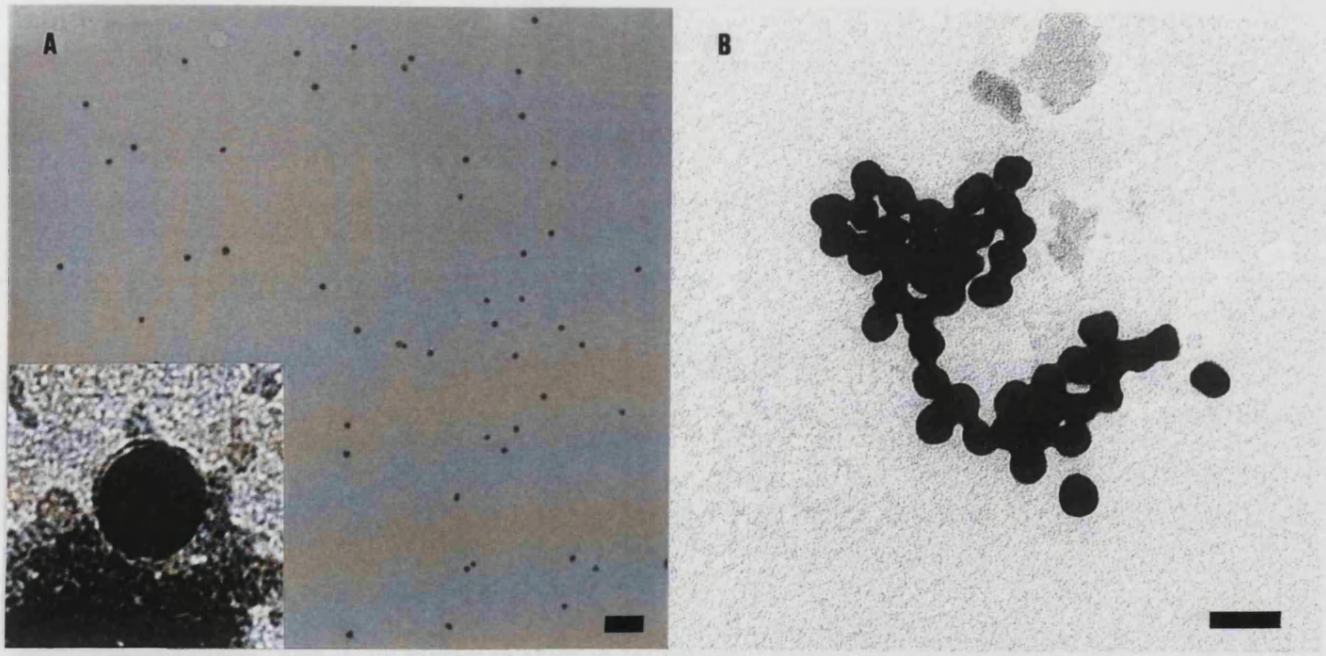

Figure 10 A) TEM micrograph of the antibody conjugated gold colloid, scale bar 50nm. Inset shows the appearance of a layer around each particle upon staining. B) TEM micrograph of colloidal gold particles without conjugated antibodies, showing the 'necking' effect upon drying, scale bar 20nm.

Antibody conjugated gold particles invariably were separated by a gap of several nanometers. This suggests the conjugated antibodies prevent the 'necking' of particles due to coverage of each particle by protein. Staining of the antibody conjugated gold colloid revealed the presence of a grey layer around each particle (Fig. 10a, inset).

Both the titration and the UV-vis absorbance spectra suggest that the conjugation of antibodies to a gold colloid prevents the colloidal aggregation seen in an unconjugated colloid upon salt addition. It has been suggested[28] that the mode of interaction between the gold particles and antibodies is a result of a combination of three separate, but dependent phenomena. These are electrostatic, between the negatively charged gold particle and the positively charged protein, hydrophobic interactions, between the antibody and the surface of the gold and dative binding, between the electrons of the gold atoms and the numerous sulfur atoms of the protein. Thus, this suggests that the conjugation procedure, to determine the minimum concentration of antibodies able to prevent aggregation, results in coverage of the colloidal particles with protein. These antibody covered gold particles are then prevented from 'ripening' due to increased ionic strength, as the counter ions responsible for the aggregation of colloidal particles in solution are unable to render particles in close proximity, a necessity for particle growth to occur.

The conjugation of antibodies to colloidal silver particles followed a similar procedure to the conjugation of gold particles although the production of a stable silver colloid, with a narrow particle size distribution, proved a more difficult task than for the gold colloid. The reaction of the colloid to the addition salt was followed with UV-vis spectroscopy, shown in Fig. 11a. The spectra shown in Fig. 11 show the effect of NaCl on the absorbance profile of the silver colloid and the effect of antibody conjugation. The absorbance profile numbered 1, in spectrum A, is that for the native silver colloid in buffer, whereas spectrum 2 shows the absorbance of the same volume of silver colloid with added NaCl, demonstrating a broader absorbance profile. Examination of the silver colloid, several hours after the addition of the NaCl revealed a transparent solution containing a black precipitate on the floor of the cuvette. The silver colloid without salt remained the same yellow/green colour.

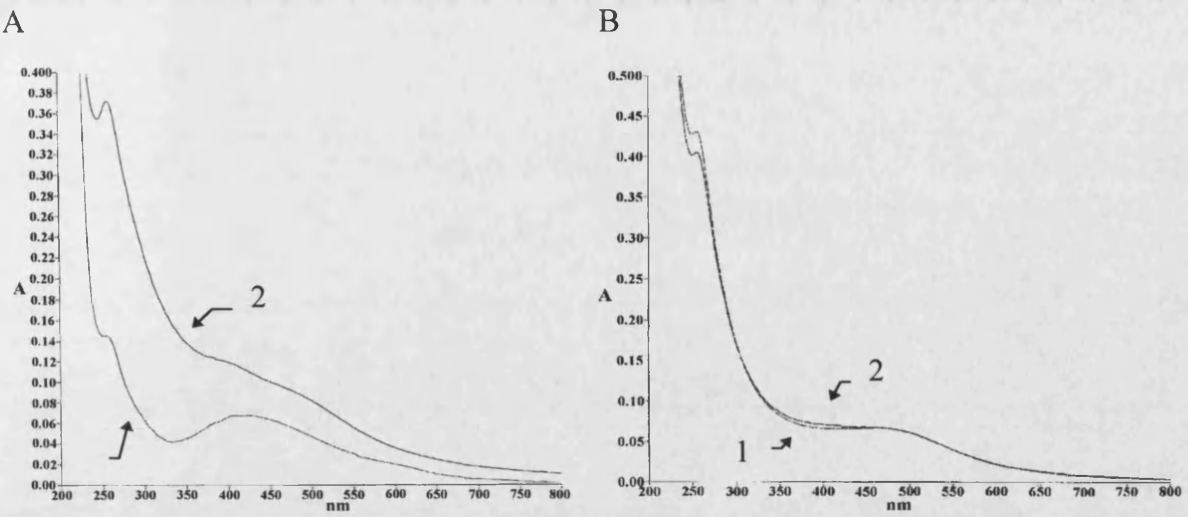

Figure 11 A) Ultraviolet absorbance spectrum showing the effect of adding salt to the silver colloid. Spectrum 1 shows the silver colloid in buffer and spectrum 2 shows the absorbance profile after the addition of 10% aqueous NaCl. B) Shows the effect of antibody conjugation upon adding 10% aqueous NaCl, spectrum 1 shows profile after 10mins and spectrum 2 after 12 hours.

The conjugation of antibodies to the silver colloid was investigated with UV-vis spectroscopy, employing a similar protocol to that of the gold-antibody conjugates. The conjugation of Anti-biotin IgG to the silver particles was performed at a lower pH and was performed in the dark, due to the suspected increase in the sensitivity of the silver colloid to UV light. The same antibody concentration found for the gold conjugation protocol was used, as it was decided that a comparable quantitative titration to establish minimum antibody concentration, would not yield analogous results. This was decided as there was no associated colour transition, upon addition of salt, and also the large particle distribution size negated the use of a semi-quantitative protocol. Upon addition of NaCl, the UV absorbance spectrum (1) was obtained (Fig 11b). The spectrum was again recorded after 12 hours to observe any change in absorbance, which might be indicative of colloidal particle ripening, this is recorded as 2 in Fig.11.

These data suggest the conjugation of Anti-biotin IgG antibodies to the colloidal silver particles was successful in inhibiting NaCl induced colloidal aggregation. Fig 11b demonstrates that the broad peak, associated with salt induced colloidal ripening, was not evident and that the sharp absorbance profile did not change significantly with respect to time. Comparison of A and B does reveal that the conjugation of antibodies to the silver colloid did appear to alter the absorbance profile of the colloid. It should be noted that

Fig. 10b does reveal a slight difference in the absorbance characteristic of the Anti-biotin conjugated silver colloid after 12 hours. This could be accounted for by the presence of the much smaller colloidal silver particles. These particles are smaller than the antibodies and so an increase in ionic strength would enable them to coalesce, forming much larger silver particles, as the protein would not inhibit this process.

5.3.3 Antigen Synthesis

Both the homo-janus antigen and the hetero-janus were characterised by FAB mass spectrometry, NMR and FTIR, to confirm the predicted structures of the synthesised antigens.

Homo-Janus Antigen

I) Fast Atom Bombardment (FAB)Mass Spectrometry

FAB mass spectrometry was performed on a small sample of the synthesised homo-janus antigen to verify the molecular weight of the molecule. The spectrum obtained is shown in Fig. 12.

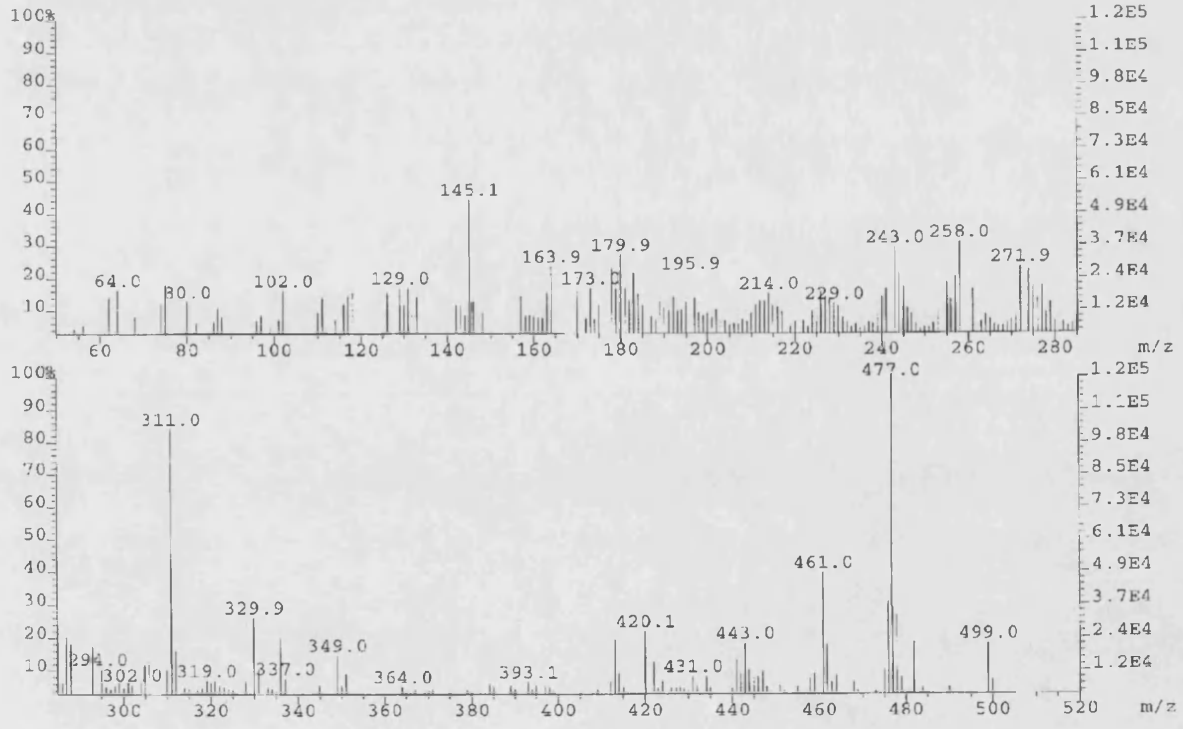

Figure 12 FAB mass spectrogram showing the fragmentation pattern of the homo-janus antigen.

Analysis of the fragmentation pattern obtained in Fig. 12 reveals the largest m/z ratio to correspond to a molecular weight of 477. Considerations of the molecular structure of the homo-janus antigen (Fig. 13) indicates that this corresponds exactly to the expected molecular ion of the homo-janus antigen ($C_{20}H_{24}N_6O_8$, *bis*-N-2,4-dinitrophenyl octamethylenediamine, mp 205°C, Mr 476).

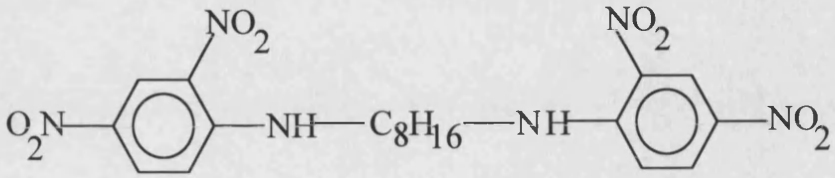

Figure 13 Diagrammatic representation of the homo-janus antigen consisting of two dinitrophenyl groups separated by a 10 atom spacer arm.

The next biggest peak seen in the spectrum shows a molecular weight of 311. This would concur with molecular fragments in which one of the dinitrophenyl groups has been lost. The majority of the other peaks represent less significant smaller fragments.

II) Fourier Transform Infrared Spectroscopy (FTIR)

FTIR spectroscopy was performed on the homo-janus antigen to verify the presence of certain chemical groups. The spectrum obtained for a mull of the homo-janus sample is shown in Fig. 14.

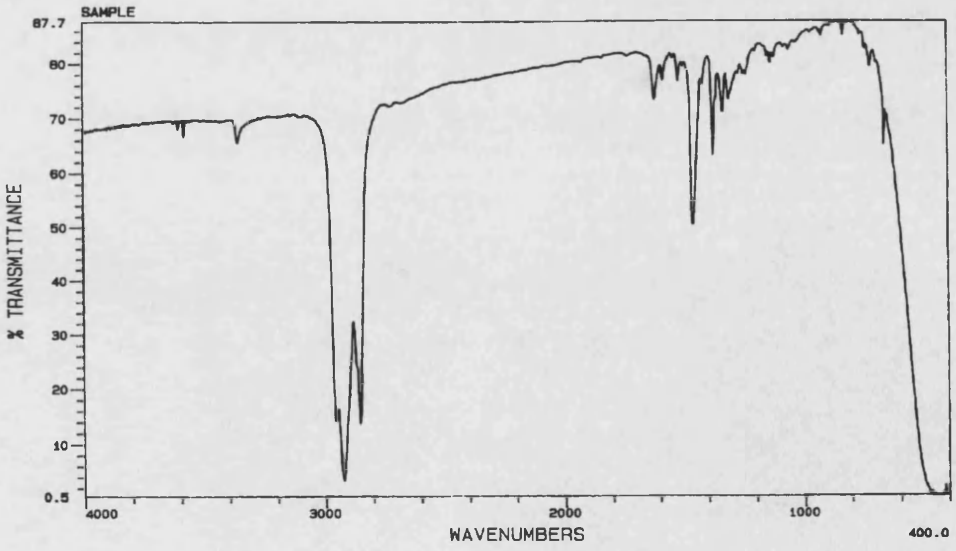

Figure 14 FTIR (NaCl) spectrum obtained for the homo-janus antigen.

There exist peaks corresponding to the nitrogen substituents, 1290cm^{-1}(NH bend) and 3400cm-1 (NH stretch). The strong peak at 1550-1510cm^{-1} corresponds to the NO aryl antisymmetric stretch of the dinitrophenyl groups.

III) ^{1}H NMR

The synthesis of the homo-janus antigen involved the nucleophilic substitution of 2,4-dinitrofluorine with 1,8-diaminooctane, resulting in the double headed DNP molecule seen in Fig. 13. The spectra seen in Fig. 15 compare ^{1}H NMR data obtained for 1,8-diaminooctane (A) and the homo-janus antigen (B).

A.

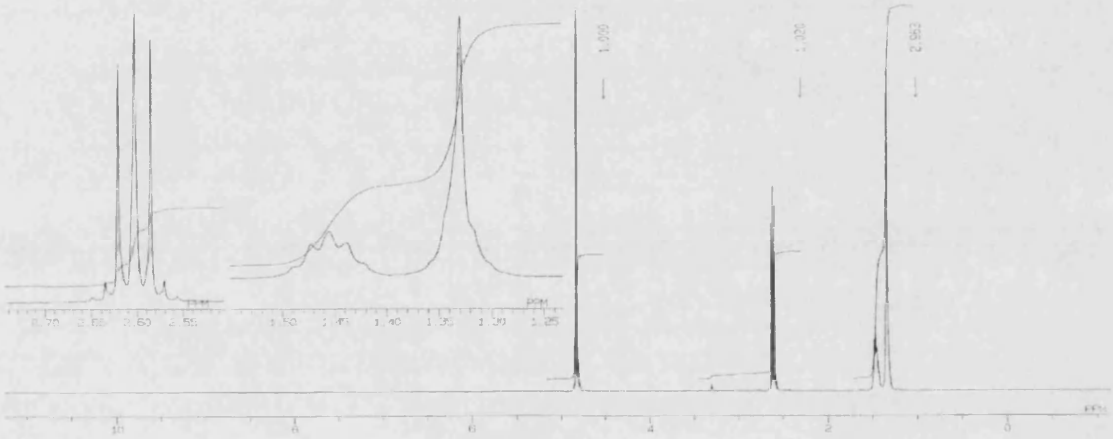

B.

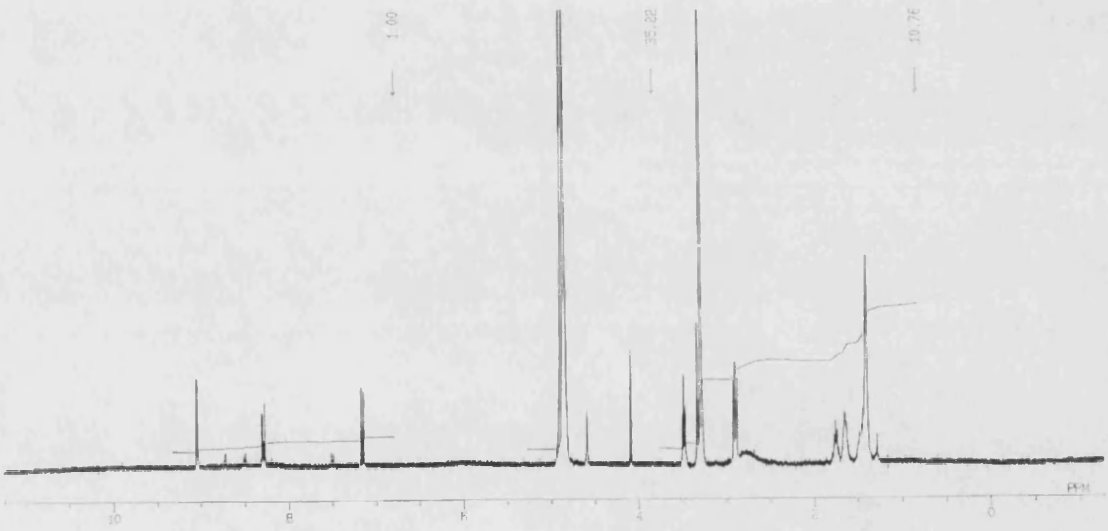

Figure 15 A) NMR spectrum for 1,8-diaminooctane B) NMR spectrum obtained for the homo-janus antigen. Both samples were analysed using deuterated methanol.

Figure 15b gives the chemical shifts 7.0-9.5 (m, 6H, ArH), 4.9 (s, 4H, CH), 3.4 (m, 2H, CH), 1.8 (s, 12H, CH). The presence of the aromatic protons gives a clear indication that the coupling of the dinitrophenyl groups to 1,8-diaminooctane (Fig. 15a) was successful.

The mass spectrometry, FTIR and NMR spectra confirm the synthesis of the homo-janus antigen to have been successful, resulting in the double headed DNP structure seen in Fig. 13.

Hetero-Janus Antigen

I) Fast Atom Bombardment (FAB)Mass Spectrometry

FAB mass spectrometry was performed on a small sample of the synthesised hetero-janus antigen to verify the molecular weight of the molecule. The spectrum obtained is shown in Fig. 16. Analysis of the fragmentation pattern obtained reveals the largest m/z ratio to correspond to a molecular weight of 652.1. Considerations of the molecular structure of the hetero-janus antigen (Fig. 17) indicates that this corresponds almost exactly to the expected molecular ion of the hetero-janus antigen ($C_{28}H_{41}N_7O_9S$, Mr 651). The spectrum shows the fragmentation to be dominated by the molecular ion, the remainder of the peaks representing very small fragments.

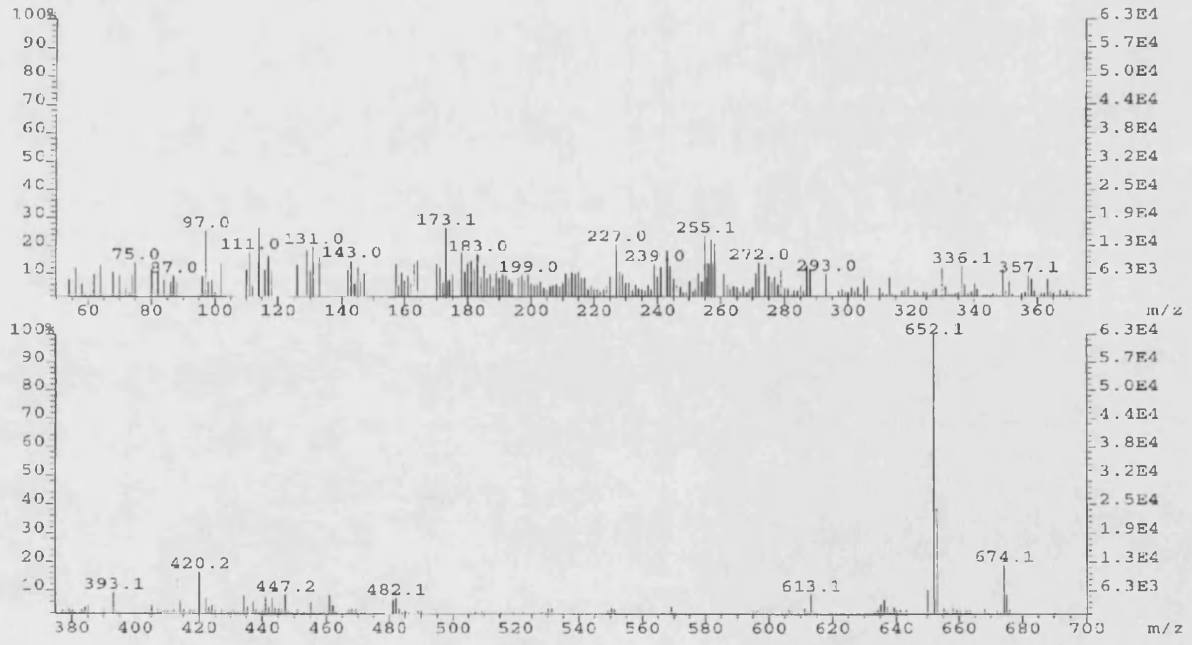

Figure 16 FAB mass spectrogram of the hetero-janus antigen.

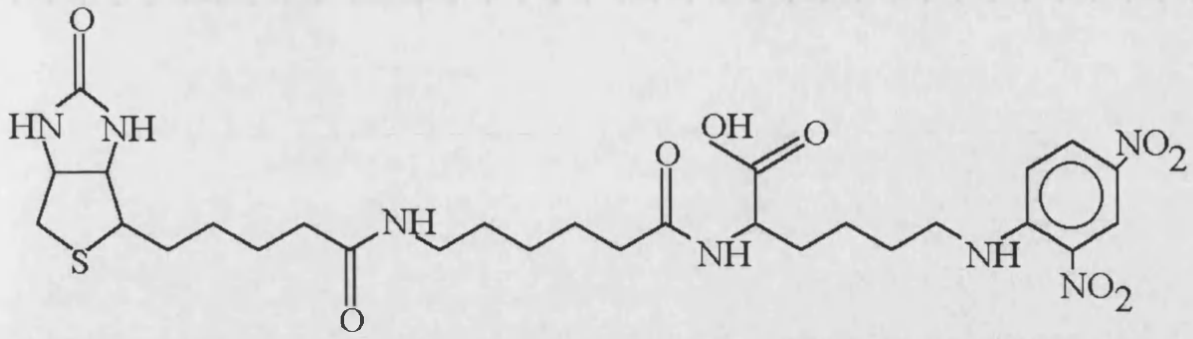

Figure 17 Diagrammatic representation of the hetero-janus antigen consisting of dinitrophenyl and biotin groups separated by a 20 atom spacer arm.

II) Fourier Transform Infrared Spectroscopy (FTIR)

FTIR was performed on the homo-janus antigen to verify the presence of certain chemical groups. The spectrum obtained for a mull of the hetero-janus sample is

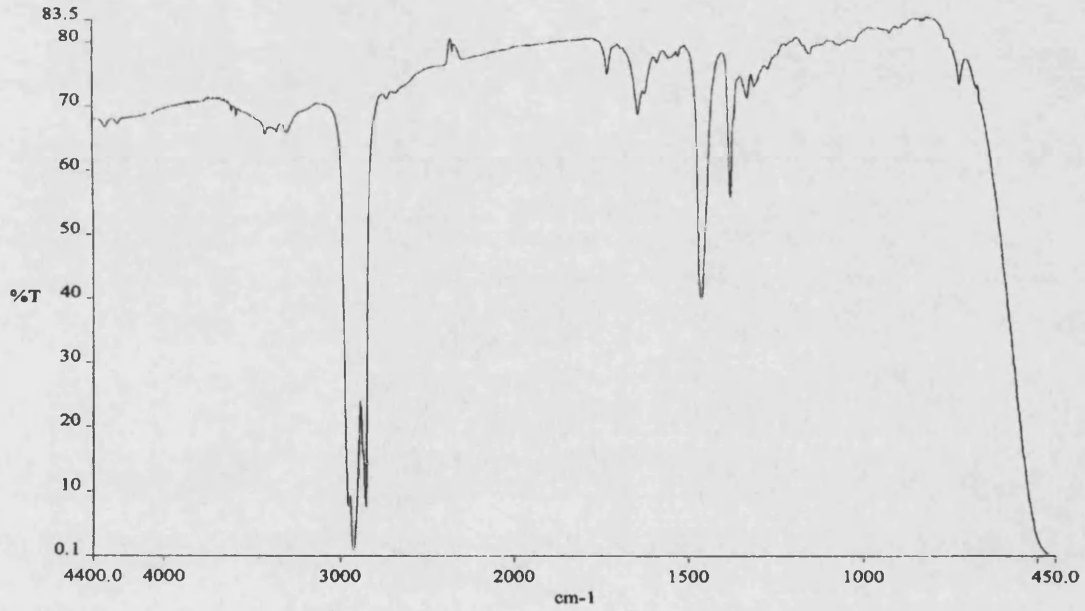

Figure 18 FTIR spectrum obtained for the hetero-janus antigen.

shown in Fig. 18. Several prominent peaks are seen corresponding to the substituent chemical groups of the hetero-janus antigen. A characteristic group of the hetero-janus antigen is the presence of the amide bond seen as several peaks, 3350-3100cm^{-1} (amide H-bonded) and 1650-1620cm^{-1}(secondary amide). There are also peaks corresponding to the nitrogen substituents, 1290cm^{-1}(NH bend). The peak corresponding to the carboxylic acid comprises the 3000-2500cm^{-1}(OH stretch, broad) and 1725-1700cm^{-1}(CO stretch,

strong). The strong peak at 1550-1510cm^{-1} corresponds to the NO aryl antisymmetric stretch of the dinitrophenyl groups.

III) ^{1}H NMR

The synthesis of the hetero-janus antigen involved the coupling of the long arm biotin (sodium sulfosuccinimidyl-6-biotinamidohexanoate, Vector labs), Fig.19, to DNP-lysine, through coupling to the primary amine of the amino acid.

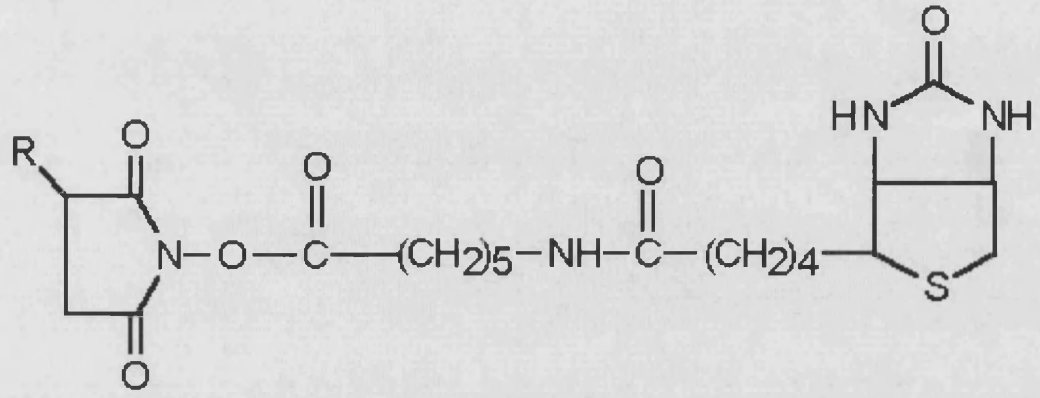

Figure 19 Structure of the 'long arm' biotin used in the synthesis of the hetero-janus antigen.

The use of the long arm biotin was deemed essential in the synthesis of the hetero-janus antigen. Thus ^{1}H NMR of this compound was first compared to an NMR spectrum for (+)-Biotin[29] in DMSO-d_3 (Fig. 20a). ^{1}H NMR obtained for the long arm biotin in methyl-d_3 alcohol (CD_3OD, Aldrich) is shown in Fig. 20b. Comparison of these spectra, despite the different solvents employed, show the characteristic profile of the biotin moiety of the long arm biotin molecule.

A

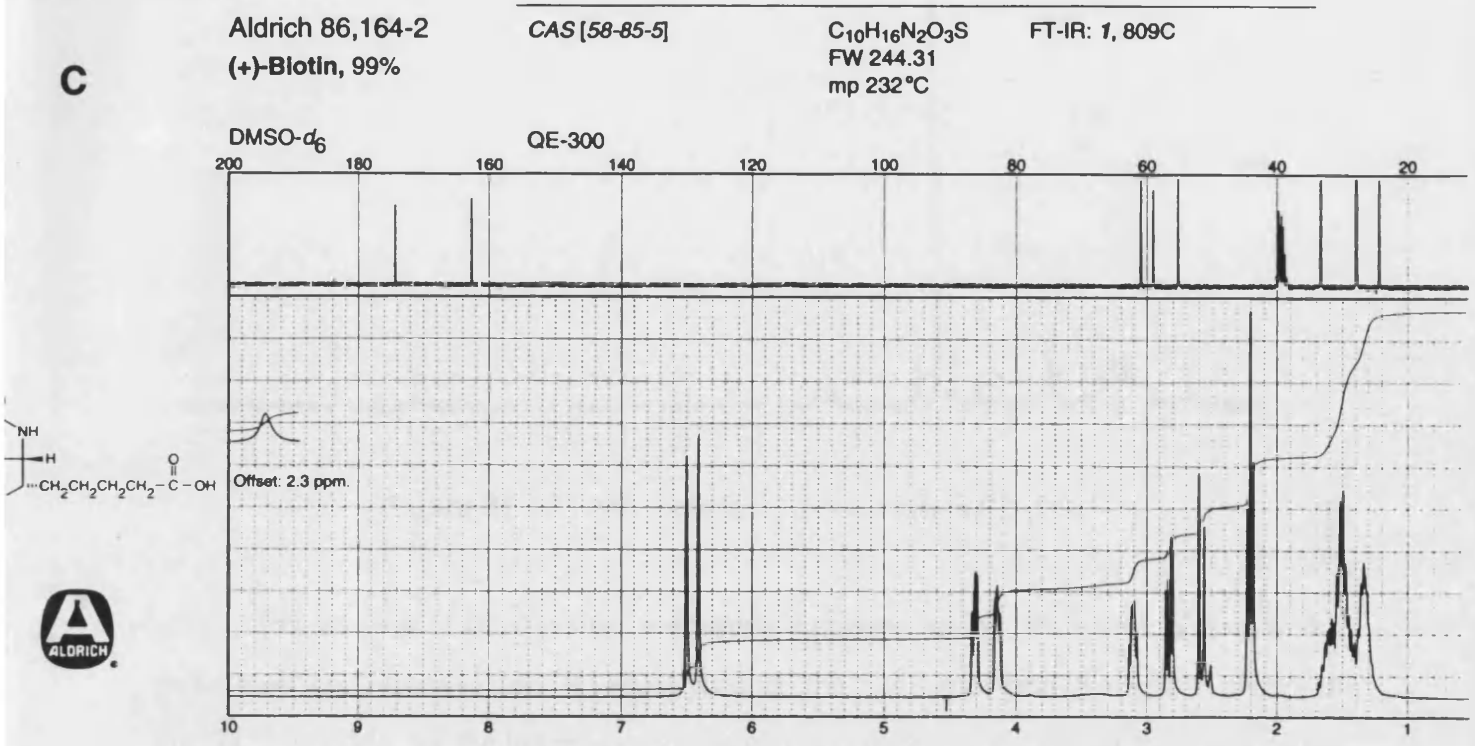

B

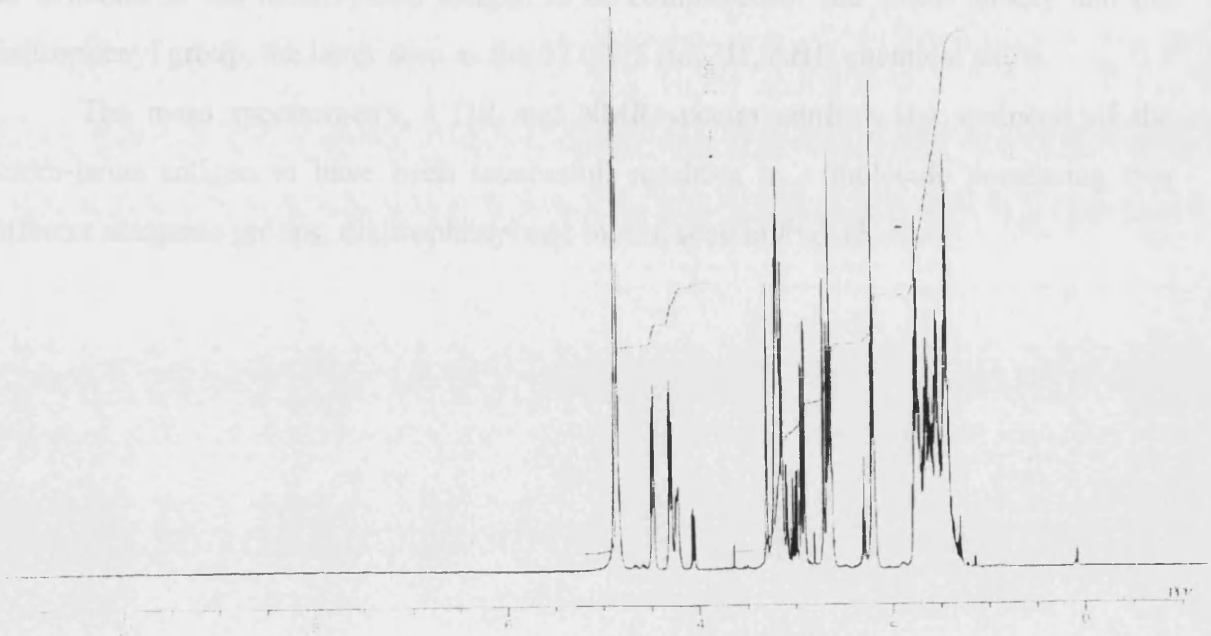

Figure 20 A) NMR spectrum from Aldrich book[30] for (+)-Biotin in DMSO-d_6. B) NMR spectrum obtained for long arm biotin in CD_3OD.

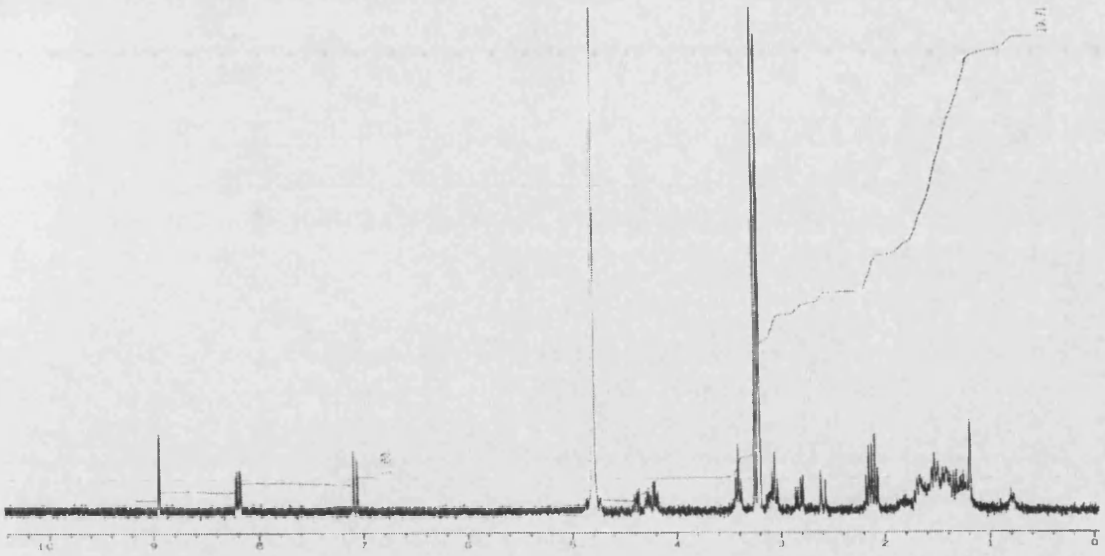

Figure 21 ^{1}H NMR for hetero-janus antigen in CD_3OD.

The reaction of DNP-lysine, possessing a primary amine, with the long arm biotin under basic conditions yielded a yellow product, the NMR spectrum of which is shown in Fig. 21. The NMR for the hetero-janus antigen is noisy due to the partial solubility of the product in the solvent chosen. A number of deuterated solvents were used, although the expense of the materials dictated that a compromise should be reached in which all samples were soluble to the maximum degree. Comparison of Fig. 21 to Fig. 22 confirms the structure of the hetero-janus antigen to be comprised of the biotin moiety and the dinitrophenyl group, the latter seen as the δ7.0-9.5 (m, 3H, ArH) chemical shifts.

The mass spectrometry, FTIR and NMR spectra confirm the synthesis of the hetero-janus antigen to have been successful, resulting in a molecule possessing two different antigenic groups, dinitrophenyl and biotin, seen in Fig. 15.

5.3.4 Fabrication of Self-Assembled Macroscopic Mono- and Bi-metallic Materials.

I) Homo-Janus Induced Self-Assembly of Gold Particles.

The effect of the addition of synthesised 'homo-janus' antigens, possessing two dinitrophenyl groups separated by an eight carbon spacer, to Anti-DNP antibody conjugated gold particles was followed by UV-vis spectroscopy (Fig. 22). The spectra obtained compare two experiments, namely a control sample, consisting of a solution of gold colloid with conjugated anti-DNP antibodies in a saline borax buffer, and a solution of exactly the same composition, but to which the homo-janus antigen was added. The spectra show the change in absorbance of the system as a function of time.

The results obtained from the control sample clearly demonstrate the stability of the gold colloid, due to the same absorbance being recorded over the duration of the experiment. In contrast, the addition of the homo-janus antigen to the solution perturbs the system, resulting in a spectrum of increasing then decreasing absorbance. There is also an initial sharp increase in absorbance, probably due to the addition of the choromphoric homo-janus compound. This is quickly followed by an equally sharp fall in absorbance.

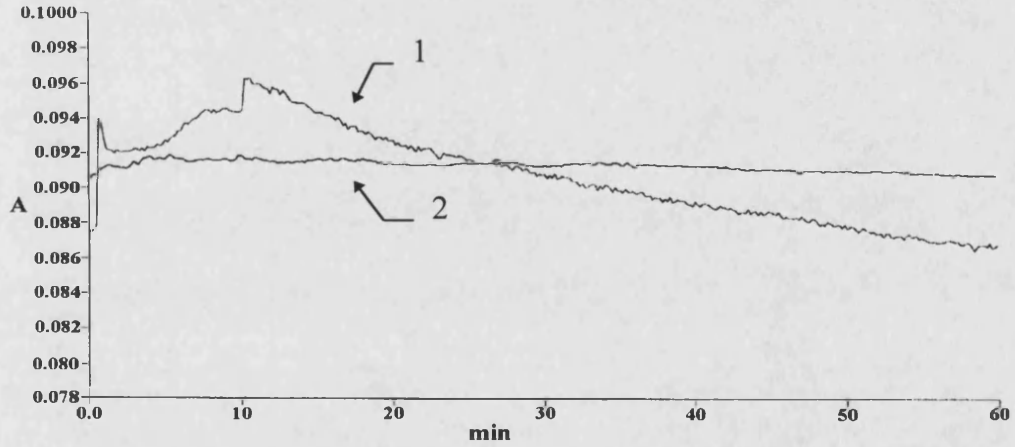

Figure 22 Spectra (560λ) showing the change in absorbance over time of an antibody conjugated gold colloid to which the homo-janus antigen has been added (1). The control consists of a sample of identical constitution, without the addition of the homo-janus antigen (2).

This could indicate that the initial recognition of the antigen by the conjugated antibodies, possessing a high degree of affinity for the antigen, is a very fast process, contributing to the fall in absorbance. The spectrum then demonstrates a steady increase in the

absorbance of the system over a period of time, which peaks at around 10-12mins. The trend then displays a gradual fall in absorbance, eventually falling below the initial absorbance and below that recorded for the control. This effect may be explained by the formation of larger aggregates over time. The formation of larger aggregates will be more difficult, due to effect of shear forces upon the antigen recognition growth mechanism, this would explain the gradual increase in absorbance. This effect peaks then gravity would tend to sediment the large aggregates, resulting in a gradual fall in absorbance, to a point where its falls below the absorbance found at the start of the experiment. On examination of the cuvettes after 24 hours, an absorbance of approximately 0.06 was recorded, together with the observation that the bottom of the cuvette was now lined with a purple precipitate. These data suggest the formation of these aggregates to have continued over the extended time period, to an extent where a large proportion of the colloidal particles had precipitated out of solution, accompanied by a colour change from red to pink. No such transformations were observed in the control sample which remained red, with no precipitate.

These data suggest that the addition of the homo-janus antigen to a sample containing colloidal gold particles conjugated with Anti-DNP antibodies results in an increase in absorption. This may be explained by assuming the cross-linking of the conjugated colloidal particles by the antigen introduced to the sample, resulting in aggregates of colloidal particles and a subsequent increase in absorption. This process then proceeds in stages, eventually leading to a fall in absorbance, below that recorded for the colloid, and the emergence of a macroscopic purple precipitate.

This experiment was repeated on a smaller scale, in eppendorf tubes, to ascertain the nature of the precipitate. In a typical experiment, 0.1ml of the Anti-DNP conjugated gold particles were mixed with 30μl of a 10% NaCl solution and 15μl of a supersaturated aqueous homo-janus solution then added. The tube was warmed then incubated at 4°C for 4 hours, after which large purple precipitates were observed, which were transferred to a TEM grid for analysis. The grids were washed several times in distilled water and blotted before analysis. TEM micrographs of the grid revealed the purple precipitate to be comprised of aggregates of individual gold particles (Fig. 23). A range of aggregate sizes was observed, from small clusters comprising relatively few particles (Fig. 23a) to much

larger aggregates of hundreds of particles (Fig. 23b).The micrographs clearly show that each of these clusters have individual particles separated by a gap of several nanometers, with far fewer instances of the fused colloidal particles associated with unconjugated colloid (Fig. 10b). The micrographs in Figs 23b,c and d also show evidence of particle stacking and Fig. 23b also reveals a linear mode of self assembly, in the form of chains of individual particles.

These data suggest that the initial hypothesis of the homo-janus antigen being able to cross link the antibody conjugated gold particles is substantiated. The control sample remained stable for many months, exhibiting no precipitate, whereas the addition of the homo-janus antigen resulted in the formation of a purple macroscopic precipitate. TEM analysis of this precipitate revealed it to be comprised of hundreds of individual colloidal gold particles. These precipitates display motifs not seen in close packed colloidal particles dried onto TEM grids, such as three dimensional particle stacking and chains of individual gold particles.

An insight into the nature of the self assembly process is also revealed by Fig. 23b, which shows a large aggregate to be comprised of a linear motif of linked particles forming short chains. This phenomenon may be due to the nature of the binding of antibodies to colloidal particles. The bond between protein and colloid is strong, resulting from Van der Waals, ionic attraction and dative binding between the numerous cystienes and methionines of the antibody to the colloidal particle. It is reasoned that each colloidal particle possesses a number of antibodies adsorbed onto the surface, resulting in a complete coverage of the particle. Many antigen binding pockets will lie tangentially to the spherical surface. Consequently, upon binding of another particle, steric and repulsive forces play a greater role in further aggregation, resulting in the binding sites at opposing ends of this two particle aggregate having lower free energies, facilitating the formation of particle chains. The binding of particles to form three dimensional aggregates does occur, as seen in TEM, but is kinetically slower. It is reasoned that the process is reversible due to the nature of the antibody-antigen interaction, but further work is necessary to validate this assumption.

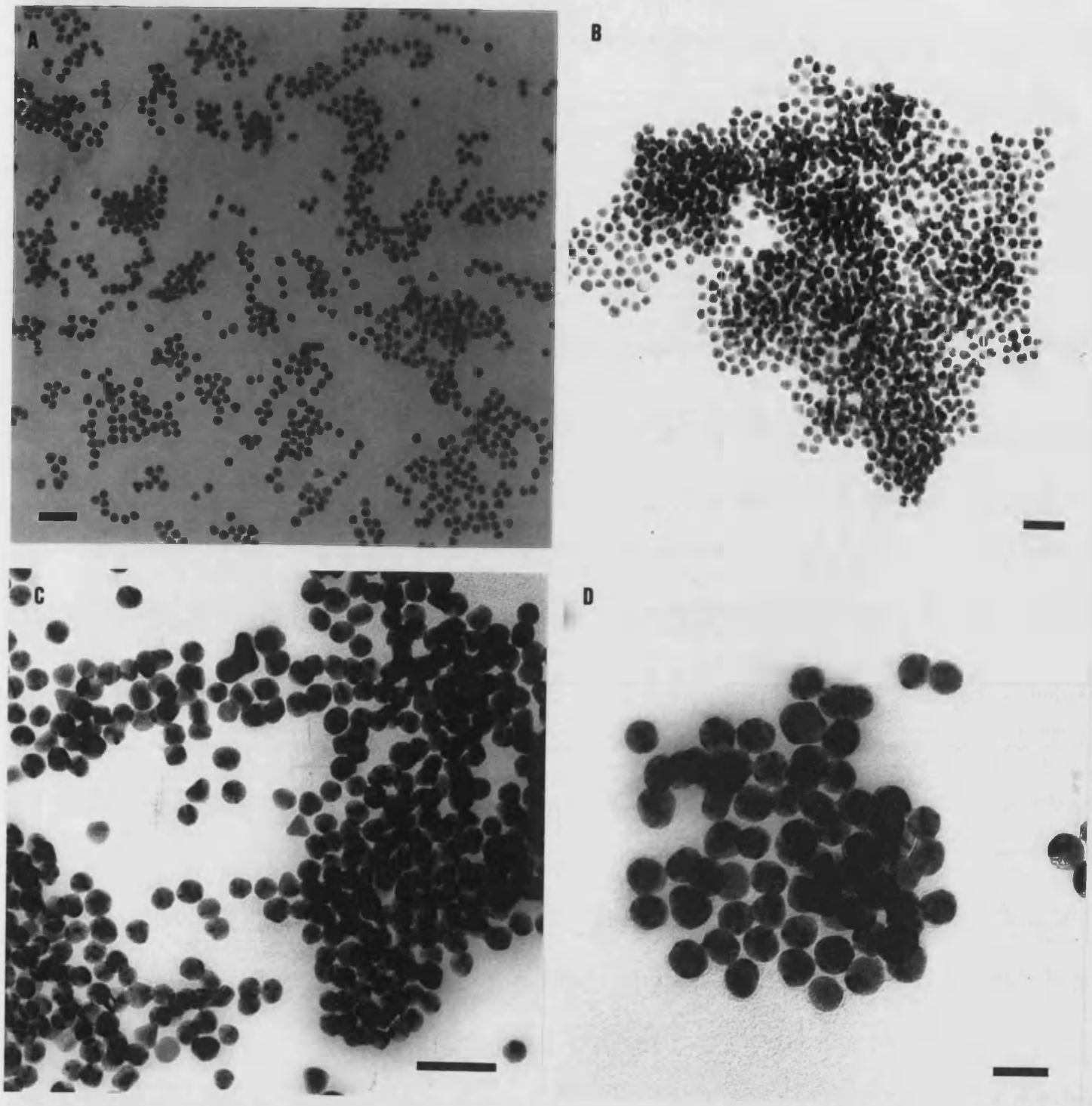

Figure 23 A) TEM showing small self assembled colloidal particle clusters found upon addition of the homo-janus antigen to a solution of antibody conjugated colloidal gold particles. Scale bar, 50nm B) A large self assembled cluster of gold nanoparticles, displaying motifs of self assembly, such as particle stacking and chains of particles. Scale bar, 50nm. C) and D) Higher resolution images of clusters, detailing the dense stacks of particles from the self assembly process. On comparison to the native colloid it can be seen that a gap separates the majority of particles. Scale bar 20nm.

II) Hetero-Janus Induced Self Assembly of Gold Particles

A similar protocol was followed, to that detailed in the previous section, in an attempt to form gold aggregates using the 'hetero-janus' antigen. Two different antibodies were used to prepare Au sols consisting of nanoparticles with surface-attached proteins of either Anti-DNP IgE or Anti-biotin IgG, both of which were stable in saline buffer for several months. The change in absorbance upon addition of the hetero-janus antigen, to a solution containing a 1:1 ratio of Au nanoparticles coated with Anti-DNP

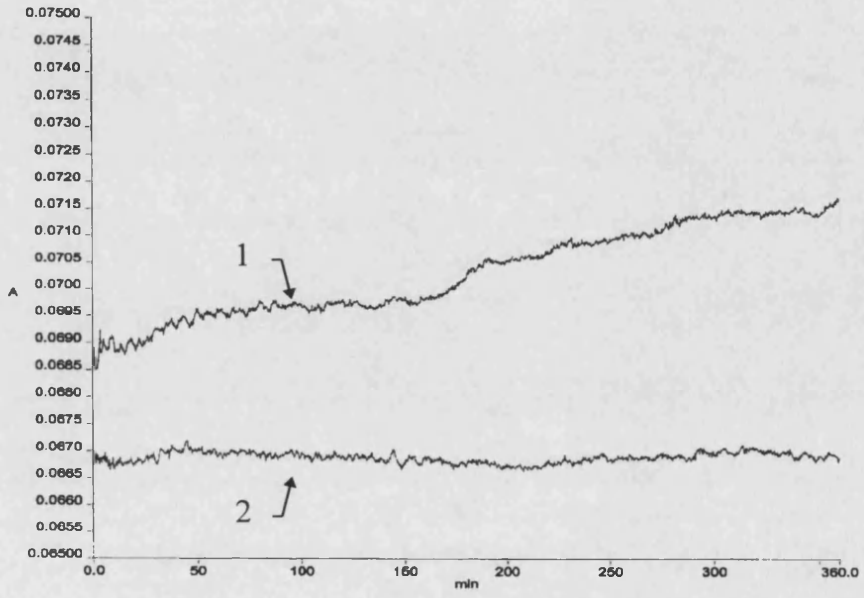

Figure 24 Time course (560λ) showing the change in absorbance, with respect to time, of a 1:1 mixture of Anti-DNP and Anti-biotin conjugated Au colloids, to which the hetero-janus antigen is added (1). The spectrum marked 2 is the control, to which no antigen was added.

IgE or Anti-biotin IgG was followed by UV spectroscopy, for a duration of 6 hours (Fig. 24). The spectrum marked 1 shows the steady increase in absorption of the sample, to which the hetero-janus antigen has been added. In contrast, the spectrum marked 2 is the control sample, with no added antigen, displaying no increase in absorption. Examination of the cuvette, after a duration of 24 hours, revealed small filamentous precipitates. It should be noted that this experiment involved the use of very dilute solutions, due to the scarcity of the products involved. Consequently this graph cannot be compared kinetically to that for the homo-janus experiment (Fig. 22), but does give an indication of the increase in absorbance upon addition of the antigen.

To investigate the nature of the filamentous precipitate formed, the experiment was again repeated, but employing the same concentrations of reactants as for the scaled down homo-janus experiment outlined in the previous subsection. Upon addition of the antigen to the sample and storage at 4°C, a large purple filamentous precipitate was observed in the eppendorf tube after approximately 2 hours, almost half the time recorded for the homo-janus system. This macroscopic precipitate was gauged to be between two and three millimetres long. To determine the nature of this large precipitate and other smaller precipitates, they were transferred to a TEM grid using a pipette and washed in distilled water several times. Low magnification TEM analysis of the grid then revealed large fibrous structures, spanning entire subdivisions of the grid. Subsequent increases in the magnification revealed these filaments to be comprised of thousands of individual colloidal gold particles (Fig. 25). As can be seen from Fig. 25a, the body of the filament is extremely dense and therefore determination of information concerning the structure of the filament was impossible. Consequently, micrographs were taken of the edge of the filament, though incremental magnification steps (Fig. 25b,c and d), to reveal the composition of the linear structure. Some indication of the structural motifs observed for the homo-janus system (Fig. 23b) are seen in Fig. 25d, where short linear chains of colloidal gold particles are seen on the periphery of the filament at high magnification.

A more detailed insight into the nature of the self assembly of this huge macroscopic filamentous structure, comprised of thousands of individual colloidal particles, comes from the discovery of similar fibrous aggregates on the same TEM grid displaying a more open structure, possibly representing an earlier stage of the self assembly process (Fig. 26). Again, increasingly higher magnifications were performed on this filament (Fig. 26a,b and c) and HRTEM images revealed the structure to be comprised of long chains of colloidal gold particles, arranged into seemingly random orientations, resulting in a network of these particle chains (Fig. 26d).

These data suggest that the hetero-janus antigen, added to a buffered solution of a 1:1 mixture of Anti-DNP conjugated and Anti-biotin conjugated colloidal gold particles, results in the directed self assembled of huge filamentous structures.

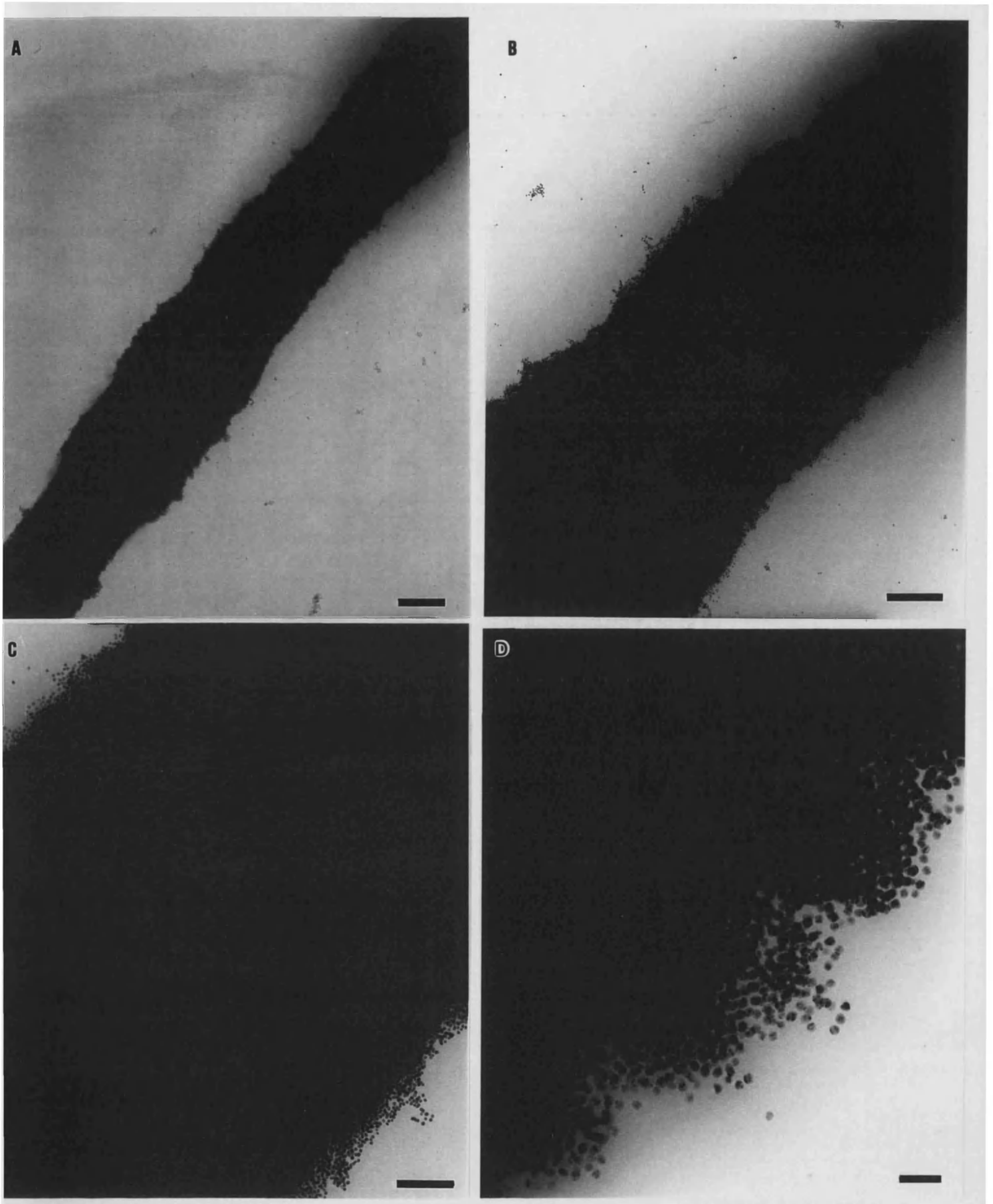

Figure 25 A) TEM micrograph of a hetero-janus induced precipitate. Scale bar 1μm. B) Higher magnification TEM micrograph of the precipitate, revealing it to be comprised of thousands of individual colloidal gold particles. Scale bar, 500nm. C) and D) High magnification images showing the linear nature of the arrangement of colloidal gold particles within the precipitate. Scale bars 200 and 50nm respectively.

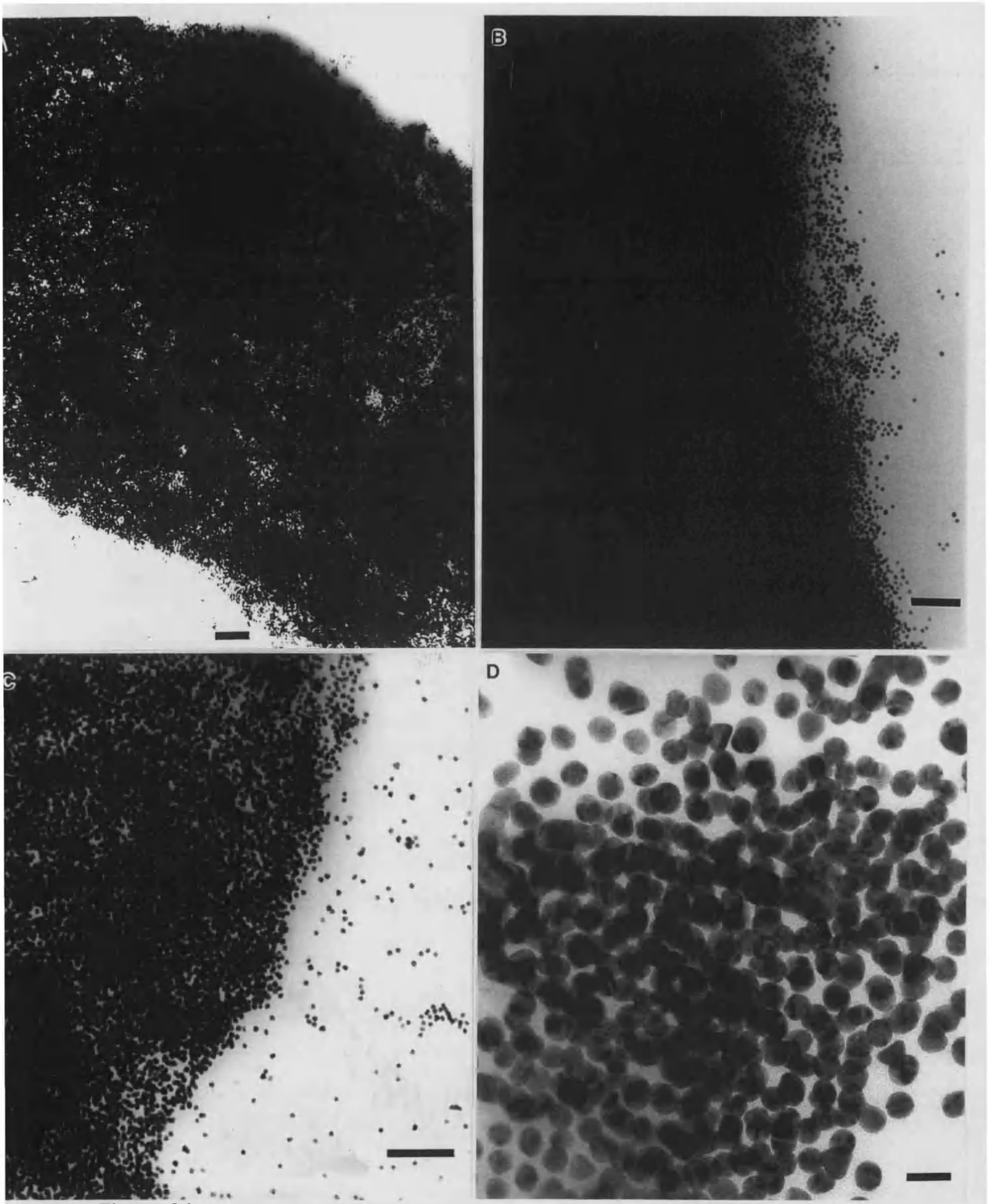

Figure 26 A) TEM micrograph showing a hetero-janus induced precipitate displaying a more open structure. Scale bar 200nm. B) and C) Higher magnification images of the precipitate, displaying the nature of the filament structure. Scale bars 200nm. D) HRTEM micrograph of a single cluster on the filament periphery, showing the linear nature of the colloidal aggregation. Scale bar, 20nm.

This contrasts sharply with the aggregates found using the homo-janus antigen (Fig. 23). The only variable that differs when comparing these two protocols, assuming IgE and IgG to be identical, is the antigen. This suggests that the antigen itself is responsible for this dramatic difference in the mode of self assembly. Structurally, the hetero-janus antigen is a much longer molecule possessing 20 atoms between the head groups recognised by the antibodies. On antibody recognition of one head group there would be much less influence of steric hindrance for subsequent binding of a second particle, resulting in a kinetically faster growth of aggregate. The relative flexibility of the hetero-janus antigen, compared to the homo-janus antigen, would also possess a greater number of degrees of freedom in solution, which may contribute to a more efficient 'docking' of antibody conjugated colloidal particles. The linear nature of the higher ordered self-assembled structure produced would then occur according to the mechanism proposed in the previous section, albeit faster due to the comparative ease of antibody recognition. It should be noted that previous work[30] has shown a distance of 8 carbons to be the minimum to allow efficient antigen binding.

III) Hetero-Janus Induced Self Assembly of Bimetallic Gold/Silver Aggregates

The work undertaken in the preceding subsection, demonstrating the use of the hetero-janus antigen in the production of self assembled structures, alluded to the fabrication of bi-metallic structures, comprising two species of antibody conjugated colloidal particles. Two different antibodies were used to prepare Au and Ag sols consisting of nanoparticles with surface-attached antibodies of either Anti-DNP IgE or Anti-biotin IgG. Thus, Anti-DNP conjugated gold particles and Anti-biotin conjugated silver particles were produced. The difference in absorbance, upon addition of the hetero-janus antigen to a 1:1 mixture of antibody conjugated gold particles, was followed by UV-vis spectroscopy (Fig. 27).

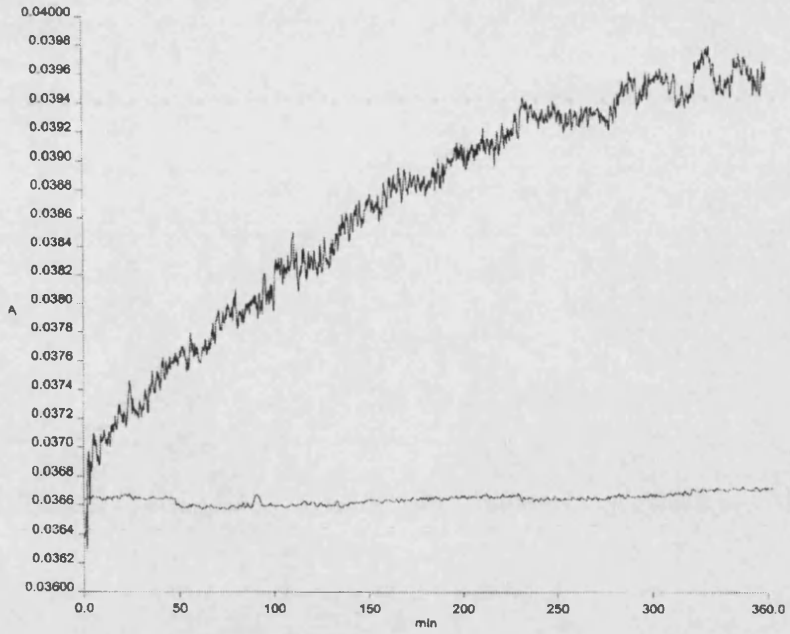

Figure 27 Time course (λ560nm)showing the increase in absorbance upon addition of the hetero-janus antigen to a sample of antibody conjugated gold and silver particles (1). The control sample (2) shows no change in absorption of an identical sample to which no antigen was added.

This graph shows that the addition of the hetero-janus antigen to the heterogeneous sample of antibody conjugated colloidal gold and silver particles, results in an increase in absorbance (1) on comparison with the control sample (2). This suggests, in an analogous fashion to the homo-janus system, that the antigen is cross linking the colloidal particles, resulting in an increase in absorbance of the sample. The absorbance profile obtained also differs markedly from the monometallic aggregates seen previously. Examination of the sample after a period of 24 hours, revealed the presence of a black precipitate on the floor of the cuvette. Again, scaling down experiments performed in eppendorf tubes resulted in the formation of a black precipitate, which was transferred to a TEM grid for analysis. Micrographs of the sample revealed a huge, very dense precipitate, possessing a linear shape (Fig. 28), although not as regular or as long as the hetero-janus mono-metallic aggregate described in the previous subsection. The edge of the aggregate was examined under higher magnification (Fig. 28a, inset) and revealed the precipitate to be comprised of thousands of individual particles. To investigate the nature of the precipitate, smaller clusters in close proximity to the large aggregate were examined (Fig.28bi) and ii)). These revealed the aggregate to be comprised of particles displaying a range of sizes and

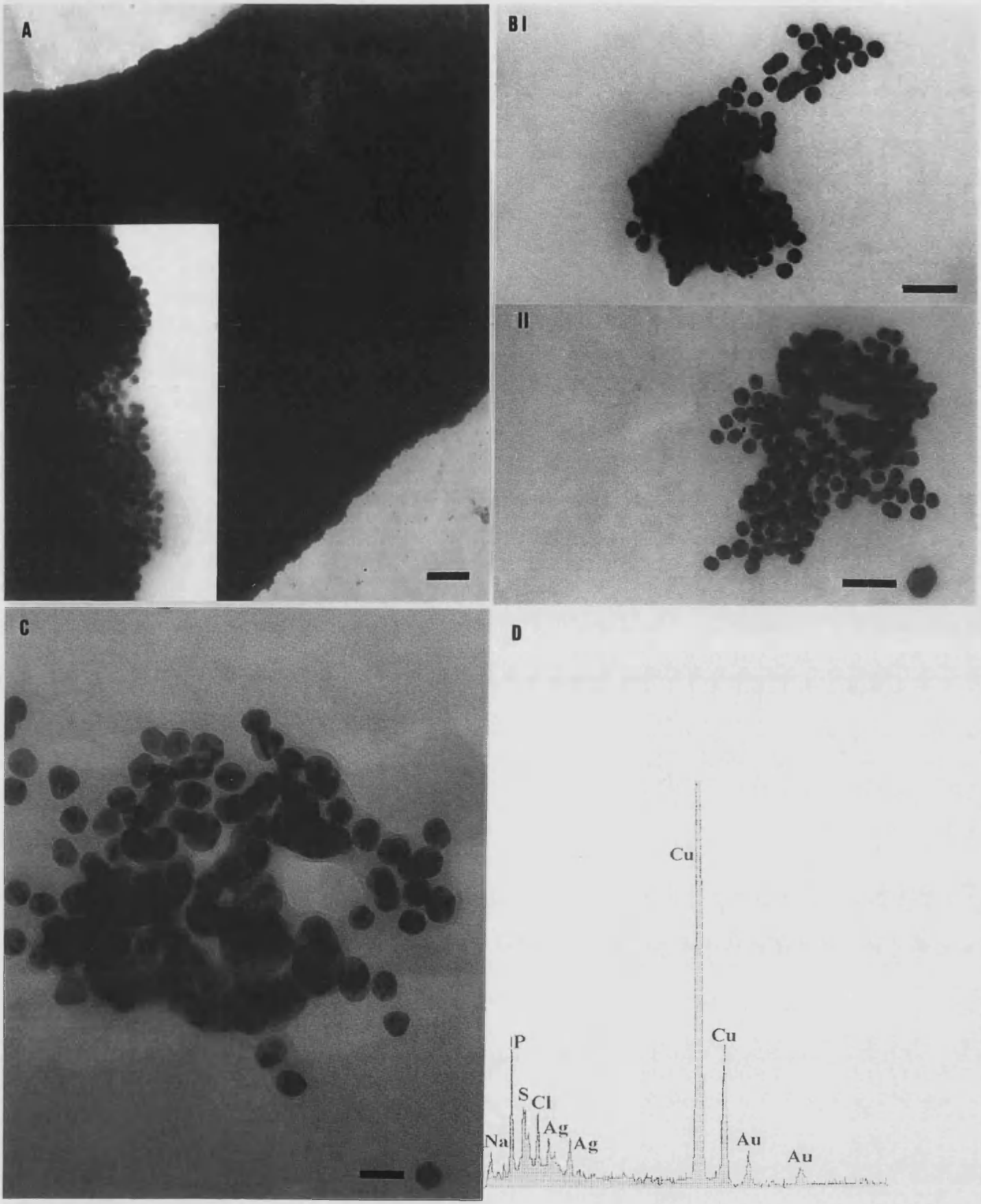

Figure 28 A) TEM micrograph showing the huge linear precipitate from the Au/Ag system. Scale bar 2μm. Inset shows a HRTEM image of the edge of the precipitate. B) i) TEM image of a cluster in close proximity to the precipitate, showing the irregular Ag and regular Au particles. Scale bar 50nm ii) TEM image of a small cluster, showing the dense aggregate resulting from stacking. Scale bar 50nm C) HRTEM showing particles of different morphology, indicative of Au and Ag particles. Scale bar 20nm. D) EDXA showing peaks for Ag and Au.

morphologies. High resolution images of these clusters (Fig. 28c) give a clearer picture of the composition of these clusters. EDXA performed upon this cluster (as well as every cluster encountered and the large filamentous precipitates) gave peaks for Ag and Au (Peaks for Na and Cl were also found, due to the high concentration of NaCl used in the experiment).

These data, although in no way quantitative, suggest the hetero-janus antigen to have cross-linked the antibody conjugated gold and silver particles, to form a huge macroscopic bi-metallic aggregate. TEM micrographs of the clusters revealed spherical particles, possessing a mean diameter of 12nm, together with particles displaying elongated morphologies and huge irregular shaped particles (Fig. 28b and c). This suggests the former to be the gold particles, due to previous experiments demonstrating their relative stability under experimental conditions. The latter must therefore be silver particles that have previously been shown to be both irregular in size and also sensitive to environmental perturbance, such as changes in pH and ionic strength. Thus, under experimental conditions necessary for antibody induced colloidal self assembly, these particles may have tended to ripen, probably due to the fluctuation in pH and buffer conditions. This resulted in silver particles displaying a much broader range of diameters when compared to the gold colloid. The conjugation of antibodies was also a less efficient procedure, as the colloid was more sensitive to pH and consequently the conjugation procedure had to occur at a lower pH. The combination of these effects may have lead to a less efficient mode of self assembly, when compared to the hetero-janus induced mono-metallic gold system. Consequently, TEM analysis confirmed the precipitate to be comprised of a much more random arrangement of particles in each precipitate.

Although the TEM data provided compelling evidence for co-assembly of a bimetallic network of nanoparticles, the degree of integration observed in the images was not as high as would be expected for a process regulated solely by biomolecular recognition. This could be because the Ag particles were less homogeneous in size than the Au clusters and susceptible to self-association at the experimental pH of 9. Further work, involving metallic and semiconductor colloids with better size matching and pH stability is in progress.

5.4 Conclusions and Future Work

This work has shown for the first time the use of antibodies, together with the technique of 'antigen (or hapten) engineering', can be employed to induce the directed self assembly of metallic nanoparticles in creating mono and bi-metallic aggregates with higher ordered structures, a characteristic not seen in previous work. It has been shown that the synthesis of a homo-janus antigen, comprising two dinitrophenyl groups, separated by an eight atom spacer arm, is capable of inducing the self assembly of aggregates comprised of gold particles with conjugated Anti-DNP antibodies. The addition of the hetero-janus antigen to a sample containing gold particles with either Anti-DNP or Anti-biotin conjugated antibodies was also shown to induce self-assembly of huge filamentous aggregates, possessing length scales of millimetres. Preliminary experiments utilising the hetero-janus antigen also revealed an ability to create bi-metallic aggregates from a heterogeneous sample of colloidal gold and silver possessing Anti-DNP and Anti-biotin conjugated antibodies respectively.

It was shown that the formation of aggregates is due to specific antibody-antigen interactions. All experiments involved saline conditions (essential for optimum antibody activity) and it was demonstrated that antibody conjugation to colloidal particles prevented salt induced aggregation. It should be noted that storage for 6 months of a sample of conjugated gold particles in saline solution revealed no precipitate. The addition of the homo-janus antigen was then shown to induce precipitate formation. A control sample performed, replacing the conjugated Anti-DNP antibody with Anti-biotin antibodies with subsequent addition of the homo-janus antigen, resulted in no precipitation. This effect strengthens the suggestion that antibody-antigen interactions are entirely responsible for the aggregation observed. Similar experimental conditions were thus employed in the formation of hetero-janus antigen induced aggregation, utilising a heterogeneous solution of Anti-DNP and Anti-biotin conjugated gold particles. Comparison of these two mono-metallic systems suggests the mode of self assembly to be affected greatly by the design of the antigen. It has previously been reported[30] that the eight carbon spacer between two antigenic binding sites is the minimum possible to induce simultaneous antibody binding. Thus, the design of a hetero-janus antigen, possessing a 20 atom spacer, would negate the effect of antibody steric hindrance upon

antigen recognition. This may account for the huge differences, both kinetic and visual, seen in the formation of colloidal gold aggregates.

The schematic shown in Fig. 29 shows the routes developed in this work in the fabrication of self assembled nanoparticulate materials. In general, the development of bio-derived routes to organised forms of inorganic matter should be a powerful tool towards targeted structures, due to the high specificity of biomolecular interactions. The potential of antibody-antigen coupling, as a strategy for the directed self-assembly of metallic nanoparticles into extended three dimensional networks that can exhibit higher order structures, such as wires and filaments, presents an entirely new approach to 'bottom-up' synthesis of materials and holds promise for numerous future applications. The ability to fabricate aggregates with controlled connectivity requires more sophisticated engineering of the antibody-antigen interface, however, the knowledge and methodologies currently available in molecular immunology should be sufficient to address these problems.

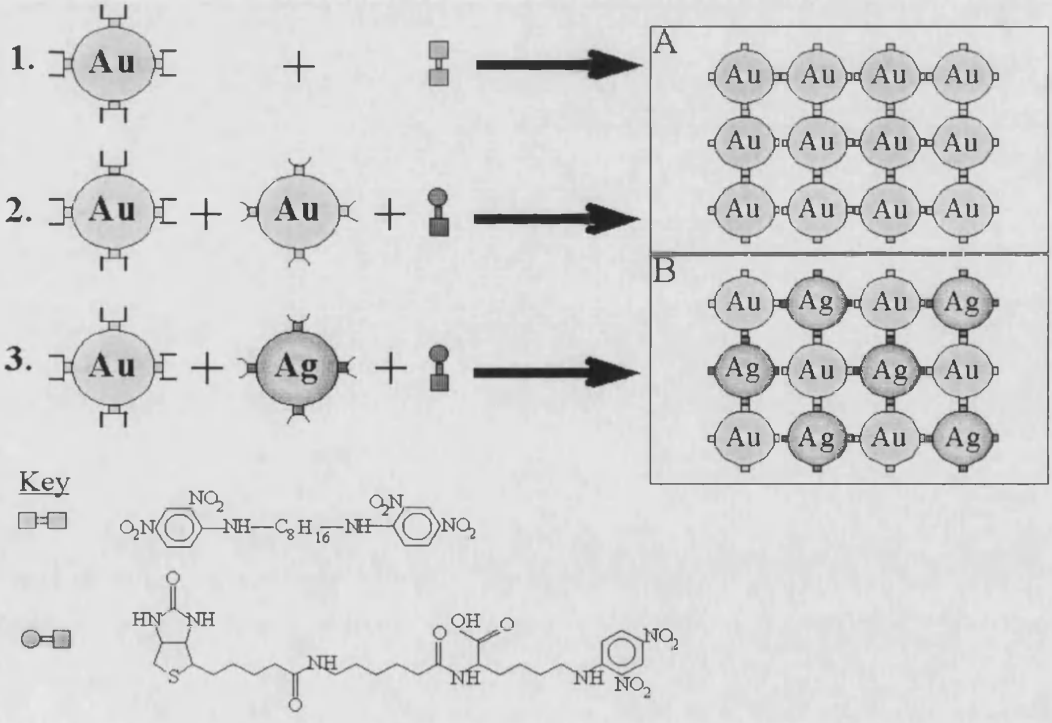

Figure 29 Schematic showing the synthetic routes developed in this work for the production of mono- and bi-metallic aggregates. 1) homo-janus mono-metallic system 2) hetero-janus mono-metallic system 3) Hetero-janus bi-metallic system. Key shows the homo-janus and hetero-janus antigen respectively.

Future work would concentrate of specific areas of this work to establish more quantitative data. This work has shown the potential of the system employed and also the versatility of the use antigen-antibody recognition in the field of nanoscopic self assembly. For example, dynamic light scattering experiments would be undertaken to give a greater understanding of the kinetics of the system. Investigation into the effect of temperature, pH and ionic strength upon the characteristics of self assembly, building on results obtained in this work, would also be investigated. For example, it was found that temperature was important in the homo-janus system, but less so in the hetero-janus system. The need for optimal conditions in efficient antigen recognition may necessitate the heating of the homo-janus system, due to the minimal spacer arm length, whereas the hetero-janus antigen does not possess such innate steric constraints upon antibody recognition and so temperature may not have such a drastic impact on the self assembly. The inherent flexibility of the system could be exploited to allow the fabrication of a wide range of self assembled materials by the tailored synthesis of just two of the constituents of the system, namely colloid and antigen synthesis. The synthesis of a wide range of colloids would allow the fabrication of further bi-metallic semi-conducting materials, which could find applications such as energy stores, solar panels and novel electronic devices, through use of colloids possessing large and small band gaps. The technique of 'antigen engineering' has already shown that relatively small differences in antigen design result in very different modes of self assembly, culminating in materials of contrasting size and morphology. The design of poly-janus antigens, coupled with the synthesis of stable colloids, may allow the fabrication of precise poly-metallic materials, comprised of 'crystalline' arrangements of colloidal particles due to the spatial arrangement of antigenic determinants of the antigen.

5.5 References

1. C.Petit, A.Taleb, M.-P,Pileni (1998) Self-organization of magnetic nanosized cobalt particles, *Adv. Mater.*, **10**, p259-262
2. C.B.Murray, C.R.Kagan, M.G.Bawendi (1995) Self-organization of CdSe nanocrystals into three-dimensional quantum dot superlattices, *Science*, **270**, p1335-1338
3. T.Vossmeyer (1995) Self-assembly of a two-dimensional superlattice of molecularly linked metal clusters. *Science*, **267**, p1746-1479
4. B.A.Korgel, D.Fitzmaurice (1998) Self-assembly of silver nanocrystals into a two-dimensional nanowire array, *Adv. Mat.*, **10**, p661-665
5. R.P.Andres, J.D.Bielefeld, J.I.Henderson, D.B.Janes, V.R.Kolagunta, C.P.Kubiak, W.J.Mahoney, R.G.Osifchin (1996) Self-assembly of a two-dimensional superlattice of molecularly linked metal clusters, *Science*, **273**, p1690-1693
6. M.Brust, D.Bethell, D.J.Schiffrin C.J.Kiely (1995) Novel gold-dithiol nano networks with non-metallic electronic properties, *Adv. Mat.*, **7**, p795-797
7. W.Shenton, D.Pum, U.B.Sleytr, S.Mann (1998). Biocrystal templating of CdS superlattices using self-assembled bacterial S-layers, *Nature,* **389**, p585-587
8. S.Dieluweit, D.Pum, U.B.Sleytr, (1998).Formation of a gold superlattice on an S-layer with square lattice symmetry, *Supramol. Sci. in press*
9. S. A. Davis, S. L. Burkett, N. H. Mendelson, S.Mann (1997) Bacterial Templating of Ordered Macrostructures in Silica and Silica-Surfactant Mesophases, *Nature,* **385**, p420-423
10. C.A.Mirkin, R.L.Letsinger, R.C.Mucic, J.J.Storhoff (1996). A DNA-based method for rationally assembling nanoparticles into macroscopic materials, *Nature*, **382**, p607-609
11. A.P.Alivisatos (1996).Organization of "nanocrystal molecules" using DNA, *Nature,* **382**, p609-611
12. N.K.Jerne (1973) The Immune System, *Sci.Am.*, **229**, p52-60
13. R.R.Porter (1973) Structural studies of Immunoglobulins, *Science*, **180**, p713-716

14. P.M.Alzari, M.B.Lascombe, R.J.Poljak (1988) Three dimensional structure of Antibodies, *Annu.Rev.Immunol.*, **6**, p555-580

15. D.R.Davies, S.Sheriff, E.A.Padlan (1988) Antibody-Antigen complexes, *J.Biol.Chem*, **263**, p10541-10544

16. J.A.Berzofsky, I.J.Berkover (1984) *Antigen-antibody interactions, In Fundamental Immunology* (W.E.Paul, ed.), p595-644, New York, Raven Press

17. R.L.Stanfield, T.M.Fieser, R.A.Lerner, I.A.Wilson (1990) Crystal Structures of Antibody to a peptide and its complex with peptide Antigen, *Science*, **248**, p712-719

18. D.G.Schatz, M.A.Oettinger, M.S.Sclissel (1992) Recombination and Regulation in Antibody Production, *Annu. Rev. Immunol*, **10**, p359-383

19. J.M.Varga, G.F.Klein, P.Fritsch (1990) Binding of a monoclonal IgE (Anti-DNP) antibody to radio-derivatized polystyrene-DNP complexes, *FASEB Journal*, **4**, p2678-2684

20. N.N.Gorgani, S.B.Smith, J.G.Altin (1996) The formation of insoluble immune complexes between ovalbumin and anti-ovalbumin IgG in at least two distinct phases dependent on reactant concentration and ionic strength, *Immunology*, **1317**, p45-54

21. Y.K.Sykulev, D.A.Sherman, R.J.Cohen, H.N.Eisen (1992) Quantitation of reversible binding by particle counting: Hapten-antibody interaction as a model System, *PNAS*, **89**, p4703-4707

22. L.Wilson, P.Matsudaira (1993) *Antibodies in Cell Biology*, New York, Academic Press,

23. D.E.Yelton, M.D.Scharff (1981) Monoclonal antibodies: a powerful new tool in biology, *Annu.Rev.Biochem.*, **50**, p657-680

24. Z.Eshhar, M.Ofarim, T.Waks (1979) Antibodies of Anti-DNP specificity, *J.Immunology*, **124**, p775-780

25. K.Dakshinamurti, R.Bhullar, A.Scoot, E.Rector, A.Sehon (1986) Production and characterisation of a monoclonal antibody to biotin, *Biochem J.*, **237**, p477-482

26. J.Turkevich, P.Stevenson, J.Hillier (1951). *Discuss. Faraday Soc*, **11**, p55-75,

27. P.Lee, D.Melsel (1982). Adsorption and surface-enhanced Raman of dyes on silver and gold sols, *J. Phys. Chem*, **86**, p3391-3395

28 http://info.med.yale.edu/cellimg/gold.html

29 C.J.Pouchert, J.Behnke (1993) Aldrich library of ^{13}C and ^{1}H FT NMR spectra, ed.1, Vol. 1.

30 R.C.Valentine, N.M.Green, (1967) Electron Microscopy of an Antibody-Hapten Complex. *J .Mol. Biol*, **27**,p615-617

Chapter 6

Antibody Induced Self Assembly of Ferritin/Colloidal Gold Composites

The whole is more than
the sum of the parts

Aristotle

6.1 Introduction

This chapter is a continuation of the application of antibodies to the fields of colloidal chemistry, materials synthesis and nanotechnology. The work explores the production of hybrid organic/inorganic aggregates, specifically those formed between the iron storage protein ferritin and colloidal gold particles. This approach utilises the specificity of antibodies, but in a contrasting way to that of Chapter 5, which introduced the idea of 'antigen engineering'.

The work sets to mimic the native function of antibodies, by synthesising chemically modified ferritin, possessing an external surface populated by antigenic biotin groups. The introduction of these modified ferritin molecules to buffered colloidal gold particles, possessing adsorbed Anti-biotin antibodies on their surfaces, results in the formation, and eventual precipitation, of large, self assembled hybrid materials. Overall, the work is an investigation into the potential of this system and sets the precedent for future research.

6.1.1 Inorganic/organic hybrid materials

The fabrication of hybrid inorganic-organic materials often results in a material having an increase in modulus and tensile strength. Nanostructured composites may also result in materials with unusual properties, differing substantially from their constituents. This offers the opportunity of designing materials exhibiting certain desirable, or 'engineered' characteristics and properties. The synthesis of hybrid composite materials has employed a variety of protocols including sol-gel techniques[1,2], gels[3], multilayers[4], clays[5] and self assembly[6]. The current generation of hybrid materials is providing examples displaying novel optoelectronic[7], catalytic[8] and biological[9] behaviour.

Biomineralization is a natural process whereby nature synthesises nanostructured composites, for example bone and shells[10]. There are several examples of biologically based hybrid inorganic-organic materials, two such examples are composites based on threads of bacteria[11], with catalytic applications, and inorganic composites of spider silk[12].

6.1.1 Ferritin

Males contain about 3.5 g and females 2.2 g of elemental iron, which is distributed in essentially 3 compartments. The major functional compartment contains about 70 % of total body iron complexed to haemoglobin, myoglobin, proteins of the electron transfer pathway, catalase, peroxidase, ribonucleotide reductase and many other proteins in the cell[13]. The second compartment, comprising 30 % of total body iron, is the intra-cellular storage compartment and consists of iron complexed in a non-toxic, inactive state as ferritin and haemosiderin[13].

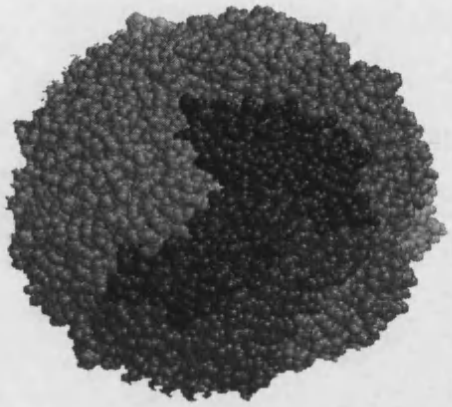

Figure 4 Computer reconstructed image of the iron storage protein ferritin, viewed perpendicular to the 3-fold axis[18].

Mammalian ferritin consists of a protein shell of 24 subunits, surrounding a core of hydrated ferric oxide containing different amounts of phosphate[14]. Apo (or metal free) ferritin can accommodate up to 4500 iron atoms[15]. The structure of ferritin is roughly spherical (actually a rhombic dodecahedron), with an external diameter of 130, an internal diameter of 75 and possesses both 3 and 4-fold channels. These channels have been implicated in the internalisation of iron through the three fold channel and subsequent release of iron through the 4-fold channel[16]. (For a detailed account of the structure of ferritin, see Chapter 3 - 'The Synthesis of Quantum Dots Using the β60 Capsid of Lumazine Synthase').

6.2 Materials and Methods

Monoclonal Anti-biotin immunoglobulins, at a concentration of 2.4mg/ml, were obtained from Sigma Immunochemicals. Purified horse spleen ferritin (50mg/ml) was also obtained from Sigma. Long arm water soluble biotin (sodium sulfosuccinimidyl-6-biotinamidohexanoate, 50mg) was obtained from Vector laboratories.

Colloid Synthesis and Antibody conjugation

A gold colloid was synthesised as described in Chapter 5, but the sol was allowed to age to produce particles possessing diameters of approximately 20nm. Antibodies were conjugated to gold particles under identical conditions to those described in Chapter 5.

Functionalisation of ferritin

I) DNP functionalisation: A 4.5ml solution of 1M $NaHCO_3$ (Aldrich) was added to 0.5ml of horse spleen ferritin (50mg/ml) to give approximately 25mgs of ferritin. This solution was then heated to 37°C on a water bath and stirred vigorously. To the solution, 50mg of 2,4-dinitrofluorobenzene (Aldrich) was added dropwise, and the solution left to stir for 30mins.

A sephadex column (G25, Sigma) was prepared and 5ml of the cooled DNP functionalised ferritin (DNP-Fn) added to the top of the column and eluted with distilled water. The brown solution separated into an upper brown band and a lower brown/yellow band. The lower band was collected and 0.01% NaN_3 added before storage at 4°C.

A UV-vis spectrum was taken of the resultant brown/yellow band collected and run against a blank consisting of distilled water. The concentration was then adjusted to 1mg/ml for future experiments.

Gel electrophoresis was performed on the DNP-ferritin. Wells were run of increasing concentrations (5, 10 and 15μg/ml), compared to a well of native horse spleen ferritin (20μg/ml).

II) Biotin functionalisation: Biotin functionalisation was carried out according to the protocol supplied by Vector laboratories, detailed as follows. Ferritin (10mgs) was dissolved in 5ml of HEPES ([*N*-(2-hydroxyethyl) piperazine-*N*'(2-ethanesulfonic acid)])

buffer (100mM) and 0.5M NaOH added, to give pH8.5. To 200µl of double distilled water, 5mg of water soluble 'long-arm' biotin (sodium sulfosuccinimidyl-6-biotinamidohexanoate) was added, 40µl of this biotin solution was then added to 5ml of the 2mg/ml ferritin in HEPES buffer. The resulting ferritin/biotin solution was left to slowly stir at room temperature for 4 hours. The biotin functionalised ferritin solution was subsequently added to a dialysis bag (10kDa cut off) and dialysed against HEPES buffer for 24 hours at 4°C. The concentration of protein was then adjusted to 1mg/ml for future experiments before adding 1% NaN_3 and storage at 4°C.

Gel electrophoresis was performed on the biotinylated ferritin sample. Wells were run consisting of increasing concentrations of the biotinylated ferritin (5, 10 and 15µg/ml) and compared against native horse spleen ferritin (20µg/ml).

Formation of ferritin gold aggregates

A preliminary titration was performed to ascertain the approximate concentrations required for the equivalence point as follows.

Antibody conjugated gold colloid (µl)	Biotinylated ferritin (µl)	1M NaCl (µl)	2mMBorax buffer (µl)
100	0	10	90
100	2	10	88
100	5	10	85
100	10	10	80
100	15	10	75

All solution mixed well and left unstirred for 48 hours at 4°C.

6.3 Results and Discussion

The first subsection in the results section describes two methods of functionalising ferritin with specific chemical groups that are recognised by antibodies i.e. DNP and biotin. The next subsection then describes methods of forming hybrid aggregates from these chemically modified ferritin molecules and gold particles possessing conjugated antibodies with affinities for the chemically modified ferritin.

6.3.1 The Chemical Modification of Ferritin

I) DNP functionalisation of ferritin (DNP-Fn)

The yellow/brown band eluted from the sephadex column was analysed with UV absorbance spectroscopy, to verify the presence of protein and also the degree of DNP substitution on the surface of the ferritin particle. The spectrum can be seen in Fig. 2.

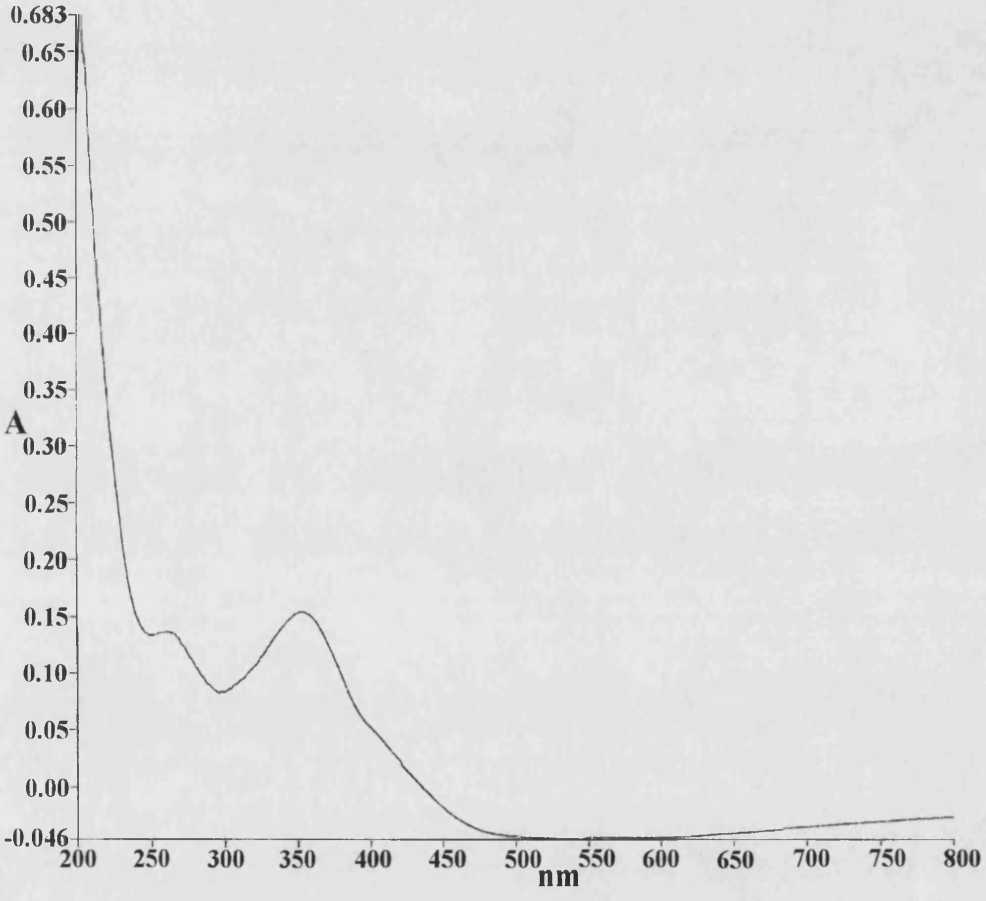

Figure 2 UV absorbance spectrum of DNP functionalised ferritin, showing peaks at 280nm and 360nm, representing protein and DNP respectively.

The spectrum shows two peaks, at 280nm and 360nm, corresponding to the absorbancies of the aromatic side chains of the protein and the substituted benzene ring of DNP respectively. To calculate the substitution ratio of DNP groups on the surface of ferritin, the following methodology was employed[17]. The extinction coefficient of ferritin[13] was taken as E_{280}=1.78 x 10^4 M^{-1} cm^{-1} $subunit^{-1}$, based on the subunit mol. wt. of 19,824. The spectrum gives an absorbance at 280nm of 0.136 and a path length of 1cm was then used to calculate the concentration of ferritin as $8.8x10^{-8}$ moles. To calculate the number of moles of DNP, 0.067mmol of DNP[17] was taken to correspond to A=1 at E_{360}. Thus, an absorbance of 0.149 was recorded, corresponding to $9.3x10^{-6}$moles of DNP. The spectrum obtained therefore reveals a substitution ratio of approximately 1 mole of ferritin per 100 moles of DNP, implying a high substitution ratio on the surface of each ferritin molecule.

The resultant yellow/brown solution of DNP-Fn remained transparent for several weeks when stored at 4°C, but displayed evidence of protein denaturation on longer storage with a brown precipitate accumulating on the floor of the vial. This precipitate presumably consisting of the iron cores of ferritin, released upon degradation of the protein cage. This process conforms to that for known DNP functionalisation of a number of proteins[17].

The DNP functionalisation of ferritin was found to affect the role of ferritin as an iron storage protein. Experiments designed to functionalise the surface of Apo ferritin with DNP produced data suggesting the procedure was successful, but attempts to reconstitute the iron core resulted in a brown precipitate on addition of aqueous Fe(II). This suggests the ability of ferritin to sequester iron atoms was lost, which may be due to the high degree of negative surface charge, with important amino acids around or inside the 3-fold channel possessing substituted DNP groups.

Gel electrophoresis was performed on a sample of the DNP-Fn and compared to native ferritin (Fig. 3).

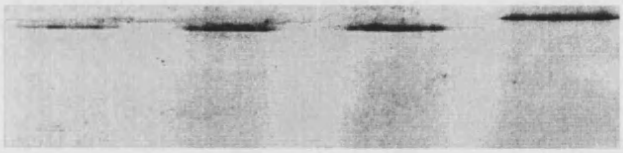

Figure 3 Gel electrophoresis of DNP-Fn, from right to left, *well 1* native ferritin (20μg/ml), *wells 2,3 and 4* being DNP-Fn of decreasing concentration (15,10,15μg/ml).

The gel shows that the functionalised ferritin travels further, when compared to the control samples. This again demonstrates the effect of DNP functionalisation on the properties of ferritin. The movement of protein molecules in an applied electric field is proportional to the net charge on the protein. The functionalisation of ferritin with DNP gives a protein with a higher negative surface charge, compared to native ferritin, and therefore a greater velocity in the applied field.

Biotin functionalisation of ferritin (B-Fn).

The biotinylation of ferritin was performed according to a well established coupling procedure, a technique used in molecular biology for the production of biotinylated ferritin used in assays. The procedure resulted in a clear brown solution, indistinguishable to that for aqueous native ferritin. The B-Fn sample remained stable for several months at 4°C, with no visible precipitate. It should be noted that the long-arm variety of biotin was chosen to ensure antibody recognition of the hapten, through minimisation of steric hindrance.

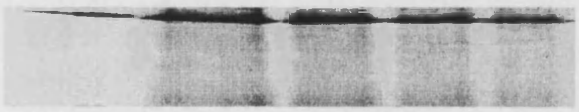

Figure 4 Gel obtained for B-Fn.. From left to right, *well 1*: native ferritin (20μg/ml), *well 2,3,4 and 5*, B-Fn (15,10,15μg/ml).

Gel electrophoresis performed on the biotinylated ferritin revealed only a very slight difference in velocity, when compared to native ferritin. This suggests that the functionalisation of ferritin with biotin results in a molecule displaying a very similar electrostatic potential, which is expected due to the uncharged nature of the long-arm biotin molecule.

TEM analysis was performed to ascertain the effect of functionalisation of ferritin, with DNP and biotin, on its structural integrity. A sample of native ferritin, stained with

uranyl acetate to reveal the protein, was also analysed for comparison with the functionalised ferritin (Fig. 5a).

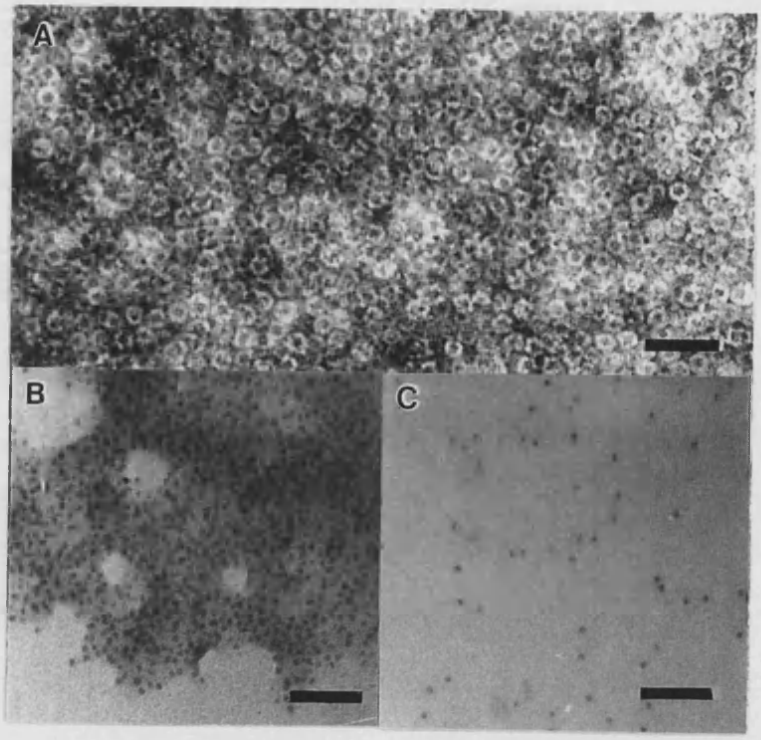

Figure. 5 A) TEM micrograph of uranyl acetate stained native ferritin. Scale bar 50nm B) TEM micrograph of unstained DNP-Fn. Scale bar 50nm C) TEM micrograph of unstained B-Fn. Scale bar 50nm.

The micrograph reveals a very concentrated sample of ferritin, dried down onto a TEM grid, showing a monodisperse plane of spherical particles, each possessing a diameter of approximately 13nm. It should be noted that unstained samples of ferritin reveal only their iron cores. Examination of an unstained sample of DNP-Fn, at a concentration of 1mg/ml, revealed large aggregates of iron cores (Fig.5b) whereas a sample of B-Fn, of the same concentration as DNP-Fn, revealed a monodisperse spread of iron cores (Fig. 5c).

These data suggest that the functionalisation of ferritin was successful and the reaction schemes are envisioned to be those shown in Fig. 6, where nucleophilic attack, of the dinitrofluorobenzene and biotin nucleophiles respectively, result in chemical modification of the amines on the surface of each ferritin. These modified ferritin particles displayed contrasting properties, with respect to native ferritin. UV-vis spectroscopy indicated that there was a high substitution ratio of DNP groups on the surface of the ferritin molecules and gel electrophoresis demonstrated that this substitution had a marked effect on the electrostatic properties of the molecule.

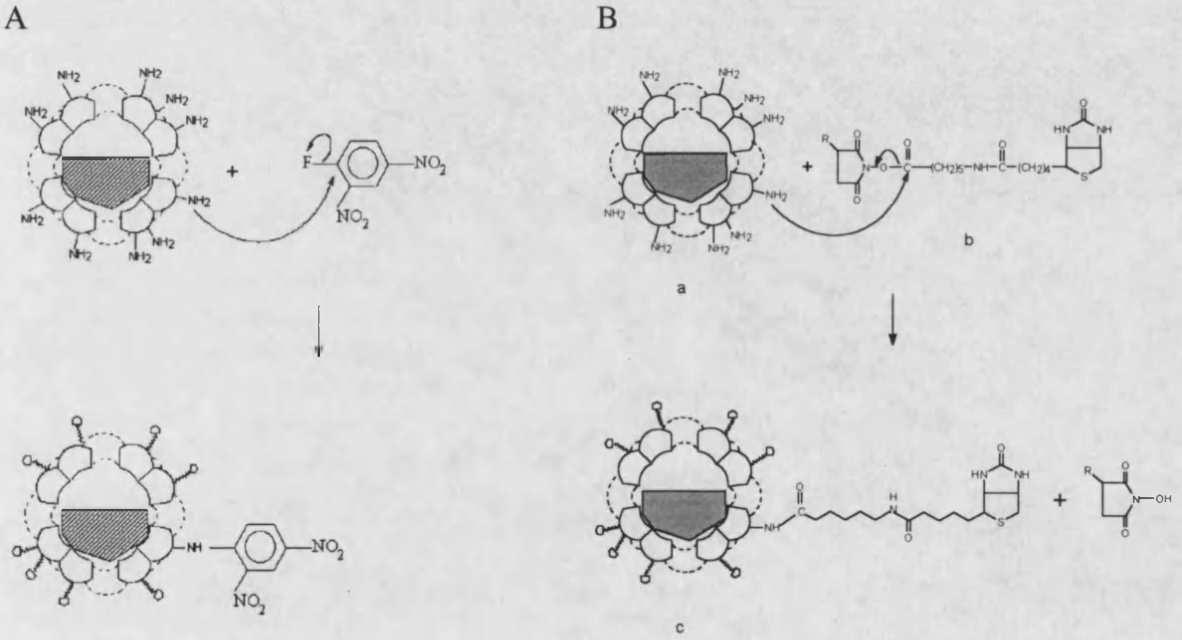

Figure 6 Schematic diagrams showing the chemical modification of the amines found on the surface of ferritin with A) DNP and B) Biotin. The structure of the 'long-arm' biotin, minimising the effect of steric hindrance upon antibody recognition, is shown. (diagrams courtesy of M.Li)

The presence of such a large number of charged amino acids on the surface of the protein would account for the increased velocity of DNP-Fn through the gel, when compared to native ferritin. Gel electrophoresis of B-Fn revealed no such comparable effect on the behaviour of ferritin in an electric field, which can be explained by consideration of the biotin molecule, which has no constituent charged groups.

TEM micrographs showed that DNP-Fn possessed a tendency to form large aggregates, when compared to native ferritin and biotinylated ferritin. This could be explained by the presence of so many H-bond accepting oxygen groups on the surface of the ferritin molecules which could induce the aggregation behaviour seen by TEM. Re-suspension of the DNP-Fn molecules in a 1:1 solution of methanol/water resulted in a relatively monodisperse instance of DNP-Fn, when compared to an aqueous sample. This behaviour represents an interesting phenomenon as native ferritin denatures easily in such solvents, whereas the DNP-Fn remained stable for several weeks. The fact that DNP-Fn could only be dispersed in these solvents, confirmed that its use in the formation of hybrid antibody induced aggregates was not possible, due to the effect of methanol on the activity of antibodies. Conversely, the functionalisation of ferritin with the biotin derivative produced a monodisperse arrangement of ferritin molecules, as observed for native ferritin. This property made B-Fn an ideal candidate for the production of self assembled hybrid materials

6.3.2 Formation of Bio-Inorganic Gold /Ferritin aggregates

The formation of ordered precipitates of gold and ferritin was investigated through a combination of TEM and UV-vis spectroscopy. The titration experiment, detailed in the materials and methods section, was used to determine the concentrations needed to induce precipitation ('equivalence zone'). The solutions were incubated at 4°C for 24 hours prior to examination, which revealed the sample with the largest precipitate to be tube 3, containing 100µl Anti-biotin conjugated gold particles, 5µl B-Fn, 10µl NaCl and 85 µl buffer.

For UV-vis analysis of aggregate formation, these quantities were scaled up, but the total volume of 4ml meant a 10 times dilution factor, which could not be avoided due to scarcity of the modified protein. The duration of the experiment, to monitor the change of absorbance, was 6 hours and the results obtained shown in Fig. 7. The two spectra recorded (1 and 2) represent the sample of biotinylated ferritin added to gold particles with conjugated Anti-biotin, and the control sample respectively. The control sample consisted of an identical sample preparation, where the Anti-biotin antibodies conjugated to the gold colloid had been replaced by Anti-DNP antibodies. The experiment revealed

an increase in absorption for sample 1, this contrasted sharply with the control sample, which remained constant.

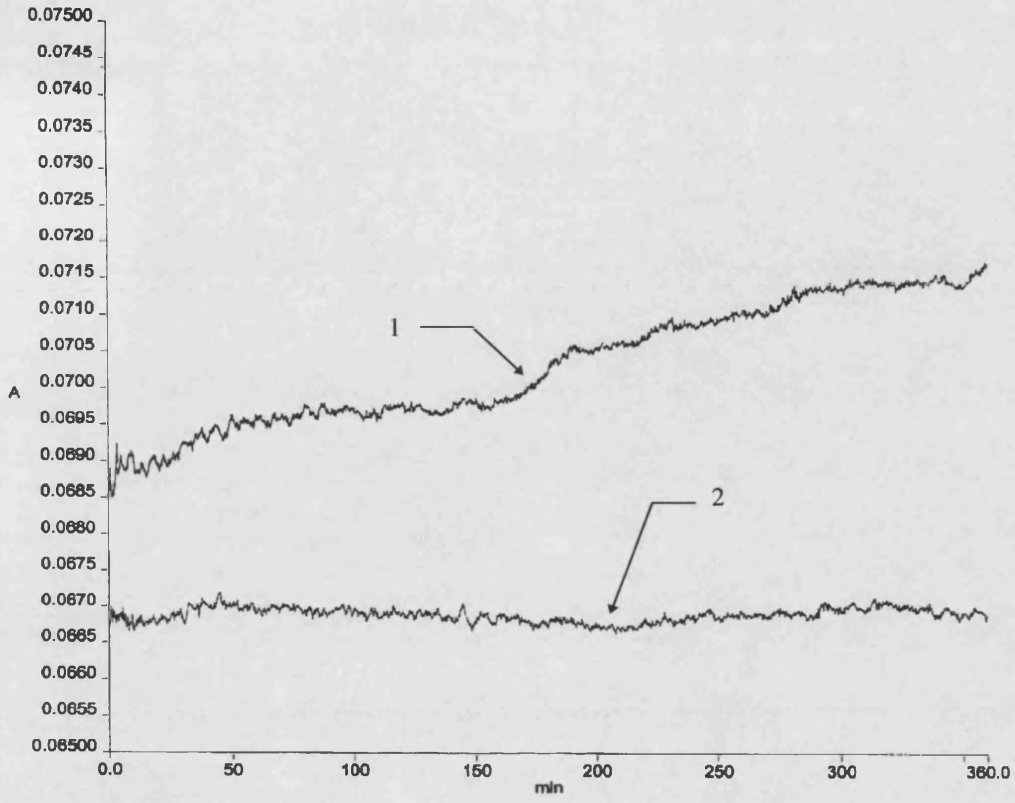

Figure 7 Comparison of the change in absorbance of 1) B-Fn added to Anti-biotin conjugated gold particles and 2) B-Fn added to Anti-DNP conjugated gold particles and B-Fn. (λ560nm)

Examination of the cuvettes 24 hours after the completion of this experiment also revealed the absorbance of sample 1 to have fallen to approximately 0.06 and black precipitates were visible on the floor of the cuvette. The control sample remained the same and no precipitate was seen.

TEM analysis was undertaken to reveal the nature of the precipitate. An experiment was performed, replicating the conditions in the UV experiment, to produce a precipitate. The black precipitates, which tended to be small and amorphous, were transferred to a copper TEM grid, washed and blotted prior to analysis. Electron micrographs revealed huge aggregates (Fig. 8a), which HRTEM confirmed to be comprised of large, dense particles with diameters between 18 and 20nm together with interstitial smaller particles possessing a diameter of approximately 8nm (Fig. 8b).

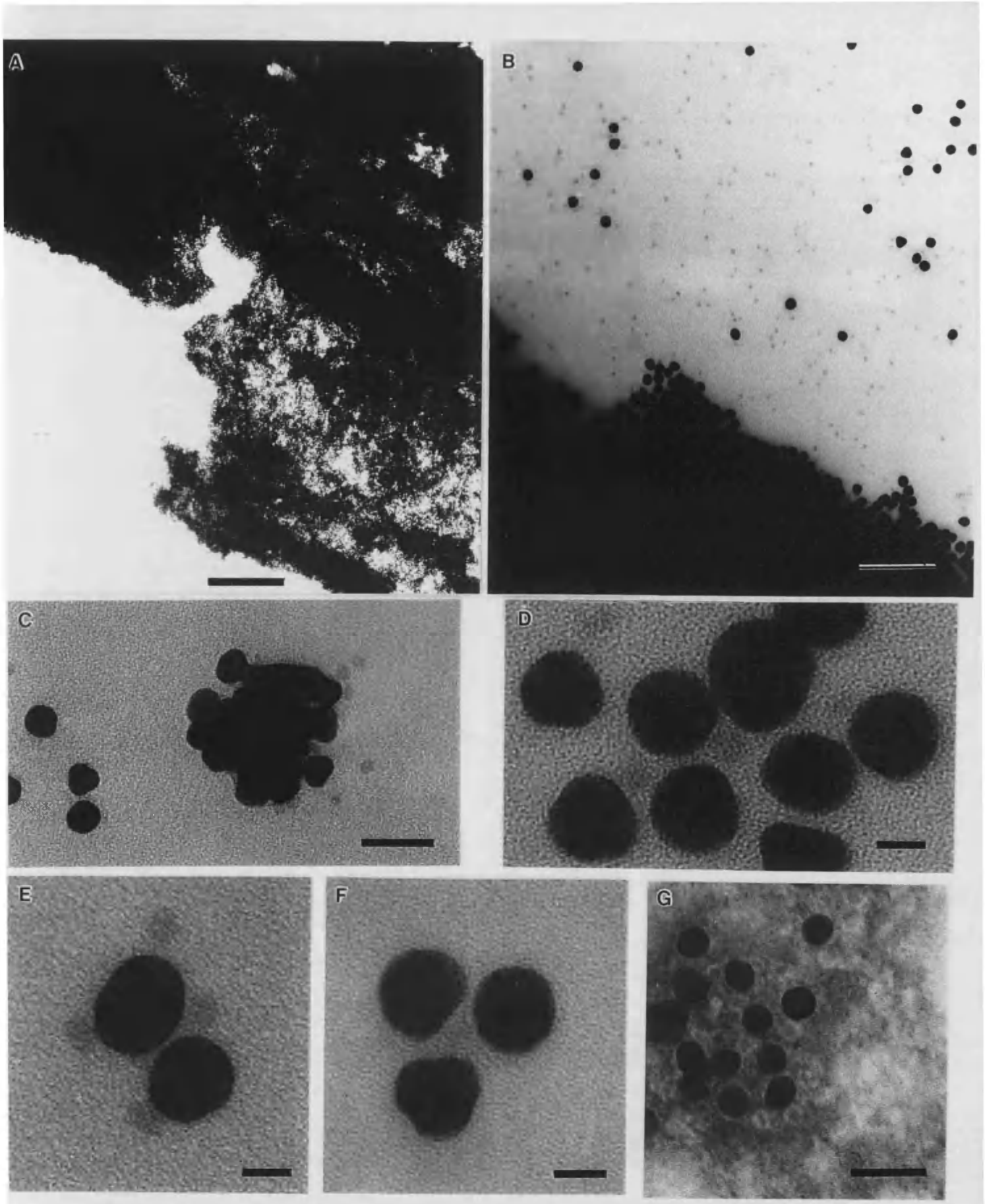

Figure 8 A) TEM micrograph showing the huge precipitous masses resulting form the addition of B-Fn to Anti-biotin conjugated gold particles. Scale bar 200nm B) Higher magnification micrograph of the precipitate, showing it to be comprised of two types of particles. Scale bar 100nm C) TEM micrograph of a small cluster showing the presence of both particle types. Scale bar 50nm D),E),F) HRTEM micrographs showing the close association of the gold particles with ferritin particles. Scale bars 10nm G) Uranyl stained cluster verifying the presence of the protein shell of ferritin. Scale bar 50nm.

Analysis of clusters found on the grid invariably had the smaller particles associated (Fig. 8c) and HRTEM of clusters composed only of several of the larger particles again confirmed this phenomenon (Fig. 8d,e and f). Examination of Fig.8d also shows a grey outline around each of the gold particles, indicative of the adsorbed antibodies. The negative staining of these clusters, with a 2% uranyl acetate solution revealed a halo around each of the smaller particles, giving them a total diameter of approximately 13nm. EDXA analysis, on smaller stained aggregates (Fig. 9), gave peaks for gold and iron, together with uranium and copper, the latter being due to the negative stain and the TEM grid.

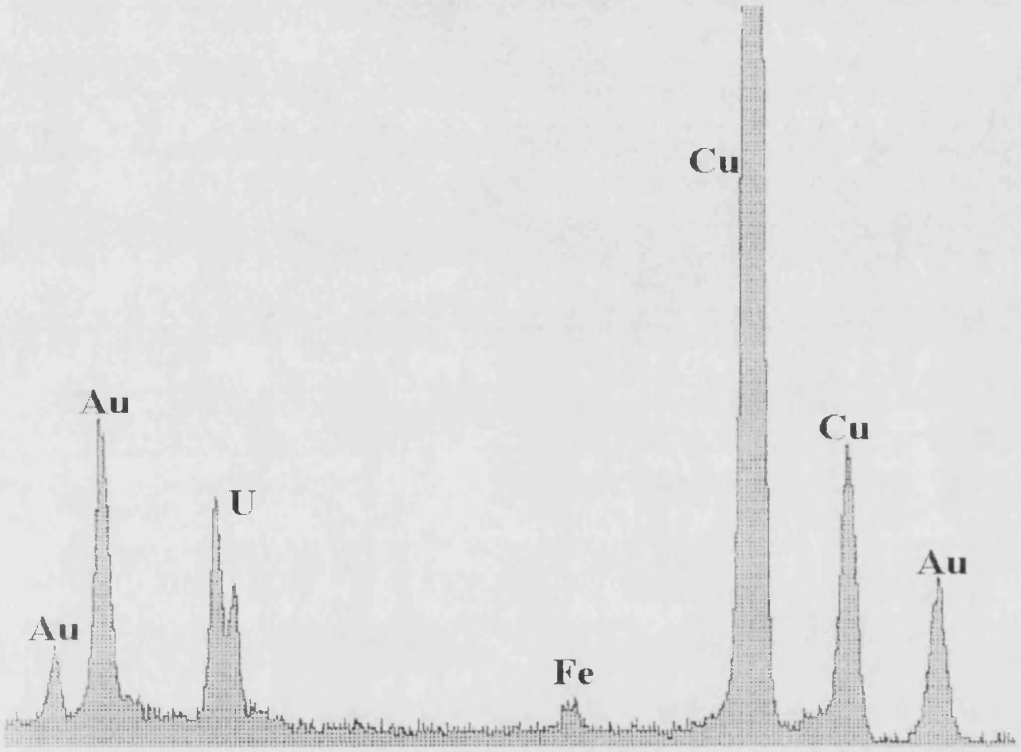

Figure 9 EDXA of the Au/B-Fn aggregate, showing peaks for Au and Fe. The Cu and U peaks being due to the TEM grid and negative stain respectively.

These data suggest that the precipitate observed is formed by the self assembly of Anti-biotin conjugated gold particles and biotinylated ferritin. Under the appropriate conditions, huge macroscopic aggregates are formed that eventually precipitate from solution. The UV-vis spectra obtained show that the addition of the biotinylated ferritin to a given concentration of Anti-biotin conjugated gold particles, results in an increase in absorption over a 6 hour time period. This effect is not seen when the antibodies

conjugated to the gold particles are Anti-DNP. It can be inferred from this that specificity of the Anti-biotin antibodies for the biotin on the surface of the functionalised ferritin is entirely responsible for the aggregation behaviour seen, as the conjugation of morphologically identical immunoglobulins, differing only in the hapten binding pocket, produces no similar effect. This then discounts any aggregation behaviour due to non-specific protein-protein interaction.

The staining of these precipitates revealed the protein shell of individual ferritin molecules to be intact and EDXA analysis confirmed the presence of iron and gold. TEM analysis invariably showed small gold particle clusters closely associated with ferritin molecules and these unstained smaller clusters, seen on the periphery of the larger precipitate (Fig. 8a) further suggest the nature of the binding in these large aggregates. Figs. 8d,e, and f show a variety of 'elements', of which the self assembled aggregates could conceivably be comprised, although evidence of direct antibody-antigen recognition is not established. Negative staining of these small clusters (Fig. 8g) confirmed the protein shell of ferritin to be intact, further strengthening the hypothesis of antibody recognition of antigenic ferritin being responsible for the aggregation. An indication of the reason for the high packing density of the ferritin/gold composite, when compared to the gold/gold composites of Chapter 5, can be explained due to the difference in radius between the ferritin and the gold particles. This would facilitate the formation of a more closely packed structure upon antibody/antigen recognition.

6.4 Conclusion and Future Work

This work has shown for the first time the feasibility of creating organised assemblies of inorganic and organic moieties, on the nanometer scale, through the application of the specific binding properties of antibodies to their respective antigens. The work is in no way a detailed study and characterisation of the properties of this approach, but an investigation into its potential for the production of hybrid materials. Thus, further work would concentrate on a better characterisation of the kinetics of the system, through application of techniques such as dynamic light scattering.

The method employed uses the specificity of the antibody-antigen interaction, albeit in a different manner to that of Chapter 5. Here, the antibody conjugated colloidal gold particles recognise antigens attached to the ferritin molecules, thus the protocol employed mimics the native function of antibodies in their recognition of specific haptens, which in this case are the biotin groups attached to the surface of the ferritin (Fig. 9).

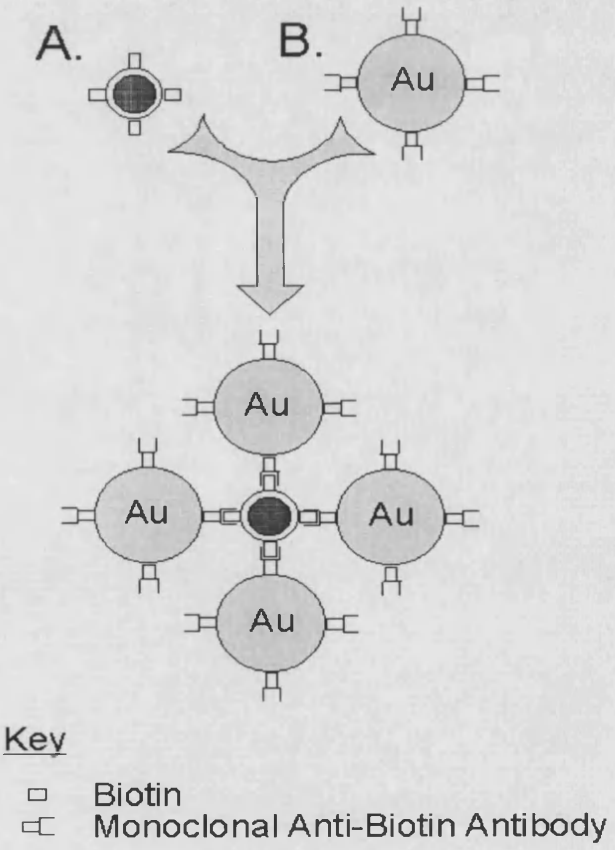

Figure 9 Schematic showing the production of hybrid organic/inorganic aggregates from A) Biotinylated ferritin and B) Gold particles with conjugated antibodies, using antibody specificity.

This approach does not have the inherent flexibility of the 'antigen engineering' approach introduced in the previous work, but this is compensated for by the ease of aggregate fabrication. This system also lacks the potential for formation of precisely positioned spatial elements that a topologically engineered antigen may allow, due to the random binding of the antibody to the surface of each ferritin molecule. One aspect of the system employed here is the ability to functionalise the surface of ferritin, producing a variety of potential antigenic binding sites. It was shown that two very different synthetic strategies could be performed, resulting in both DNP and biotin functionalised ferritin molecules. Although the DNP functionalised ferritin displayed a tendency for self aggregation, rendering the molecule unsuitable for the protocol employed here, it nevertheless demonstrates an alternative strategy in the chemical modification of ferritin.

A possible advantage of this system is the production of a range of inorganic/organic solids exhibiting very close packed structures, due to the difference in the diameters of the ferritin and gold particles. These 'radius ratio' packing schemes were investigated in this work by the use of gold particles that were allowed to age, resulting in particles with average diameters of 20nm, these diameters being much larger than those of the ferritin molecules. The results by TEM show very densely packed structures, comprising both ferritin and gold particles, and high resolution images invariably showed gold particles closely associated with ferritin molecules.

Ferritin represents a very versatile molecule and permits the fabrication of a wide range of nanocomposite materials (Chapter 1 : Introduction). This may allow the synthesis of a variety of magnetic and non-magnetic hybrid structures, comprising antibody conjugated metallic particles and ferritin molecules with cores composed of distinct inorganic materials. These structures could be 'tuned' to provide new and novel materials possessing unique electronic properties. For example, the mineralization of the interior of ferritin with materials having a very different band gap to that of gold, may allow the synthesis of a macroscopic electron transfer device, which could find photosynthetic applications. The bio-compatibility of such structures also permits a number of possible bio-medical materials.

6.5 References

1 J.Wen, G.L.Wilkes (1996) Organic/Inorganic hybrid network materials by the sol-gel approach, *Chem.Mater.*, **8**, p1667-1681

2 W.F.Doyle, D.R.Uhlmann (1988) *Ultrastructure Processing of Advanced Ceramics*, eds. J.D.McKenzie, D.R.Ulrich, Wiley, New York, p795-799

3 M.J.Michalcyzk, K.G.Sharp (DuPont), 1995, *US Patent 5548051*

4 S.Moss, M.Noh, K.Jeong, D.H.Kim, D.C.Johnson (1996) Synthesis of designed W-WSe_2 heterostructures from superlattice reactants, *Chem.Mater.*, **8**, p1853-1857

5 H.Shi, T.Lan, T.J.Pinnavaia (1996) Interfacial effects on the reinforcement properties of polymer - organoclay nanocomposites, *Chem.Mater.*, **8**, p1584-1587

6 S.L.Burkett, S.Mann (1996) Spatial organisation and patterning of gold nanoparticles on self assembled bio-lipid tubular templates, *J.Chem.Soc.Comm.*, **3**, p321-322

7 N.D.Kumar, G.Ruland, M.Yoshida, M.Lal, J.Bhawalker, P.N.Prasad (1996) Novel approaches for 3D optical data storage in polymeric media, *Mater. Res. Soc. Symp. Proc.*, **435**, p535-540

8 U.Schubert (1994) Catalysts made of organic-inorganic hybrid materials, *New J.Chem.*, **18**, p1049-1058

9 J.I.Zink, J.S.Valentine, B.Dunn (1994) Biomolecular materials based on sol-gel encapsulated proteins, *New J.Chem.*, **18**, p1109-1115

10 S.Mann (1997) Biomineralization : the form(id)able part of bio-inorganic chemistry, *J.Chem.Soc-Dalton Trans.*, **21**, p3953-3961

11 S. A. Davis, S. L. Burkett, N. H. Mendelson, S. Mann (1997) Bacterial Templating of Ordered Macrostructures in Silica and Silica-Surfactant Mesophases, *Nature,* **385**, p420-423

12 E.L.Mayes, F.Vollrath, S.Mann (1998) Fabrication of magnetic spider silk and other silk composites using inorganic nanoparticles, *Adv.Mater.*, **10**, p801-805

13 B.Xiu, N.D.Chasteen (1991) *J.Biol.Chem*, **266**, p19965-19970

14 J.G.Wardeska, B.Viglione, N.D.Chasteen (1986) Metal ion complexes of Apo-ferritin, *J.Biol.Chem.*, **261**, p6677-6683

15 G.C.Ford, P.M.Harrison, D.W.Rice, J.M.Smith, A.Treffry, J.L.White, J.Yariv (1984) Ferritin, design and function of an iron storage protein, *Phil.Trans.R.Soc.Lond.* B., **304**, p551-585

16 T.Douglas, D.R.Rippol (1998) calculated electrostatic gradients in recombinant human H-chain ferritin, *Protein Science*, **7**, p1083-1091

17 L.Hudson, F.C.Hay (1989) *Practical Immunology*, 3rd ed., Blackwell Scientific Publications

18 http://wunmr.wustl.edu/EduDev/Ferritin/xray.html

VIRAL SYSTEM

The particular field which excites me is the division between living and non-living as typified by proteins, viruses, bacteria and chromosome structure. The eventual goal, which is somewhat remote, is the description of these in terms of their structure.

Francis Crick

Chapter 7

Inorganic-Organic Nanotube Composites From Template Mineralization of Tobacco Mosaic Virus

...there is a God precisely because Nature itself, even in chaos, cannot proceed except in an orderly and regular manner

Immanuel Kant

7.1 Introduction

The processing of nanoscale materials into higher order microstructures necessitates the use of building blocks which can be assembled on longer length scales, for example 'nanotubes'[1]. One possibility is to exploit the synthesis[2,3] or self-assembly[4] of functionalised nanotube templates, for the production of anisotropic hybrid materials.

This chapter addresses the problem of constructing nanomaterials with high aspect ratios, by using a tubular virus known as tobacco mosaic virus. The virus is shown to act as a template for the production of a variety of inorganic/organic nanotube composites and is also shown to exhibit self assembly properties, allowing the fabrication of higher order structures.

7.1.1 Nanotubes

Carbon Nanotubes. Nanotubes are defined as tubular structures with nanometer dimensions. Nanotubes receiving most interest are those comprised solely of carbon, discovered by Sumio Iijima[5]. Carbon nanotubes are essentially small graphite sheets rolled into tubes and capped with semi-spherical buckminsterfullerene molecules at opposing ends.

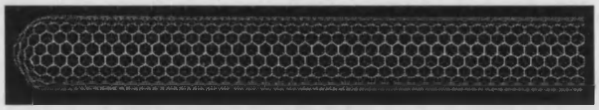

Figure 5 Computer generated image of a carbon nanotube (http://chemistry.miningco.com/library/weekly/aa082498)

Carbon nanotubes are synthesised under extreme conditions, such as high temperature and intense pressure, the resulting nanotubes possessing unique properties, such as a tensile strength greater than steel, conductivity equal to copper and unsurpassed heat conductivity[6]. These properties ensure the continued interest of carbon nanotubes, for example in the fabrication of nanotube based transistors[7], tips for Atomic Force Microscope[8] and nanotube composites[9].

Non-Carbon Nanotubes. Self-organisation of nanotubular structures, made of materials other than carbon, is a field of great interest, exemplified by the following statement by F.Giulieri[10]

'*Much attention has been given to microstructures with cylindrical geometry such as rods, tubules and ribbons. Some of these structures have potential as building blocks in biomolecular engineering (delivery vehicles, microsurgery materials, etc.) or as novel elements of molecular devices for information processing and signal generation in materials sciences (composites, liquid crystal media for electroptics and microelectronics)*'.

There are numerous chemical methods of synthesising non-carbon nanotubular materials, leading to materials such as organic fibres[11], silica fibres[4] and multi-element coaxial nanocables[12]. Self assembled nanotubular structures have also been synthesised that consist of cyclic peptides able to span plasma membranes[13], with possible applications ranging from cytotoxic agents to novel drug delivery agents.

Template synthesis of nanotubular composites represents an alternative method of fabrication, with a great variety of templates employed, including nucleopore membranes[14,15], lipids[16], mesoporous MCM[1] and even multi-walled carbon nanotube composites, formed through capilliary action[18]. The potential uses of nanotubular templates in materials synthesis is shown schematically in Fig 2.

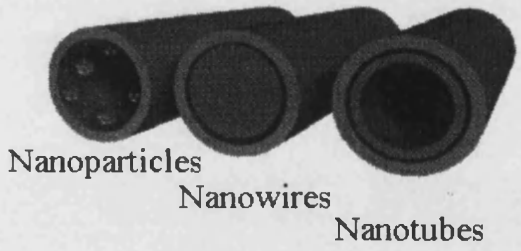

Figure 6 Schematic showing the possible templating strategies employed in the fabrication of non-carbon nanotube composites[1].

Recently, biologically inspired alternatives to nanotube fabrication have emerged, including the use of enzymes. Glutamine synthetase from *E.Coli*, is a toroidal shaped enzyme that has been shown to self assemble into protein tubes in the presence of divalent ions[18]. Specific amino acid substitutions, by site directed mutagenesis, also induce the enzyme to aggregate laterally, forming two dimensional protein sheets.

7.1.2 Viruses

Viruses are genetic elements that have, through the process of evolution[19], acquired a protein coat ('capsid') and are able to exist independently of normal cellular metabolism, yet still depend on cellular machinery for replication. All viruses have only a limited amount of nucleic acid in their genome and therefore parasitise host cells.

Viruses are a unique group of infectious agents, whose distinctiveness resides in their simple, acellular organisation and pattern of reproduction. A complete viral particle (or virion) consists of one or more molecules of DNA or RNA, enclosed in a coat of protein and sometimes other layers. These additional layers may be very complex, containing carbohydrates, lipids and additional proteins. Viruses can exist in two phases, extracellular and intracellular[20]. Virions, the extracellular phase, possess few, if any, enzymes and cannot reproduce independently of living cells. In the intracellular phase, viruses exist primarily as replicating nucleic acids that induce host metabolism to synthesise virion components; complete virions eventually being released. A vast oversimplification of viral replication starts with the shedding of the capsid upon cellular infection, followed by replication of the viral chromosome inside the host cell to form identical copies. After the synthesis of new capsid proteins, from virally encoded messenger RNA, formation of new viral particles occurs through spontaneous self-assembly of the capsid proteins around each individual viral chromosome.

Virus morphology has been studied intensely over the past decades, progress coming from a variety of techniques such as electron microscopy, and virions have been discovered ranging in size, from about 10 to 300nm in diameter. The largest viruses, such as poxviruses, are about the same size as the smallest bacteria and can be observed in a light microscope[21]. The variety of viral morphologies encountered include:

1) Icosahedral capsids. These capsids appear spherical under the electron microscope. Examples include satellite tobacco mosaic virus and cowpea chlororotic virus.
2) Helical capsids which may be either flexible or rigid. An example is tobacco mosaic virus

3) Enveloped viral structure. Consisting of a membranous layer surrounding the nucleocapsid. Enveloped viruses have a roughly spherical shape, but are somewhat variable. Examples include influenza virus and HIV.

4) Complex viruses have a capsid symmetry that is neither purely icosahedral nor helical. They may possess tails or have complex, multi-layered walls surrounding the nucleic acid. Examples include bacteriophages and poxviruses.

7.1.3 Tobacco Mosiac Virus

Tobacco mosaic virus (TMV) is a cylinder of protein arranged around a helical RNA core (Fig. 2). TMV has a structure consisting of 2130 identical protein subunits, arranged in a helical motif around a single strand of RNA, forming a hollow protein tube, 300nm in length, 18nm in diameter, with a 4nm wide channel through the centre of the virion[22-23]. The RNA is buried deep in the protein, each protein subunit interacting with three nucleotides. TMV is a remarkably stable virus, structural integrity retained at temperatures of up to 90°C and pH extremes.

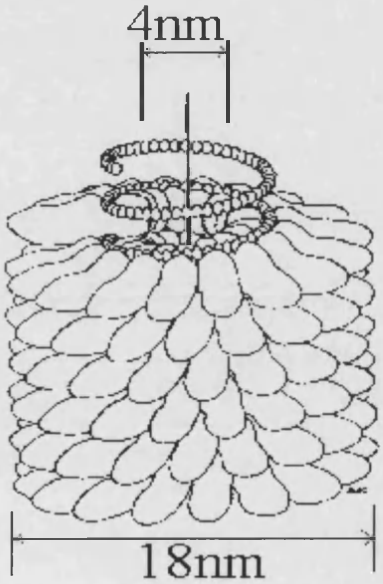

Figure 2 Schematic diagram of Tobacco Mosaic Virus (TMV), showing the helical symmetry and central channel of the capsid and overall dimensions[24]

The information for forming the complex TMV macromolecule is contained in the subunits themselves and TMV particles are able to self assemble in a test tube from RNA and purified protein molecules. TMV can be dissociated into its protein and RNA components by agents such as acetic acid. In 1955, Heinz Fraenkel-Conrat and Robley Williams[24] showed that the dissociated coat subunits and RNA of TMV spontaneously reassemble, under suitable conditions, into viral particles indistinguishable from the original TMV. This was the first known example of the self assembly of an active biological structure.

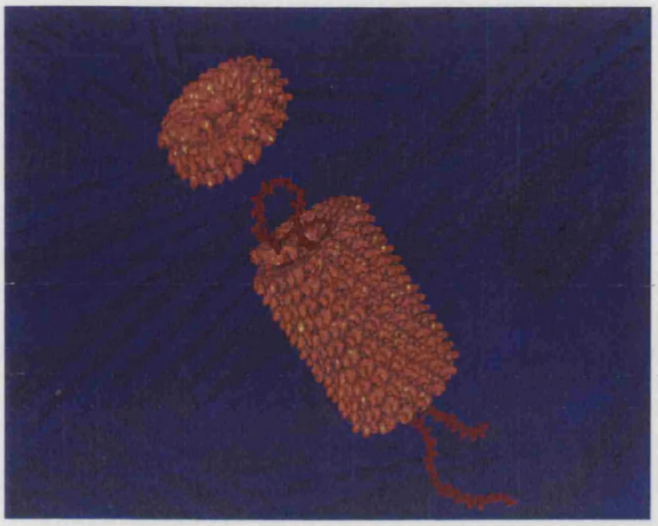

Figure 3 Computer generated reconstruction of TMV, showing the addition of a single 'lock-washer'. Negatively stained TMV particles can be seen in the background. (Reproduced by kind permission of Prof. G.Stubbs www.molbio.vanderbilt.edu)

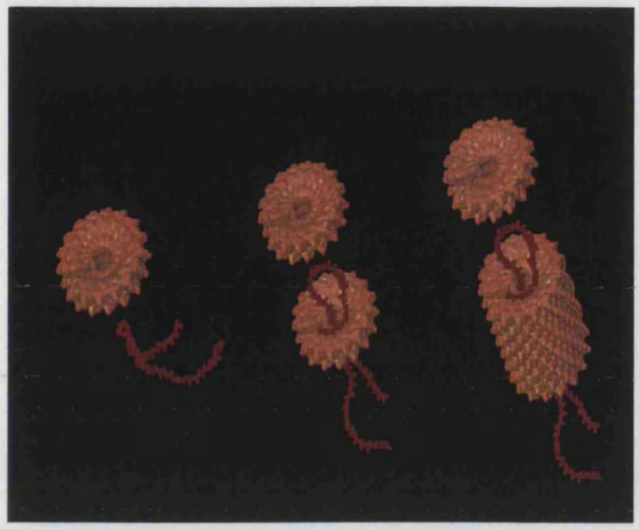

Figure 4 Computer generated images of TMV, showing the stages of self assembly. (Reproduced by kind permission of Prof. G.Stubbs :www.molbio.vanderbilt.edu)

The mechanism of TMV self assembly was elucidated by Aaron Klug[25]. The coat protein alone forms a two-layered disc consisting of 34 subunits, where each layer of the disc is a ring of 17 subunits, which is nearly the same as a single turn in the TMV helix. A critical property of the disc is that its subunits can slide over each other, forming a two-turn helix called a 'lockwasher' (Fig. 3). The disc interacts more rapidly with TMV RNA than with foreign RNA and assembly starts with the insertion of an RNA loop into the central hole of the two layered protein disc, the protein disc is then transformed into the lock-washer. New discs then add to the looped end of the RNA and the TMV particle proceeds to assemble in this stepwise fashion (Fig. 4).

7.2 Materials and Methods

Tobacco mosiac virus, the *Vulgare* (or U1) strain, was obtained from Professor Gerald Stubbs, Vanderbilt University, Nashville, Tennessee. The TMV concentration was 30mg/ml and stored in 10mM sodium phosphate buffer at pH7. TMV was diluted to concentrations of 0.1mg/ml or 0.5 mg/ml for use in mineralization experiments.

I) CdS TMV

A TMV suspension (0.1mg/ml) was incubated in a (2-([tris(hydroxymethyl) methyl)] amino)-1-ethane-sulfonic acid) (TES) buffered solution of 10mM $CdCl_2$ (pH 7.2) for 6 hours. Droplets of these solutions were placed on a parafilm-covered glass slide positioned in a vacuum dessicator. H_2S gas was allowed to slowly diffuse into each droplet and aliquots were removed at varying time intervals over a period of 1 hour and air-dried onto nickel TEM grids.

II) PbS TMV

A suspension of TMV (0.1mg/ml) was incubated in a TES buffered solution (pH5.5) of 1mM $Pb(NO_3)_2$ for 1 hour. H_2S was allowed to diffuse through the solution at a steady rate and 0.4ml aliquots of the resultant black suspension were added to a centrifugal filtration device (0.2μm Mol.Wt cut off, Millipore) spun at 5000 rpm for 30 minutes, in order to remove extraneous particulate matter. The filtrate was re-suspended in buffer, concentrated and aliquots added to TEM grids for analysis.

III) SiO_2 TMV

A suspension of TMV (0.1mg/ml) was added to an ethanol/water mixture (1:1) which was then acidified to pH 2.5 with dilute HCl. Tetraethoxysilane (TEOS) was added and the solution left to stir for 24 hours. Aliquots (0.1ml) were removed and centrifuged in a Centricon 10 centrifugal filtration device (Mol. Wt. Cut-off 10 Kda, Millipore) designed for a microcentrifuge. Distilled water (0.05ml) was added and the pellet re-suspended and then re-centrifuged. This procedure was undertaken three times to remove excess TEOS.

IV) Ag TMV

A suspension of TMV was added to a 1mM solution of $Ag(NO)_3$ and the solution left to stir for a period of 72 hours. Hydroquinone (10mM, Aldrich) was added and the solution left to stir in the dark for 1 week. Aliquots of the resultant brown solution were filtered in a Centricon-10 (10Kda Mol.Wt cut off, Millipore) spun at 5000 rpm for 30 minutes and TEM grids prepared.

V) Fe TMV

A suspension of TMV was mixed with an acidic solution containing 1mM $(NH_4)_2SO_4 \cdot FeSO_4 \cdot 6H_2O$ and 2mM $FeCl_3$. The solution was left to stand for 2 minutes. 1M NaOH was added dropwise to give a final pH of 9, producing a brown precipitate. An aliquot (0.4ml) of the mineralized suspension was placed in a centrifugal filtration device, with a 0.2μm filter (Millipore). The suspension was then centrifuged at 5000 rpm for 30 minutes. The filtrate was re-suspended in 0.4ml of buffer and concentrated. Droplets of the re-suspended material were placed on nickel TEM grids, which were subsequently washed with distilled water. The remaining mineralized TMV suspension was left for 6 months at room temperature and then filtered, washed and analysed by TEM.

7.3 Results and Discussion

Two methods were employed to directly image native TMV, these being negative staining, with a 2% aqueous solution of uranyl acetate, (Fig 5) and metal shadowing with tungsten (Fig 6). Both methods show explicitly the morphology of the TMV particle. Negative staining of the sample revealed the hollow tube nature of the capsid, through penetration of the stain into the central channel. The diameter of each virion is verified

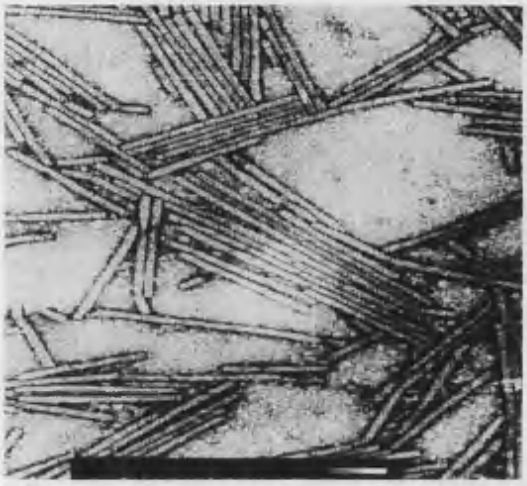

Figure 5 TEM micrograph of uranyl acetate stained TMV rods. Scale bar 100nm.

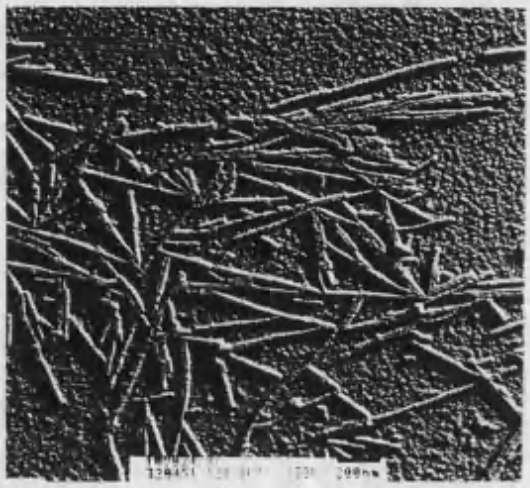

Figure 6 TEM of a tungsten shadowed specimen of TMV, explicitly showing the tubular morphology of each protein rod. Scale bar 200nm.

to be 18nm, with a central channel of 4nm. The length of TMV has previously been shown to be 300nm, but Fig. 5 reveals virions with a range of lengths. This effect is due to the complementarity of the ends of each particle, which promotes the formation of longer aggregates as each virion, upon storage, tends to pick up or lose subunits (personal communication with G.Stubbs). This results in TMV particles displaying lengths that deviate significantly from that for native TMV particles. The metal shadowing also gives a greater impression of the tubular morphology of TMV. Both images demonstrate a tendency of TMV to aggregate side by side when mounted on the TEM grid and also a slight tendency for end-to-end aggregation.

Cadmium Sulfide TMV

Tobacco mosaic virus, at a concentration of 0.1mg/ml, incubated for 24 hours in a buffered solution of 10mM $CdCl_2$, showed no sign of protein denaturation, as inferred from the transparent nature of the solution. Indeed, samples incubated for several months displayed none of the characteristic signs of protein degradation and examination of the solution by TEM revealed intact TMV particles. Addition of aliquots of this solution to TEM grids and subsequent examination with TEM, revealed large networks of TMV (Fig. 7), aggregated in a radial fashion around a dark central 'hub'. S-mode EDXA revealed this hub to have a high concentration of cadmium.

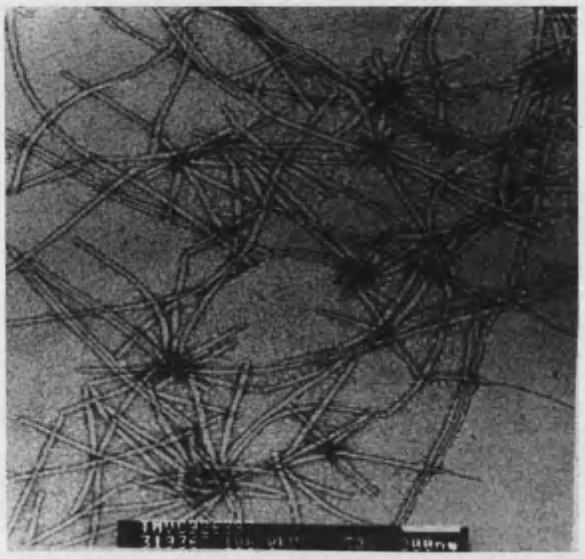

Figure 7 TEM micrograph of TMV incubated with cadmium, showing the formation of TMV 'networks', scale bar 200nm.

Droplets of the buffered TMV/$CdCl_2$ solution (20µl) were regularly spaced on a parafilm covered microscope slide, to ensure a surface tension induced spherical shape to each droplet. H_2S was allowed to diffuse into the droplets and at regular time intervals each droplet, which displayed increasing intensities of yellow, was removed using a micro-pipette and transferred directly to a nickel TEM grid, the grids were then washed several times in a drop of distilled water. TEM examination of each grid revealed the presence of mineralized tubular structures comprised of an electron dense outer crust around an 18nm pellucid core (Fig 8a). The length of the tubular structure lying transverse, with respect to the micrograph, has a length of approximately 730nm.

EDXA of these tubular structures revealed the presence of both cadmium and sulfur, with a peak for nickel arising due the TEM grid (Fig. 8b). Selected area electron diffraction (SAED) of individual tubes (Fig. 8b, inset) confirmed the surface to be composed of a regular crust of cadmium sulfide nanocrystals (d-spacings 0.336, 0.206, 0.176, 0.133, 0.118nm, corresponding to the zinc blende structure, Fig. 8c).

A

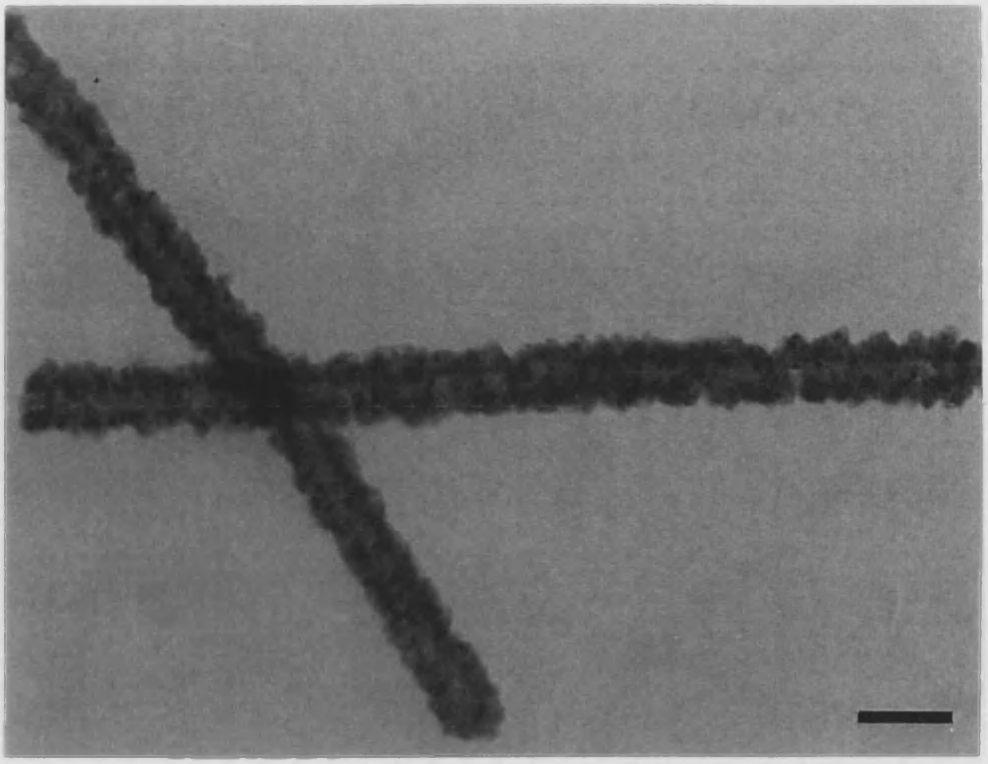

B

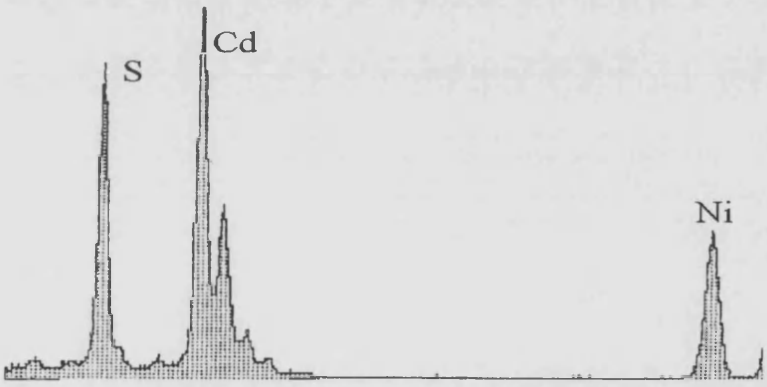

C

Electron Diffraction d-spacings for Zinc Blende CdS (nm)	Electron Diffraction d-spacings for CdS TMV (nm)
3.38	3.38
2.07	2.05
1.75	1.75
1.33	1.33
1.18	1.18

D

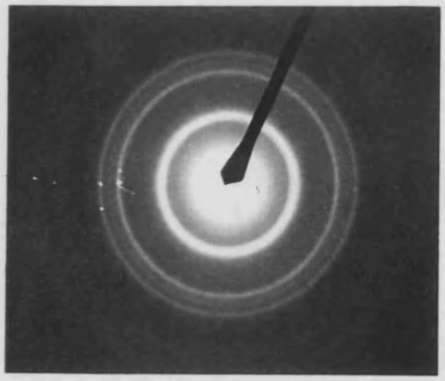

Figure 8. A) TEM micrograph showing the specific mineralization of the surface of TMV with cadmium sulfide, Scale bar 50nm. B) EDXA verifying the presence of peaks for cadmium and sulfur for the micrograph shown above. C) Table comparing the d-spacings of the zinc blende polymorph of CdS with those obtained from the mineralized TMV sample shown in the above micrograph. D) Electron diffraction pattern from CdS TMV.

The diffraction pattern also revealed the mineralized crust to possess no crystallographic orientation, due to the concentric ring pattern. High resolution TEM (HRTEM) was employed to visualise the crystalline nature of the tubules. Fig. 9 shows a high resolution image of the surface of one of the tubular structures. The arrows indicate nanocrystals comprising the mineral crust and a d-spacing measured for these lattice fringes was found

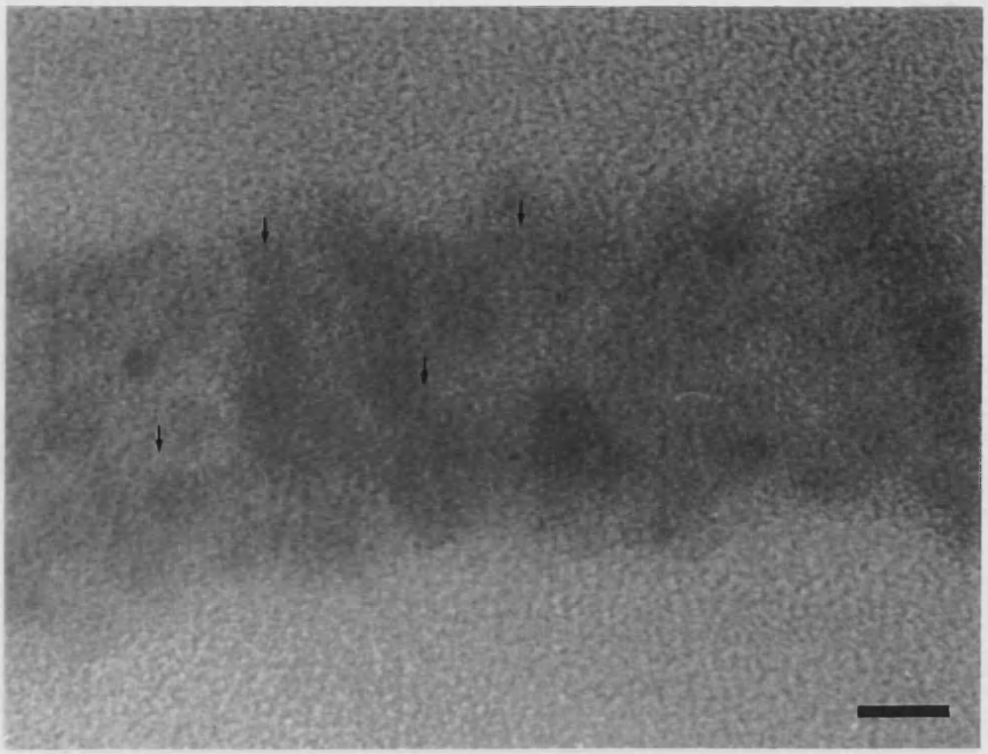

Figure 9 HRTEM micrograph revealing the nanocrystalline nature of the surface of the CdS mineralized TMV particle. Arrows show nanocrystals. Scale bar 5nm.

to be 3.4Å, corresponding to the 110 face of crystalline zinc blende

These data suggest that the incubation of TMV particles in a cadmium chloride solution, and subsequent exposure of this solution to H_2S, produces specific mineralization of the surface of individual TMV particles, culminating in the formation of TMV/CdS nanotube composites. A striking example of the effect of mineralization on the structure of TMV can be seen in Fig. 8a. This micrograph shows both mineralized virions, in the foreground, together with unmineralized virions in the background. The mineralization of TMV was confirmed by EDXA, with electron diffraction and HRTEM also revealing the inorganic phase to be composed of individual nanocrystals, with diameters less than 10nm. This system also demonstrates the potential for the formation of higher ordered self assembled structures, as seen in Fig. 8a. Here, mineralized TMV

composites can be seen, possessing lengths of over 700nm. This suggests that the CdS system may induce further aspects of end-to-end self assembly, resulting in structures with very high aspect ratios. TMV particles have been shown to self assemble in this manner under neutral conditions, due to the complementarity of each particle (personal communication with G.Stubbs), but this process may be accentuated due to the ionic environment of the buffered solution. There also exists a calcium binding site at the ends of TMV and this may bind cadmium due to their similar ionic radii, resulting in a cross-linking effect.

The diffusion of H_2S into the cadmium incubated TMV solution results in a relatively wide range of mineralization states, although some degree of control can be exerted when the flow of H_2S is kept steady and sample removed at regular time intervals. Two contrasting states of mineralization are shown in Fig. 10. Fig. 10a demonstrates that the mineralization process of TMV can be arrested at any time, resulting in TMV particles with a relatively thin inorganic coat. The process can also be allowed to proceed, producing very heavily mineralized virions (Fig. 10b). A very interesting aspect of the CdS mineralization of TMV is the ability of the virions to self assemble into higher order structures. Fig. 10c and d show examples of radial and linear modes of self assembly respectively. The radial mode of self assembly was observed in cadmium incubated TMV (Fig. 7) and it can be inferred that this structure was mineralised *in situ,* giving the composite seen in Fig. 10c. The micrograph also demonstrates the effect of TMV template mineralization compared to bulk precipitation, the latter revealed as spherical crystals of CdS next to the mineralized TMV particles. The linear mode of self assembly is dramatically seen in Fig. 10d, showing a self assembled CdS/protein composite over a micron in length.

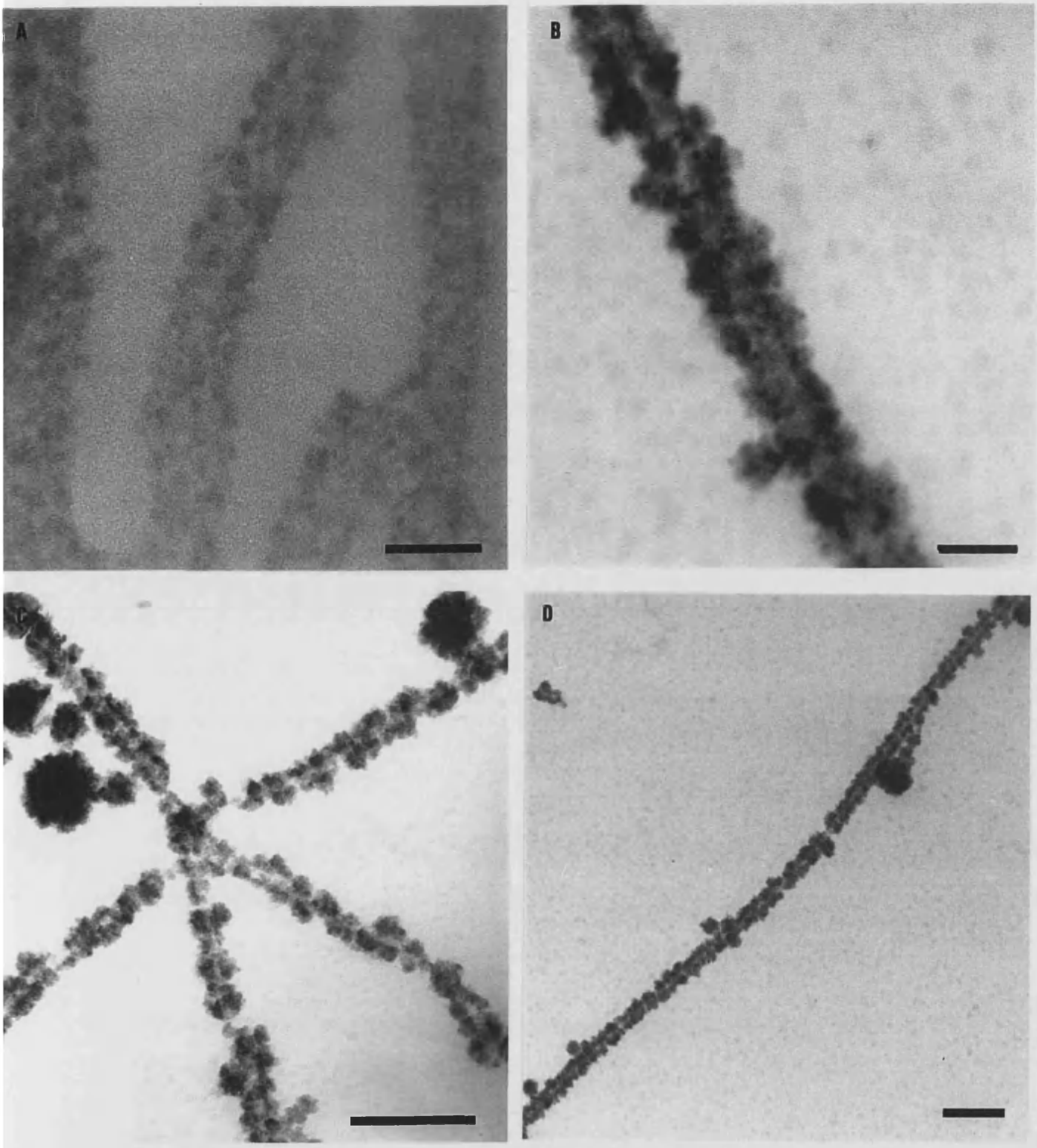

Figure 10 A) TEM micrograph showing an early stage in the mineralization process. Scale bar 50nm B) Micrograph showing a much later stage of mineralization indicated by the electron dense mineralized surface of the virion. Scale bar 50nm C) Radial self assembled structure mineralized *in situ*. Scale bar 200nm. D) Higher order linear self assembled TMV/CdS nanocomposite. Scale bar 200nm.

II) Lead Sulfide TMV

Incubation of TMV (0.1mg/ml) in buffered $Pb(NO_2)_3$ for 24 hours, with subsequent controlled exposure to H_2S, instantaneously produced a black precipitate. Aliquots of the precipitate were filtered in a centrifugal filtration device with a diameter greater than 0.5μm, to remove bulk precipitate. Droplets of the supernatant were then added to a TEM grid for analysis. Examination of these grids revealed tubular composite structures, analogous to those found in the CdS TMV system, displaying an extremely opaque, irregular surface (Fig. 11).

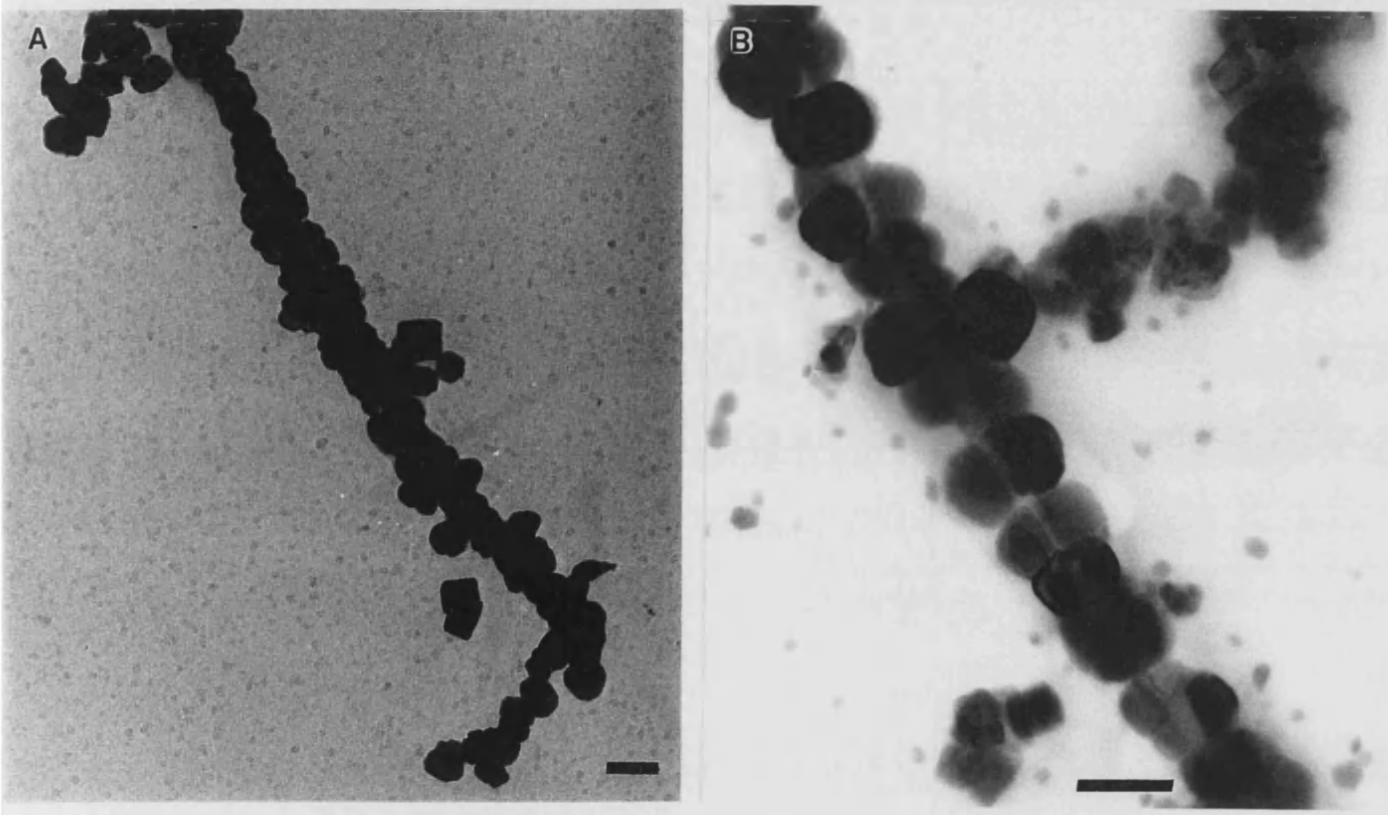

Figure 11 A) Micrograph of PbS mineralized TMV system. Scale bar 50nm B) PbS mineralized TMV, showing regular arrangement of elliptical particles along the length of the virion. Scale bar 50nm.

The surface of these tubular structures comprised a variety of rhombic and elliptical morphologies.

EDXA confirmed the presence of lead and sulfur (Fig. 12a) and selected area diffraction patterns gave a concentric ring pattern (Fig. 12bii), indicating non-crystallographic orientation of the nucleated PbS crystals on the surface of each virion. SAED data were consistent with single domain PbS nanocrystals with the rock salt structure (*d*-spacings 0.344nm (111), 0.295nm (200), 0.209nm (220), 0.178nm (311))(Fig. 12bi).

A

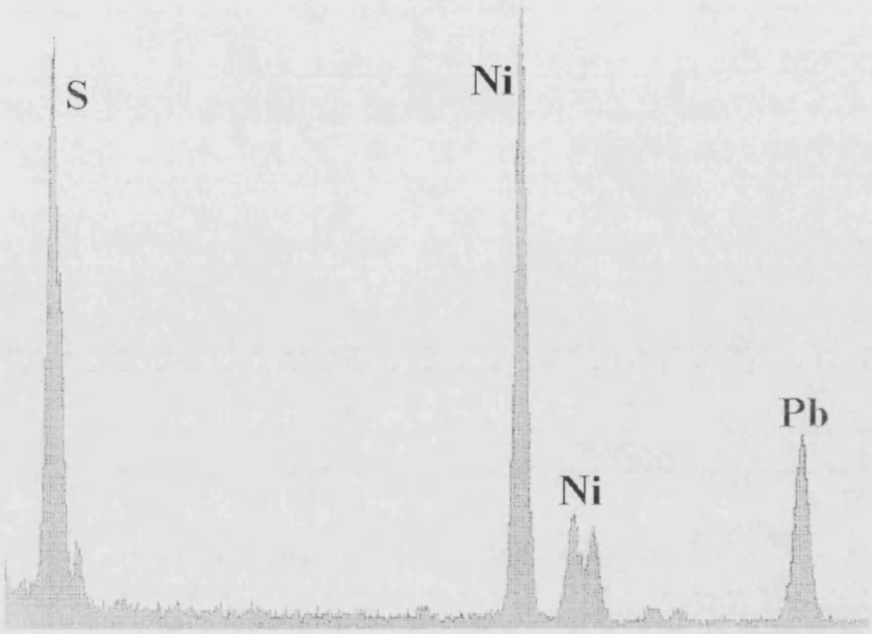

B i)

d-Spacings for the rock salt structure of PbS (nm)	d-Spacings for the PbS mineralized TMV (nm)
3.44	3.44
2.95	2.90
2.09	2.12
1.78	1.78

ii)

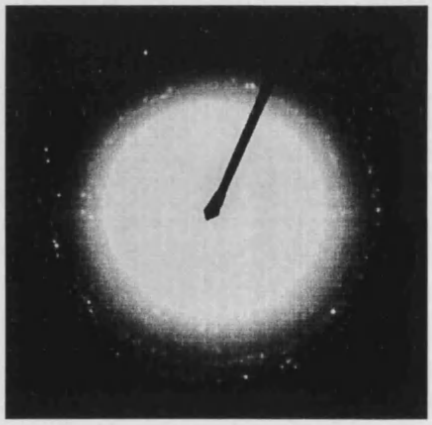

Figure 12 A) EDXA of PbS mineralized TMV B)i) Table comparing the d-spacings of rock-salt PbS to PbS mineralized TMV C) SAED pattern obtained for PbS mineralized TMV.

HRTEM was used to investigate the crystalline nature of the mineralized surface (Fig.13). Images obtained show the mineralized crust of individual virions to be comprised of nanocrystals which were up to 30nm in size and either prismatic or irregular in shape.

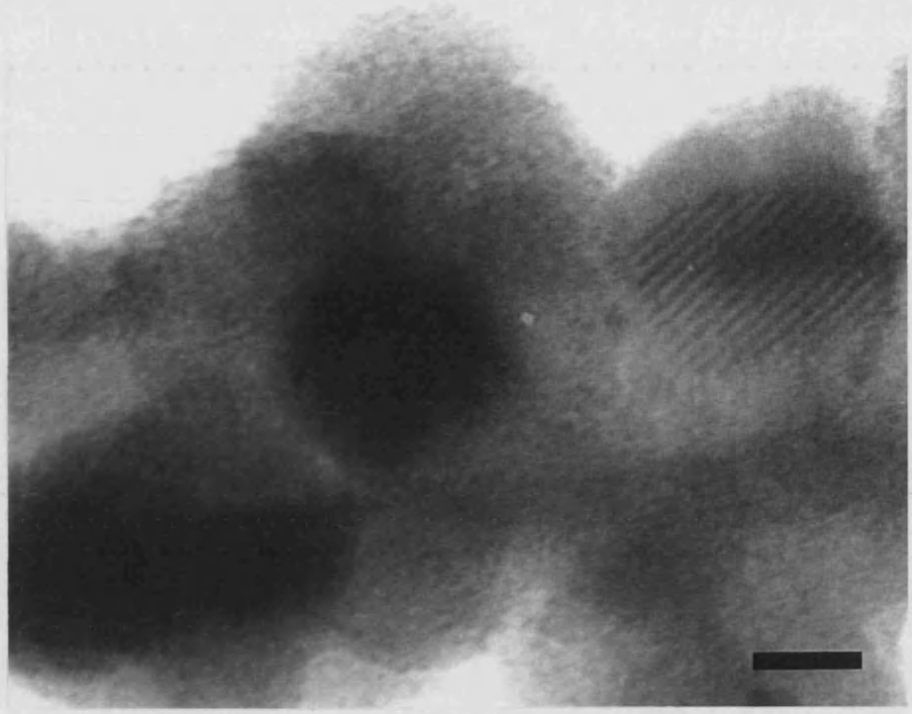

Figure 13 HRTEM micrograph showing individual nanocrystals of PbS nucleated on the surface of the TMV virion. The lattice pattern seen is the result of the superposition of two lattice planes. Scale bar 10nm

A similar self assembly of mineralized virions was seen in the PbS system as in the CdS system, where mineralized composites with a length of several hundred nanometers was observed. Fig. 11b shows a PbS mineralized TMV virion with a length of over 700nm, which again suggests a composite comprised of at least two self assembled TMV proteins.

These data demonstrate the potential of TMV as a nanoscopic tubular template in the formation of a PbS/TMV nanotube composite. This system also indicates the robust nature of the protein, in being able to retain its three dimensional structure despite incubation with the very strong oxidising agent, $Pb(NO_3)_2$. The self assembly of TMV into inorganic/organic composites was also observed in this system, probably occurring through a similar mechanism as CdS TMV, although the binding of Pb(II) ions to the calcium ion binding site would be excluded. Comparison of the mineral morphology between CdS and PbS mineralized TMV rods may also be explained by the huge differences in ionic radius. The smaller cadmium ions would bind easily to the negative nucleation sites on the virion surface, with little steric hindrance. In contrast, the much larger lead ions would bind to similar nucleation sites but steric hindrance would prevent neighbouring nucleation sites to be occupied by lead ions. It should also be noted that the

PbS TMV composites displayed a more pronounced curvature on comparison with the CdS TMV composite.

III) Fe TMV

Incubation of TMV (0.1mg/ml) in an Fe(II)/Fe(III) solution (mole ratio of 1:2) and subsequent addition of 1M NaOH, to give pH9, resulted in a brown precipitate. An aliquot of this suspension was filtered in a centrifugal filtration device and subsequently examined by TEM. Micrographs revealed tubular structures with an irregular, bulbous, surface morphology (Fig. 14a).

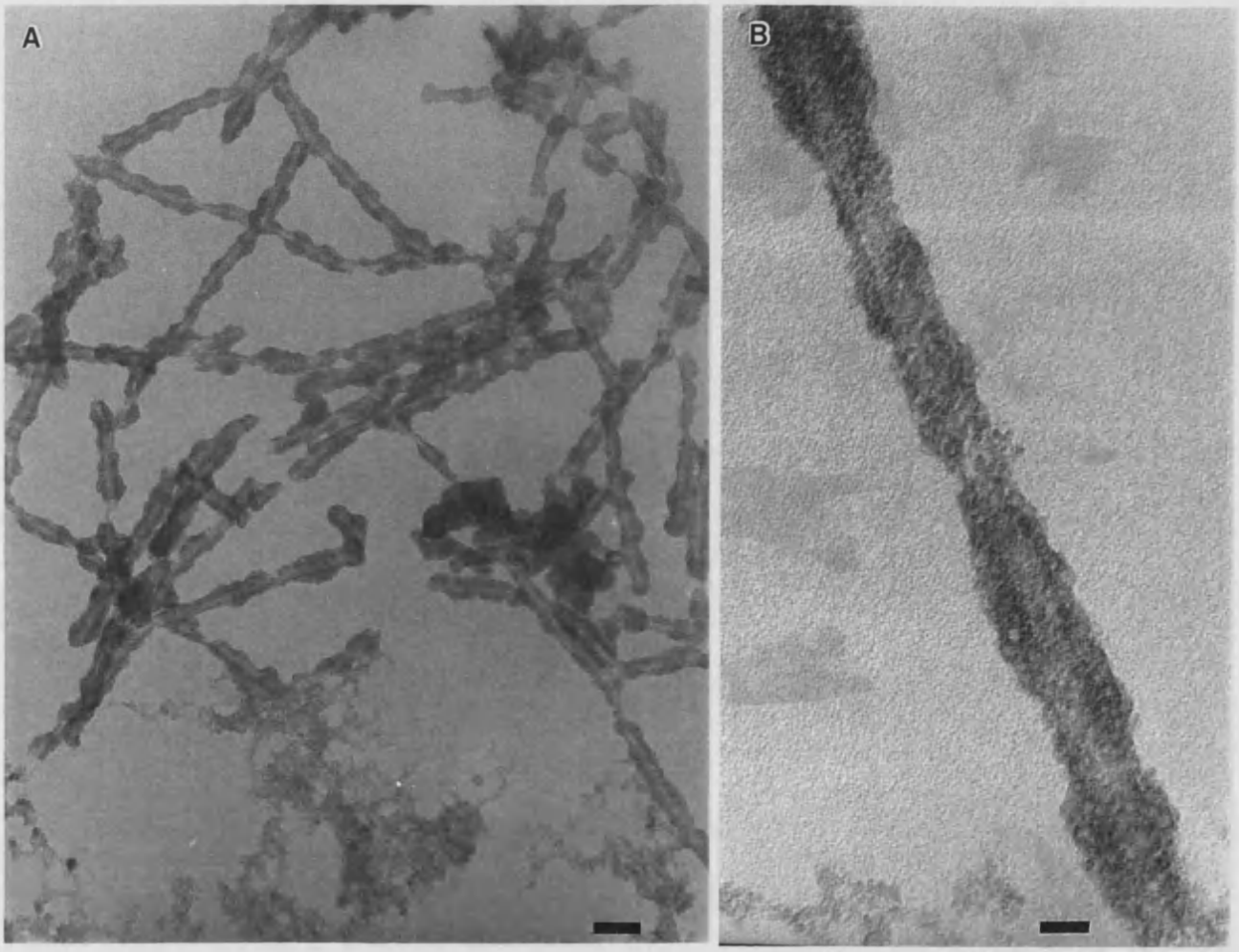

Figure 14 A) TEM micrograph of iron mineralized TMV particles. Scale bar 50nm B) HRTEM micrograph of a single Fe TMV particle, showing the amorphous mineral crust. Scale bar 20nm.

High resolution TEM revealed no lattice images, only an amorphous crust, nucleated on the surface of the virion. EDXA confirmed the presence of iron (Fig. 15a) and diffuse diffraction patterns were obtained by SAED (Fig. 15b).

A B

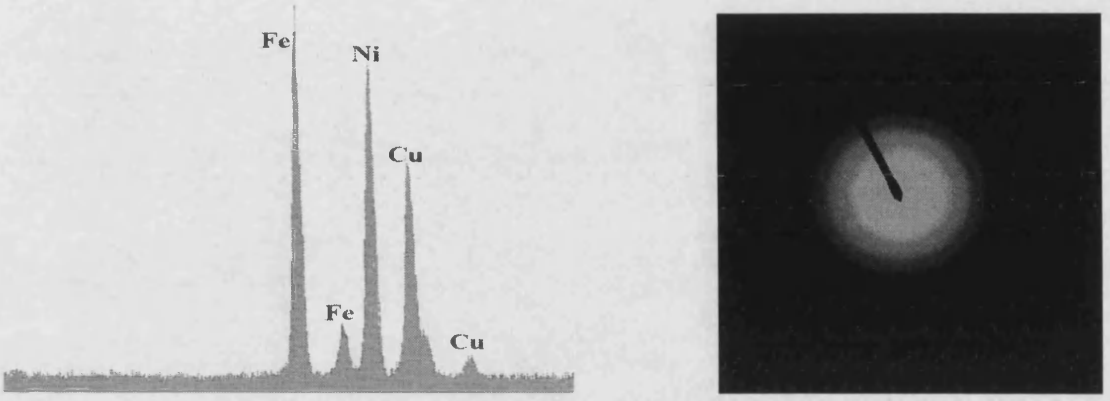

Figure 15 A) EDXA spectrum of Fe TMV verifying the presence of iron. B) SAED pattern of Fe TMV, implying an amorphous structure to the iron.

These data suggest TMV is also able to act as a template in the formation of iron oxide nanotubes under basic conditions, although HRTEM and SAED data indicate the iron mineral to be amorphous.

The iron mineralized TMV sample was allowed to age for 6 months at 4°C and the solution was filtered and re-examined using TEM. Analysis of the iron mineralized system again showed tubular structures, but now the mineral had obtained a more crystalline appearance (Fig. 16a) and HRTEM was able to confirm that the mineralized tubules were now covered in a plate-like mineral (Fig. 16b).

The difference in crystallinity of the iron mineralized TMV particles upon ageing, is demonstrated when observing the electron diffraction pattern, which shows a more crystalline mineral, corresponding to a poorly crystalline iron oxide, ferrihydrite, (d-spacings; 0.254 (110), 0.224 (200), 0.174 (114), 0.147 (106) nm) (Fig. 17).

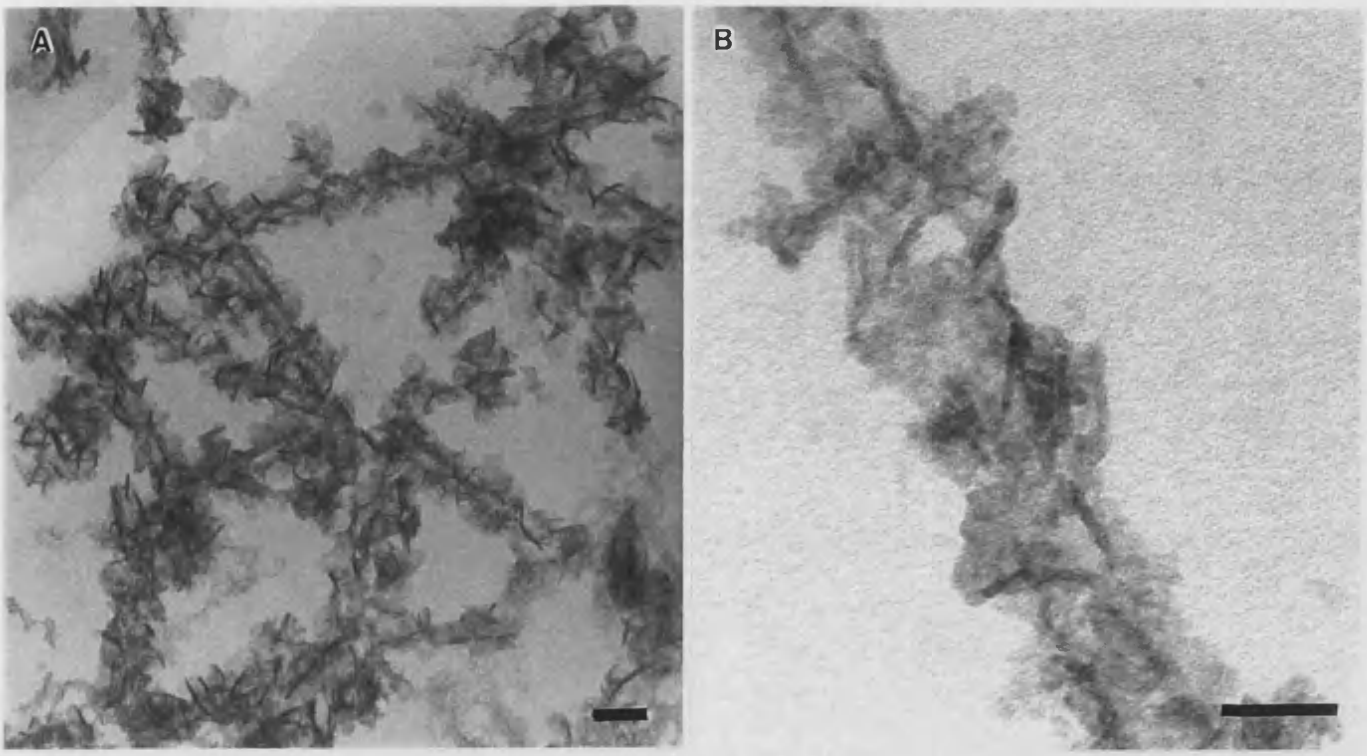

Figure 16 A) TEM micrograph showing iron mineralized TMV particles allowed to age for six months resulting in a more crystalline mineral. Scale bar 50nm B) HRTEM micrograph clearly showing the plate-like nature of the iron mineral nucleated on the surface of a single TMV particle. Scale bar 20nm.

A

d-Spacings for ferrihydrite (nm)	d-Spacings obtained for aged Fe TMV (nm)
3.29	3.20
2.47	2.52
1.93	1.85
1.73	1.70

B

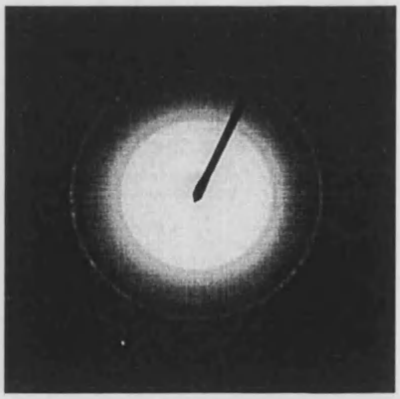

Figure 17 A) Table comparing the d-spacings of ferrihydrite to those for the aged Fe TMV sample. B) SAED pattern obtained for the aged Fe TMV sample, indicating a greater crystallinity due to the emergence of extra rings.

Ageing of the Fe TMV sample appears to promote a greater crystallinity to the iron mineral. This implies the amorphous iron sample may have acted as a template, allowing the continued crystallisation of ferrihydrite, albeit a poorly crystalline form. Further investigation will investigate the protein induced formation of ferrihydrite.

IV) Si TMV

The use of TMV as a template in the formation of a number of TMV nanotube composites has been shown to occur under a wide range of conditions. TMV was now tested as a potential template in sol-gel reactions under acidic conditions. A suspension of the virions was added to a solution of tetraethoxysilane (TEOS) in acidified ethanol and the resulting precipitate filtered and washed prior to TEM analysis. Droplets of this transparent solution were place on TEM grids, the grids blotted and washed several times in distilled water. TEM analysis revealed high contrast images of electron dense tubular particles, with a width of approximately 24nm and lengths >1μm (Fig. 18). This contrasted sharply to native unstained TMV particles, which are visualised as faint grey linear structures. EDXA verified peaks for silicon (Fig. 18, inset), and SAED patterns, corresponding to an amorphous mineral phase, were obtained.

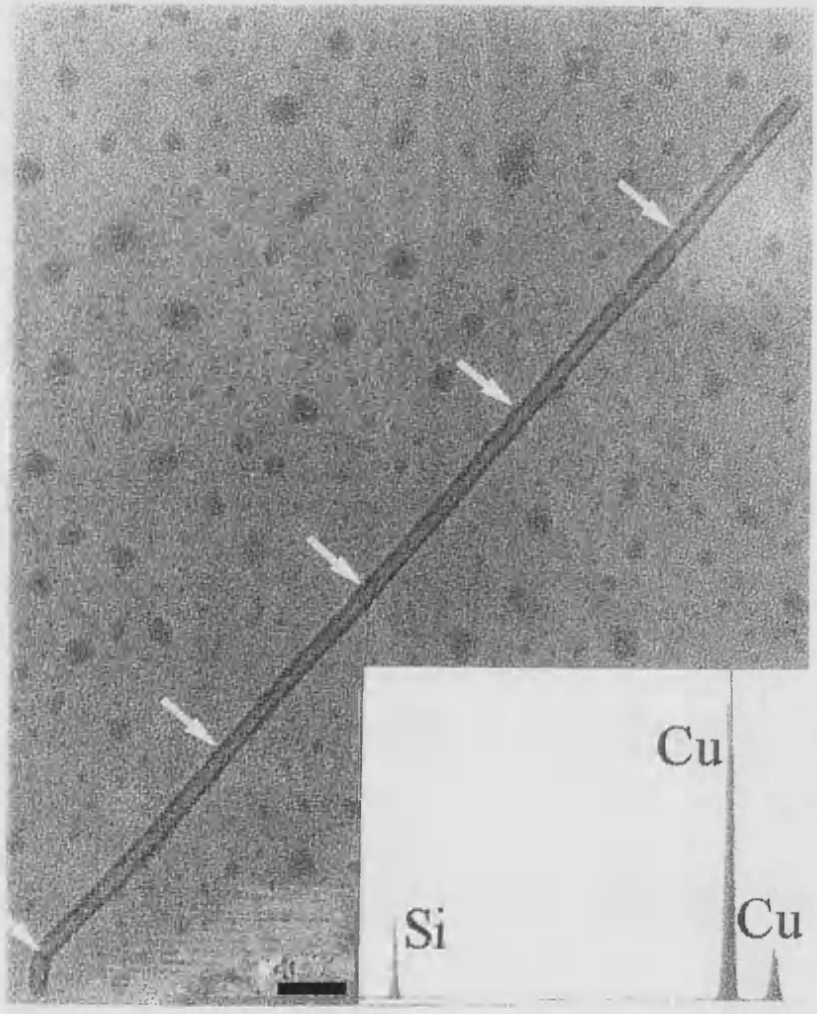

Figure 18 A) TEM micrograph showing a self assembled silica TMV nanotube composite. The ends of the individual constituent TMV particles are indicated by white arrows. Scale bar 50nm. Inset shows EDXA obtained from the structure, verifying the exclusive presence of silica.

These data indicate that the TMV particles are mineralized with a thin (~3nm) wall of silica, which is uniformly deposited along the length of the outer surface of the protein microstructure. The most striking aspect of this system of TMV mineralization was the prevalence of many silicified nanotubes, that were several times the length of individual TMV particles, suggesting that the virions exhibited the same end-to-end self-assembly observed in previous systems. Fig. 18 shows the tubular composite to be comprised of 5 individual TMV tubes, the ends of which are indicated by arrows.

These data suggest that TMV acts as a template in the formation of silica mineralized nanotubes, although further characterisation needs to be undertaken. The self assembly of TMV/silica particles seems most prevalent in this system. This mode of higher order self-assembly has been observed for TMV in the previous mineralized TMV systems and is due to complementary hydrophobic interactions between the dipolar ends of the helical structure. The tendency to aggregate, head-to-tail may be accentuated under the acidic conditions employed here because the mutual repulsion between amino acid residues, Glu50 and Asp77, is minimised by protonation. In the case of silica mineralization from acidic (pH < 3) solutions, there will be strong interactions between the TMV particles and anionic silicate species formed by hydrolysis of TEOS, because the protein surface is positively charged below the isoelectric point, and there are also a significant number of serine and threonine groups on the virion surface, providing a number of hydroxyl groups. One interesting aspect of this self-assembly is that the formation of these higher ordered inorganic/organic structures may be synthesised *in situ,* as the processing of the system, to eliminate excess TEOS, was quite thorough and yet these huge linear structures, over a micron in length, were still obtained.

7.4 Conclusion and Future Work

These results show for the first time the use of a tubular viral template in the production of a wide range of inorganic/organic nanotube and self assembled nanotubular composites. Indeed, the use of a biological template in the fabrication of nanotubes represents an entirely new synthetic strategy in the realisation of anisotropic structures. The surface chemistry of TMV, coupled with the unusual high stability of the protein assembly, provides a structured substrate for the site-specific nucleation of a variety of inorganic solids at a range of pH values and reaction conditions. The helical nature of the capsid assembly also provides a spatially symmetrical arrangement of nucleation sites, facilitating the formation of regularly mineralized virions.

The overall scheme of the utilisation of TMV in the formation of nanotubular composites is seen in Fig 19.

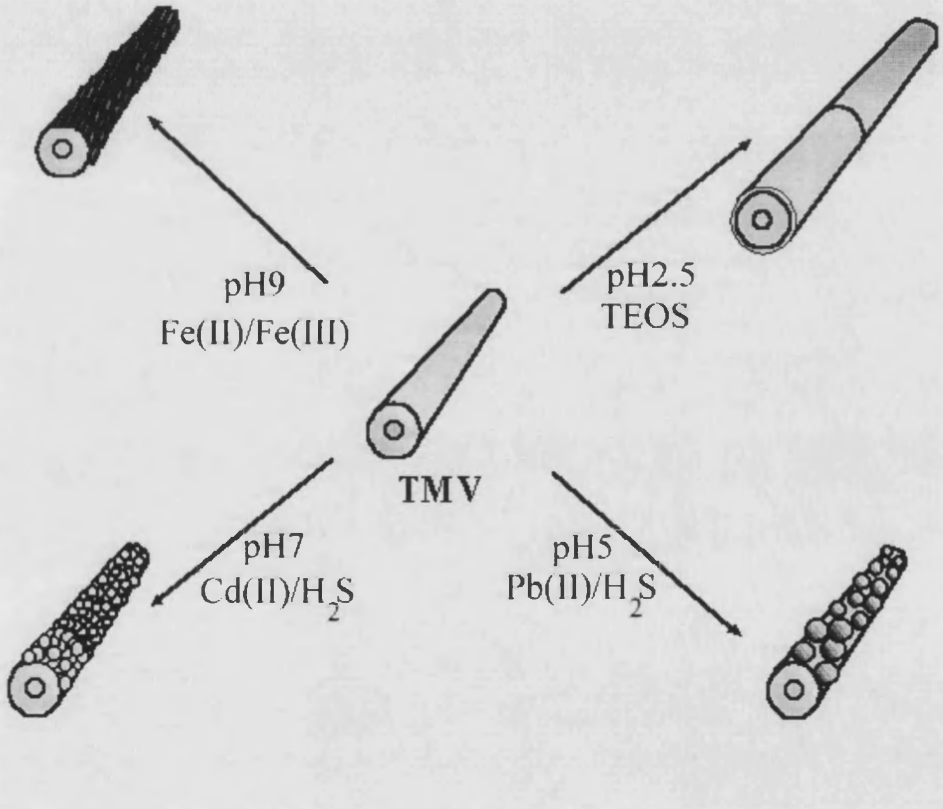

Figure 19 Schematic showing the potential of TMV in the formation of a wide variety of nanotube composites.

The schematic demonstrates that TMV can function at a range of pH values as a nucleation template. Acidic conditions were employed to form huge self assembled

silica/TMV macro-tubes, as well as nanocrystalline templated nanotube arrays of PbS nanocrystals. Neutral pH was used to form exceptionally uniform CdS/TMV nanotube composites, possessing well arranged nanocrystals in the range of 5nm. Basic conditions were also employed to form nano-filaments of iron, displaying two distinct morphologies, dependent upon the ageing time.

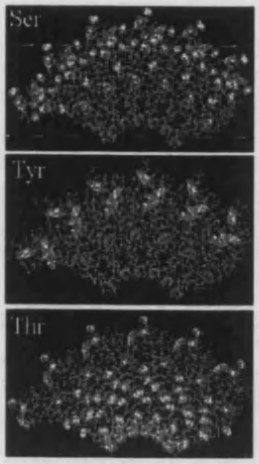

Figure 20 Computer generated images of TMV subunits arranged to show the surface location of hydoxyl containing amino acids, Ser, Tyr, Thr.

Silica mineralization of TMV resulted in very uniform, self assembled structures. The acidic conditions used would confer a net positive charge to the protein, resulting in a number of potential binding sites for the nucleation and subsequent polymerisation of the silica ions. There also exist numerous amino acid residues on the surface with exposed hydroxyl groups, which may serve to increase the affinity of each TMV surface for the silicate ions (Fig. 20). Future work would establish whether the internal channel remains accessible for positive ions to bind. It should therefore be possible in the longer term to couple the assembly of TMV superstructures with inorganic materials synthesis, for the fabrication of hierarchical inorganic-organic nanocable composites, with extremely high aspect ratios, possessing an internal mineralized conducting wire. Preliminary experiments intended to mineralise the interior channel with a conducting silver wire have produced tantalising results displaying evidence of the templating of silver wires 4nm in diameter.

In comparison to silica, preferential deposition of CdS, PbS and Fe oxides on the TMV external surface can be explained by specific metal-ion binding at the numerous glutamate and aspartate surface groups (Fig. 21). Interestingly, the inner surface has a high spatial density of glutamic acid residues, suggesting that nucleation within the 4 nm wide inner channel might have been expected under these conditions. Indeed it is difficult to ascertain whether specific nucleation within the central channel of each virion has occurred, due to the outer mineralized surface obscuring this observation with TEM. Further experiments would try to block the metal-ion binding sites on the external

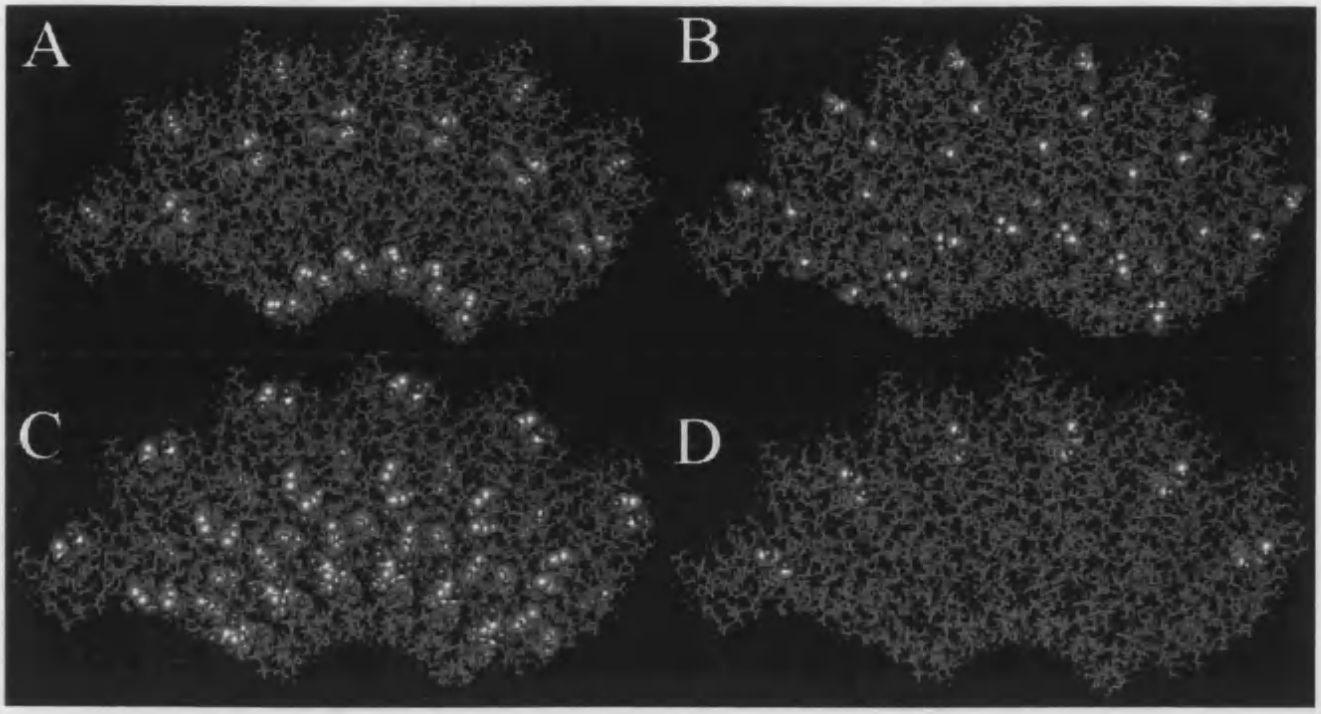

Figure 21 Computer generated images of seven subunits of TMV arranged as they would be in a native TMV particle with the uppermost side being exposed to the environment and the innermost representing the internal channel. A and B show the amino acids glutamic acid and aspartic acid and C and D represent arginine and lysine respectively. The high concentration of lysine seen in the centre of the protein is implicated in the association with the viral RNA.

surface, in order to facilitate the specific nucleation of viral-encapsulated inorganic nanowires. One aspect of TMV structure that needs further investigation affecting the mineralization of the interior of TMV is that the virus structure forms a 'faraday cage' (personal communication with Prof. G.Stubbs). This structural characteristic allows RNA to pass through the internal channel during self assembly, despite the high degree of negative charge (Fig. 22). Nothing is known about the affect of this structural feature on the internal binding of ions, but recently new initiatives have been suggested for its investigation. It may also be possible in the longer term to control the assembly of mineralized TMV superstructures - as observed for the silica and iron oxide systems - in order to extend the hierarchical organisation of nanotubular composites produced by biomolecular templating.

In summary, the use of TMV as a biotemplate in the formation of nanotubular assemblies presents a wealth of future work. The main aspect will focus upon the higher ordered self assembly of the virus into macro-assemblies, possessing lengths of several

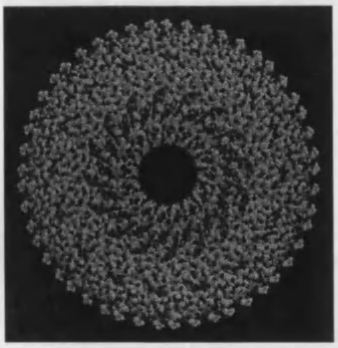

Figure 22 Computer generated image of a cross section of a TMV particle, revealing the 4nm internal channel lined with glutamic acid residues.

microns. This mode of self-assembly could be coupled with the mineralization of the internal channel, which would lead to the formation of an insulated nanowire.

Another interesting avenue of research could be investigation into the self assembly aspects of TMV. As mentioned, the self-assembly of individual particles is initiated through the formation of precursor discs, under appropriate conditions these discs can be isolated. A change in chemical environment then facilitates the transformation of these discs into the 'lock-washer' structure, which associate and eventually form the TMV particle. This process is likened to a molecular switch, which may be tailored in some way to allow the self-assembly of huge protein tubes via the controlled self assembly of the constituent discs. The coupling of this process to the internal and external mineralisation, developed in this chapter, could produced specific self assembled nanocircuitry, with conducting inner cores.

7.5 References

1 M.J.McLachlan, P.Aroca, N.Coombs, I.Manners, G.A.Ozin (1998) MCM-41 precursors to Magnetic Iron Nanostructures, *Adv. Mater.*, **10**, p144-147

2. G.Che, R.B.Lakshimi, C.R.Martin, E.R.Fischer, R.S.Ruoff (1998) Chemical vapour deposition based synthesis of carbon nanotubes and nanofibres using a template method., *Chem. Mater.*,**10**, p260-265

3. A. Zettl (1996) Non carbon Nanotubes, *Adv. Mater,***8**, p443-445.

4. Q. Huo (1997) High Quality hexagonal phase mesoporous silica fibres, *Adv. Mater,* **9**, p 974-976.

5. S.Iijima (1991) Carbon Nanotubes, *Nature*, **354**, p56-58

6. R.F.Service (1998) Superstrong Nanotubes Show They Are Smart, *Science*, **281**, p940-942

7. P.G.Collins, H.Bando, A.Zettl, (1998) Nanoscale electronic devices on carbon nanotubes, *Nanotechnology*, **9**, p153-157

8. G.Nagy, M.Levy, R.Scarmozzino, R.M.Osgood, H,Dai, R.E.Smalley, C.A.Michaels, G.W.Flynn, G.F.Mclane, (1998) Carbon nanotube tipped atomic force microscopy for the measurement of <100nm etch morphology on semiconductors, *Appl.Phys.Lett.*, **4**, p529-531

9. S.A.Curran, P.M.Ajayan, W.J.Blau, D.L.Carrol, J.N.Coleman, A.B.Dalton, A.P.Davey, A.Drury, B.McCarthy, S.Maier, A.Strevens (1998) A composite from poly(m-phenylenevinylene-co-2,5-dioctoxy-p-phenylenevinylene) and carbon nanotubes, *Adv. Mater.*, **10**, p1091-1093

10. F.Giullieri, M.P.Krafft, J.G.Rjess (1994) *Angew.Chem.Int.Ed.Engl*,**33**, p1514-1515

11. F.M.Menger, S.S.Lee, X.Tao (1995) Noncovalent synthesis of Organic Fibres, *Adv. Mater*, **7**, p660-671

12. Y.Zhang, K.Suenaga, C.Colliex, S.Iijima (1998) Coaxial Nanocable: Silicon Carbide and Silicon Oxide Sheathed with Boron Nitride and Carbon, *Science*, **281**, p973-975

13. M.R.Ghadiri (1995) Self assembling Nanoscale Tubular Assemblies, *Adv. Mater.*, **7**, p675-677
14. Z.Cai, J.Lei, W.Liang, V.Menon, C.R.Martin (1991) Molecular and supermolecular origins of enhanced electronic conductivity in template-synthesised polyheterocyclic fibrils. *Chem.Mater.*, **3**, p960-967
15. C.R.Martin, L.S.Van Dyke, Z.Cai, W.Liang (1990) Template synthesis of organic microtubules, *J.Am.Chem.Soc.*, **112**, p8976
16. D. D. Archibald, S. Mann (1993) Template Mineralization of self-assembled Anisotropic Lipid Microstructures, *Nature*, **364**, 430
17. P.M.Ajayan, S.Iijima (1993) Capillarity-induced filling of carbon nanotubes, *Science*, **361**, p333-334
18. M.J.Dabrowski, W.M.Atkins (1995) Engineering Macromolecular Self-Assembly : Molecular Tubes Vs. Protein Sheets, *Adv. Mater.*, **7**, p1015-1017
19. R.Martienssen (1998) Transposons, DNA methylation and gene control, *Trends Gen.*, **7**, p263-264
20. D.I.Friedman (1992) Interaction between bacteriophage lambda and its E.Coli host, *Curr. Opin, Genet. Dev.*, **2**, p727-738
21. F.M.Ohnesorge, J.H.Horber, W.Harbele, C.P.Czerny, D.P.E.Smith (1997) AFM review study on pox virus and virus cells, *Biophysical Journal*, **4**, p2183-2194
22. Stubbs, G., (1990) Molecular structure of viruses from the tobacco mosaic virus group, Seminars in Virology 1, 405-412.
23. Stubbs, G., (1984) *Macromolecular interactions in tobacco mosaic virus : Biological Macromolecules and Assemblies*, Vol. I, Wiley, New York, p149-202
24. H.Fraenkel-Conrat, R.C.Williams (1955), *Proc. Natl. Acad. Sci. U.S.A.*, **41**, p690-695
25. A.Klug, (1983) From molecules to biological assemblies, *Angew. Chem. Int. Ed. Engl.*, **22**, p565-636

Chapter 8

Summary and Perspectives

Some see things as they are and ask why.
I dream of things that never were and ask why not

George Bernard Shaw

8.1 Summary

The work described in this thesis has attempted to formulate the foundation of a new area of materials synthesis, that of nanophase biomolecular chemistry. Through the systematic application of biomaterials from the major divisions of life, the scope and potential of the use of biomolecules in the field of materials synthesis was detailed. A number of areas were addressed, including template mineralization, self assembly and the formation of hybrid disciplines, combining synthetic techniques with biomolecular chemistry. It was shown that biomolecules can be used in a number of ways to produce solutions to problems of current technological interest, from quantum dot synthesis and superlattices to nanotubular composites and self assembled nanostructured materials.

A major aspect of the work is the versatility of each system upon application to the area under investigation. Invariably, each system was shown to display higher properties that enabled a flexibility in synthesis, resulting in a number of further avenues of research not possible with comparable synthetic protocols. For example, tobacco mosaic virus was shown to act as a highly specific template in the fabrication of a number of inorganic/organic nanotube composites. TMV was also shown to possess the ability to self assemble into hierarchical 'tubes of tubes', due to the properties of TMV to associate end-to-end. In a number of systems, this higher order self assembly was accentuated by the experimental conditions. Lumazine synthase was shown to act as a template in the synthesis of quantum dots, but also to possess the ability to rearrange the subunits of the protein into alternative morphologies, most notably tubes. Previous utilisation of templates in inorganic crystallisation employed the use of static templates, whereas lumazine synthase represents a dynamic template offering the potential of controlled mineralization in the synthesis of inorganic morphologies. Although unequivocal evidence for the ability of this enzyme to induce the formation of tubular minerals was not given, it seem reasonable to assume that the templating action of these higher order structures would remain feasible. S-layers were also shown to act as highly specific templates in the fabrication of superlattice arrangements of CdS quantum dots. Almost all synthetic methodologies employed in the fabrication of quantum dot arrays have been restricted to two dimensional arrays. Colloidal crystallisation has been shown to be useful in the production of three dimensional arrangements of nanoparticles[1], but obviously

lacks any degree of control. However, S-layers were shown to produce two-dimensional arrays of nanoparticles and the system also demonstrated the capability of self assembly into two-tier double layers, which were shown to fabricate regular three dimensional arrays of CdS nanoparticles. The ability of S-layers to self assemble into these three dimensional templates can also be attained through the use of Langmuir-Blodgett (LB) technology[2]. Thus, the restrictions inherent to a number of templating strategies in the formation of nanoparticultate arrays was again surpassed by use of this biomaterial.

The formation of three dimensional structures through non-template based self assembly strategies was then explored by use of another class of biomaterial, antibodies. This hybrid system, combining synthetic chemistry with biomolecular chemistry, was shown to produce colloidal aggregates on a scale not seen in previous work. The system was shown not to be restricted to the problems of previous methodologies and preliminary work into the production of bi-metallic aggregates was outlined. Through a combination of refinement of the antibody/colloid conjugates and antigen engineering, it is anticipated that a variety of polymetallic aggregates could be synthesised.

Overall, the crux of each chapter was to address one aspect of current technological interest with a biomolecular system from the eukaryotic, prokaryotic and viral domains of life. This ideology was validated and a number of higher order systems, surpassing present methodologies in the area, were also found. Consequently, a number of materials possessing novel properties for the fabrication of a new generation of materials was produced. For example lumazine synthase composites represent particularly exciting examples, with possible applications ranging from new antibiotics to drug delivery systems. Tobacco mosaic virus composites show promise in the fabrication of insulated 'co-axial cables', with diameters of a few nanometers, holding promise for the fabrication of nano-cicuitry, high density memory stores and highly efficient biosensors from S-layer composites may also be fabricated. Antibody induced organisation of matter also possesses a myriad of potential applications, resulting from both two and three dimensional hybrid structures, including photochemical cells, biosensors applications and nanodevices.

One intriguing aspect of the use of biomaterials, not explored in this work but presenting exciting prospects for the future, is the production of hybrid biomaterial

systems possessing the collated properties of a number of different biomolecules in a single system, for example hybrid inorganic/organic nanosuperstructures from antibody induced aggregation of the higher order structures of lumazine synthase.

8.2 Perspectives

Advances in biomolecular and chemical sciences have opened up the possibility of utilising biomaterials in technology. All systems employed in this work have capitalised on the properties of protein assemblies, therefore representing only a small area of biomolecule application. The other main classes of biomaterial, with potential for the fabrication of future biologically based materials, are bio-lipids and nucleic acids.

Nucleic acids have received an enormous amount of recent attention, with a number of applications from matter organisation[3], DNA crystals[4] and nano-polyhedra[5]. A recent fusion of DNA technology with silicon technology has resulted in 'bio-chips' of small DNA strands anchored onto the surface of silicon wafers[6]. These DNA chips are set to revolutionise molecular biology and genetics through application in the understanding of the complexities of gene expression. There is thus an unabated interest in the utilisation of DNA in the fabrication of new materials, with undoubted production of a number of future DNA based materials. The nucleic acid RNA may also enter the stage in the production of nucleic acid based materials, but currently the isolation of suitable amounts of raw material is costly and consequently a disadvantage.

Bio-lipids are the other main class of biomaterial and so far have received continued interest, with vesicles and liposomes being perhaps the main application, for example in gene delivery[7]. Langmuir-Blodgett films are promising matrix materials that resemble biomembranes in a number of respects, but are not restricted by the two layers[8]. Multilayer films are deposited on a solid surface by stacking monomolecular layers at the air-water interface. The resulting films possess interesting electrical and non-linear optical properties, but more importantly, may serve to embed ordered arrangements of macromolecules. The anticipated scope of LB films includes piezoelectric devices and pyroelectric detectors, photoelectric devices and optical sensors[9]. It has also been suggested that LB films could also serve as dynamic memory devices[10].

Proteins do however possess the greatest potential in the fabrication of materials for the future, due to their unparalleled physicochemical diversity. Genetic engineering makes it possible to alter the primary and therefore tertiary structure of proteins, resulting in modified function and organic chemistry can also be used to tailor these proteins with additional properties. Spectacular advances in molecular biology continue to allow greater precision in the manipulation of the molecules of life and electronic engineering may even allow the control and detection of signals emitted from certain classes of protein molecule. These techniques may therefore offer the conversion of individual proteins into custom designed 'organo-machines'.

Commercial use of biomaterials requires that they compete with silicon-based devices in terms of production cost and functional performance. Niches for which present day technologies are not suited represent the most promising aspect. Biosensors are just one example, being composed of a molecular recognition unit and a transducer that converts a chemical signal into electrical or optical output. Computing represents another area of potential application, with bacteriorhodopsin (see Chapter 1) representing the most viable contender for the construction of a biological computer as well as neural networks based on two dimensional arrays of this light driven proton pump[11].

Nature has spent billions of years perfecting a plethora of biomolecules, participating in a myriad of specialised roles in order to sustain life. By blurring the line between synthetic and natural, these biomolecules can become elements in novel hybrid materials, setting the stage for new biological computers, medical diagnostic tools, chemical sensors and an armada of raw materials for nanotechnology.

8.3 References

1 Z.L.Wang (1980) Structural analysis of self-assembling nanocrystal superlattices, *Adv.Mater.*, **10**, p13-29

2 U.B.Sleytr, M.Sara, P.Messner, D.Pum (1994) Two-dimensional protein crystals : Fundamentals and applications, *Journal of Cell Biochemstry*, **56**, p171-176

3 C. A.Mirkin, R. L.Letsinger, R. C.Mucic, J. J.Storhoff (1996) A DNA-based method for rationally assembling nanoparticles into macroscopic materials, *Nature,* **382**,p607-609.

4 E.Winfree, F.Liu, L.A.Wenzier, N.C.Seeman (1998) Design and self assembly of two-dimensional DNA crystals, *Nature*, **394**, p539-544

5 Y.Zhang, N.C.Seeman (1994) The construction of a DNA truncated octahedron, *J.Am.Chem.Soc.,* **116**, p1661-1669

6 R.F.Service (1998) Microchip arrays put DNA on the spot, *Science*, **282**, p396-399

7 L.L.Mak, D.Henderson, E.A.Bauer, W.K.Hottler (1995) In-vitro and in-vivo approaches to cutaneous gene therapy using liposome-mediated gene transfer, J.Biol.Chem, 104, p629-635

8 P.Ball (1994) *Designing the molecular world : Chemistry at the frontier*, Princeton, 1st ed., Princeton University press.

9 A.Ulman (1991) *An introduction to ultrathin organic films-from Langmuir-Blodgett to self assembly*, Boston, Academic Press.

10 P.E.Burows, E.G.Wilson (1990) The inchworm memory-a new molecular electronic device, *Journal of Molecular electronics*, **6**, p209-220

11 D.Haronian, A.Lewis (1991) Elements of a unique bacteriorhodopsin neural network architecture, *Appl.Opt.*, **30**, p597-608

Publications

Synthesis of cadmium sulphide superlattices using self-assembled bacterial S-layers

Wayne Shenton*†, Dietmar Pum‡†, Uwe B. Sleytr‡ & Stephen Mann*

* *School of Chemistry, University of Bath, Bath BA2 7AY, UK*
‡ *Center for Ultrastructure Research and Ludwig Boltzmann Institute for Molecular Nanotechnology, Universität for Bodenkultur Wien, Vienna, Austria*
† *These authors contributed equally to this work*

Methods for organizing materials at the nanometre scale have advanced tremendously in recent years[1,2]. One important objective is the synthesis of patterned arrays of inorganic nanocrystals[3–6], whose optical, electronic and magnetic properties might find technological uses, for example as memory elements. Techniques such as colloidal crystallization[7–9], monolayer deposition[10–12], multilayer casting[13], molecular crosslinking[14,15], the use of complementary interactions[16,17] and the synthesis of nanoparticles in patterned etch pits[18] have been used to organize nanocrystals into superlattices. Here we describe the use of bacterial S-layers—self-assembled, two-dimensionally ordered films of proteins that feature in many bacterial cell walls—as templates for the *in situ* nucleation of ordered two-dimensional arrays of cadmium sulphide nanocrystals about 5 nm in size. Nucleation of the inorganic phase is confined to the pores between subunits in the S-layers. Two-tier stacks of nanoparticles can be formed in the presence of double-layered protein crystals. The structural diversity of S-layers[19,20], their ease of self-assembly on a wide range of substrates and the potential for surface chemical modification suggest that this approach could be exploited to offer a wide range of ordered nanoparticle arrays.

With a few exceptions, S-layers represent an almost universal feature of archaebacterial cell envelopes, and have been identified in many different species of nearly every taxonomic group of walled eubacteria[19,20]. S-layers are two-dimensional crystalline structure of single protein or glycoprotein monomers (relative molecular mass, M_r, 40,000 to 200,000), and exhibit either oblique ($p1$, $p2$), square ($p4$) or hexagonal ($p3$, $p6$) lattice symmetry with spacings between the morphological units in the range 3–30 nm (ref. 20). Most S-layers are 5–15 nm in thickness, possess pores of identical size and morphology in the 2–6 nm range, and have inner and outer surfaces that are markedly different in topography and physicochemical properties[21]. Although considered primarily as a filtration and structural matrix, S-layers have been implicated in cell wall biomineralization[22,23], suggesting a possible biomimetic role for these proteins as templates in materials chemistry.

Our approach to using S-layer templates for inorganic superlattice construction is illustrated in Fig. 1 (see Methods for details). Figure 2a shows a typical monolayer of the self-assembled S-layer of *Bacillus stearothermophilus* NRS2004/3a variant 1. The sample was negatively stained with uranyl acetate, which penetrates the nanoporous protein structure to reveal an oblique lattice (space group, $p1$; $a = 9.8$ nm, $b = 7.5$ nm, $\theta = 80°$). The protein fine structure, which appears white in the stain exclusion pattern, is imaged to a resolution of ~2 nm. Similar studies with recrystallized S-layers of *B. sphaericus* CCM 2177 revealed a square lattice with a unit cell length of 13 nm (data not shown). Mineralization of the exposed inner face of the self-assembled proteins (see Methods) produced S-layers that were decorated with an organized array of CdS nanoparticles in register with the underlying periodicity of the protein lattice (Fig. 1a). Thus, an oblique inorganic superlattice ($a = 9.8$ nm, $b = 7.5$ nm, $\theta = 80°$) was formed using self-assembled *B. stearothermophilus* NRS 2004/3a variant 1 S-layers (Fig. 2b), whereas a square superlattice ($a = 13$ nm) was templated on the inner face of recrystallized *B. sphaericus* CCM 2177 S-layers (Fig. 2c). In both systems, the CdS clusters were discrete, relatively uniform in size (mean values; 5 nm (oblique lattice); 8 nm (square lattice)) and rounded in shape. Mineralized arrays with domain sizes up to 1 μm were observed.

Electron-diffraction patterns and high-resolution lattice images obtained with transmission electron microscopy (TEM) indicated that the CdS nanoparticles were crystalline with d spacings corresponding to the zinc blende structure (d spacings, 0.336, 0.206, 0.176, 0.133, 0.118 nm). The patterns showed no preferential orientation, indicating that the particles were not crystallographically aligned on the hydrophilic inner face of the assembled S-layer subunits. Although the presence of the inorganic array dominated the TEM images, a faint pattern of the protein structure with its typical handedness of connecting arms was visible in the background. This observation suggests that Cd(II) also stains the S-layer template, and that the CdS nanoparticles are deposited within the network of nanopores which are located between the protein subunits. This was confirmed by the digital diffraction patterns which showed only low-order reflections for the reciprocal oblique lattice of the S-layer monolayer.

CdS mineralization of the exposed outer face of *B. stearothermophilus* NRS2004/3 variant 1 S-layers (Fig. 1b) produced arrays of discrete 2–3 nm sized CdS particles that were preferentially deposited on the S-layer template (Fig. 2d). Electron diffraction gave broadened ring patterns with d spacings consistent with the zinc blende structure. Close examination of the micrographs revealed some periodicity in the CdS array but the extent of replication was significantly less than that observed for the nanoparticles formed on the inner surface of the protein template (Fig. 2b). In both cases, the results suggest that the inorganic clusters are located within the nanopores of the protein matrix. The inter-subunit spaces are larger on the inner face because of the higher surface corrugation compared with the relatively flat outer surface[24]. This difference in topography could account for the larger size of the CdS nanoparticles, as well as the increased fidelity in the periodicity of the inorganic arrays deposited on S-layers recrystallized with the inner face exposed. In addition, the inner face has a net negative charge and is less hydrophobic than the charge-neutral outer surface, suggesting that electrostatic binding of Cd(II) ions might also be important in site-directed nucleation.

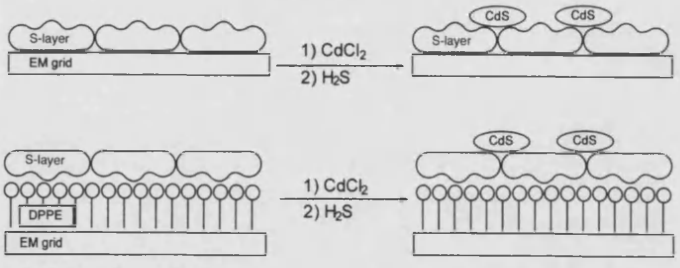

Figure 1 Substrate-assisted self-assembly of bacterial S-layer monolayers used for biocrystal templating of CdS superlattices. **a**, Recrystallization of S-layers on electron microscope grids produces a nanoporous monolayer with the corrugated negatively charged inner face exposed to the external medium. **b**, Corresponding orientation of a recrystallized S-layer formed under a Langmuir monolayer of the lipid, dipalmitoylphosphatidylethanol (DPPE) and transferred by horizontal dipping to an electron microscope grid. By this method, the charge-neutral outer face of the self-assembled S-layer is exposed[30]. In both systems, addition of a Cd(II) solution, followed by reaction with H_2S, results in site-specific nucleation in the inter-subunit regions to produce an organized array of CdS nanoparticles.

We also investigated the synthesis of CdS nanocrystal arrays using dispersed S-layer structures formed by recrystallization from bulk aqueous solution (see Methods). A well-defined square superlattice ($a = 13$ nm) of 5-nm-sized CdS crystallites was deposited on S-layers of *B. sphaericus* CCM2177 after 100 min of exposure to H_2S in the presence of Cd(II) (data not shown). In contrast, mineralization of the dispersed microstructures formed in suspensions of *B. stearothermophilus* NRS2004/3a variant 1 S-layers produced characteristic stripe patterns of organized CdS nanocrystals (Fig. 3A). Energy-dispersive X-ray analysis showed the presence of Cd and S throughout the S-layer sheets, and electron diffraction and high-resolution lattice imaging indicated that the individual CdS nanoparticles within the striped regions were non-oriented, ~5-nm-sized single crystals with the zinc blende structure. The most common stripe pattern consisted of fringes, 16 nm in width and spaced at ~32 nm, which were aligned parallel to the longer unit-cell vector of the underlying S-layer lattice (Fig. 3A). Digital diffraction patterns obtained from these images indicated that the stripe patterns were Moiré fringes which originated from the superimposition of two oblique CdS/protein superlattices with the longer base vector in common (Fig. 3B). The diffraction patterns showed mirror symmetry, indicating that the constituent S-layer/CdS monolayers were in a back-to-back orientation within a double-layered microstructure. In addition, the additional low-order reflection at 0.25 times the spacing of the longer reciprocal base vector (Fig. 3B) originates from the difference vector between the two shorter reciprocal base vectors, and corresponds to a repeat distance of 30 nm (4×7.5 nm) in the Moiré pattern. In this particular arrangement, the two associated back-to-back S-layers are in accurate register at every fourth row of the double-layered microstructure (Fig. 3C).

The data indicate that the double-layered protein template can be used to produce a stacked inorganic–organic assembly, consisting of an ordered two-tier arrangement of CdS nanocrystalline arrays. Previous experiments with polycationic ferritin, which is a topographical marker for net negatively charged domains on S-layer lattices, showed that the inner faces of the two constituent layers of the double-layered sheets were juxtaposed[25]. Thus, inorganic precipitation directly onto the exposed surfaces of the dispersed sheets should replicate the nanoporous lattice of the flat outer faces. As this face was relatively ineffective as a template when mounted as a lipid/protein monolayer on TEM grids (Fig. 2d), mineralization of the double-layered structure possibly involves Cd(II) penetration of the architecture followed by *in situ* sulphidation within the confined spaces of the corrugated internalized inner faces. Further work is required to determine the precise location of the CdS nanocrystallites in these hierarchical materials.

Although the inorganic nanoparticles are not crystallographically orientated within the S-layer matrix, the preferential deposition of CdS in association with the dispersed S-layers, rather than in bulk solution, suggests that molecular interactions between the functional groups of the protein surface and Cd(II) ions in solution could be important for the construction of the superlattice arrays. As previous studies have shown that S-layer proteins can be chemically modified with many different types of functional groups and molecules[26], tailoring the surface properties of these biocrystal templates to wet chemical synthesis could have significant advantages over metallization procedures[27] in fabricating a wide range of organized inorganic nanomaterials with semiconducting, magnetic or electronic properties. In particular, there is at present great interest in the formation of metal cluster arrays for coulomb charging behaviour in nanoelectronic digital circuits[28]. The strin-

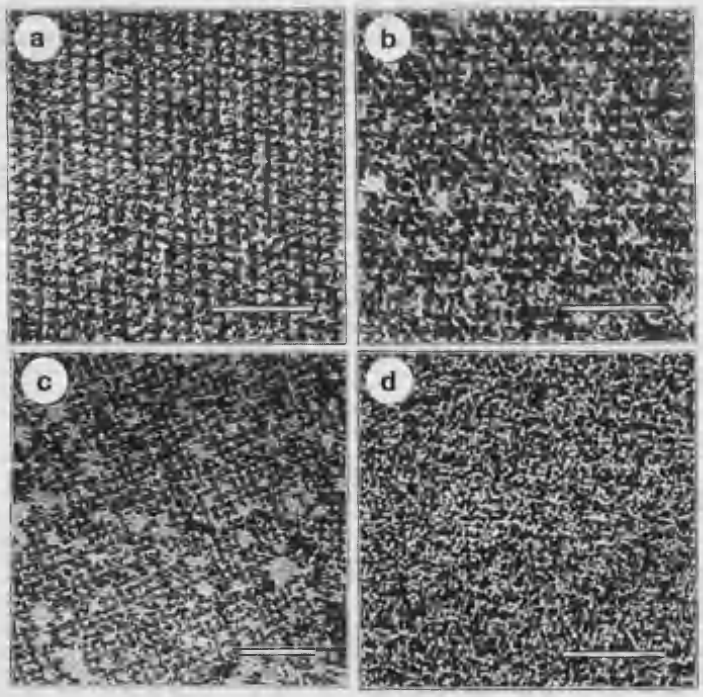

Figure 2 a, TEM micrograph of a negatively stained self-assembled S-layer of *B. stearothermophilus* NRS 2004/3a variant 1; scale bar, 60 nm. **b**, As for **a** but without staining and after CdS mineralization of the exposed inner face. The TEM image shows an oblique periodic array of uniform 5-nm-size CdS nanocrystals; scale bar, 60 nm. **c**, TEM micrograph showing a square CdS superlattice on the inner surface of a self-assembled *B. sphaericus* CCM2177 S-layer; scale bar, 100 nm. **d**, TEM micrograph of the mineralized outer face of an S-layer from *B. stearothermophilus* NRS2004/3a variant 1, showing CdS nanoparticles associated with the protein surface. The array shows weak periodicity (more readily observed by viewing the micrograph on its side); scale bar, 60 nm.

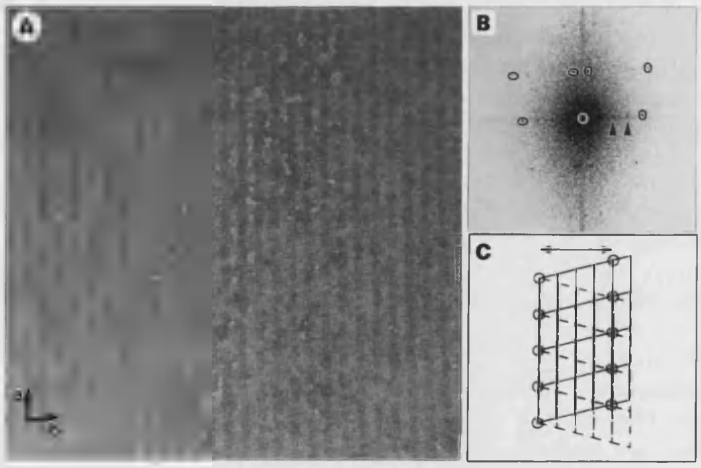

Figure 3 A, TEM micrograph of a mineralized double-layered sheet of *B. stearothermophilus* NRS2004/3a variant 1 S-layers, showing organized array of CdS nanoparticles and 32-nm stripe pattern due to Moiré effects; scale bar, 100 nm. **B**, Corresponding digital diffraction pattern showing superimposed oblique lattices with the longer reciprocal vector in common. The two reciprocal lattices are distinguished by either 0 or O symbols placed around their constituent reflections. The white circle corresponds to the centre spot and is the origin for both lattices. The composite pattern has mirror symmetry and additional lower-order reflections (arrow heads) spaced at 0.25 times the length of the longer reciprocal base vector. **C**, Sketch showing the relationship between two S-layers in back-to-back orientation within the double-layered sheet. The oblique real space lattices are coaligned on the longer axis and in register every four rows along the shorter base vector (arrow).

gent requirement for particle size monodispersity in such applications might be circumvented by directly synthesizing the nanoparticles in the presence of a suitable patterning agent. For this reason, the chemical synthesis of gold superlattices using S-layer templates is the principal objective of current and future work. □

Methods

S-layer proteins were extracted from isolated bacterial cell walls of *B. stearothermophilus* NRS 2004/3a variant 1 and *B. sphaericus* CCM 2177 as described previously[25]. S-layer subunits were reassembled on carbon-coated formvar-covered nickel TEM grids by placing the grids onto the surface of a 1 mg ml^{-1} buffered solution of the protein monomers for 2 h, after which the grids were removed by horizontal lifting, washed with distilled water, and the recrystallized S-layers chemically fixed with gluteraldehyde[29]. Recrystallized S-layers were mineralized by placing TEM grids containing unstained protein monolayers onto drops of 10 mM $CdCl_2$ solution for 2 h. The grids were then lifted and surplus solution removed by blotting before being placed in a vaccuum dessicator containing a dish of acidified Na_2S solution. Slow reaction of the hydrated samples with H_2S occurred for up to 2 d, after which the grids were removed and directly transferred into the electron microscope. Dispersions of self-assembled S-layers from either *B. stearothermophilus* NRS 2004/3a variant 1 or *B. sphaericus* CCM 2177 were incubated for 2 d in buffered (pH 7.2) 10 mM $CdCl_2$ solution. Drops of this suspension were then mounted on Ni TEM grids and placed in a vaccuum dessicator containing acidified Na_2S solution. Hydrogen sulphide gas was allowed to diffuse into the droplets over a period of 3 h, during which the grids were removed sequentially at regular time intervals, blotted on filter paper, washed with distilled water and left to dry in the air.

Received 11 March; accepted 8 July 1997.

1. *Nanostructured Materials* (spec. iss. eds Bein, T. & Stucky, G. D.) *Chem. Mater.* **8,** 1569–2194 (1996).
2. Mann, S. & Ozin, G. A. Synthesis of inorganic materials with complex form. *Nature* **382,** 313–318 (1996).
3. Chan, Y. N. C., Schrock, R. R. & Cohen, R. E. Synthesis of single silver nanoclusters within spherical microdomains in block copolymer films. *J. Am. Chem. Soc.* **114,** 7295–7296 (1992).
4. Spatz, J. P., Roescher, A. & Möller, A. Gold nanoparticles in micellar poly(styrene)-β-poly(ethylene oxide) films; size and interparticle distance control in monoparticulate films. *Adv. Mater.* **8,** 337–334 (1996).
5. Burkett, S. L. & Mann, S. Spatial-organization and pattening of gold nanoparticles on self assembled biolipid tubular templates. *Chem. Commun.* 321–322 (1996).
6. Braun, P. V., Osenar, P. & Stupp, S. I. Semiconducting superlattices templated by molecular assemblies. *Nature* **380,** 325–328 (1996).
7. Murray, C. B., Kagan, C. R. & Bawendi, M. G. Self-organization of CdSe nanocrystals into 3-dimensional quantum dot super lattices. *Science* **270,** 1335–1338 (1995).
8. Vossmeyer, T. *et al.* A double diamond superlattice built up of $Cd_{17}S_4(SCH_2CH_2OH)_{(26)}$ clusters. *Science* **267,** 1476–1479 (1995).
9. Motte, L., Billoudet, F., Lacaze, E. & Pileni, M.-P. Self-organization of size-selected nanoparticles into three dimensional superlattices. *Adv. Mater.* **8,** 1018–1020 (1996).
10. Colvin, V. L., Goldstein, A. N. & Alivisatos, A. P. Semiconductor nanocrystals covalently bound to metal surfaces with self-assembled monolayers. *J. Am. Chem. Soc.* **114,** 5221–5230 (1992).
11. Dabbousi, B. O., Murray, C. B., Rubner, M. F. & Bawendi, M. G. Langmuir-Blodgett manipulation of size selected CdSe nanocrystals. *Chem Mater.* **6,** 216–219 (1994).
12. Whetten, R. L. *et al.* Nanocrystal gold molecules. *Adv. Mater.* **8,** 428–433 (1996).
13. Kimizuka, N. & Kunitake, T. Organic 2-dimensional templates for the fabrication of inorganic nanostructures. *Adv. Mater.* **8,** 89–91 (1996).
14. Brust, M., Bethall, D., Schiffrin, D. J. & Kiely, C. J. Novel gold dithiol nanonetworks with non-metallic electronic properties. *Adv. Mater.* **7,** 795–797 (1995).
15. Andres, R. P. *et al.* Self-assembly of a 2-dimensional superlattice of molecularly linked metal clusters. *Science* **273,** 1690–1693 (1996).
16. Mirkin, C. A., Letsinger, R. L., Mucic, R. C. & Storhoff, J. J. A DNA based method for rationally assembling nanoparticles into macroscopic materials. *Nature* **382,** 607–609 (1996).
17. Alivisatos, A. P. *et al.* Organization of nanocrystal molecules using DNA. *Nature* **382,** 609–611 (1996).
18. Heath, J. R. *et al.* Spatially confined chemistry: fabrication of Ge quantum dot arrays. *J. Phys. Chem.* **100,** 3144–3149 (1996).
19. Sleytr, U. B., Messner, P., Pum, D. & Sara, M. (eds) *Crystalline Bacterial Cell Surface Proteins* (Landes Co., Austin, & Academic, San Diego, 1996).
20. Beveridge, T. J. Bacterial S-layers. *Curr. Opin. Struct. Biol.* **4,** 204–212 (1994).
21. Sara, M. & Egelseer, E. in *Crystalline Bacterial Cell Surface Proteins* (eds Sleytr, U. B., Messner, P., Pum, D. & Sara M.) 103–131 (Landes Co., Austin, & Academic, San Diego, 1996).
22. Schultze-Lam, S. & Beveridge, T. J. Nucleation of celestite and strontianite on a cyanobacterial S-layer. *Appl. Environ. Microbiol.* **60,** 447–453 (1994).
23. Lowenstam, H. A. in *Mechanisms and Phylogeny of Mineralization in Biological Systems* (eds Suga, S. & Nakara, H.) 3–8 (Springer, Tokyo, 1991).
24. Sara, M., Pum, D., Kuepcue, S., Messner, P. & Sleytr, U. B. Isolation of two physiologically induced varient strains of *Bacillus stearothermophilus* NRS 2004/3A and characterisation of their lattices. *J. Bacteriol.* **176,** 848–860 (1994).
25. Messner, P., Pum, D. & Sleytr, U. B. Characterisation of the ulstrastructure and self assembly of the S-layer of *Bacillus stearothermophilus* strain NRS 2004/3A. *J. Ultrastruct. Mol. Struct. Res.* **97,** 73–88 (1986).
26. Sleytr, U. B. & Sara, M. Bacterial and archael S-layer proteins: Structure-function relationships and their biotechnological applications. *Trends Biotechnol.* **15,** 20–26 (1997).
27. Douglas, K., Devaud, G. & Clark, N. A. Transfer of biologically derived nanometer scale patterns to smooth substrates. *Science* **257,** 642–644 (1992).
28. Tucker, J. R. Complementary digital logic based on the coulomb blockade. *J. Appl. Phys.* **71,** 4399–4402 (1992).
29. Pum, D., Sara, M. & Sleytr, U. B. Structure, surface charge and self assembly of the S-layer lattice from *Bacillus coagulans* E38-55. *J. Bacteriol.* **171,** 5296–5303 (1989).
30. Pum, D. & Sleytr, U. B. Large scale reconstitution of crystalline S-layer proteins at the air–water interface and on lipid films. *Thin Solid Films* **244,** 882–886 (1994).

Acknowledgements. W.S. thanks the University of Bath for a postgraduate studentship. This work was supported in part by the Austrian Science Foundation, Project S7204 and S7205, the Austrian Ministry of Science and Transportation, and the Austrian National Bank.

Correspondence and requests for materials should be addressed to S.M. (e-mail: s.mann@bath.ac.uk) or U.B.S. (e-mail sleytr@edv1.boku.ac.at).

Submitted to Adv. Mater. October 1998

Directed self-asssembly of nanoparticles into macroscopic materials using antibody-antigen recognition.**

By Wayne Shenton, Sean A. Davis and Stephen Mann *

[*] Prof. S. Mann, W. Shenton,
Department of Chemistry, University of Bath,
Bath BA2 7AY, UK.
current address: School of Chemistry, University of Bristol, Bristol BS8 1TS, UK.
Correspondence should be addressed to S.M (email: s.mann@bris.ac.uk).

[**] We thank the University of Bath for support of a postgraduate studentship to W.S. and the Leverhulme Trust for a postdoctoral fellowship to S.A.D.

The organization and patterning of inorganic nanoparticles into two- and three-dimensional functional structures is a potential route to chemical, optical, magnetic and electronic devices with useful properties. A range of non-lithographic protocols, including solvent evaporation of hydrophobic colloids [1-3], molecular cross-linking in colloidal aggregates[4-6] and template-directed synthesis using porous protein crystals [7,8] or bacterial superstructures[9] have been reported. Recently, two reports have highlighted the potential of using complementary DNA oligonucleotides attached to the surfaces of gold nanoparticles[10,11]. Here we describe a new biomolecular-derived route to the self-assembly of inorganic nanoparticles using the recognition properties of surface-attached antibodies. Our strategy involves the attachment of IgE or IgG antibodies with specificities to dinitophenyl (DNP) and biotin, respectively, to individual Au nanoparticles, followed by addition of antigens with appropriate double-headed functionalities. Antigens with homo- (DNP-DNP) or hetero- (DNP-biotin) "Janus" structures connected by at least an eight-atom spacer were synthesized for this purpose. The formation of specific antibody-antigen cross-links between the particles results in the formation of metallic or bimetallic aggregates comprising covalently-linked Au, or Au and Ag nanoparticles. In addition, we show that higher-order structures in the form of macroscopic filaments of the self-assembled nanoparticles are produced under certain conditions.

The versatility of using preformed nanoparticles, in association with antigen engineering should make it possible to produce a wide range of poly-metallic nanoparticle aggregates with specific cross-linked structures, compositions and macroscopic architectures. To test the feasibility of using antibody-antigen interactions in nanoparticle self-assembly, we studied three systems (Figure 1). Firstly, we attached anti-DNP IgE antibodies to 12 nm-sized nanoparticles to a give claret red sol which, unlike the non-conjugated (citrate-coated) colloid, was stable for several weeks in 0.1 M NaCl solutions. TEM micrographs showed discrete Au nanoparticles of uniform size distribution which were well-separated when air-dried onto the TEM support film (Fig. 2a). An antigen molecule (bis-N-2,4-dinitrophenyloctamethylenediamine), consisting of two DNP headgroups separated by a

linear eight-carbon chain, was synthesized by nucleophilic addition of 1,8- diamino-octane to 2,4-dinitrofluorobenzene, and added at an equivalence ratio to a saline solution of the anti-DNP IgE-coated Au nanoparticles. No aggregation was visible after mixing, but leaving the colloid unstirred for several hours at 4oC gave a macroscopic purple precipitate and a clear supernatent. These observations, along with corresponding turbidity measurements of the aggregating sols (data not shown), suggest that the DNP moieties at each end of the antigen molecules covalently cross-link the surface-attached IgE antibodies to produce a conjugated hybrid material with long range interconnectivity. This was confirmed by TEM examination of the precipitate which revealed large disordered 3-D networks of discrete Au nanoparticles (Fig. 2b).

As a second example, we employed two different antibodies which were used to prepare Au sols consisting of nanoparticles with surface-attached molecules of either anti-DNP IgE or anti-biotin IgG, both of which were stable in saline solutions for several weeks. A synthetic antigen with DNP and biotin groups at different ends of the molecule was synthesized by nucleophilic coupling of the primary amine moiety of DNP-lysine to sulfosuccimidyl-6-biotinamidohexanoate. FAB mass spectrometry, 1H NMR and FTIR spectroscopy data were consistent with a single product with the two haptens separated by a flexible spacer chain of 19 atoms. Addition of the hetero-Janus antigen to a solution containing a 1:1 ratio of Au nanoparticles coated with anti-DNP IgE or anti-biotin IgG, produced a purple filamentous precipitate and clear supernatent after 24hrs at 4oC. In some experiments, a single macroscopic thread could be observed suspended in the solution. Examination of the precipitate by TEM showed the presence of millimetre-long filaments which consisted of densely packed 3-D networks of Au nanoparticles (Fig. 3). Similar structures were not prevalent in the presence of the DNP-DNP antigen, suggesting that the increased conformational flexibility of the larger DNP-biotin hetero-construct facilitates long range aggregation of the Au nanoparticles. Indeed, the double-headed DNP connector requires at least eight carbon atoms to be effective in inducing the precipitation of soluble anti-DNP antibodies from solution[12]. The increased propensity for the antibody-coated nanoparticles to be assembled into unusual higher-order "Au-wires" in the presence of the flexible DNP-biotin antigen suggests that initial cross-linking interactions between particles can induce a directional bias in the network as it is extended by further antibody-antigen coupling. Filamentous structures of Au nanoparticles cross-linked with alkyl dithiols[6] have also been reported, although they appear to be limited to the meso- rather than the macro-scale as described here. The degree of anisotropy may be particularly large for the antibody-antigen system because of the large steric and electrostatic repulsive forces associated with coupling to neighbouring, rather than spatially separated, protein macromolecules on the surface of individual Au nanoparticles. Consequently, a single connection between two particles could produce differences in the antigen-binding affinities of the remaining uncoupled surface-attached antibodies, depending on their proximity to the interparticle cross-link. Overall, even small differences in the binding affinities could give rise to preferential alignment into particle chains and macroscopic filaments.

Finally, we have used our synthetic DNP-biotin antigen to demonstrate that bimetallic nanoparticle aggregates can be directed by biomolecular recognition. A dispersion of Au nanoparticles with surface-attached anti-DNP IgE molecules was mixed at a ratio of 1 : 1

with a Ag colloid (mean size = 12 nm) consisting of surface conjugated anti-biotin IgG antibodies, and an equivalent of the hetero-Janus antigen added. Whereas mixtures of the antibody-covered colloids alone showed no increase in turbidity, addition of the DNP-biotin antigen gave a black precipitate and clear supernatent when stored unstirred in the dark for 12 to 24 hours. TEM and energy dispersive x-ray analysis showed that the resulting hybrid materials consisted of heterogeneous aggregates and filaments of densely packed Au and Ag particles (Fig. 4). Although the TEM data provided compelling evidence for co-assembly of a bimetallic network of nanoparticles, the degree of integration observed in the images was not as high as would be expected for a process regulated solely by biomolecular recognition. This could be because the Ag particles were less homogeneous in size than the Au clusters and susceptible to self-association at the experimental pH of 9. Further work, involving metallic and semiconductor colloids with better size matching and pH stability is in progress.

In general, the development of bio-derived routes to organized forms of inorganic matter should be a powerful tool towards targeted structures due to the high specificity of biomolecular interactions. We have demonstrated the potential of antibody-antigen coupling as a strategy for the directed self-assembly of metallic nanoparticles into extended 3-D networks that can exhibit higher order structures such as wires and filaments. The ability to fabricate aggregates with controlled connectivity requires more sophisticated engineering of the antibody-antigen interface. However, the knowledge and methodologies currently available in molecular immunology should be sufficient to address these problems.

Experimental

Synthesis of homo-Janus DNP-DNP antigen: 1.0g of 1,8-diaminooctane (7 mmoles, Aldrich) was added to 15ml H2O followed by 1.5g Na2CO3 (14 mmoles) and dissolved by heating to 50oC on a water bath. 1.0g of 2,4-dinitrofluorobenzene(5 mmoles, Aldrich) was added directly to the rapidly stirred solution, followed by 50ml of water and the temperature raised to 60oC for 20mins, and then left to cool. The resulting yellow precipitate was filtered through a Buchner funnel and washed with aliquots of dil. Na2CO3 followed by dil.HCl. The yellow precipitate was placed in an oven at 80oC for 30 mins and then in a vacuum dessicator for 24hrs. The product showed low solubility in aqueous solutions and all experiments were subsequently performed using a saturated aqueous solution of the antigen. FTIR (NaCl); 3400 (NH), 1680 (NH), 1510 cm-1 (NO). 1H NMR spectroscopy (CD3OD) (, 7.0-9.5 (m, 6H, ArH), 4.9 (s, 4H, CH), 3.4 (m, 2H, CH), 1.8 (s, 12H, CH). FAB mass spectrometry; m/e = 477, (expected = 477).

Synthesis of hetero- Janus DNP-biotin antigen : 30 mg of DNP-Lysine (100 (moles, Aldrich) was dissolved in 20 ml H2O. The pH of the solution was raised to 10.5 by addition of 1 M NaOH. 50 mg of sodium sulfosuccinimidyl-6-biotinamidohexanoate (90 (moles, Vector Laboratories) was added slowly to the vigorously stirred solution. The pH of the solution was maintained at 10.5 over several days and the reaction monitored by thin layer chromatography. Dil. HCl was then added to give a pH of 2.5, that resulted in a yellow precipitate which was filtered on a Buchner funnel and washed with 30ml of acidified distilled water and air dried for 10mins. The yellow precipitate was place in a vacuum dessicator for several days. The product was reasonably soluble in aqueous

solutions although saturated solutions were usually employed in subsequent experiments. FTIR (NaCl) 3300 (OH), 1680 (NH), 1510 cm-1 (NO). 1H NMR spectroscopy (CD3OD). (, 7.0-9.0 (m, 3H, ArH). FAB mass spectrometry; m/e = 652.1 (expected =652).

Colloid synthesis. Au colloids were prepared according to the procedure described by Turkevich et al[13]. A solution of tetrachloroauric acid was prepared by dissolving 10mg HAuCl4.3H2O in 95ml distilled, deionized water. This solution was heated to boiling and 5ml of 1% aqueous sodium citrate solution was then added to the vigorously stirred solution. A claret red sol formed after several minutes. A Ag colloid was prepared in the dark as previously described[14]. AgNO3 (10 mg, pH = 6.8, Aldrich) was dissolved in 500 ml of ditilled, deionized water and brought to boiling. A solution of 1% sodium citrate (10ml) was added and the solution was kept boiling for 1hr. The sols were stable in the dark if kept at pH 6.8.

Surface attachment of antibodies. Monoclonal anti-DNP IgE and anti-biotin IgG antibodies (Sigma Immunochemicals) were attached to the surfaces of Au nanoparticles by identical procedures. Typical experiments involved raising the pH of the Au sol to 9 (ie. above the iso-electric point) by the addition of 0.5 M NaOH, followed by addition of the predetermined amount of antibody in borax buffer (typically, 10 (l of the 10 (g/ml antibody solution was added to 0.1 ml of the colloid). The sols were stable for several months. Preliminary titrations, utilising the red to blue colour change of the native Au colloid when exposed to high salt concentrations, were used to determine the correct antibody/colloid ratio required for effective surface coverage. This was ascertained by the increased stability (no red to blue colour change) of the Au colloid in the presence of a monolayer of surface-attached antibodies. Thus, exposure of these antibody-conjugated Au particles to 0.1M NaCl revealed no particle growth as shown by uv/vis spectroscopy, indicating that the colloidal ripening observed under these conditions for the uncoated colloid was arrested due to the adsorbed protein molecules. This was an important consideration because saline solutions were necessary for effective use of the antigens in the self-assembly experiments. Similar methods were used for the Ag colloid except that the anti-biotin IgG antibody was coupled to the nanoparticle surface at pH 6.8.

Antigen-directed self-assembly of aggregated structures. Synthesized Janus antigens were added to saline solutions (0.1 M NaCl , pH = 9) of the antibody-coated colloidal dispersions and left unstirred at 37oC for 30mins, and then incubated at 4oC for 12 to 24 hours. The amount of antigen required to achieve the equivalence ratio, and hence extensive cross-linking, was determined by a series of concentration-dependent experiments. Typically, between 10 and 30 (l of the saturated antigen solution were added to 0.1 ml of the Au/antibody colloid.

References

[1]. C. Petit, A. Taleb, M.-P. Pileni, Adv. Mater., 1998, 10, 259.
[2]. C. B. Murray, C. R. Kagan, M. G. Bawendi, Science, 1995, 270, 1335.
[3]. T. Vossmeyer,. Science 1995, 267, 1746.
[4]. B. A. Korgel, D. Fitzmaurice, Adv. Mat., 1998, 10, 661.
[5]. R. P. Andres, et al. .Science, 1996, 273, 1690.
[6]. M. Brust, D. Bethell, D. J. Schiffrin, C. J. Kiely,. Adv. Mat., 1995, 7, 795.
[7]. W. Shenton, D. Pum, U. B. Sleytr, S. Mann, .Nature 1997, 585-587.
[8]. S. Dieluweit, D. Pum, U. B. Sleytr, Supramol. Sci.1998, in press.
[9]. S. A. Davis, H. M. Patel, E. L. Mayes N. H. Mendelson, G. Franco, S. Mann, Chem. Mater. 1998, 10, 2516.
[10]. C. A. Mirkin, R. L. Letsinger, R. C. Mucic, J. J. Storhoff, Nature, 1996, 382, 607.
[11]. A. P. Alivisatos,. Nature 1996, 382, 609.
[12]. R. C. Valentine, N. M. Green J .Mol. Biol, 1967, 27, 615.
[13]. J. Turkevich, P. Stevenson, J. Hillier, Discuss. Faraday Soc, 1951, 11, 55.
[14]. P. Lee, D. Melsel, J. Phys. Chem, 1982, 86, 3391.

Submitted to Adv. Mater. **August 1998**

Inorganic-Organic Nanotube Composites From Template Mineralization of Tobacco Mosaic Virus**

By *Wayne Shenton, Trevor Douglas, Mark Young, Gerald Stubbs and Stephen Mann**

[*] Prof. S. Mann, W. Shenton,
Department of Chemistry, University of Bath,
Bath BA2 7AY, UK.

Dr T. Douglas, Department of Chemistry, Temple University,
Philadelphia, Pennsylvania 19122-2585, USA.

Prof. M. Young, Department of Plant Sciences, Montana State University,
Bozeman, MT 59101 USA

Prof. G. Stubbs, Department of Molecular Biology, Vanderbilt University,
Nashville, TN, USA.

[**] We gratefully acknowledge Giuseppe Ruggiero for work on computer-generated images of TMV.

The use of biological molecules, assemblies and systems in the development of inorganic materials synthesis continues to offer new and exciting alternatives to conventional synthetic strategies.[1] Biological templates, such as protein cages[2,3], viroid capsules[4], bacterial rhapidosomes[5], S-layers[6] and multicellular superstructures[7], biolipid cylinders[8,9], and DNA[10-13], have been utilized to direct the deposition, assembly and patterning of inorganic nanoparticles and microstructures. In this paper, we report a new approach to the template-directed synthesis of inorganic-organic nanotubes using tobacco mosaic virus (TMV).

TMV is a remarkably stable virion, remaining intact at temperatures up to 90°C and between pH values of 2 to 10. Each viral particle consists of 2130 identical protein subunits arranged in a helical motif around a single strand of RNA to produce a hollow protein tube, 300nm x 18 nm in size, with a 4 nm-wide central channel.[14,15] The internal and external surfaces of the protein consist of repeated patterns of charged amino acid residues, such as glutamate, aspartate, arginine and lysine.[16] In principle, these functionalities should offer a wide variety of nucleation sites for surface-controlled inorganic deposition, which in association with the high thermal and pH stability, could be exploited in the synthesis of unusual materials such as high-aspect-ratio composites and protein-confined inorganic nanowires. Here we show that TMV is a suitable template for reactions such as co-crystallization (CdS and PbS), oxidative hydrolysis (iron oxides) and sol-gel condensation (SiO_2) (Fig. 1).

Specific nucleation of CdS on the surface of dispersed particles of TMV was achieved by exposing a buffered suspension of the virions in 10 mM $CdCl_2$ to H_2S gas for up to 6 hours. Transmission electron microscopy (TEM) revealed the presence of mineralized tubular structures, approximately 50 nm in width, which consisted of a 16 nm thick electron dense outer crust and a 18nm diameter internal core. (Fig 2a). Energy dispersive x-ray analysis (EDAX) confirmed the presence of cadmium and sulfur in individual filaments, and high resolution lattice images indicated that the inorganic coating consisted of disordered aggregates of crystalline CdS particles, 5 nm in size (Fig 2b). The lattice spacings were in agreement with those obtained by selected area electron diffraction (SAED) of individual mineralized tubules which showed powder patterns (*d*-spacings; 0.336nm (111), 0.206nm (220), 0.176nm (311), 0.133nm (331), 0.118nm (422), corresponding to CdS nanoparticles with the Zn-blende crystal structure. The results were therefore consistent with a relatively uniform coating of CdS nanocrystals on the external surface of the TMV template. Although nucleation of CdS within the 4 nm diameter internal cavity of the protein structure could not be completely ruled out, most of the sample appeared to consist of hollow CdS-virion nanotubules.

Similar results were obtained when dispersions of TMV in buffered $Pb(NO_3)_2$ were exposed to H_2S gas. TEM and EDXA indicated that the black precipitate consisted of heavily mineralized TMV particles, approximately 40 nm in width (Fig 3). Individual virions were completely coated with a densely packed layer of PbS crystallites which were up to 30 nm in size and either prismatic or irregular in shape. Lattice images (Fig 3, inset) and SAED data were consistent with single domain PbS nanocrystals with the rock salt structure (*d*-spacings 0.344nm (111), 0.295nm (200), 0.209nm (220), 0.178nm (311)).

We also tested TMV as a potential template for sol-gel reactions. A suspension of the virions was added to a solution of tetraethoxysilane (TEOS) in acidified ethanol and stirred for 24 hours. The resulting white precipitate was filtered and re-suspended in distilled water prior to TEM analysis, which showed high contrast images of electron dense viral particles with a width of approximately 24nm (Fig. 4). EDAX showed the presence of Si, and SAED patterns corresponding to an amorphous mineral phase were obtained. The data indicate that the TMV particles are mineralized with a thin (3 nm) silica shell which is uniformly deposited along the length of the outer surface of the protein microstructure. Interestingly, many of the silicified nanotubes were several times the length of individual TMV particles (Fig. 4) suggesting that the virions self-assemble end-to-end along their long axis under the reaction conditions used. This mode of higher order self-assembly has been observed for TMV and is due to complementary hydrophobic interactions between the dipolar ends of the helical structure. The tendency to aggregate head-to-tail is accentuated under acidic conditions because the mutual repulsion between amino acid residues Glu50 and Asp77 is minimized by protonation.[17]

Iron oxide mineralization of TMV particles was achieved by addition of NaOH to a dispersion of virions in acidic Fe(II)/Fe(III) solution. A brown precipitate, which consisted of mineral-coated hollow TMV nanocylinders (Fig. 5a), was observed at alkaline pH values. The TEM/SAED data indicated specific nucleation and growth of the poorly crystalline iron oxide, ferrihydrite (*d*-spacings; 0.254 (110), 0.224 (200),

0.174 (114), 0.147 (106) nm), predominantly on the external surface of the protein microstructure. Whereas the initial stages of deposition gave rise to a coherent but irregular iron oxide coating (Fig. 5a), ageing the system for up to 6 months showed extensive outgrowth in the form of plate-like crystals of ferrihydrite (Fig. 5b). More regular, ultra-thin coatings of iron oxide were achieved by slow aerial oxidation of dispersions of TMV in anaerobic Fe(II) solutions at pH 6.5 (Fig. 5c). The mineralized virions had an average width of 22 nm, indicating that the iron oxide film was only 2 nm thick on the external surface of the protein template. Energy dispersive x-ray analysis confirmed the presence of iron and SAED data were consistent with an amorphous iron oxide mineral. Negative staining of the mineralized virions did not visualize the protein structure, confirming that inorganic deposition was specifically located on the external surface of the viral particle. In addition, many of the mineralized nanotubes were substantially longer than individual TMV particles (Fig. 5d). Aspect ratios up to 270 were observed compared with a value of 20 for the individual viral particles. These observations indicate that further assembly processes, similar to those observed for silicified TMV, can take place during iron oxide precipitation to produce mineralized structures organized on longer length scales.

Our results demonstrate the versatility of TMV as a template for the fabrication of a range of nanotubular inorganic-organic composites. The surface chemistry of TMV coupled with the unusual high stability of the protein assembly provide a structured substrate for the site-specific nucleation of a variety of inorganic solids at a range of pH values and reaction conditions. In the case of silica mineralization from acidic ($pH < 3$) solutions, there will be strong interactions between the TMV particles and anionic silicate species formed by hydrolysis of TEOS, because the protein surface is positively charged below the isoelectric point, and there are also a significant number of arginine and lysine groups on the virion surface (Fig. 6). In comparison, preferential deposition of CdS, PbS and Fe oxides on the TMV external surface can be explained by specific metal-ion binding at the numerous glutamate and aspartate surface groups (Fig. 6). Interestingly, the inner surface has a high spatial density of glutamic acid residues suggesting that nucleation within the 4 nm wide inner channel might have been expected under these conditions. Further experiments are in progress to block the metal-ion binding sites on the external surface in order to facilitate the specific nucleation of viral-encapsulated inorganic nanowires. It should also be possible in the longer term to control the assembly of mineralized TMV superstructures - as observed for the silica and iron oxide systems - in order to extend the hierarchical organization of nanotubular composites produced by biomolecular templating.

Experimental

TMV (strain, *vulgare* (U1), 30mg/ml) was stored in 10 mM sodium phosphate buffer at pH 7 and diluted to concentrations of 0.1mg/mL or 0.5 mg/mL for use in mineralization experiments.

CdS mineralization: A TMV suspension was incubated in a buffered solution of 10mM $CdCl_2$ (pH 7.2) for 6 hours. Droplets of the solution were mounted on a parafilm-covered glass slide placed in a vacuum dessicator. H_2S gas was allowed to slowly

diffuse into each droplet and aliquots were removed at varying time intervals over a period of 1 hour and air-dried onto nickel TEM grids.

PbS mineralization: H_2S gas was bubbled for 1 hour at a constant rate through a suspension of TMV in buffered 1 mM $Pb(NO_3)_2$ solution (pH 5.5). Droplets of the resulting black suspension were air-dried onto nickel TEM grids which were subsequently washed several times with distilled water.

Silica mineralization: A suspension of TMV was added to an ethanol/water mixture which was then acidified to pH 2.5 with dilute HCl. Tetraethoxysilane (TEOS) was added and the solution left to stir for 24 hrs. Aliquots (2 μL) were removed and centrifuged using a Centricon 10 micro-centrifuge. Distilled water (8 μL) was added and the pellet re-suspended and then centrifuged. This procedure was undertaken three times to remove excess TEOS.

Iron oxide mineralization: Two methods were used. Firstly, a suspension of TMV was mixed with an acidic solution containing 1 mM $(NH_4)_2SO_4 \cdot FeSO_4 \cdot 6H_2O$ and 2 mM $FeCl_3$ and left standing for 2 mins. 1 M NaOH was added dropwise to give a final pH of 9, producing a brown precipitate. An aliquot of the mineralized suspension was placed in a centrifugal filtration device with a 0.2 micron filter (Millipore). The suspension was centrifuged at 5000 rpm for 30mins. Droplets of the re-suspended material were placed on nickel TEM grids, which were subsequently washed with distilled water. The remaining mineralized TMV suspension was left for 6 months at room temperature and then filtered, washed and analysed by TEM. Secondly, anaerobic aliquots of $(NH_4)_2SO_4 \cdot FeSO_4 \cdot 6H_2O$ (15μL, 12 mM) were added to a stirred suspension of TMV (0.5 mg/mL) in MES buffer (0.1M, pH 6.4) and allowed to oxidise in air for 1 hour between additions (4 additions in total). The resulting suspension was washed with buffer and concentrated with a Microcon100. A drop of the concentrated sample was placed on carbon-coated Cu grids and examined by TEM.

TEM data were collected using either a JEOL 2000FX analytical TEM equipped with a Link AN10000 EDXA microanalysis system or Philips 400T TEM with a Kevex analyser.

References

[1]. *Biomimetic Materials Chemistry*, (Ed. S. Mann), VCH, , New York, **1996.**

[2]. K. K. W. Wong, T. Douglas, S. Gider, D. D. Awschalom, S. Mann, *Chem. Mater.* 1998, **10**, 279.

[3]. K. K. W. Wong, S. Mann, *Adv. Mater.,* **1996,** *8*, 928.

[4]. T. Douglas, M. Young, *Nature*, **1998**, *393*, 152.

[5]. M. Pazirandeh, S. Baral, J. R. Campbell, *Biomimetics*, **1992**, *1*, 41.

[6]. W. Shenton, D. Pum, U. Sleytr, S. Mann , *Nature*, **1997**, *389*, 585

[7]. . S. A. Davis, S. L. Burkett, N. H. Mendelson, S. Mann, *Nature,* **1997**, *385*, 420.

[8]. D. D. Archibald, S. Mann, *Nature*, **1993**, *364*, 430.

[9]. S. Baral, P. Schoen, *Chem. Mater.* **1993**, *5*, 145.

[10]. E. Braun, Y. Eichen, U. Sivan, G. BenYoseph, *Nature*, **1998**, *391*, 775.

[11]. C. A. Mirkin, R. L. Letsinger, R. C. Mucic, J. J. Storhoff, *Nature,* **1996**, *382*, 607.

[12]. A. P. Alivisatos, K. P. Johnsson, X. Peng, T. E. Wilson, C. J. Loweth, M. P. Bruchez, P. G. Schultz, *Nature*, **1996,** *382*, 609.

[13]. J. Coffer, S. Bigham, X. Li, R. Pinizzotto, Y. Rho, R. Pirtle, I. Pirtle, *Appl. Phys. Lett.* **1996**, 69, 3851.

[14]. G. Stubbs, *Seminars in Virology* **1990**. *1*, 405.

[15]. G. Stubbs, in *Biological Macromolecules and Assemblies*, Vol. I: *The Viruses* (Eds; A. McPherson, F. Jurnak), Wiley, New York, **1984**, pp. 149-202.

[16]. K. Namba, G. Stubbs, *Acta Crystallogr., A*, **1985**, *41*, 252.

[17]. B. Lu, G. Stubbs, J, Culver, *Virology* **1996**, *225*,11.